2020

Advanced Methods for Numerical Modelling of Regional Seas

Bruciaferri, Diego

http://hdl.handle.net/10026.1/15809

http://dx.doi.org/10.24382/1095
University of Plymouth

Advanced Methods for Numerical Modelling of Regional Seas

by

Diego Bruciaferri

A thesis submitted to the University of Plymouth
in partial fulfilment for the degree of

Doctor of Philosophy

School of Biological and Marine Sciences

March 2020

Acknowledgements

It has been an amazing journey this PhD and in the next few lines I would like to acknowledge and thank all the many people who took part on it.

First of all, the biggest thank goes to my Director of Studies Prof. Georgy Shapiro (University of Plymouth, UK) for his contagious passion for physics and oceanography, our long and fruitful discussions about geophysical fluid dynamics and ocean modelling and his many stories on life. This PhD would not have been possible without his guidance, advices, patience and encouragement. I would like also to thank my second and third supervisors, Prof. Tal Ezer (Old Dominion University, USA) and Dr. Fred Wobus (University of Plymouth, UK), for their constant assistance, suggestions and constructive ideas along the way.

I would like to thank also my viva examiners Prof. David Marshall (University of Oxford, UK) and Dr. Daniel Hatton (University of Plymouth, UK) for their valuable comments and suggestions which greatly helped to improve this PhD dissertation.

Thanks also to all the members of the Plymouth Ocean Forecasting Centre and Coastal Processes Research Group, for the nice time spent together and the work done. A special thank goes to my colleagues and now friends Francesco and Jose, for all the coffees, 'nerd' movies and science-based chats: I will never forget this amazing PhD period! I would like to thank also all my PhD and Marine Building colleagues and friends - Alessandro, Olivier, Mark, Erin, Marcus, Guio Mar, Carlos, Adam, Oliver, Yogang, Lewis, Davide. It has been great to share the office during these four years and thanks for all the sports played together and the nice dinners, beers and gigs we had - they made this period of my life even more enjoyable!

A huge thank goes also to my amazing family, my parents and my brothers, for their constant presence and support, always with me in all the important moments of my life: thanks for always believing in me!

... and then there is you, this PhD is also yours. Muchas gracias!

Author's declaration

At no time during the registration for the degree of Doctor of Philosophy has the author been registered for any other University award without prior agreement of the Doctoral College Quality Sub-Committee.

Work submitted for this research degree at the University of Plymouth has not formed part of any other degree either at the University of Plymouth or at another establishment.

This research was funded by the University of Plymouth.

Relevant scientific conferences and symposiums were regularly attended throughout the duration of this thesis, at which work was often presented and several papers were prepared for publication. At the time of completion of this thesis, two papers have been published in refereed journals and another one has been submitted for consideration of publication in a refereed journal.

Author contribution

The scientific material presented in this thesis was developed as part of multi-author publications.

- **Paper 1**: The idea of the Multi-Envelope s-coordinate system (MEs) was initially suggested by Prof. Shapiro and further developed by the author. The author developed the mathematical definition of MEs and introduced it in the NEMO ocean model, making several modifications to the model code. The author designed and conducted the numerical experiments and analysed the results producing all the the figures. The paper was written by the author with contributions from Prof. Shapiro and Dr. Wobus (some of the Introduction, as well as small parts of the Methods and Discussion).

- **Paper 2**: The idea of studying the effect of optimising the numerical mesh for the main dynamical processes on the accuracy of the simulation was developed in collaboration with the supervisors. The author set up the four Black Sea numerical models, developed the code to create the general curvilinear horizontal grid and the Black Sea envelopes and introduced the Bosphorus parameterization in the NEMO code. The author designed the numerical experiments and carried out all the simulations. Dr. Stanichny provided atmospheric forcing data. The author validated the results against observations together with Dr. Francis and Mr. Hilton. The paper was written by the author with corrections and comments offered by the entire supervisory committee and Dr. Zatsepin.

- **Paper 3**: The idea of studying the effect of different vertical mixing regimes in the Dead Sea was initially proposed by Prof. Shapiro and Dr. Gertman and further developed by the author. The author developed the modified vertical mixing parameterization and introduced it in the NEMO code under the supervision of the Director of Studies. The author set up the numerical model and designed the numerical experiments under the supervision of the Director of Studies. Dr. Gertman and Dr. Manasrah provided atmospheric and hydrological data. The author analised model results and produced all the scientific outputs and figures. The paper was written by all the authors. The author of this thesis wrote the part on the numerical modelling using part of the results included in Chapter 5 of this thesis.

Word count for the main body of the thesis: ≈ 51400

23rd June 2020

PhD outputs

Refereed Journal Publications

Under review

- Shapiro, G.,Gertman, I., Manasrah, R., **Bruciaferri, D.**. *The effect of thermohaline staircases on the sea level in the Dead Sea* (*submitted to Journal of Marine Systems*).

Peer-reviewed articles

- **Bruciaferri, D.**, Shapiro, G.I. and Wobus, F. (2018) *A multi-envelope vertical coordinate system for numerical ocean modelling.* Ocean Dynamics, Volume 68(10), Pages 1239-1258, doi:10.1007/s10236-018-1189-x.
- **Bruciaferri, D.**, Shapiro, G., Stanichny, S., Zatsepin, A., Ezer, T., Wobus, F., Francis, X., Hilton, D. *The development of a 3D computational mesh to improve the representation of dynamic processes: the Black Sea test case*, Ocean Modelling, 146 (2020), 101534, doi:10.1016/j.ocemod.2019.101534.

Conference presentations, posters and seminars

- **D. Bruciaferri**, G. Shapiro, S. Stanichny, A. Zatsepin, T. Ezer, F. Wobus, X. Francis and D. Hilton. *A new numerical model for the Black Sea circulation.* Geophysical Research Abstracts. Vol. 21, EGU2019-5933, 2019, April 2019 (*Oral*).
- **D. Bruciaferri**, G. Shapiro, S. Stanichny, A. Zatsepin, T. Ezer, F. Wobus, X. Francis and D. Hilton. *A numerical model of the Black Sea circulation using a*

structured multi-envelope mesh with variable resolution. Met Office seminars, 5^{th} March 2019, Exeter (UK) (*Oral*).

- **D. Bruciaferri**, G. Shapiro, S. Stanichny, A. Zatsepin, T. Ezer, F. Wobus, X. Francis and D. Hilton. *An advanced numerical model of the Black Sea.* PlyMSEF conference, Plymouth Marine Laboratoty, 5^{th} February 2019, Plymouth (UK) (*Oral*).
- G. I. Shapiro, R. Manasrah, I. Gertman and **D. Bruciaferri**. *The effect of different types of water column structure on the sea level in the Dead Sea.* Geophysical Research Abstracts. Vol. 20, EGU2018-19780, April 2018 (*Poster*).
- **D. Bruciaferri**, G. I. Shapiro and F. Wobus. *An Advanced Vertical Coordinate System to Improve the Representation of the Oceanic Transport in Regional Non-Isopycnal Ocean Models.* Abstract 310863 presented at 2018 Ocean Sciences Meeting, Portland, OR, 12-16 February 2018 (*Oral*).
- **D. Bruciaferri**, G. I. Shapiro and F. Wobus, *The development of an advanced vertical discretisation scheme for a regional ocean model.* Geophysical Research Abstracts. Vol. 19, EGU2017-7276, April 2017 (*Poster*).
- **D. Bruciaferri**, G. I. Shapiro, F. Wobus, *A coupled ocean-wave modeling system to investigate the role of the wave-induced turbulence on the Cold Intermediate Water formation in the Black Sea - The scientific approach*, NPOP conference, Bristol (UK), April 2016 (*Poster*).

Grants Awarded

Plymouth Marine Institute Education Fund: Grant-in-aid 2019. £400 awarded to attend EGU 2019, Vienna (Austria).

Abstract

Name: Diego Bruciaferri

Title: Advanced Methods for Numerical Modelling of Regional Seas

Regional seas are of paramount importance for human life. They play a key role in the planetary Earth system dynamics while they also represent a fundamental component of the global economy, making the overuse of ocean resources and the consequent degradation of local marine ecosystems a major concern of our society. Regional ocean modelling represents a powerful and efficacious tools to understand, manage and preserve the changing oceans and seas. This PhD research focuses on improving some of the techniques used for the numerical modelling of regional seas. This is done by developing a novel vertical discretisation scheme for numerical ocean modelling and conducting numerical experiments in an idealized domain as well as in two complex and contrasting real marine environments, the Black Sea and the Dead Sea.

In Chapter 3 a Multi-Envelope generalised coordinate system for numerical ocean modelling is introduced. In this system, computational levels are curved and adjusted to multiple 'virtual bottoms' (aka envelopes) rather than following geopotential levels or the actual bathymetry. This allows defining computational levels which are optimised to best represent different physical processes in different sub-domains of the model. In particular, we show how it can be used to improve the representation of tracer advection in the ocean interior. The new vertical system is compared with a widely used z-partial step scheme. The modelling skill of the models is assessed by comparison with the analytical solutions or results produced by a model with a very high resolution z-level grid. Three idealised process-oriented numerical experiments are carried out. Experiments show that numerical errors produced by the new

scheme are much smaller than those produced by the standard z-partial step scheme at a comparable vertical resolution. In particular, the new scheme shows superiority in simulating the formation of a cold intermediate layer in the ocean interior and in representing dense water cascading down a steep topography.

Chapter 4 deals with the numerical modelling of the Black Sea hydrodynamics. The Black Sea is one of the largest land-locked basin in the world. Due to the vulnerability of its unique marine ecosystem, accurate long-term modelling of its hydrodynamics is needed. Any ocean model contains inaccuracies which deviate simulations from reality and data assimilation (DA) is a widely used method to improve model results. Whilst there is abundance of sea surface data, measurements of water column profiles to be used for DA are much scarcer. Therefore, a model which generates smaller errors in free-run (without DA) is needed. In this Chapter we first compare the skills of four NEMO based Black Sea models in free-run which use different discretization schemes. We conclude that the best results are obtained with the model (named CUR-MEs) which uses Multi-Envelope curved vertical s-levels and a curvilinear horizontal grid. It has increased horizontal resolution ($\approx 950m$) over the shelf-break and lower resolution ($\approx 6km$) in areas where the scale of relevant processes is larger (about 20 km). The Multi-Envelope system is designed to optimize the representation of the Cold Intermediate Layer (CIL). Second, we compare CUR-MEs in free-run with the CMEMS operational Black Sea model using DA (CMEMS reanalysis). We conclude that in many aspects the skills of the two models are similar, and CUR-MEs is slightly better for representing independently obtained profiles. Finally, we investigate the variability of the Mean Kinetic Energy of geostrophic currents and the CIL simulated by our CUR-MEs model and CMEMS reanalysis.

In Chapter 5 we tackle the numerical modelling of the Dead Sea. From 1980s−1990s the Dead Sea water level is constantly decreasing, and currently it has an unprecedented rate of approximately 1.1 m/year. Since 2000, double-diffusive thermohaline staircases have been regularly observed during summer periods. Despite the increasing role of anthropogenic pressures, the evaporation−precipitation balance is still a significant factor which contributes to the recess of the sea level. In this Chapter we study the effect of different vertical mixing regimes on the features of Dead Sea water column and their potential impacts on its rate of evaporation. The methodology is based on simulating the evolution of the Dead Sea water column presenting thermohaline staircases with two contrasting numerical models. One is named SPP and it uses a standard vertical mixing scheme which does not take into account the presence of thermohaline staircases. The second is named MPP and it uses a vertical mixing parameterization compatible with the presence of step-like structures in the water column. Sensitivity experiments show that numerical horizontal pressure gradients errors, though small in both models, are higher in the MPP model, due to its ability to preserve the step-like structures of the initial condition which conversely are smoothed out in the SPP model. Realistic experiments indicate that, under the same atmospheric conditions, a vertical mixing regime typical of a water column presenting step-like structures might be able to reduce the heat transport to greater depths in comparison to a more diffusive diapycnal mixing, contributing to an increase of the Dead Sea water level recession by up to 0.1 m/year during the modelling period of August 2016.

Perhaps some day in the dim future it will be possible to advance the computations faster than the weather advances and at a cost less than the saving to mankind due to the information gained. But that is a dream. – L. F. Richardson, 1922

Imagination is more important than knowledge. Knowledge is limited. Imagination encircles the world. – A. Einstein, 1929

Contents

List of Figures

List of Tables

1. Introduction

1.1 The importance of the numerical modelling of regional seas

Human life depends on the oceans and seas. Approximately 40% of the human population is located within 100 km of the sea and much of the industrial activity takes place in coastal areas, involving sectors such as fisheries, mineral and hydrocarbons extraction, transport, recreation and offshore power generation. For example, it has been estimated that over 90% of global fish catches come from shelf seas, making coastal waters the dominant source of fish caught by humans all over the world (Simpson and Sharples, 2012).

Regional oceanic and coastal processes strongly influence the planetary Earth system dynamics, playing an active role in the global thermohaline circulation and water mass formation, sea level changes, the majority of the biogeochemical cycles and the global ecosystem (Brink and Robinson, 2005a; Robinson and Brink, 2006). For example, regional large-scale dense water cascades, such the ones occurring off the Artic and Antartic continental shelves, can drive or influence the formation of major ocean water masses, so affecting global energy fluxes, budgets and climate changes (e.g., Shapiro (2003); Ezer (2006); Wobus et al. (2013)). In addition, the shelves of many regional seas are areas of high primary production and they are supposed to play a very significant role in the global carbon cycle (Joint and Pomroy, 1993; Thomas et al., 2004; Simpson and Sharples, 2012). Regional coastal zones are also generally more responsive to external forcing than the open ocean, so that climate changes are likely to have the greatest impact and be experienced first in these areas (Mooers, 1999; Sündermann et al., 2001; Doukakis, 2008; Holt et al., 2014, 2018).

The massive exploitation of marine coastal resources (e.g., Jackson (2001); Gertman and Hecht (2002); Shapiro (2011); De Dominicis et al. (2018)) and the high anthropogenic pressure near the coasts (e.g., Mee (1992); Thomas et al. (2004); Conley et al. (2009); Carpenter (2018)) significantly threatens the integrity of the coastal ecosystems, making coastal management and protection issues an important concern of many national and international institutions (Mooers, 1999; Flemming, 2002).

Ocean modelling represents one of the most powerful and efficacious tools we can use to understand, manage and preserve the changing oceans and seas at regional scales. It permits to obtain a skillful quantitative estimate of the hydrodynamics over a selected oceanic region with a resolution that resolves the relevant physical quantities, a fundamental information required for the best management and preservation of the marine environment. Numerical modelling is a formidable task, allowing to carry out hindcasts and analysis of the dynamics in the last decades, accurate short term forecasts of regional seas states, as well as high resolution longer term climate projections and possible future scenarios for limited regions of the ocean (Robinson and Sellschopp, 2002).

1.2 Aims of the PhD research

The term *regional sea* is used to refer to both open ocean and inland seas. *Seas* of the World Oceans are limited regions of the oceans with local distinguishing oceanographic characteristics (Talley et al., 2011a). They include coastal ocean, marginal or semi-enclosed seas as well as portions of the oceans that are not divided off by land (Kantha and Clayson, 2000b). *Inland seas* are the termini of inland drainage basins (inflows but no outflows) that are partially to completely surrounded by tectonically stable continental crust (Condie, 2016). Some of them (e.g., the Caspian Sea) are the remnants of large oceans that closed in the geologic past, while others occur mainly in arid or semi-arid climatic zones (e.g., the Dead Sea) where net evaporation exceeds precipitation (Waiser and Robarts, 2009; Condie, 2016).

Many regional seas include some of the most complex environments in the world, where the prevailing physical processes encompass a broad range of spatial and time scales of interest (e.g., Ezer et al. (2005); Shapiro et al. (2011); Simpson and Sharples (2012)). The dynamic of a specific oceanic region depends on a variety of factors, including the geometry, geographical location and the dominant surface and coastal forcing (e.g., Kantha and Clayson (2000b)). This, creates particular and quite complex challenges for the numerical modelling of the hydrodynamics of regional and coastal seas (e.g., Holt et al. (2017)).

Numerical ocean models are inevitably affected by errors which compromise the accuracy of a simulation (e.g., Haidvogel and Beckmann (1999)). Data assimilation is a widely used method to constrain model drift, extending model prediction skill (e.g., Edwards et al. (2015)). However, while satellites provide an abundance of data of sea surface parameters, the measurements of water column properties are much scarcer (e.g., Pinardi and Woods (2002)). Therefore there is a need for models which generate smaller errors in free run (without data assimilation) and hence would require less observational data.

The overall aim of this PhD research is to contribute in improving of some of the techniques used for the numerical modelling of regional seas. This will be done by developing a novel vertical discretisation scheme for numerical ocean modelling and conducting numerical experiments in an idealized domain as well as in two complex and contrasting real marine environments. The first study case is the Black Sea, a low salinity ≈ 2.2 km deep semi-enclosed sea with a wide shelf. The second study case involves the Dead Sea, a hypersaline ≈ 300 m deep inland sea with narrow shelves.

The following are the research questions behind this PhD study:

1) The choice of the vertical coordinate system is of fundamental importance when designing an ocean model, especially in those regional areas where local multi-scale processes interact with large-scale oceanographic features. One of three basic vertical coordinates, z-level, terrain-following or isopycnic is often used in ocean models, but each has its own limitations and numerical errors (e.g., (Griffies et al., 2000a)).

   RESEARCH QUESTION:
   Is it possible to develop a vertical coordinate system able to optimise the representation of the prevailing physical processes at stake by combining the advantages of each standard vertical coordinate system but minimising their disadvantages?

2) Several numerical models of the Black Sea hydrodynamics exist, the majority of which uses standard discretization schemes. However, none of the current methods are free from errors. For example, most of the Black Sea numerical models in free-run fail to correctly reproduce the dynamics of the Cold Intermediate Water (e.g., Peneva and Stips (2005)).

   RESEARCH QUESTIONS:
   Is it possible to improve the accuracy of a Black Sea simulation in free-run mode by optimising the 3D computational mesh for the prevailing physical processes?

   Is the level of accuracy of this free-running simulation comparable with that of a data-assimilating model?

3) The sea level in the Dead Sea is currently decreasing at an unprecedented rate of approximately 1.1 $m/year$ (Lensky and Dente, 2017). After 2000, thermohaline staircases formed by salt fingering have been observed regularly during

summer in the water column of this hypersaline lake (Gertman et al., 2015; Arnon et al., 2016). Numerical modelling of the Dead Sea is very challenging (Brenner et al., 2015).

RESEARCH QUESTION:
What is the effect of different vertical mixing regimes on the structure of the water column in the Dead Sea and the potential impact on its evaporation rate?

1.3 Structure of the dissertation

The thesis is organised as follows.

In Chapter 2, first a review of some of the main characteristics of the dynamics of regional seas (Sec. 2.1) and the common practice used in regional ocean modelling (Sec. 2.2) is given. After, the main aspects of the physical oceanography and the numerical modelling of the Black Sea (Sec. 2.3) and Dead Sea (Sec. 2.4) and the principal features of the numerical ocean model used in this thesis (Sec. 2.5) are detailed.

In Chapter 3, a new vertical coordinate system named Multi-Envelope s-coordinate (MEs) is introduced. The new MEs is tested in an idealised process-oriented numerical set-up for horizontal pressure gradients errors, shelf cascading and the formation of a cold intermediate layer over a permanent thermocline. The accuracy of MEs is compared with the one of a widely used z-coordinate system with partial steps. Section 3.2 details the features of the new vertical coordinate system, Sec. 3.3 describes the set up of the three numerical experiments while the results are presented, analysed and discussed in Sec. 3.4. The main conclusions are summarised in Sec. 3.5.

In Chapter 4, the effect of optimising the 3D computational mesh for the prevailing physical processes on the accuracy of a Black Sea simulation is assessed and quantified. The four numerical models implemented for this study together with the design of the numerical experiments, the external datasets used to validate or to compare with models results and metrics used to asses models accuracy are described in Sec. 4.2. In Sec. 4.3, numerical results are presented and discussed while Sec. 4.4 summarises our main conclusions.

In Chapter 5, the effect of different vertical mixing regimes on the structure of the water column in the Dead Sea and the potential impact on its evaporation rate is investigated. Two contrasting numerical ocean models of the Dead Sea hydrodynamics are used to simulate the evolution of a water column initially presenting thermohaline staircases. Section 5.2 describes the two Dead Sea numerical models while Sec. 5.3 details the characteristics of the two numerical experiments. Section 5.4 presents, analyses and discusses the numerical results while Sec. 5.5 details the main conclusions.

In Chapter 6, the main findings of this thesis are summarised and recommendations for further research are given.

2. Literature review

In this Chapter, a review of the main aspects of the numerical modelling of regional seas and the main characteristics of the two study cases of this thesis is given. The Chapter is organised as follows. Section 2.1 describes the main physical processes occurring over the continental shelf and the shelf-break, common features of many regional seas (e.g., the Mediterranean Sea, the Bay of Biscay, the North Sea, the Arctic and Antarctic seas, the Black Sea, the Gulf of Mexico and the Caribbean Sea). Section 2.2 summarizes some of the state-of-the-art techniques used in regional ocean modelling. Sections 2.3 and 2.4 detail the main aspects of the physical oceanography and the numerical modelling of the Black Sea and the Dead Sea, respectively. Then, Sec. 2.5 presents the principal features of the numerical ocean model used in this thesis.

2.1 The Shelf Seas Dynamics

Shelf or coastal seas are among the most complex marine environments in the world (Haidvogel et al., 2000). They represent that portions of the oceans which are closest to the land and where marine water submerges the continental shelf (Huthnance, 1995), extending all the way from the coastline (including estuaries) to the edge of the abyssal plain of the adjoining basin (Kantha and Clayson, 2000b).

By definition they include two distinct morphological regions, the *shelf* and the *continental slope* (Brink and Robinson, 2005b). Shelf areas represent the 7.6% of the world oceans and the 13.3% of the Atlantic ocean (Sverdrup et al., 1942), typically spanning depths increasing from zero at the coast to $\approx$ 200 m at the shelf break and horizontal extension spanning from few to several hundred kilometres (Csanady, 1982). Continental slopes starts at the shelf break and are regions where there is a rapid increase in depth down to abyssal depths of 4 to 5 km over a short distance on the order of 20 to 100 km (Simpson and Sharples, 2012).

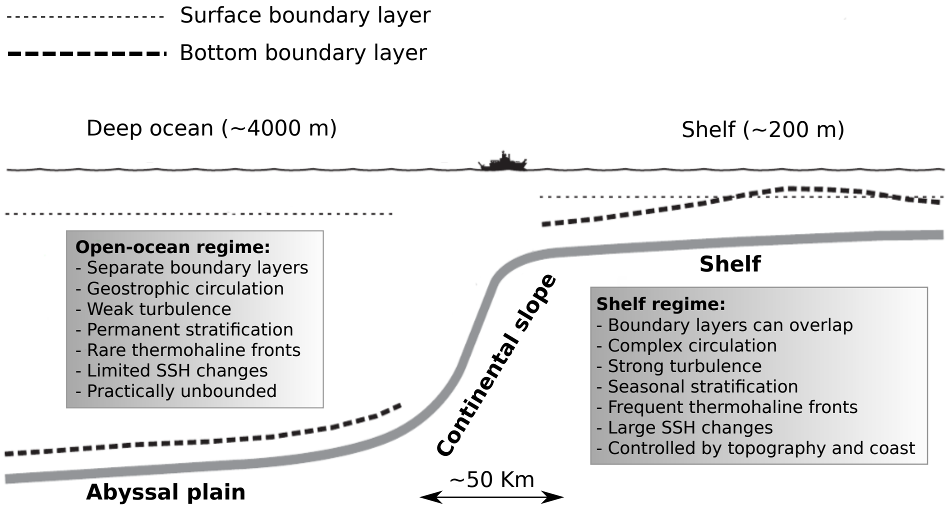

Fig. 2.1: Sketch outlining the morphology of the abyssal plain, the continental slope and the shelf (not in scale) and the contrasting dynamical regimes characterising the deep ocean and the shelf sea (redrawn after Simpson and Sharples (2012)). SB indicates the shelf-break.

The geography of these seas is very varied, including semi-enclosed seas, broad open shelves, narrow shelves exposed to the open ocean and coastal seas behind barrier islands (Holt et al., 2017). While many of the largest shelf seas can be found at high latitudes, sea-ice interactions are not considered in this thesis and the investigation is limited to liquid water modelling.

In addition, the attention is restricted to marine processes with characteristic length and time scales ranging from the large$-$ $\mathcal{O}(100-1000)$ km to the meso$-$ $\mathcal{O}(10-100)$ km and submeso$-$scales $\mathcal{O}(0.1-10)$ km, not considering smaller scale processes such as the ones occurring on the inner shelf and surf zone.

2.1.1 The dynamical regime of shelf seas

Physical forcing and mechanisms driving the ocean dynamics over the continental shelf and in the deep ocean are similar. For example, both marine environments are strongly influenced by the turbulent exchanges of heat and momentum between the atmosphere and the sea or by the Earth's rotation (Kantha and Clayson, 2000b; Simpson and Sharples, 2012).

However, coastal seas present a markedly distinct hydrodynamics. This is largely due to their proximity to land and their shallow depths, which causes their dynamical regime to differ radically in a number of aspects from that of the deep ocean (Holt et al., 2017), as illustrated in Fig. 2.1.

Shelf seas present highly energetic and turbulent surface and bottom frictional boundary layers, which occupy a large proportion of the total depth and which may overlap, promoting the complete mixing of the water column (Rippeth et al., 2001; Burchard et al., 2008). By contrast, in the deep ocean the upper and bottom mixed layers represent only a very small fraction of the total water depth, leaving a large interior region normally close to geostrophic balance and characterised by a very weak turbulence (Simpson and Sharples, 2012).

Ocean waves entering shallow waters grow in amplitude to conserve energy flux. This makes the shelf seas areas where, for example, tides and surface waves can be large and may represent a leading order process in the evolution of the coastal circulation and the vertical mixing (Huthnance, 1981; Simpson, 1998; Klingbeil et al., 2018; Valiente et al., 2019).

Coastal seas also present small thermal and mechanical inertia. This causes them to respond vigorously to the external forcing to which they are exposed, namely from the overlying atmosphere, the continental land and the adjoining deep ocean basin (Holt et al., 2017).

Winds (and to a lesser extent, the atmospheric pressure fluctuations, see e.g. Gill and Schumann (1974)) produce vigorous motions in the coastal oceans. For example, in shelf areas storms can cause large set-downs/set-ups (Masselink et al., 2016; Staneva et al., 2016) and wind-driven coastal upwelling/downwelling (Csanady, 1982) while in the open ocean wind forcing rarely causes strong sea surface height changes (Kantha and Clayson, 2000b; Talley et al., 2011b).

Shelf waters are also highly susceptible to the amount of the solar radiation they receive. This promotes the formation of well-mixed waters during colder months while it tends to develop a seasonal stratification in the warmer season. On the other hand, the deep ocean presents a permanent stratification which is generally not in thermal equilibrium with the overlying atmosphere (Rippeth, 2005; Holt et al., 2010).

Fresh water discharges from the continental land represent another important source of buoyancy forcing in the shelf seas, inducing buoyancy driven coastal currents which represent an important component of the shelf sea circulation (Simpson, 1997; Chapman, 2000; Hill et al., 2008).

In shelf seas, the local vertical structure of the water column is strongly determined by the dominant balance between stabilizing buoyancy forcing from surface heating and freshwater inputs, on the one hand, and mechanisms promoting vertical mixing, namely tides and wind stress, on the other (Simpson and Hunter, 1974; Simpson and Bowers, 1981). As a consequence, unlike in the open ocean, thermal and haline fronts are very common in coastal seas. They are generated by the influence of freshwater runoff, by surface heat fluxes interacting with horizontal variations of tidal mixing or by the inherently contrasting regimes of deep and shelf waters at the shelf edge (Simpson et al., 1978, 1981; Sharples and Simpson, 2009; Ivanov and Belokopytov, 2012).

Differently from the unbounded open ocean, shelf seas are also regions where extreme changes (compared with the water depth) in topography and irregularities in the coast exert a fundamental control on the hydrodynamics (Holt et al., 2009). For example, in coastal areas the oscillatory tidal motions can interact with local topographic (e.g sandbanks) or coastal (e.g. headlands) features and induce a mean circulation (Huthnance, 1973; Robinson, 1983; Polton, 2015). Also, the lateral and vertical boundaries of the continental shelf may act as an efficient waveguide for the propagation of sub-inertial motions generated elsewhere, promoting the development of a great variety of coastally trapped waves (Huthnance, 1975; Gill, 1982; Brink, 1991).

Relevant time scales of the coastal ocean are tidal or inertial cycles and diurnal or synoptic periods, i.e. $\mathcal{O}(1)$ day, therefore much shorter than the ones characterising the deep ocean. At the same time, the influence of the offshore ocean makes the life time of mesoscale eddies, i.e. order of week(s), another relevant time-scale over the continental shelf (Klingbeil et al., 2018).

Also the horizontal length scales of the dominant physical processes are generally much smaller than in the deep ocean. For example, let's consider barotropic tides propagating on the shelf as a Kelvin wave with scale given by the external Rossby radius $L_R = \sqrt{gH}/f$, where H is the water depth and f is the Coriolis parameter. As pointed out by Holt et al. (2017), in deep waters the Rossby radius L_R is large (> 1000 km) even at high latitude while on the shelf and near the coast it is ≈ 100 km. This is also the case for the first baroclinic Rossby radius $L_1 = c_1/f$ (where c_1 is the first-mode internal wave phase speed), which is the characteristic horizontal length scale of baroclinic eddies: it has values < 7 km over continental shelves (e.g. Fennel et al. (1991)), while in the deep ocean it is between 10 and 100 km (< 10 km at high latitude oceans).

Because of their dynamical regime, the coastal seas are the most dynamic regions of the ocean, where the circulation results from the combination of numerous complex physical processes comprising a broad range of spatial and temporal scales of variability. A complete and extended review of dominant coastal physical processes can be found, for example, in Huthnance (1995), Brink and Robinson (2005b) and Simpson and Sharples (2012).

Which of the many processes dominate the coastal ocean depends on a variety of factors, including the geometry, geographical location and the characteristics of the adjoining basin. Each shelf sea has therefore a unique dynamics, arising from the specific regional features of the various external forcing (Kantha and Clayson, 2000b).

2.1.2 Physical processes over the continental slope

The continental slope represents the region where the profound differences between the shelf and the deep ocean regimes must be reconciled. In particular, the shelf edge is where these contrasting dynamical systems exist in rather close proximity and where this mutual adjustment creates rather special oceanographic processes, which are of crucial importance for the exchanges of material between the open ocean and the shelf seas (e.g., Huthnance et al. (2009); Holt et al. (2009); Zhou et al. (2014); Brink (2016)).

The steep topography of the slope in combination with the Earth's rotation imposes a particular and quite strong constraint on the large-scale geostrophic currents. In fact, in proximity of the steep continental slope the steady geostrophic flow tends to follow isobaths at all depths (Taylor-Proudman theorem, e.g. Pedlosky (1982)) or, equivalently, goes along contours of the Coriolis parameter divided by the water depth (f/h) (potential vorticity conservation, e.g. Cushman-Roisin and Beckers (2011)).

Bathymetric steering represents a defining feature of the ocean dynamics, governing the establishment of pronounced currents over continental slopes in many parts of the world ocean. Despite the fact they are all constrained to flow parallel to the topography, along-slope currents can arise from a number of different mechanisms.

At the western margins of the ocean for example, relatively narrow jet-like western boundary currents form as a result of the large-scale oceanic gyre circulation flowing under the influence of the latitudinally varying Coriolis forcing (Stommel, 1948). In this case, westward intensified boundary currents flow close to the shelf edge simply because of the potential vorticity conservation constraint. On the other hand, at the eastern boundaries of the ocean basins the wind-driven basin-scale circulation is weaker and other mechanisms promote along-slope currents. For example, in the eastern margin of the North Atlantic a strong and persistent flow along the continental slope of northwest Europe exists driven by the mutual adjustment of both shelf and oceanic regimes to the meridional density gradient, a process sometimes referred to as JEBAR (i.e. Joint Effect of Baroclinicity and Bottom Relief, Sarkisyan (1969); Sarkisyan and Ivanov (1971); Cane et al. (1998)). In this case the steep topography of the slope represent a key factor in the forcing mechanism, and therefore this type of currents are often referred as 'slope currents'.

In constraining currents to be parallel to the isobath, topographic steering also inhibits cross-isobath currents, largely isolating coastal regions from the large-scale dynamics of the open ocean and often creating strong shelf-break thermohaline fronts (Wright and Parker, 1976; Pingree et al., 1982; Cenedese et al., 2013). Cross-slope flow can only occur where the along-slope currents are no longer in geostrophic balance (Brink, 2016), namely when:

- *The flow is unsteady.* This is the case for the oscillatory tidal flow, for example.
- *The flow is energetic.* In this case, the Rossby number is large (> 0.1, Simpson and Sharples (2012)) and non-linear terms in the momentum equation become significantly important.
- *Frictional effects are important.* This is the case in the surface and bottom boundary layers.

Figure 2.2 shows some of the main physical processes responsible for cross-slope transport.

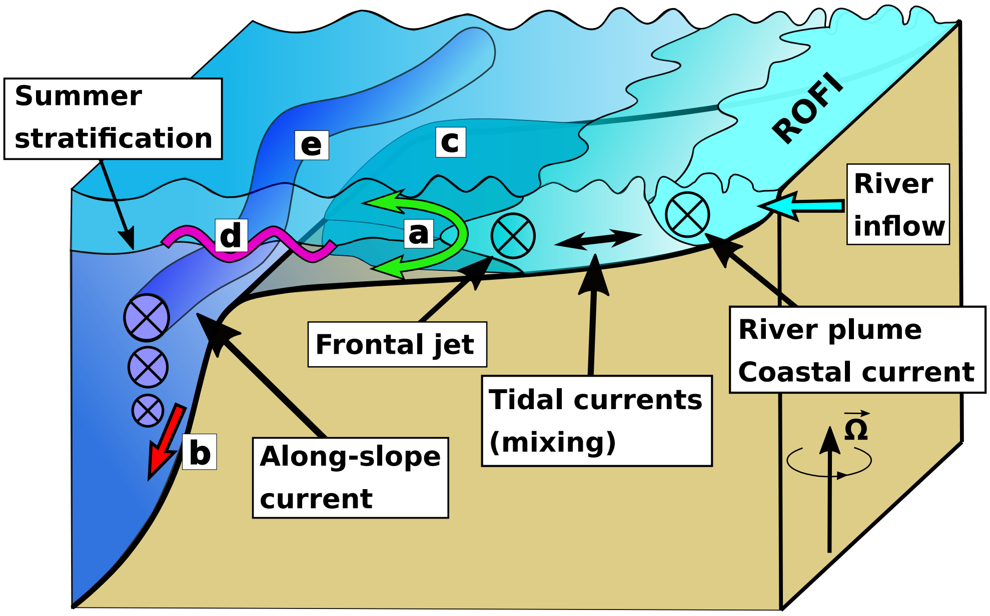

Fig. 2.2: Conceptual sketch illustrating the continental shelf regime and the main processes driving cross-shelf transport: (a) Wind-driven up-down-welling circulation; (b) Ekman drainage; (c) Cascading; (d) Internal waves at the shelf-edge (e) Meanders and eddies in the along-slope current. Redrawn after Huthnance et al. (2009).

Strong and steady along-slope wind stresses acting at the ocean surface can deviate the slope dynamics form geostrophy, inducing substantial cross-slope transfer via *downwelling–upwelling* flows at the ocean margin (e.g. Cushman-Roisin and Beckers (2011), see process *a* in Fig. 2.2).

Another dominant mechanism inducing cross-slope transport is the *Ekman drainage* (mechanism *b* in Fig. 2.2), forced by the interaction between the often barotropic along-slope current and the seabed over the slope (e.g., Shapiro and Hill (1997); Simpson and Sharples (2012)).

Shelf-ocean exchange can be promoted also by *cascading*, a specific type of buoyancy-driven current in which dense water formed by cooling, evaporation or freezing in the surface layer over the continental shelf descends down the continental slope to a greater depth (Nansen (1913); Cooper and Vaux (1949); Whitehead (1987); Huthnance (1995); Shapiro (2003), see descending dense water mass labelled *c* in Fig.

2.2).

Internal tides generated by the interaction of barotropic tides over the slope and the stratification of the water column are a globally ubiquitous phenomena (see magenta wave labelled d in Fig. 2.2). They propagate as a series of internal waves on to, and away from, the shelf, therefore promoting the transport of material across the isobaths (Holligan et al., 1985; Sharples et al., 2001).

Strong horizontal variations in the velocity or density field of a steady large-scale along-slope flow may develop dynamical instabilities which break geostrophy and lead the formation of mesoscale energetic structures driving transport across the shelf edge (Huthnance, 1995; Shapiro et al., 2000; Brink, 2016). These can be either *meanders/eddies* or coherent currents, with the only requirement to have a strong non-linear dynamics characterised by a large Rossby number (see the meander e in the along-slope current of Fig. 2.2). Several studies investigated the importance of this type of shelf-ocean exchanges all over the world, e.g. Chern et al. (1990); Shapiro et al. (2010); Zhang and Gawarkiewicz (2015); Nencioli et al. (2016). Eddies and meanders increasing cross-frontal transfer can be generated also by irregularities in the topography (e.g. Oey1992).

There is growing evidence (e.g., Badin et al. (2009); Brink and Cherian (2013)) that tidal mixing fronts inshore of the shelf-break may drive the generation of coastal mesoscale eddies potentially able to increase cross-shelf flow. However, their role in the coastal dynamics and shelf-ocean transport has still to be clearly understood (Holt et al., 2017).

2.2 Numerical Ocean Modelling at regional scales

In this section, a review of the approaches used in regional ocean modelling is given. The discussion is restricted to three-dimensional, free-surface numerical ocean models which simulate the evolution of temperature and salinity under the Boussinesq and hydrostatic approximations. The prime focus is on the state-of-the-art computational meshes and sub-grid-scale parameterizations used for modelling the coastal ocean. A more complete review of the numerical techniques used in coastal and regional modelling can be found in e.g. Mooers (1999); Dyke (2001); Holt et al. (2017); Klingbeil et al. (2018).

2.2.1 Computational meshes

The small spatial scales characterising the local processes and the geography of many regional seas (coastline, bathymetry, straits) pose a significant challenge when simulating the hydrodynamics of these seas.

In the horizontal direction, two options exist to refine the resolution of the numerical grid: (i) increasing the quasi-uniform resolution of the whole grid or (ii) introducing a multi-scale capability that allows refinement in specific locations (Holt et al., 2017).

Downscaling via nesting a high resolution regional model inside a model with larger lateral domain and coarser resolution is the most common approach to multi-scale modelling. However, the accuracy at which information can be exchanged between the two domains and the degradation of the solution at the boundary represents an important concern (e.g. Greenberg et al. (2007); Kourafalou et al. (2015)).

Current ocean models mainly use structured curvilinear horizontal grids with local orthogonal quadrilaterals (Liu et al., 2017). These grids offer a good degree of compromise between flexibility and accuracy, allowing to improve the representation of many coastal processes – e.g. the propagation of Kelvin waves and land-ocean interactions through the alligning of grid lines with the coast (Adcroft and Marshall, 1998; Greenberg et al., 2007; Chassignet and Marshall, 2008; Griffiths, 2013). However, they rely upon analytical coordinate transformations which may limit their multi-scale capability, often allowing the refinement of a single region of interest (Holt et al. (2017), see also Fig. 2.3(b)).

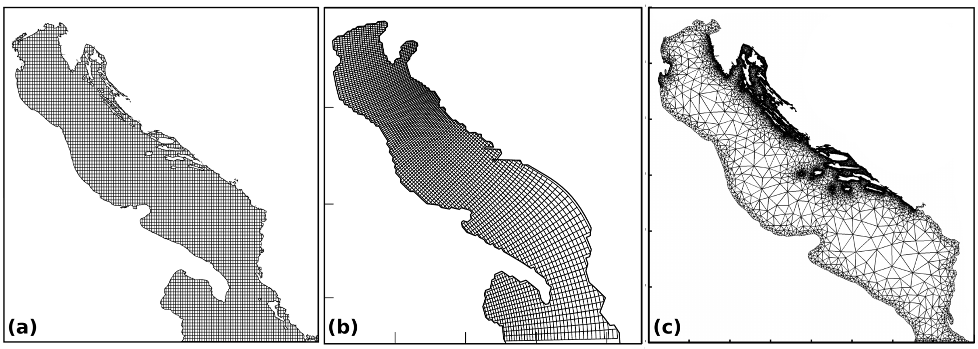

Fig. 2.3: Differences between constant and variable resolution structured and unstructured grids in the Adriatic Sea. (a) Structured geographical grid with constant resolution. (b) Structured coastline-following orthogonal curvilinear grid with increased resolution in the northern part of the basin (Zavatarelli et al., 2002); (c) Unstructured triangular grid with increased resolution along Croatian coasts (Janeković and Kuzmić, 2005).

Unstructured grids are inherently suited to resolve dynamics encompassing a range of scales (see Fig. 2.3(c)), offering a geometric flexibility that goes beyond the functionality allowed by nesting or generalized curvilinear grids (Piggott et al., 2008; Holt et al., 2009; Haidvogel et al., 2017). However, issues of numerical efficiency and accurate transport schemes can be still important (Danilov, 2013; Danilov and Wang, 2015; Haidvogel et al., 2017).

In the vertical direction, model levels must be able to represent the important interactions between flows and topography over the continental shelf and to resolve the sharp pycnoclines which often characterise these areas (see the review given in Sec. 2.1.1 and Sec. 2.1.2).

Typical vertical grids used in ocean modelling are based on z-geopotential, s-terrain-following or isopycnal ρ-vertical coordinates. However, all of them present limitations (e.g. Griffies (2004), see also Fig. 2.4 and Fig. 2.5).

Geopotential coordinates (Fig. 2.4(a)) are generally not recommended for coastal models, since they offer low accuracy in simulating near-bottom dynamics due to their step-like representation of topographic slopes and they experience difficulties

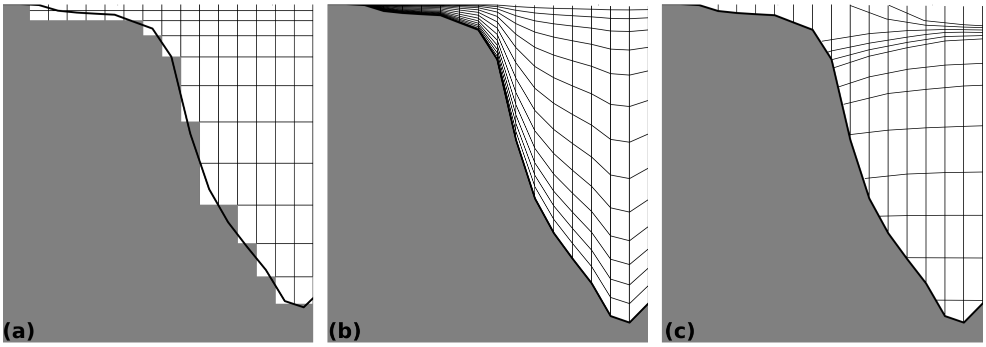

Fig. 2.4: Sketch depicitng (a) $z-$geopotential, (b) $s-$terrain-following and (c) $\rho-$isopycnal vertical coordinates. .

in dealing with large variations of the water level (e.g., large maximum tidal range and flooding events) (Klingbeil et al. (2018) and references therein).

Terrain-following coordinates (Fig. 2.4(b)) represent a natural framework for coastal models, since they can guarantee the needed resolution in well-mixed areas and offer a smooth representation of the flow down the slope (e.g., Mellor et al. (2002); Ezer et al. (2002)). However, they introduce an error in computing horizontal pressure gradients (e.g., Haney (1991); Mellor et al. (1994)).

When using s-coordinates, the horizontal pressure gradient consists of two terms:

$$\begin{aligned} \nabla p &= (\nabla_s - \nabla_s z \partial_z) p, \\ &= \nabla_s p + \rho g \nabla_s z, \end{aligned} \tag{2.1}$$

where the hydrostatic balance $\partial_z p = -\rho g$ is used to obtain the second relation (Griffies et al., 2000a). In equation 2.1, ∇p is the horizontal pressure gradient taken along surfaces of constant depth z while $\nabla_s p$ and $\rho g \nabla_s z$ represent the components of the horizontal pressure gradient along and across surfaces of constant s, respectively. Considering the geostrophic balance and ocean currents with typical values of $1-10^{-1}$ ms^{-1}, a scale analysis can be used to show that oceanic horizontal pressure gradients (the ∇p term) at mid latitudes ($f = 10^{-4}\ s^{-1}$) ranges between 10^{-2} and 10^{-1}

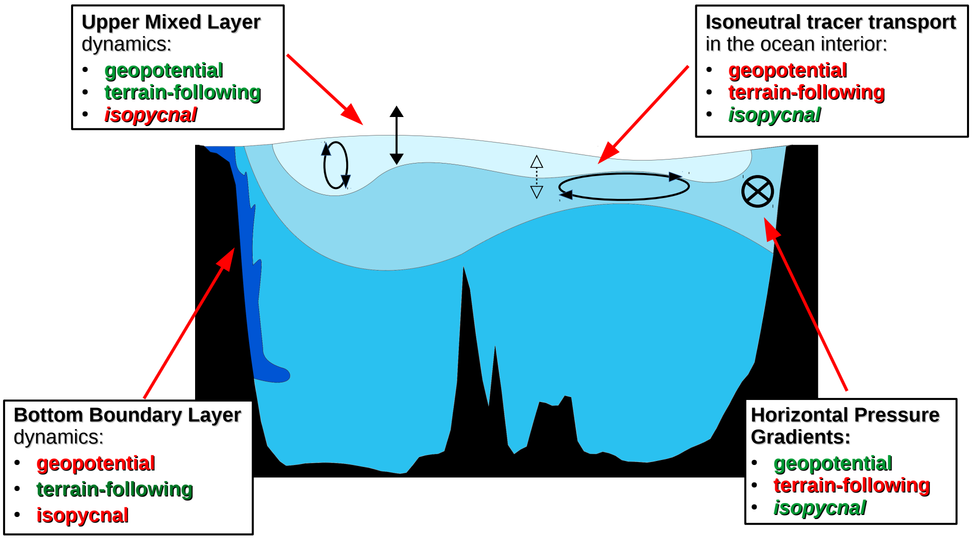

Fig. 2.5: Sketch depicting four of the main processes leading the ocean dynamics and the 'suitability' of the three geopotential, terrain-following and isopycnal vertical coordinates in representing them (green means 'good' while red means 'poor' suitability).

Nm^{-3}. In the ocean, the slope of terrain-following s-levels ($\nabla_s z$) can reach 1/100 to 1/10, especially next to the continental shelves, making the 'sigma coordinate correction term' $\rho g \nabla_s z$ of the same order of $\nabla_s p$ (e.g., Griffies (2004)). Therefore, in s-coordinates the horizontal pressure force becomes the result of two sizeable terms, each having separate numerical errors that generally do not cancel, generating spurious pressure forces that drive non-trivial unphysical currents (Haney, 1991; Mellor et al., 1994).

One method to avoid horizontal pressure gradient errors could be to use the so called vorticity-velocity formulation, i.e. eliminating pressure from the governing equations by taking the curl of the momentum equations (e.g., Dennis et al. (1979); Speziale (1987); Canuto et al. (2007)). However, when applied to ocean modelling problems such an approach experiences few issues that make it much less competitive and appealing than the common pressure-primitive equations method. One problem arises from the fact that the World Ocean with its many islands and continents is a multipli-connected region where the specification of the Dirichlet boundary conditions for the stream function may result quite a complex task (see Bryan (1969) for the details). A second problem is that the vorticity-velocity method specifies more elliptic equations than the primitive variable formulation, which are more complex to solve out efficiently on vector and parallel processors and for complicated basin shapes (e.g. Kantha and Clayson (2000b); Griffies et al. (2000a)).

Both $z-$ and $s-$ vertical coordinates are also prone to the contamination of weak diapycnal exchanges with strong isopycnal processes in cases the computational surfaces cross the isopycnals (e.g., Holt et al. (2017) and references therein).

The latter affects less isopycnal models (Fig. 2.4(c)), especially at regional scales. However, ρ-coordinates are not recommended for shelf seas models given their problems in dealing with weakly stratified areas (e.g Griffies et al. (2000a)).

Several solutions have been proposed to minimise the disadvantages of the various vertical coordinate systems. A review is given in Sec. 3.1 and Sec. 4.1 (for the specific case of the Black Sea) of this thesis or in Holt et al. (2017) (sec. 3.1.2) and Klingbeil et al. (2018)(sec. 4.2).

2.2.2 Sub-grid physics parameterizations

Turbulent vertical mixing schemes of shelf seas models must be able to resolve the rapidly varying vertical structure of both the upper and bottom boundary layers and the vertical stratification arising from their mutual interactions (Holt et al., 2017).

For this reason, two-equation turbulence closure models (e.g. Mellor and Yamada (1982) or $k-\epsilon$) are preferred in regional coastal models (Klingbeil et al., 2018), generally with satisfactory results (e.g Holt and Umlauf (2008); Maraldi et al. (2013); Wobus et al. (2013); Hordoir et al. (2018)). The tuning of the length-scale limiter (Galperin et al., 1988; Umlauf and Burchard, 2003, 2005) typically applied in these models to deal with stably stratified flows should be carried out carefully (Holt and

Umlauf, 2008; Hordoir et al., 2018). Two-equation turbulence models are used also in basin-scale and global ocean simulations (e.g., Ezer and Mellor (2000); Qiao et al. (2004)), although they may experience difficulties due to the coarse temporal (i.e. long baroclinic timestep) and vertical resolutions of these type of configurations (Holt et al. (2017)).

Another approach consists in the direct algebraic computation of the vertical eddy coefficients from bulk properties of the water column, as it is the case for the Pacanowski and Philander (1981) or the KPP (Large et al., 1994) parameterizations. Successful implementations of the Pacanowski and Philander (1981) scheme to coastal ocean scenarios are reported by Lermusiaux (2001); Ciliberti et al. (2015); Trotta et al. (2016, 2017) while Durski (2004); Wilkin (2005) showed that the KPP scheme can be used in shelf seas simulations with good results.

Laplacian and/or biharmonic diffusion of momentum and tracers is usually applied in ocean modelling to parameterise the lateral turbulent mixing not explicitly resolved by the model (e.g. Kantha and Clayson (2000b); Hecht and Hasumi (2008)). Whilst this is generally justified for large scale models, it is not clear if it is needed in regional models, due to their higher horizontal resolution (e.g. Holt and James (2006)).

One common approach of regional ocean models is to neglect lateral turbulent fluxes and rely on the numerical diffusion of the advection scheme (Holt and James, 2006; Klingbeil et al., 2018). Another solution is to use lateral diffusivity and viscosity parameters either constant in space and time or scale-selective, i.e. depth-dependent (e.g. Wakelin et al. (2009)) or flow- and resolution-dependent (Smagorinsky, 1963).

While there is consensus about lateral diffusion acting mainly along-isopycnals in the open ocean, it is still not clear if this is the case also for weakly stratified coastal areas (e.g. Griffies (2004)). Moreover, implementing isoneutral diffusion with sloping vertical coordinates require some attentions (e.g. Beckers et al. (2000); Griffies et al. (2000a)). For this reasons, it is common practice in regional shelf-sea models to use either geopotentially oriented explicit diffusion (e.g. Barnier et al. (1998); Marchesiello et al. (2009); Furner (2012); Lemarié et al. (2012)) or to diffuse only the tracer anomaly computed with respect to climatological values (Mellor and Blumberg, 1985; Ezer and Mellor, 2000; Ezer et al., 2005).

2.3 The Black Sea study case

2.3.1 Main features of the Black Sea physical oceanography

The Black Sea is one of the most studied seas of the World Ocean (Stanev, 2005) and is one of the largest and deepest in-land basin of the world, located on the border between Europe and Asia. It is connected to the Sea of Azov through the Kerch straits and to the Atlantic Ocean via the Marmara, Aegean and Mediterranean seas through, respectively, the Bosporus, Dardanelles and Gibraltar narrow straits (Shapiro, 2008). The total surface area of the sea is 416790 km^2 while its maximum depth ranges between 2210 m and 2258 m (Ivanov and Belokopytov, 2012).

The Black Sea bottom topography includes three distinct zones (see Fig. 2.6(a)): the *shelf* (depths $\leq$ 200 m) represents 25% of the whole basin, the *continental slope* (depths between 200 and 2000 m) occupies the 40% of the entire sea area and the *abyssal plain* (depths $\geq$ 2000 m) covers about the 35% of the Black Sea area (Ivanov and Belokopytov, 2012).

The most vast shelf zone of the Black Sea ($\approx$ 220 m wide, 16% of the total sea area) is located in the north-western part of the basin, has a quite gentle slope and is where Europe's large rivers flows. To the contrary, the narrow shelf zones located along the Caucasian, Anatolian and southern Crimean coasts rarely exceeds 15 km in width, are much steeper and have numerous submarine canyons and channel extensions (see Fig. 2.6(b), Ivanov and Belokopytov (2012)).

According to recent evaluations of the global climate (e.g Kottek et al. (2006); Peel et al. (2007)), the northern coast of the sea can be regarded as a continental climate

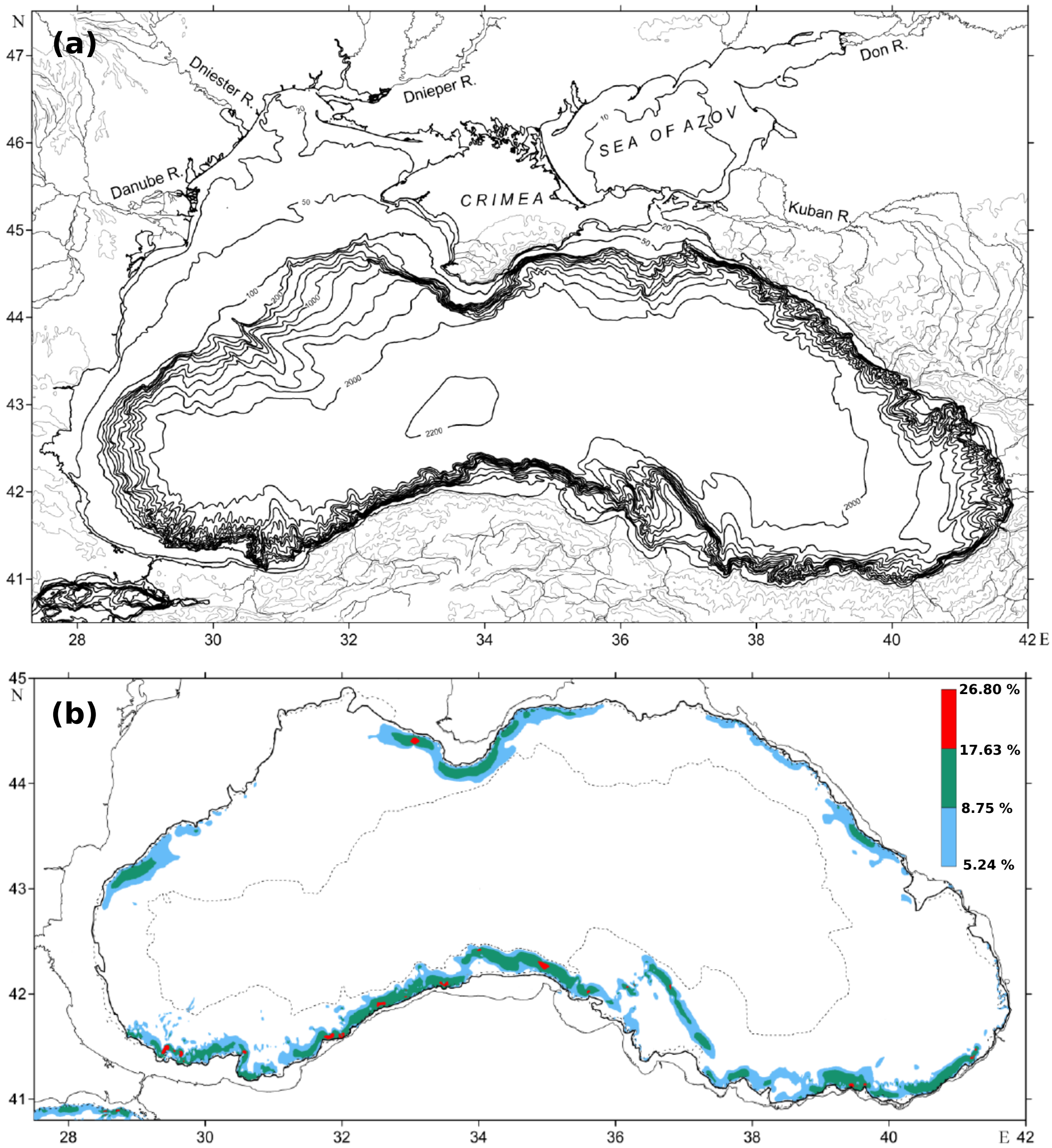

Fig. 2.6: (a) Map of the Black Sea bottom topography based on the International Bathymetric Chart of the Mediterranean Sea (IBCM, in m); (b) Position of the shelf break in the Black Sea according to the GEBCO 2008 (bold black line). Solid color indicates values of the bottom slope with range: $5.24\% - 8.75\%$, $8.75\% - 17.63\%$ and $17.63\% - 26.80\%$, dotted lines show isobath of 200 m and 2000 m. Modified from Ivanov and Belokopytov (2012).

zone, the south-western part of the coast near Istanbul as a Mediterranean climate area while the rest of the Black Sea coast can be classified as temperate climate (subtropical or maritime).

The average annual air temperature over the Black Sea presents a uniform north-south gradient, from 10°C in Odessa and Ochakov area to values exceeding 14°C in the southern coast. Winters can be quite cold in the northern part of the basin, with air temperature that can reach values below 0°C, while a milder winter season characterises the southern and eastern areas (Ivanov and Belokopytov, 2012).

The atmospheric circulation over the Black Sea is cyclonic during most of the year (Shapiro, 2008). The wind stress vorticity is maximum during winter while it reaches its minimum in late spring or early summer, when in many areas of the sea the vorticity becomes negative (anticyclonic) (e.g. Stanev (1990); Efimov et al. (2002); Kubryakov and Stanichny (2015)).

The Black Sea receives heat from March to August while it gives off heat to the atmosphere from September to February. The radiation budget (short- and long-wave radiation) presents maximum values in June (Simonov and Altman, 1991; Schrum et al., 2001) or July (Efimov and Timofeev, 1990), while it has minimum values in November (Ivanov and Belokopytov, 2012). The total turbulent heat flux from the sea to the atmosphere (sensible and latent heat fluxes) shows minimums in April (Simonov and Altman, 1991) or in May (Efimov and Timofeev, 1990) and maximums in autumn (Ivanov and Belokopytov, 2012).

Volume and salt budgets in the Black Sea can be written as

$$E + P + Q_R + Q_B^{in} + Q_B^{out} = 0, \tag{2.2}$$

$$Q_B^{in}\, S_{in} + Q_B^{out}\, S_{out} = 0, \tag{2.3}$$

where E and P are surface water fluxes due to evaporation and precipition, respectively, and Q_R is the flux of freshwater from rivers' discharges. Q_B^{in} represents the Boshorus flux of deep Mediterranean waters with salinity S_{in} flowing in the Black Sea while Q_B^{out} is the Bosphorus surface outflow of Black Sea waters with salinity S_{out} leaving the basin (e.g. Bulgakov and Korotaev (1984)). The exchange through the Kerch Strait can be omitted since the flow through this strait is small compared to the other terms of the water budget (Stanev, 1990).

The Black Sea represents a classical estuarine basin (e.g. Pickard and Emery (1982)) characterised by a positive water balance ($Q_R + P + E > 0$).

The freshwater budget shows negative values from July to October, with minimum reached in August, while it is positive from November to June, with maximum values in April due to the river spring flood and the minimal evaporation during this period (Ivanov and Belokopytov, 2012).

The most prominent feature of the vertical thermohaline structure of the Black Sea is the existence of extremely sharp seasonal and permanent pycnoclines, which isolate the oxigen-rich waters of the surface layer from the oxigen-depleted waters of the deep sea. The strong stratification is mainly driven by salinity, except for the upper 50 m in summer. In the upper part of the permanent halocline exists a Cold Intermediate Layer (CIL), a defining feature of the Black Sea which present water temperature minimums (e.g. Shapiro (2008)).

The Black Sea is the largest brackish basin of the world (Tuzhilkin, 2008), with a mean surface salinity of 17.85 PSU (Ivanov and Belokopytov, 2012). Its salinity results from the balance between the freshwater budget and the amount of warm and salty Mediterranean water (salinity of $\approx 34-36$ PSU) penetrating into the sea along the bottom of the Bosphorus strait (e.g. Pickard and Emery (1982); Gregg and Özsoy (2002)).

Figure 2.7 presents basin averaged monthly mean Temperature (T) vertical profiles

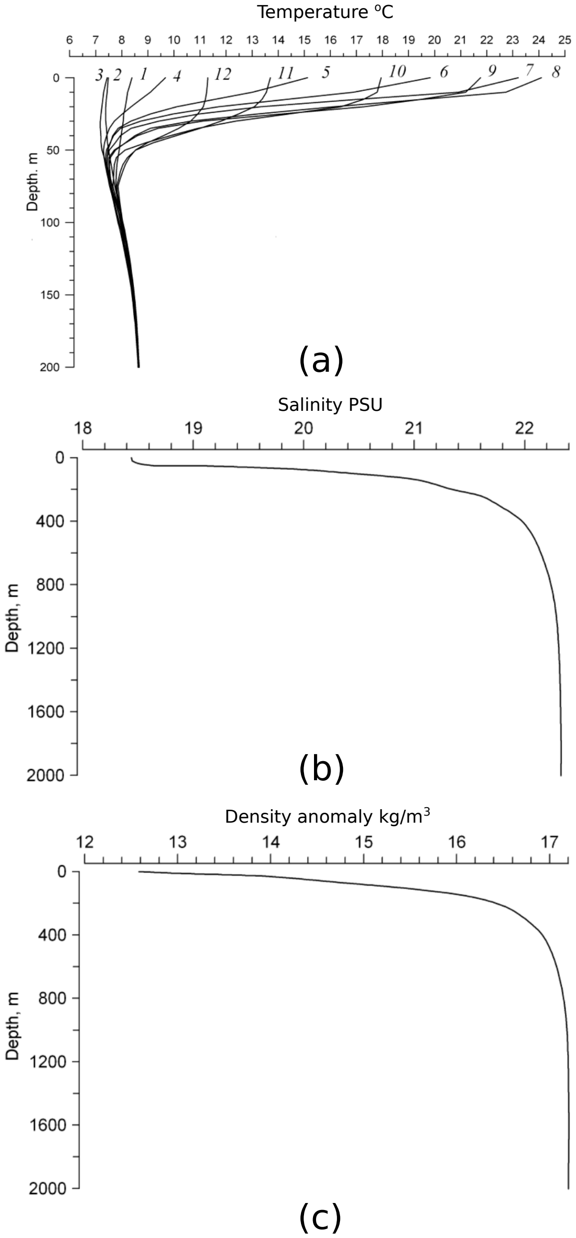

Fig. 2.7: (a) Basin averaged monthly mean temperature vertical profiles of the upper 200 m of the water column; (b) Basin averaged yearly mean salinity vertical profile of the whole water column; (c) Basin averaged yearly mean vertical density anomaly profile of the whole water column (modified from Ivanov and Belokopytov (2012)).

of the upper layer ($0 - 200$ m, Fig. 2.7(a)) and basin averaged yearly mean Salinity (S) (Fig. 2.7(b)) and density anomaly (σ)(Fig. 2.7(c)) vertical profiles of the whole water column. The density anomaly σ is defined as $\rho - 1000\ kgm^3$, where ρ is the in-situ density. The main thermohaline characteristics of the Black Sea water column are the following:

- *Upper Mixed Layer*: widely present in autumn and winter while rare in May and June. Mainly driven by temperature variability and located between 0 and $5 - 10\ m$ in spring and summer while its depth increases up to $30 - 50$ m in winter.

- *Seasonal pycnocline*: controlled mainly by the seasonal thermocline, it is located between $15 - 20$ m from April to November and its greatest development is in July-August. The seasonal thermocline is well-developed from April to August, while from September to December the thermal stratification weakens and in winter disappears. The seasonal halocline is weaker and confined close to the surface in autumn-winter while it gets stronger and deepens to ≈ 20 m in winter.

- *Sub-surface Temperature Minimum Layer*: quite shallow in March-April (depths between$20 - 30\ m$), it gradually deepens down to depths of $70 - 80\ m$ in December. By definition, it includes the *CIL*.

- *Permanent pycnocline*: mainly driven by salinity effects and it coincides with the main halocline, having a typical depth of $\approx 50 - 100$ m.

- *Stationary quasi-isothermal layer*: located at depths between $500 - 700$ m. Waters from the Marmara Sea mix with surrounding Black Sea waters, giving off heat and sinking down as colder water down to these depths where they are warmed by geothermal heat fluxes (Samodurov and Ivanov, 2002; Mamayev, 1975, 1997).

- *Bottom Mixed Layer*: located between $1650 - 1750$ m and the bottom, it

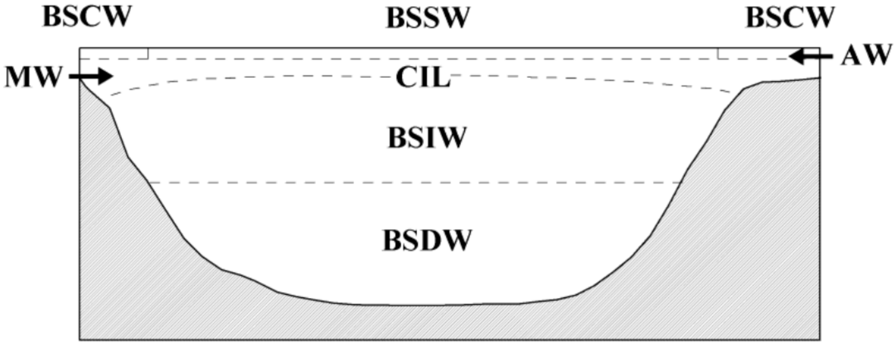

Fig. 2.8: Scheme of the vertical distribution of Black Sea water masses (from Ivanov and Belokopytov (2012)).

presents constant potential temperature ($\approx 8.897-8.903$°C and salinity 22.325–22.340 PSU). It is formed by geothermal heat driven density convection (Murray et al., 1991; Özsoy et al., 1991; Samodurov, 2009).

Generally, the vertical thermohaline structure in the central part of the Black Sea significantly differs from the one characterising its coastal areas, resulting in a classical dome-shaped basin distribution of isothermal surfaces driven by the general cyclonic circulation of the sea (e.g. Shapiro (2008)).

The Mediterranean water (MW) coming from the Marmara Sea via the Bosphorus strait ($T = 12-15$°C, $S = 34-37$ PSU, σ=26-28 kgm^{-3}) and the freshwater entering the Black Sea basin with river runoff and precipitation ($T = 0 - 28$°C, $S = 0$) are the two major water types from which Black Sea water masses originate. The Azov Sea Water (AW) ($S = 12-15$ PSU) exerts some influence in areas close to the Kerch Strait.

In the Black Sea, five major water masses exist (Ivanov and Belokopytov (2012), see Fig. 2.8): Black Sea Coastal Water (**BSCW**), Black Sea Surface Water (**BSSW**), Cold Intermediate Water (**CIW**), Black Sea Intermediate Water (**BSIW**) and Black Sea Deep Water (**BSDW**).

The CIW is a sub-surface water mass representing one of the most distinctive feature of the Black Sea. It identifies a layer of minimum temperature between the seasonal and the permanent pycnoclines. Traditionally, the criterion to identify the CIW is the 8°C isotherm (Kolesnikov, 1953).

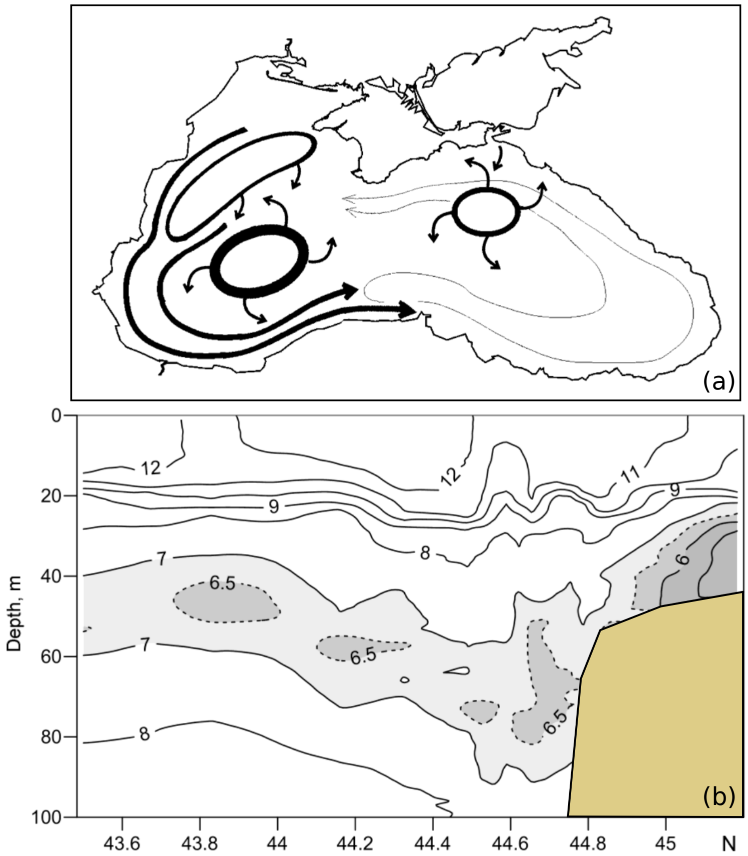

Fig. 2.9: (a) General scheme of CIW formation and advection; (b) Temperature cross section across the north-west shelf break at 30.5° E on April 4-6, 1993. (Adapted from Ivanov and Belokopytov (2012)).

The CIW is the result of winter convective mixing combined with the shallow depth of the halocline in the centres of cyclonic gyres and in shelf areas. In those areas where winter convection does not occur the CIW has an advective origin (Ivanov and Belokopytov (2012), see Fig. 2.9(a)).

In the north-western shelf, winter cooling forms CIW which cascades in the deeper basin and spreads around driven by the large-scale circulation (Kolesnikov (1953), see

Fig. 2.9(b)); in the centres of cyclonic gyres, the CIW is formed by winter convection and then advected all over the basin, similarly to deep water formation processes in the Greenland Sea and the Gulf of Lyons (Ovchinnikov and Popov, 1987).

Figure 2.10 presents the following main features of the basin-scale surface circulation:

- A coherent cyclonic boundary current often called the Rim Current or the Main Black Sea Current (Knipovich, 1932; Neumann, 1942) flowing over the continental slope due to the potential vorticity conservation constraint (e.g. Shapiro et al. (2010); see also Sec. 2.1.2).
- Two sub-basin cyclonic gyres particularly prominent in winter associated with wind cyclonic vorticity maxima (Moskalenko, 1975) or the shape of the coastline which divides the sea into two sub-basins (the apple shaped Crimean peninsula, Leonov (1960); Filippov (1968)).
- Rich mesoscale activity, with a number of typically anticyclonic vortices (as Bosphorus, Sakarya, Sinop, Kizilirmak, Sukhumi, Caucasus, Kerch, Crimea, Danube, Constantsa, and Kaliakra anti-cyclonic eddies) and quasi-permanent anticyclonic gyres in the south-east of the basin (Batumi eddy) and south of the Crimean peninsula (Sevastopol eddy) located between the coast and the Rim Current.

Although geostrophic calculations seem to support the hypothesis of an anti-cyclonic circulation in the layer below 1000 m, measurements do not confirm it (Ivanov and Belokopytov, 2012).

Three main regions with different dynamical regimes exist in the Black Sea (e.g., Boguslavsky et al. (2001); Poulain et al. (2005); Stanev (2005); Kubryakov and Stanichny (2013)): (i) a coastal zone of very variable flow, where currents speed up to $20-30$ cm/s; (ii) the Rim Current zone, where a jet-stream flow with speeds of $21-22$ cm/s up to values of $1-1.5$ m/s exist; (iii) the open sea area, where the current velocity decreases gradually from the periphery to the center, not ex-

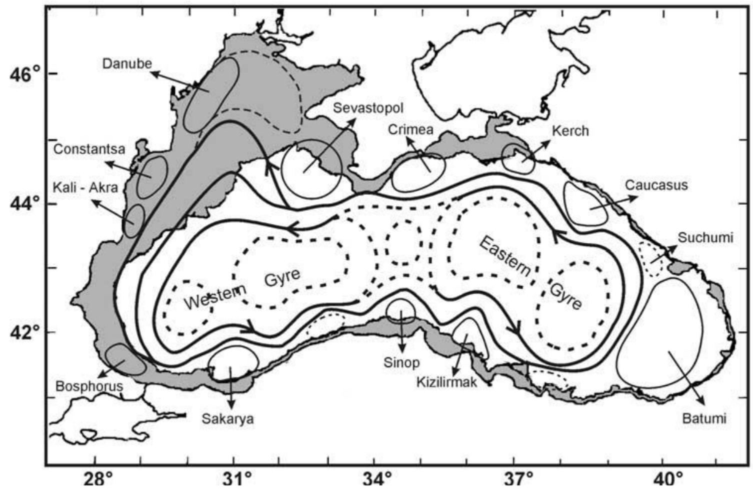

Fig. 2.10: Circulation pattern of the surface layer of the Black Sea. Solid (dashed) lines indicate quasi-permanent (recurrent) features of the general circulation (from Oguz et al. (1993); Korotaev et al. (2003)).

ceeding 10 cm/s. The current speed in the Black Sea significantly decreases with depth, especially in the layer 100-500 m, where it drops about 4 times (Ivanov and Belokopytov, 2012).

The seasonal variability of the circulation is traditionally associated with the seasonality of the external mechanical and buoyancy forcings (e.g. Korotaev (2001); Korotaev et al. (2001); Efimov et al. (2002)), which promotes the alternating of a stream-type circulation in winter and an eddy-type one in summer.

The Black Sea circulation is mainly driven by the positive curl of the wind stress combined with the buoyancy forcing from the river run-off (Shapiro, 2008). A number of studies have investigated the role of wind stresses (e.g., Stanev (1990, 2005); Oguz et al. (1995, 1996); Korotaev et al. (2001, 2003)) and buoyancy forcing (e.g., Bulgakov and Korotaev (1984); Bulgakov and Korotayev (1989); Simonov and Altman (1991); Korotaev (1997)) in driving the observed circulation pattern.

Oguz et al. (1995, 1996) and Stanev (1990) studied the role of JEBAR (see Sec. 2.1.2) in driving the formation of the Rim Current, showing that this effect is con-

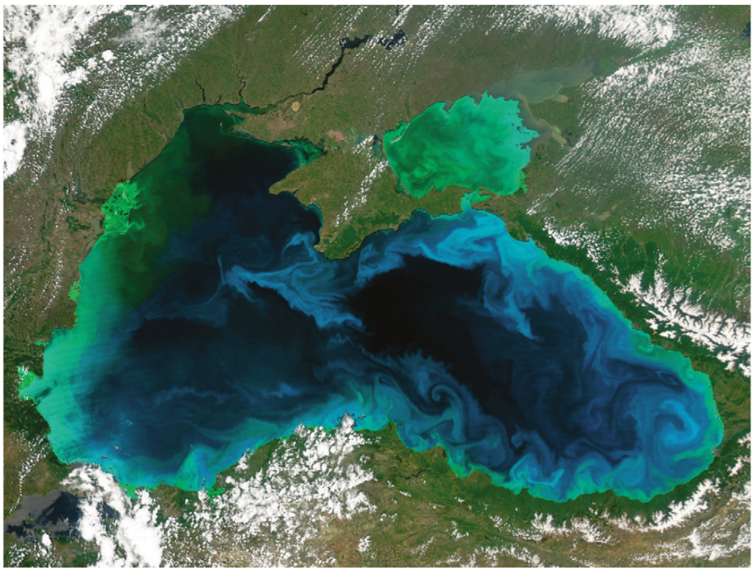

Fig. 2.11: Satellite image of the Black Sea based on MODIS data from NASA, 22 May 2004. Colors are exaggerated to show the contrasting coastal and open sea water masses. (from Shapiro (2008)).

siderably weakened in the Black Sea due to its strong stratification. Moskalenko (1975) noted that the influence of changes of the Coriolis parameter with latitude is almost negligible in the Black Sea in comparison with bottom topography effects. Tidal motion in the Black Sea is quite irrelevant: for example, Medvedev et al. (2016) showed that the estimated maximum tidal height for a 100-year period is 18 cm in this sea. In addition, the seasonal variability of the Black Sea circulation has been associated with baroclinic instabilities of the Rim Current (e.g., Eremeev et al. (1991); Stanev and Staneva (2000); Efimov et al. (2002); Blokhina and Afanasyev (2003)) or the propagation of Rossby waves from the eastern part of the sea to the west (e.g Rachev and Stanev (1997); Stanev and Rachev (1999); Stanev and Staneva (2000); Staneva et al. (2001); Korotaev (2001)).

Coastal eddies in the Black Sea are typically very energetic, elongated, anticyclonic gyres wedged between the main cyclonic Rim Current over the shelf break and the coast (Staneva et al. (2001), see also Fig. 2.11).

In contrast to mesoscale rings generated by meandering of jet currents in the ocean (i.e., Gulf Stream rings), coastal anticyclones in the Black Sea are formed mainly by barotropic-baroclinic instabilities of the Rim Current due to the high horizontal shear and horizontal friction (Blatov et al., 1984; Staneva et al., 2001; Shapiro, 2008) or the influence of the bottom topography and shoreline configuration (e.g Oguz et al. (1992); Staneva et al. (2001)).

Mesoscale eddies and meanders act as a link between the coastal environment and the open sea, providing a fundamental mechanism of transport of nutrient rich material from the coastal zone to the oligotrophic and unproductive deep sea environment in the Black Sea (e.g. Shapiro et al. (2000); Stanev et al. (2002); Zatsepin et al. (2003); Shapiro et al. (2010); Zhou et al. (2014)).

2.3.2 Numerical modelling of the Black Sea circulation

The numerical modelling of the Black Sea circulation presents some particular challenges. Staneva et al. (2001) pointed out that a realistic eddy resolving Black Sea ocean model must completely resolve the steep bathymetry, correctly simulate the annual cycle of stratification and adequately simulate and/or parameterise shallow coastal zone processes characterised by short length and time scales.

Another delicate aspect of Black Sea numerical models is the representation of water mass formation processes. According to Peneva and Stips (2005), most of the numerical Black Sea simulations fail to fairly reproduce the presence of the permanent CIL without a relaxation to the climatological temperature and salinity fields. In addition, the same study also noted the difficulties of many Black Sea models in representing the dynamic of the Bosphorus plume.

Several three dimensional primitive equation-based ocean models of the Black Sea circulation exist (Oguz et al., 2006). According to Stanev (1990), the studies by Sarkisyan and Dzioev (1974), Marchuk et al. (1975) and Dzioev and Sarkisyan (1976) can be considered the first attempts of using numerical models to investigate the Black Sea hydrodynamics. However, those models were not sophisticated enough to give the necessary insight in the basic physical mechanisms governing water masses formation, deep water ventilation, seasonal changes and sensitivity of the general circulation to all kinds of forcing controlling the Black Sea dynamics (Stanev, 1990).

In general, numerical studies performed before the 1990s had somewhat coarser horizontal and vertical resolutions, being not able to properly resolve the narrow and steep continental slope and the strong horizontal and vertical density gradients characterising the Black Sea. More recently, due to the increase of available computing resources, high resolution eddy-resolving models have become common (Oguz et al., 2006).

For example, Stanev et al. (2003, 2004) applied the GFDL Modular Ocean Model (MOM) with z-levels, rigid-lid, and an empirical-based functional representation of the vertical eddy diffusivity and viscosity while Besiktepe et al. (2001) used the Harvard Open Ocean Prediction Systems (HOPS) with similar characteristics.

On the other hand, Oguz et al. (1995); Korotaev et al. (2011); Cannaby et al. (2015) implemented the Princeton Ocean Model (POM) with bottom-following σ-coordinates, free surface and parameterizing the vertical mixing by means of advanced turbulence closure models. Similarly, Stanev and Beckers (1999); Capet et al. (2012) used the GeoHydrodynamics Environment Research model (GHER-3D) with double σ-coordinates, as did Miladinova et al. (2017) with a generalised boundary-following vertical grid.

Staneva et al. (2001) opted for the Dietrich-Center for Air-Sea Technology model (DieCAST), with similar characteristics to MOM but lower dissipation and fourth-order accuracy (Oguz et al., 2006) while Kara et al. (2005) implemented the Hybrid Coordinate Ocean Model (HYCOM).

Enriquez et al. (2005) used the Proudman Oceanographic Laboratory Coastal Ocean

Modelling System (POLCOMS) with s-levels and an artificial flat bottom at a depth of 1500 m to alleviate numerical errors in the computation of horizontal pressure gradients while Korotaev et al. (2011); Demyshev (2011) used the Marine Hydrophysical Institute model (MHI) with z-coordinate and the Pacanowski and Philander (1981) parameterization for the vertical mixing.

Recently, Shapiro et al. (2013); Zhou et al. (2014); Ciliberti et al. (2016) implemented in the Black Sea the Nucleus for European Modelling of the Ocean model (NEMO), parameterizing the vertical mixing with the Generic Length Scale (GLS) turbulent closure scheme (Umlauf and Burchard, 2003). While Shapiro et al. (2013); Zhou et al. (2014) used a novel hybrid s-on-top-of-z vertical discretization scheme, Ciliberti et al. (2016) used z-levels with partial steps.

All these models used a structured regular horizontal grid with constant resolution less than 10 km (the baroclinic radius of deformation is around 20 km in the Black Sea (Stanev, 2005)) and more than 20 levels in the vertical.

However, in the last decade a number of studies have implemented structured (e.g., Diansky et al. (2013); Gusev et al. (2017)) and unstructured (e.g., Divinsky et al. (2015); Stanev et al. (2017)) horizontal grids with variable resolution to improve the accuracy of the simulation in a specific local area of the Black Sea or to better resolve a particular process.

2.4 The Dead Sea study case

2.4.1 Main features of the Dead Sea physical oceanography

The Dead Sea is a hypersaline terminal desert lake located in the Dead Sea rift valley, between Israel and Jordan (see Fig. 2.12(a)). Geologically, the sea is situated within the pull-apart that formed along the Dead Sea rift, one of the largest pull-apart of the world. The lake's deepest point (-730 m) is the deepest terrestrial spot on Earth

(Fig. 2.12(c)) (Garfunkel and Ben-Avraham, 1996; Katz and Starinsky, 2009).

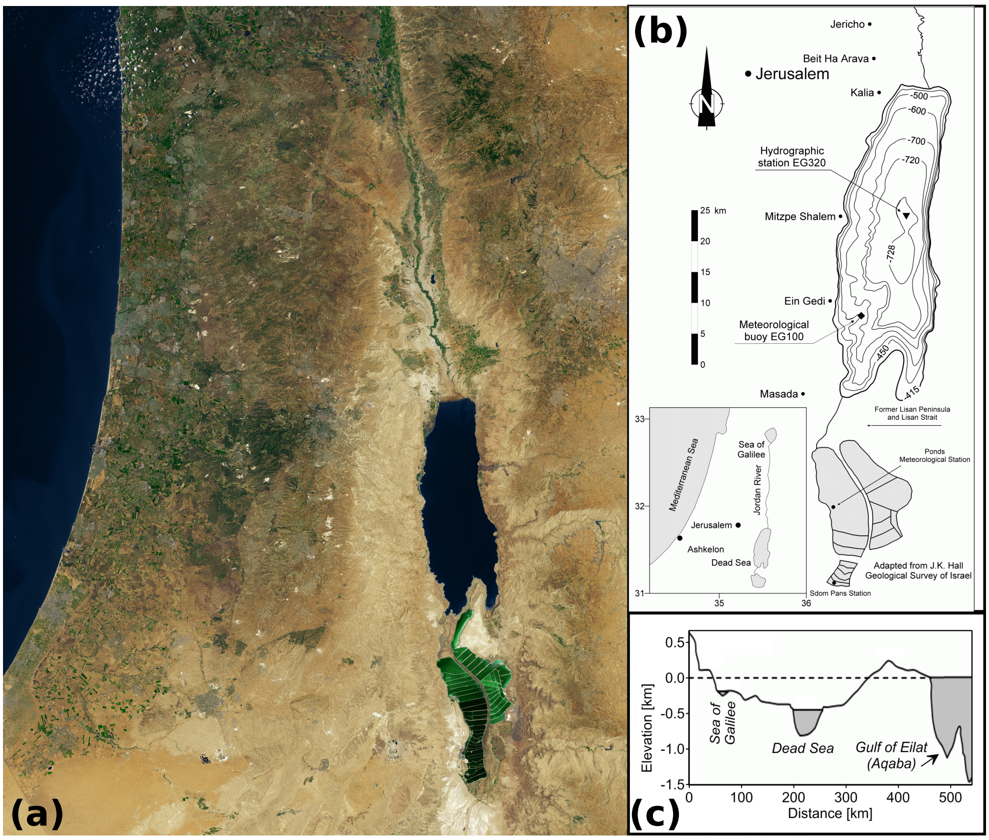

Fig. 2.12: (a) Landsat-8 satellite image acquired on 4^{th} July 2013 of the Jordan Rift Valley and the Dead Sea (from `https://www.esa.int/spaceinimages/Images/2014/11/Dead_Sea_Middle_East`); (b) Map of the Dead Sea showing the 2001 shoreline at 415 ms and the location of Israeli meteo (EG100) and hydrographic (EG320) stations (from Gertman and Hecht (2002)); (c) Sketch showing a meridional cross-section along the Dead Sea water shed (adapted after Shapiro et al. (2019)).

Until 1978 the morphology of the Dead Sea consisted of a large and deep northern basin and a smaller and much shallower southern basin connected via the Lynch straits (e.g. Neev and Emery (1967)). Since the early 1960's, the inflow of fresh waters into the Dead Sea started to diminish significantly, due to the enhanced usage by the countries controlling the fresh watershed of its waters (i.e. Israel, Syria and Jordan) (e.g. Salameh and Khawaj (1984)). In addition, Israel and Jordan also started to use the Dead Sea waters for the production of minerals.

This resulted in a negative water balance which caused an almost continuous drop of the water level from a value of -397 m (i.e. 397 m below mean sea level) in 1960 to values below -399.6 m in 1978, the depth of the Lynch straits (Anati and Shasha, 1989; Steinhorn and Assaf, 1980; Steinhorn, 1981).

As a result, the two basin separated (see Fig. 2.12(b)): the length of the Dead Sea decreased from 80 km to about 50 km, its maximum depth diminished to 328 m, its surface area diminished to 815 km^2 and its volume diminished to 146 km^3 (Neev and Hall, 1979). Dikes were erected to prevent the drying up of Southern Basin, transforming the area of the smaller basin into evaporation ponds for the production of minerals, where water is pumped in from the Northern Basin (e.g. Gertman and Hecht (2002)).

Changes in the lake water level in response to climate fluctuations have affected the Dead Sea throughout its history (Klein, 1982; Yechieli, 2006). However, the incresed anthropogenic intervention in the water balance of the lake during the 20^{th} century caused a drop of the water level of more than 20 m (see Fig. 2.13). Since 1980 the surface level of the Dead Sea has been lowered at an average rate of about 60 cm per year and for the period from 1998-2010 the lowering rate has reached about 1 m per year (e.g. Gertman et al. (2010)).

The climate in the Dead Sea area is highly arid, with a mean annual rainfall less than 100 mm. The air temperature over the lake shows values between 7.5°C and 43.4°C, while relative humidity over the Dead Sea is typically between 33% and 52%. On average, August is the hottest month (average air temperature of $\approx$ 33°C) and July is the driest (39% humidity) while January is the coldest and most humid (average temperature and humidity of 18°C and 47%, respectively). The typical speed of winds is $4 - 6$ ms^{-1} and generally they are mostly northerly during summer while in winter southerly winds are more common (Hecht and Gertman, 2003; Allan et al., 2011).

Accurate hydrological measurements of the Dead Sea waters started in 1958 (Neev

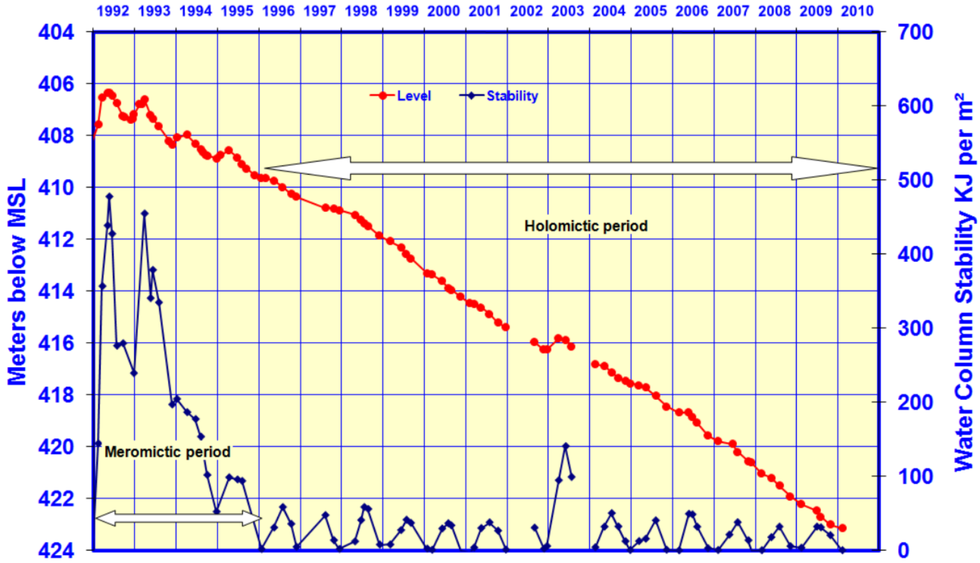

Fig. 2.13: Changes in the surface level of the Dead Sea and in the total stability of the Dead Sea water column since 1992 (from Gertman et al. (2010)).

and Emery, 1967). However, regular hydrographic observations in the deepest part of the Dead Sea (hydrological station EG320 in Fig.2.13) started only in 1975 (Steinhorn, 1981; Anati, 1997).

The Dead Sea has an extremely high salinity (about 340 $g\ kg^{-1}$) and a unique ionic composition which significantly differs from that of usual seawater. It is rich in calcium, magnesium, potassium and bromine, and relatively poor in sodium, sulfate and carbonate (e.g. Neev and Emery (1967)). For this reasons, common methods to measure water salinity can not be used in this lake (Gertman and Hecht, 2002) and the classical definition of ‘salinity’ does not apply to its waters. In order to overcome this difficulties, Anati (1999) proposed an equivalent salinity based on pycnometry named ‘quasi-salinity’. It is defined as the Dead Sea water density anomaly from 1000 $kg\ m^{-3}$ at an arbitrary reference temperature and now days it is operationally used in the analysis of observations in the Dead Sea (Gertman and Hecht, 2002).

The water column of the Dead Sea can present two opposite type of stratification regimes, either meromictic or holomictic (Steinhorn and Gat, 1983; Anati et al., 1987;

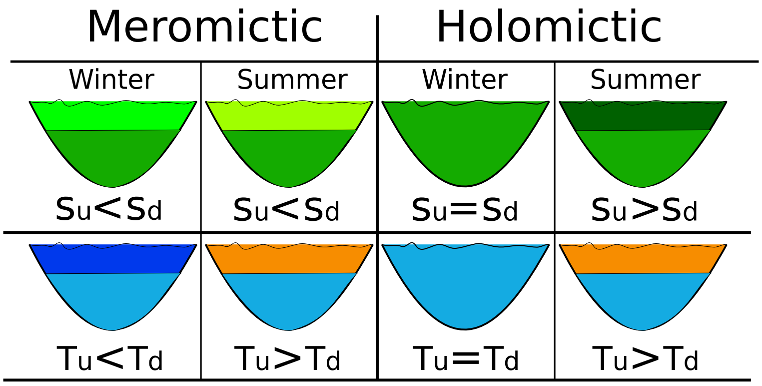

Fig. 2.14: Sketch depicting differences between meromictic and holomictic regimes in the Dead Sea. Su and Tu represent salinity and temperature of the upper mixed layer while Sd and Td are salinity and temperature in the deeper layer.

Gertman and Hecht, 2002). A meromictic lake is characterised by a stable stratification throughout the whole year while a holomictic lake presents stable stratification during the warm season and overturn and complete mixing of the water column during winter (Hutchinson (1957), see Fig. 2.14).

In the Dead Sea, the meromictic regime appears only after extremely rainy winters, when low salinity in the upper layer increases hydrostatic stability limiting winter convection (Gertman et al., 2010). In holomictic regime, winter convection is promoted by the cooling of the Dead Sea surface combined with the increasing of surface salinity due to evaporation and mechanical wind energy. In summer, a strong pycnocline typically located at a depth of $20 - 30$ m exists. It mainly results from the warming of the upper layer which stabilizes the stratification of the water column, despite the increasing of surface salinity due to enhanced evaporation (Anati, 1997; Gertman and Hecht, 2002).

For several centuries, the Dead Sea was a meromictic lake. However, due to the diminishing fresh water runoff into the lake, the salinity of the upper layer progressively increased. Eventually, during winter $1978 - 1979$, the waters of the lake overturned and the lake became holomictic for two months (Steinhorn and Gat, 1983; Anati et al., 1987). Since then, the Dead Sea entered a new phase in which it switches

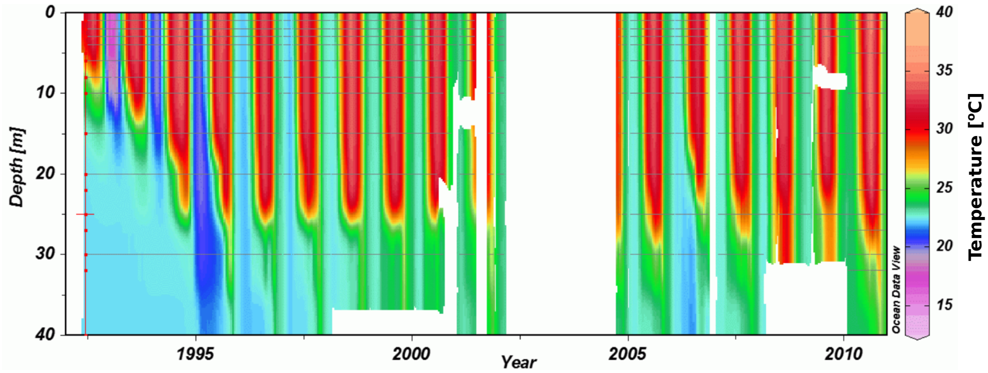

Fig. 2.15: Interannual evolution of seawater temperature measured by the thermistor string from the EG-100 meteorological platform (from Allan et al. (2011)).

from one regime to the other (Gertman and Hecht, 2002).

The overall stability of the Dead Sea is traditionally monitored by computing the energy per unit area, W in $[Jm^{-2}]$, required to completely mix the water column against its stable stratification (Anati et al., 1987):

$$W = \frac{g}{A(0)} \int_0^h \Big[\rho(z) - \hat{\rho}\Big] A(z) z \, dz, \tag{2.4}$$

where $A(z)$ is the horizontal area of the hypersaline lake at depth z, $\rho(z)$ is the observed vertical profile of potential density, $\hat{\rho} = h^{-1} \int_0^h \rho(z)\, dz$ is the depth-averaged density and h is the maximum depth of the Dead Sea.

Figure 2.13 presents the timeseries of W for the period $1992 - 2010$. From 1992 to 1995, the Dead Sea was meromictic, due to the large input of fresh water from the heavy rains of winter 1991-1992. After that event, the halocline gradually weakened and its depth progressively increased from about 12 m in 1992 to about 25 m in 1995. Eventually, in summer 1995 the salinity of the meromictic upper layer overshot the salinity of the deep water and in the autumn of the same year convection mixed the entire volume of the sea, starting a new period of holomictic regime (Gertman and Hecht (2002), see Fig. 2.15).

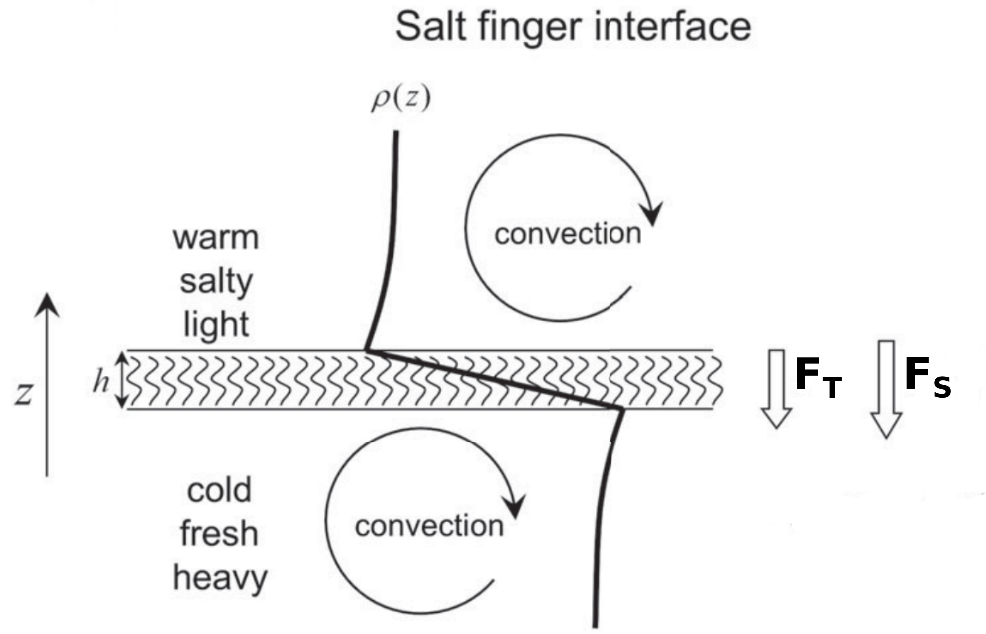

Fig. 2.16: Schematic diagram illustrating the dynamics of two-layer fingering systems (from Radko et al. (2014)).

A distinct feature of the Dead Sea holimictic regime is the development of thermohaline step-like structures in late summer and early autumn (Anati and Stiller, 1991; Gertman et al., 2015; Arnon et al., 2016). Thermohaline staircases consist of remarkably regular homogeneous layers in vertical temperature and salinity profiles separated by high gradient interfaces. Although these mixed layers can be up to tens of meters deep, they are created and maintained by double-diffusive processes operating on scales of a few centimetres (Radko et al., 2014).

Double-diffusion is a fluid instability arising from the fact that the molecular diffusivity of salt ($k_s \approx 1.1 \times 10^{-9}\ m^2s^{-1}$) is much lower than the one of temperature ($k_t \approx 1.4 \times 10^{-7}\ m^2s^{-1}$). Two different types of double-diffusive convection exist: (i) salt fingering, where salt is the destabilizing component, and (ii) diffusive convection, where the instability is driven by temperature (Stern, 1960).

In the ocean, salt fingering is the most common double-diffusive process and it is responsible for the development of T-S staircases (e.g. Stern (2003); Radko et al.

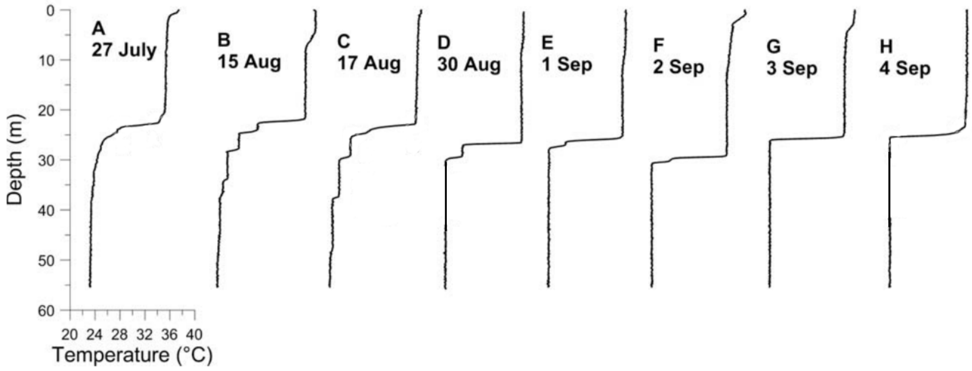

Fig. 2.17: Selected profiles illustrating key stages of sharpening and merging of thermohaline staircases (from Arnon et al. (2016)).

(2014)). Let's consider a salt-fingering system of two nearly homogeneous layers separated by a high-gradient interface with warm and salty water located on top of cold and fresh water (see Fig. 2.16). The strong interface has a thickness of few centimeters and is where salt-fingers develop: if a parcel of fluid just above the interface is displaced downward form its equilibrium position, it will rapidly adjust its temperature to that of the surrounding fluid but it will largely retain its original salinity (since $k_t >> k_s$). In such a situation, the downward flux of salt F_S is greater than the one of heat F_T. This unequal transport of heat and salt through the double-diffusive interface maintains in turn the homogeneous stratification of the two layers by driving top-heavy convection: the fluid at the top of the lower layer, immediately below the interface, consistently gains density and maintains convection; the fluid immediately above the interface loses density, which drives convection in the upper layer Radko et al. (2014)).

Thermohaline staircases have been observed in many areas of the world ocean (e.g. Fedorov (1970); Garrett (1979); Zodiatis and Gasparini (1996)) and their importance has been investigated for example by Schmitt (2005), who measured the vertical mixing in the Caribbean staircases showing that layering increases vertical diffusivity by as much as an order of magnitude relative to analogous smooth-gradient regions.

Step-like structures are observed in the Dead Sea water column in the late summer, usually in August (see Fig. 2.18). The observed thermal layering starts with the formation of several sharp steps in the temperature profile, in agreement with previous direct numerical simulations of double-diffusion processes in the ocean (e.g. Radko (2003)). At the end of August - beginning of September the thermohaline staircases eventually merge, creating a single sharp temperature step which remains until stratification is destroyed in late Autmn (Arnon et al., 2016).

Allan et al. (2011) presents measured currents profiles collected during the period 2009-2011 in few transects in the south-western part of the Dead Sea. The maximal recorded current velocity was $10 - 15$ $cm\ s^{-1}$ while average values were $\approx 5 - 10$ $cm\ s^{-1}$. During winter, currents were uniform within the water column, mostly directed southward. In summer, measurements showed a two layer structure of the circulation, with relative strong and uniform currents in the upper mixed layer and uniform weaker currents, sometimes in the opposite direction, below the pycnocline. In autumn the circulation had the same two layer structure, with currents typically northward in the upper layer while a relatively stronger flow directed southward characterised the lower layer. Generally, a very weak or no significant correlation between the currents and the local winds measured during the same period at EG100 meteorological buoy was found.

2.4.2 Numerical modelling of the Dead Sea hydrodynamics

The unique environment of the Dead Sea poses many challenges for numerical modelling of the hydrodynamics of this hypersaline lake (Brenner et al., 2015).

For example, the shallow and steep bottom topography of the Dead Sea combined with its jagged coasts and its rapidly declining water level makes the usage of terrain-following computational surfaces desirable, although errors in computing horizontal pressure gradients with curved levels represent a serious problem (Gavrieli et al., 2003).

Moreover, the peculiar ionic composition of the waters of this lake and their extremely high salinity and density prevent from using common non-linear equations of state (e.g. UNESCO-1980 or TEOS-2010) usually applied in the World Ocean (e.g., Brenner et al. (2015)).

Also, the transition between meromictic and holomictic regimes, the very sharp thermocline and the presence of thermohaline staircases during holimictic summers require the implementation of high vertical resolution and a robust and flexible vertical mixing scheme (Brenner et al., 2015).

The Dead Sea hydrodynamics has been studied using both relatively simple 1D and 2D models and more complex 3D general circulation numerical models.

For example, Vadasz et al. (1983) used a 1D numerical model to simulate long-term variations of vertical temperature, density, and salinity profiles in the Dead Sea. Asmar and Ergenzinger (2002, 2003) modelled the dynamics of the Dead Sea by approximating the sea as a a two-layer system and evaluating a series of ordinary differential equations describing mass balances on the water and major chemical species in the basin. Ivanov et al. (2002) used a one-dimensional quasi-isopycnic multilayer model with an upper mixed layer and the Anati (1997) equation of state to study the variability of the thermohaline water structure in the period $1992-2000$.

Ezer (1984) studied the currents in the Dead Sea by using the Huss and Feliks (1981) numerical model for both the atmosphere and the sea while Huss et al. (1986) used to same model to investigate the impact of the high density of the Dead Sea water on the circulation. Sirkes (1986) studied the Dead Sea's wind-driven seiches using a seiche model and a simple oceanic general circulation model, under the assumptions of homogeneous temperature and salinity fields.

During the Johannesburg 2002 World Summit, Israel and Jordan announced the joint construction of the 'Peace Conduit', an artificial conduit to transport water from the Gulf of Eilat/Aqaba to the Dead Sea. The aim of this project was to stop the drop in the Dead Sea's level and to use the ≈ 430 m elevation difference between the Gulf of Eilat and the Dead Sea as an energy source for water desalination (Allan et al., 2011).

A pilot modelling study to assess the consequences of this project on the Dead Sea marine environment was carried out by Gavrieli et al. (2003). They tested the Princeton Oceanographic Model (POM) in the Dead Sea, concluding that σ-levels introduced too high pressure gradient errors, resulting in unrealistically large velocities and instability of the model. Therefore, they used geopotential levels with a new equation of state accounting for the different ionic composition of the Dead Sea waters and very low vertical diffusivity (of the order of (10^{-9}) m^2 s^{-1}) to retain the strong summer stratification.

Following the preliminary work of Gavrieli et al. (2003), Allan et al. (2011) used POM with 50 unevely spaced σ-levels and the Anati (1997) linear equation of state to study the short-term consequences of the 'Peace Conduit' project. They were able to reduce spurious currents to an acceptable level by smoothing the bathymetry and subtracting a basin averaged density profile before computing horizontal pressure gradients (e.g. Mellor et al. (1998)). They used horizontally homogeneous atmospheric forcing and T/S initial condition by spreading atmospheric and hydrographic data measured at EG100 meteo-station and EG320 hydrographic-station, respectively.

More recently, Brenner et al. (2015) used POM with 61 σ-levels to reproduce the flood event of January-February 2013. They used the Gertman et al. (2010) equation of state, idealized or simplified surface forcing and relaxation of SST to observed value.

Padon and Ashkenazy (2018) implemented a number of MITgcm-based hydrodynamic models with different horizontal resolution, 15 z-levels and a linear equation of state to investigate non-hydrostatic effects in the Dead Sea.

2.5 NEMO ocean model

The numerical simulations of this thesis are carried out using the Nucleus for European Modelling of the Ocean (NEMO) Ocean General Circulation model code version 3.6 (Madec, 2008). NEMO solves the standard set of primitive equations usually applied to describe the motion of geophysical fluids: the incompressible, hydrostatic, Boussinesq approximated Reynolds-averaged Navier-Stokes equations for momentum and volume budgets, the tracer advection/diffusion equations for heat and salinity conservation and a diagnostic non-linear equation of state for the ocean density.

In height coordinate and vector invariant form they can be written as follows:

$$\begin{aligned}
\partial_t \mathbf{u}_h = & -(\nabla_h \times \mathbf{u}_h) \times \mathbf{u}_h - \frac{1}{2}\nabla_h|\mathbf{u}_h|^2 - w\partial_z \mathbf{u}_h - f\ \mathbf{k} \times \mathbf{u}_h \qquad (2.5)\\
& - \frac{1}{\rho_0}\nabla_h p + \mathbf{D^u} + \mathbf{F^u},
\end{aligned}$$

$$\partial_z p = -\rho\ g, \qquad (2.6)$$

$$\nabla_h \cdot \mathbf{u}_h + \partial_z w = 0, \qquad (2.7)$$

$$\partial_t \theta = -\nabla \cdot (\theta\ \mathbf{u}) + D^\theta + L^\theta + F^\theta, \qquad (2.8)$$

$$\partial_t S = -\nabla \cdot (S\ \mathbf{u}) + D^S + F^S, \qquad (2.9)$$

$$\rho = \rho\left(\theta, S, p\right), \qquad (2.10)$$

where $\mathbf{u} = \mathbf{u}_h + w\,\mathbf{k} = (u, v, w)$ is the ocean flow vector (the subscript h denotes a 2D vector with components in the meridional and zonal directions and $\mathbf{k}$ is the local upward vertical unit vector), z is the height referenced to the geoid, θ is the potential temperature, S the practical salinity and ρ is the in-situ density. $\nabla_h = (\partial_x, \partial_y, 0)$ represents the 2D differential operator while t is time, ρ_0 is the reference density, p the pressure, f is the Coriolis parameter and g is the gravitational acceleration. $\mathbf{D^u}$, D^θ and D^S parameterize sub-grid physics for momentum, temperature and salinity. $\mathbf{F^u}$, F^θ and F^S introduce surface forcing terms and L^θ describes the penetration of the radiative heat flux in the water column.

In NEMO, the equation of state $\rho(\theta, S, p)$ can be either linear (following Vallis (2006)) or non-linear. If the latter is chosen, both the EOS-80 (UNESCO, 1983) and TEOS-10 (IOC et al., 2010) formulations are available.

In this thesis, the effect of sub-grid scale dynamics on the large scale motion is parameterized as follows:

$$\mathbf{D}^{\mathbf{u}} = \nabla_h \cdot (A_h \nabla_h \mathbf{u}_h) - \Delta_h (B_h \Delta_h \mathbf{u}_h) + \partial_z (A_v \partial_z \mathbf{u}_h), \tag{2.11}$$

$$D^\theta = \nabla_h \cdot (K_h \nabla_h \theta) + \partial_z (K_v \partial_z \theta), \tag{2.12}$$

$$D^S = \nabla_h \cdot (K_h \nabla_h S) + \partial_z (K_v \partial_z S). \tag{2.13}$$

Here, A_h and B_h are the lateral Laplacian and biharmonic viscosity coefficients, respectively, while K_h is the lateral diffusivity coefficient. The harmonic operator for momentum and active tracers lateral diffusion is aligned with geopotential surfaces while the viscous fourth-order operator is discretised along model levels. A_v and K_v represent the vertical viscosity and diffusivity coefficients, respectively and NEMO provides a selection of various turbulence closure schemes to compute them.

All the simulations carried out in this thesis use closed lateral boundaries with no-slip condition and a non linear free surface formulation to describe the time evolution of the air-sea interface η. The following prognostic equation for the free surface is added to the set of equations solved by the models:

$$\partial_t \eta + \nabla \cdot \int_{-H}^{\eta} \mathbf{u}_h \, dz = -(E - P - R/A), \tag{2.14}$$

where η is the deviation of the sea surface from its unperturbed position and $E - P - R/A$ represents the freshwater budget defined in terms of water fluxes due to evaporation (E), precipitation (P) and river discharge per river mouth's area (R/A).

At the surface, the following kinematic boundary condition is applied:

$$w\Big|_{z=\eta} - \partial_t \eta - \mathbf{u}_h\Big|_{z=\eta} \cdot \nabla \eta = E - P - R/A. \tag{2.15}$$

The surface dynamic boundary conditions for momentum, heat and freshwater are:

$$\mathbf{F}^{\mathbf{u}} \equiv A_v^m \partial_z \mathbf{u}_h\Big|_{z=\eta} = \rho_0^{-1}\tau, \tag{2.16}$$

$$F^{\theta} \equiv A_v^m \partial_z \theta\Big|_{z=\eta} = (\rho_0 C_p)^{-1}(Q_{tot} - Q_{sr}), \tag{2.17}$$

$$F^{S} \equiv A_v^m \partial_z S\Big|_{z=\eta} = S\Big|_{z=\eta}(E - P - R/A), \tag{2.18}$$

where $\tau = (\tau_{\mathbf{x}}, \tau_{\mathbf{y}})$ is the wind stress, $C_p = 4000\ Jkg^{-1}K^{-1}$ is the ocean specific heat, Q_{tot} and Q_{sr} are the net and solar heat fluxes at the sea surface, respectively. The penetration in the water column of the short wave radiation Q_{sr} (L^{θ} term in Equation 2.8) can be parameterized by using a chlorophyll-independent 2-wavebands light penetration scheme (Paulson and Simpson, 1977) or the Lengaigne et al. (2007) chlorophyll-dependent 3-wavebands scheme.

For the dynamic bottom boundary condition, if not stated otherwise a log-layer enhanced quadratic bottom friction parametrisation is used, with minimum and maximum bottom drag coefficient values equal to $2.5 \cdot 10^{-3}$ and 10^{-1}, respectively (see Madec (2008) for the details).

NEMO solves the primitive equations in a horizontally orthogonal curvilinear coordinate system together with a generalised vertical coordinate $s(x, y, z, t)$ (see e.g. Kasahara (1974)). Discretization of the equations is performed on an Arakawa C type structured mesh and the transformation from the continuous coordinate system to the discrete mesh is specified in terms of the three scale factors e_1, e_2, e_3 defined

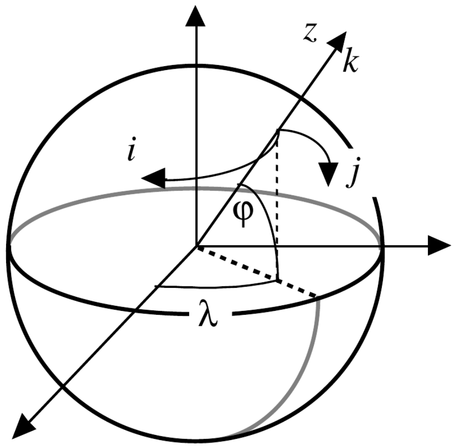

Fig. 2.18: The geographical coordinate system (λ, ϕ, z) and the curvilinear coordinate system (i, j, k) (from Madec (2008)).

as

$$e_1 = (a+z)\left[\left(\frac{\partial\lambda}{\partial i}\cos\phi\right)^2 + \left(\frac{\partial\phi}{\partial i}\right)^2\right]^{1/2}, \tag{2.19}$$

$$e_2 = (a+z)\left[\left(\frac{\partial\lambda}{\partial j}\cos\phi\right)^2 + \left(\frac{\partial\phi}{\partial j}\right)^2\right]^{1/2}, \tag{2.20}$$

$$e_3 = \frac{\partial z}{\partial k}, \tag{2.21}$$

where (i, j, k) is a set of orthogonal curvilinear coordinates on the sphere associated with the positively oriented orthogonal set of unit vectors $(\mathbf{i}, \mathbf{j}, \mathbf{k})$ linked to the earth such that $\mathbf{k}$ is the local upward vector (see Fig. 2.18). Then, $\lambda(i, j)$ represents the longitude and $\phi(i, j)$ the latitude, while a is the Earth's radius and z the altitude above a reference sea level.

In all the numerical experiments, the time-splitting formulation for the non linear free surface is applied. For calculation of the hydrostatic pressure gradient term the pressure Jacobian scheme together with a leapfrog time scheme are used. The Asselin time filter parameter is equal to 0.1. The Total Variance Dissipation (TVD) and Energy and ENstrophy (EEN) conservative schemes are chosen for tracer and momentum advection, respectively.

The specific NEMO set-up used in each particular numerical experiment is detailed in the relevant Chapter.

3. A multi-envelope vertical coordinate system for numerical ocean modelling

This Chapter has been published as Bruciaferri, D., Shapiro, G.I. and Wobus, F. (2018) *A multi-envelope vertical coordinate system for numerical ocean modelling.* Ocean Dynamics, Volume 68(10), Pages 1239-1258, doi:10.1007/s10236-018-1189-x.

3.1 Introduction

When designing an ocean model, the choice of the vertical coordinate system must be pursued very carefully (Griffies, 2004), especially in regional areas where local smaller-scale processes interact with large-scale oceanographic features (Kantha and Clayson, 2000b; Gangopadhyay and Robinson, 2002). Numerical discretisation introduces truncation errors specific to the chosen vertical coordinate system, and hence influences the representation of physical processes (Haidvogel and Beckmann, 1999). Currently, three main vertical coordinates are typically used in ocean modelling, namely z-level (geopotential), terrain-following and isopycnic, but all of them have deficiencies (see e.g Chassignet et al. 2006).

The z-level coordinates are a natural framework for describing horizontal pressure gradients. However, the z-level system generates an unnatural step-like representation of bottom topography and consequently introduces an error in simulating near-bottom processes, including dense water overflows (e.g. Ezer and Mellor 2004; Ivanov et al. 2004). Gerdes (1993a) concluded that the crude approximation to the actual topography used in z-level models results in large errors in the simulated mass transport in regions where planetary and topographic beta-effects are of comparable magnitudes. Horizontal overshoots of dense water due to step-like representation of bottom topography lead to spurious convective mixing. Recently, Ezer (2016) showed that the unrealistic representation of topographic slopes in z-ocean models has a negative impact on the simulation of the dynamics of western boundary currents and consequently of large-scale circulation.

The disadvantages of z-level grids initiated intensive development of terrain-following grids for ocean modelling (Blumberg and Mellor, 1987; Haidvogel et al., 1991; Ezer and Mellor, 1992). The terrain-following coordinate (σ-coordinate system) offers a smooth representation of bottom topography and a natural parametrisation of the bottom boundary layer (Mellor et al., 2002). However, it introduces a pressure gradient error, in particular on steep slopes (Haney, 1991; Mellor et al., 1994, 1998).

The use of computational surfaces that are not aligned with isopycnals (which is generally the case of both z- and σ-coordinate systems) in simulating tracer transport introduces the contamination of slow diapycnal processes by fast isopycnal exchanges (e.g. Roberts and Marshall 1998; Griffies et al. 2000b). As a consequence, spurious diapycnic mixing poses a major problem in non-isopycnal models (see Holt et al. 2017 and references therein). Such deficiencies are not present in vertical grids where computational levels follow isopycnals (so-called isopycnic grids), e.g. used in the MICOM ocean model, see Bleck (1998). However, isopycnic models experience difficulties in weakly stratified areas, such as over the continental shelf or in the upper or bottom mixed layers (Griffies et al., 2000a). Legg et al. (2006) compared the performance of isopycnal and z-models in representing dense cascades while Legg et al. (2009) pointed out the importance of a correct simulation of oceanic overflows in numerical climate models.

In order to minimise the disadvantages of the various vertical coordinate systems, further modifications were introduced either to the vertical grids themselves or to the numerical representation of the governing equations. For example, the introduction of shaved (Adcroft et al., 1997) or partial (Pacanowski et al., 1998) cells which slightly change the shape of 'pure' z-coordinate grids was proposed to improve the representation of bottom topography in z-models. The z-partial steps approach is now widely used for global (Barnier et al., 2006) and regional (e.g., Oddo et al. 2009; Trotta et al. 2016) ocean models. A stretched terrain-following s-coordinate system (Song and Haidvogel, 1994) and its several variants (e.g, Madec et al. 1996; Siddorn and Furner 2013) as well as advanced methods in calculation of pressure gradients (Shchepetkin, 2003) were developed to improve σ-coordinates flexibility and accuracy.

The concept of a generalised vertical coordinate system (see for example Kasahara 1974 or Mellor et al. 2002) allowed in principle the development of vertical grids of various complexity, as for example the hybrid vertical schemes where different 'pure' grids were applied to different sub-domains of the ocean. The aim of this was to better represent the differing physical processes which might prevail in different sub-domains, by using one specific grid rather than another. Examples of those methods are the HYCOM model (Bleck and Boudra, 1981; Bleck, 2002), the vertical grids by Gerdes (1993a,b), Madec et al. (1996), Shapiro et al. (2013) or the Song and Hou (2006) parametric vertical coordinate system.

The idea of Arbitrary Lagrangian-Eulerian (ALE) vertical coordinates (Hirt et al., 1974) permitted the development of z*- (Adcroft and Campin, 2004) and $\tilde{z}$-coordinates (Leclair and Madec, 2011) and the adaptive σ-based coordinate (Hofmeister et al., 2010).

A significant improvement in terrain-following schemes was achieved by introducing the idea of the 'enveloping' bathymetry, where computational surfaces follow a 'virtual bottom' (aka envelope) rather than the real bathymetry (Enriquez et al., 2005; Dukhovskoy et al., 2009; Shapiro et al., 2013). This solution allows the reduction of slopes of computational surfaces and the reduction of pressure gradient errors to an acceptable level.

In this study, we introduce the 'Multi-Envelope s-coordinate' (hereinafter MEs-coordinate). It extends the classical concept of terrain-following coordinates by defining s-levels which follow multiple envelopes rather than a single one as is the case in existing models. This approach allows to combine the ideas behind the hybrid schemes (best representation of different physics in different sub-domains of the model) and numerical improvements (e.g. enveloping) developed for 'pure' vertical discretisation grids. The new vertical system represents a generalised coordinate system, since all non-isopycnal vertical grids (both 'pure' and hybrid) can be considered a special case of MEs-coordinates.

The Chapter is organized as follows. Section 3.2 defines the MEs-coordinate, detailing its features. Section 3.3 describes the idealised model domain, the design of the three different vertical grids and the set up of the three numerical experiments. In Sec. 3.4, the results are presented, analysed and discussed. Section 3.5 summarises our main conclusions.

3.2 The Multi-Envelope s-coordinate

In this Chapter we show how the MEs system can be used to improve the representation of the oceanic transport in a non-isopycnal coordinate model. The MEs-coordinate combines the s-coordinate concept and the idea of 'enveloping' the bottom topography.

Let us consider a local Cartesian x, y, z coordinate system with a downward vertical unit vector $\hat{z}$. A stretched envelope-following s-coordinate can be defined as

$$z = S(\sigma, \eta, H_e), \tag{3.1}$$

where $\eta(x, y, t)$ is the deviation of the sea surface from its unperturbed position,

$H_e(x, y)$ is a smoothed version of the actual bottom topography (aka bathymetry envelope) and $-1 \leq \sigma \leq 0$, with $\sigma = 0$ at $z = \eta$ and $\sigma = -1$ at $z = H_e$. A general stretching function is represented by $S(\sigma, \eta, H_e)$. It can be, for example, the one by Song and Haidvogel (1994), Shchepetkin and McWilliams (2005) or Siddorn and Furner (2013).

The MEs vertical system defines n arbitrary reference surfaces (hereafter called envelopes) $H_e^k(x, y, t)$, with $0 \leq k \leq n$ and $n \in \{2m + 1\}$ with m a positive integer such that

$$\eta = H_e^0 < H_e^1 < ... < H_e^{n-1} < H_e^n, \tag{3.2}$$

Each envelope $H_e^k(x, y, t)$ moves with the free-surface according to the following equation:

$$H_e^k = h_e^k + \eta\Big(1 - \frac{h_e^k}{h}\Big), \tag{3.3}$$

where $h_e^k(x, y)$ is the depth of the k^{th} envelope when the ocean free-surface is unperturbed ($\eta = 0$) and $h = h_e^n$.

The envelopes divide the ocean model vertical domain into n sub-zones D_i, with $1 \leq i \leq n$. Each sub-zone D_i is bounded by envelopes H_e^{i-1} at the top and H_e^i at the bottom.

The non-dimensional σ_i-coordinate is defined for each sub-zone D_i as

$$\sigma_i = -\frac{z - H_e^{i-1}}{H_e^i - H_e^{i-1}}, \tag{3.4}$$

with $\sigma_i(H_e^{i-1}) = 0$ and $\sigma_i(H_e^i) = -1$. Then, the MEs-coordinate is defined as a piecewise function

$$\begin{cases} z|_{D_i} = S_i(\sigma_i, H_e^{i-1}, H_e^i), & \text{if } i \in \{2m + 1\} \quad (3.5a) \\ z(x, y, \sigma_i, t)|_{D_i} = P^3_{x,y,i}(\sigma_i), & \text{if } i \in \{2m\} \quad (3.5b) \end{cases}$$

The function $S_i(\sigma_i, H_e^{i-1}, H_e^i)$ in Equation 3.5a represents a general stretching function. For example, in the case of the classical Song and Haidvogel (1994) stretching function, MEs coordinates are defined as

$$z|_{D_i} = H_e^{i-1} + h_c^i \sigma_i - C_i(\sigma_i)(H_e^i - h_c^i - H_e^{i-1}), \tag{3.6}$$

where h_c^i is the critical depth at which transition from pure σ to the stretched s-coordinate occurs and $C_i(\sigma_i)$ is the hyperbolic function of Song and Haidvogel (1994) (their $C(s)$).

The function $P^3_{x,y,i}(\sigma_i)$ in Equation 3.5b is a complete cubic spline whose coefficients are determined by the following three constraints:

1. Monotonicity:

$$\partial_{\sigma_i} z|_{D_i} > 0, \text{ with}$$

$$\begin{cases} -1 \leq \sigma_i \leq 0, & \text{if } i = n \\ -1 < \sigma_i \leq 0, & \text{if } i < n \end{cases}$$

2. Continuity:

$$z|_{D_i}(\sigma_i = -1) = z|_{D_{i+1}}(\sigma_{i+1} = 0),$$

3. Continuity of the first derivative:

$$\partial_{\sigma_i} z|_{D_i}(\sigma_i = -1) = \partial_{\sigma_{i+1}} z|_{D_{i+1}}(\sigma_{i+1} = 0),$$

Under these conditions, the Jacobian of the transformation from z to σ is continuous, ensuring one of the requirements of improved accuracy formulated by Marti et al. (1992) and Treguier et al. (1996).

The new MEs represents a generalised coordinate system, in the sense that 'pure' and hybrid non-isopycnal vertical coordinates can be considered a special case of

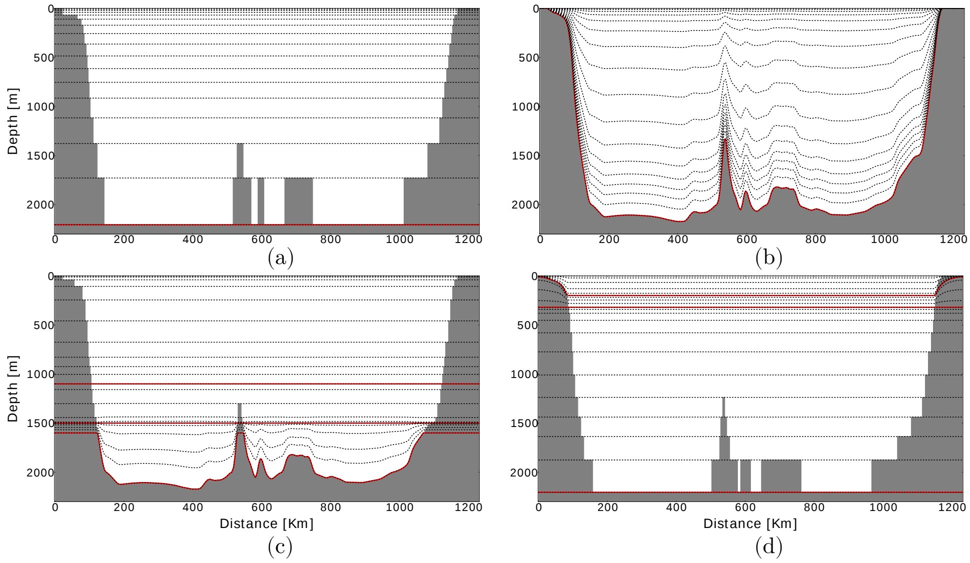

Fig. 3.1: Sketches depicting 'pure' z- (a) and σ- (b) grids and hybrid Madec et al. (1996) z-on-top-of-s (c) and Shapiro et al. (2013) s-on-top-of-z (d) approaches as retrieved with the MEs-coordinate system. Envelopes H_e^i used to define each specific configuration are shown in red.

MEs-coordinate. For example, z-grids are simply generated by defining a single horizontal envelope $H_e^1 = \max(H_B)$, where $H_B(x, y)$ is the actual bathymetry (see Fig. 3.1(a)). Similarly, terrain-following σ-coordinates can be generated by choosing $H_e^1 = H_B$, see Fig. 3.1(b)). Figures 3.1(c) and 3.1(d) show how hybrid 'z-on-top-of-s' (Madec et al., 1996) and 's-on-top-of-z' (Shapiro et al., 2013) grids, respectively, can be easily generated with the MEs vertical system. In MEs all grid cells are full, both near the bottom and in the interior, and their shape is dictated by the corresponding envelope.

An important feature of the MEs system is that envelopes H_e^i can be arbitrarily chosen surfaces. This implies that they can be designed to optimise the representation of those physical processes that are prioritised, allowing the modeller to manage and control the design of model levels with enhanced flexibility. Fig. 3.2 shows an example of MEs design by using five reference surfaces H_e^i.

In this configuration, sub-zone D_5 has model levels which follow envelope H_e^5, a

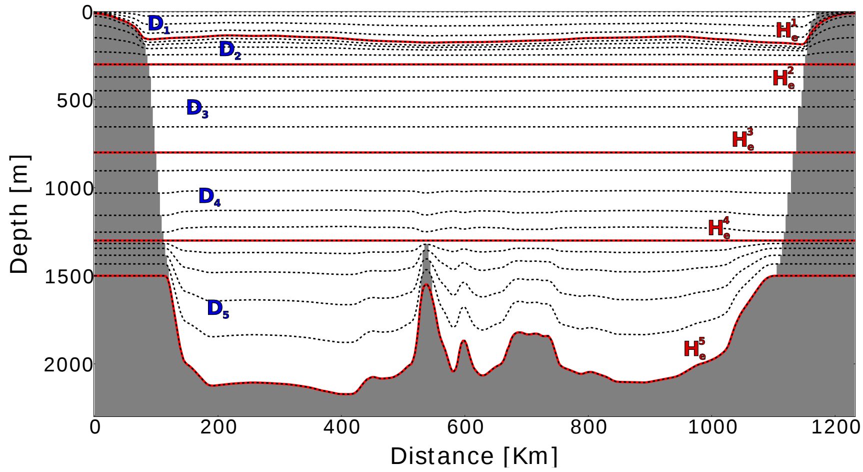

Fig. 3.2: Conceptual sketch of the MEs vertical coordinate system. In this example, five envelopes H_e^i are used to define MEs-levels.

smooth version of the actual bottom topography up to 1500 m. This enables realistic simulations of dense water overflows over the ocean bottom while reducing pressure gradient errors. In sub-zone D_3, model levels are horizontal. Zones D_2 and D_4 work as transition zones which gradually reduce the slope of s-levels towards geopotential surfaces in D_3.

The upper envelope H_e^1 follows the 'main pycnocline' (i.e. long-term mean pycnocline) in open ocean areas but it follows the topography in coastal regions. Such an envelope allows to obtain realistic simulations of both dense water cascades in shelf areas and the formation of a cold intermediate layer in the open sea. The pycnocline-shaped envelope reduces the angle between the computational surfaces and the isopycnals, and hence reduces the spurious diapycnal mixing, thus performing similar to isopycnal coordinate systems.

To clarify this effect, let us consider the idealised case of a two-layer immiscible fluid depicted in Fig. 3.3.

In this case, tracer advection and diffusion occurs exclusively along the isopycnal surface, as represented by black and green arrows in Fig. 3.3(a), and there is no

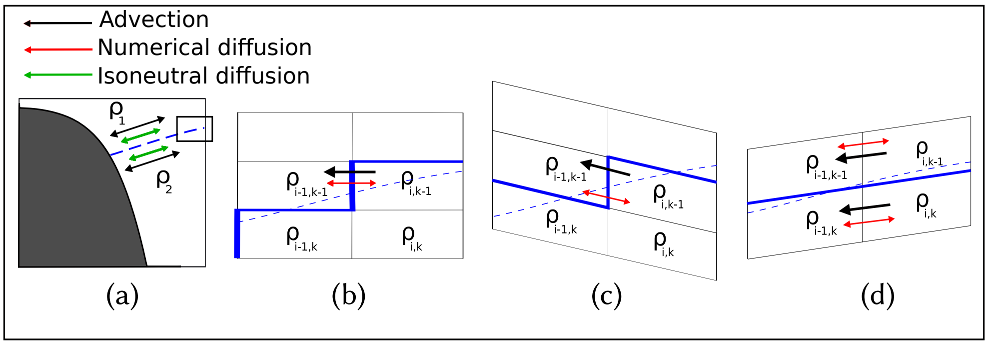

Fig. 3.3: Idealised two density layers baroclinic ocean (a) and its representation with geopotential z-levels (b), terrain-following s-levels (c) and the MEs vertical system with the upper envelope H_e^1 designed to follow the main pycnocline in open ocean areas (d). The real pycnocline is represented by the dashed blue lines, while the pycnocline simulated by the models is shown with the solid blue lines. See the text for more detailed explanations.

diapycnal mixing. Figures 3.3(b), 3.3(c) and 3.3(d) illustrate how the real isopycnal surface is represented with z-level, s-level and MEs grids, respectively.

Black arrows in Figures 3.3(b) and 3.3(c) show how advection is simulated in z- and s-models, resulting in the spurious mixing across different densities due to much stronger 'along-computational-level' numerical diffusion (see the red arrows) , which transfers mass and momentum between the density layers.

The rotation of the diffusion operator to align the lateral diffusion with isopycnals (Redi, 1982) would have reduced this undesirable effect. However, s-models typically use geopotentially oriented diffusion, because of the difficulties in computing isoneutral diffusion (Barnier et al., 1998; Marchesiello et al., 2009; Furner, 2012; Lemarié et al., 2012). Another approach (widely used in regional models) could be the subtraction of climatological temperature and salinity fields before the lateral diffusion fluxes are calculated, hence diffusing only tracer anomalies, following Mellor and Blumberg (1985).

If model levels mimic the pycnocline as in the MEs model, the angle between the isopycnals and computational surfaces is small, see Fig. 3.3(d), and the spurious diapycnal mixing arising from numerical errors of the advective schemes is significantly reduced.

In order to use the MEs grid for our computations, we modified the NEMO model code accordingly. A new module called `zgrmes` has been created. It contains a subroutine called `zgr_mes` and several functions and it is used by the `domzgr` module. The new `zgr_mes` subroutine is responsible for (i) reading the externally provided bathymetry and envelopes, (ii) computing the MEs-coordinate transformation and (iii) calculating the 3D arrays of MEs levels depths and vertical scale factors $\partial_{\sigma_i} z|_{D_i}$. In order to compute the four coefficients of the complete cubic spline $P^3_{x,y,i}$, the Fortran90 numerical library PPPACK (de Boor, 1978) was modified and introduced in the new `zgrmes` module. The introduction of the MEs discretization schemes in the NEMO code involved also modifications in the model namelist, with changes in the `namzgr` namelist group and the creation of a new namelist group called `namzgr_mes` where all the parameters defining the MEs coordinate system are declared. In addition, modifications were also made in all the NEMO code modules where the choice of the vertical coordinate system is relevant, namely `domain`, `dom_oce`, `domstp`, `domwri`, `dynhpg`, `dtatsd`, `dynldf_bilap`, `dynldf`, `dynspg_ts`, `dynvor`, `dynzdf`, `ldfdyn`, `mppini_2`, `ldfslp`, `sbcrnf`, `traldf`, `traqsr`, `trazdf`, `zdfini`, `diadct`, `dtauvd`.

3.3 Experiments to assess model skill

In this section we assess the modelling skills of the MEs scheme in comparison to the widely used z-level with partial steps scheme by performing a set of idealised numerical experiments with an axisymmetric ocean basin.

The model domain is a bowl-shape basin with a diameter of 500 km, maximum depth of 1000 m and the downward positive topography H_B defined by

$$H_B = max\left\{h_0 \exp\left(\frac{x^2}{2\sigma^2} + \frac{y^2}{2\sigma^2}\right), 1000\right\}, \tag{3.7}$$

with $h_0 = 25000\ m$, $\sigma = 8$, and $x, y \in [-40\ km\ , 40\ km]$ (see Fig. 3.4(a)). The slope at the 200 m isobath of the idealised basin is $\approx 1.5\%$.

3.3.1 Model grids

All the numerical experiments are carried out by using two models which have the same horizontal mesh but two different vertical grids: one uses the common z-level with partial steps (hereafter called zps) while the second uses the new MEs scheme. In the horizontal, the mesh has 140 grid points in both the zonal and the meridional directions and a uniform grid spacing $\Delta x = \Delta y \approx 3.57\ km$. For better comparison between the MEs against the zps vertical grid, both models have the same number of 34 numerical levels and hereafter they are called MEs-34 and zps-34, respectively. For the same reason, the computational level n^o 26 is placed at the same depth of 250 m for both grids.

One experiment is also carried out with a z-full step vertical grid at a very high vertical resolution of 150 levels (hereafter zfs-150). This simulation is used as a reference where analytical solutions are not available (see Section 3.3.2).

The zps-34 grid uses a standard NEMO-3.6 z-partial steps scheme (Fig.3.4(c)) with a minimum layer thickness of 4 m. The partial step parameters are tuned in such a way that the topography represented with 34 levels is close to the one discretised with 150 geopotential levels.

The MEs-34 grid is configured by using three *envelopes* (see Fig.3.4(d)). The middle H_e^2 and the deep H_e^3 envelopes are horizontal and located at 250 m and 1000 m respectively. Therefore, the deeper D_3 zone of the MEs grid is effectively discretised with a z-coordinate grid. The upper envelope H_e^1 of the MEs-34 grid is dome-shaped

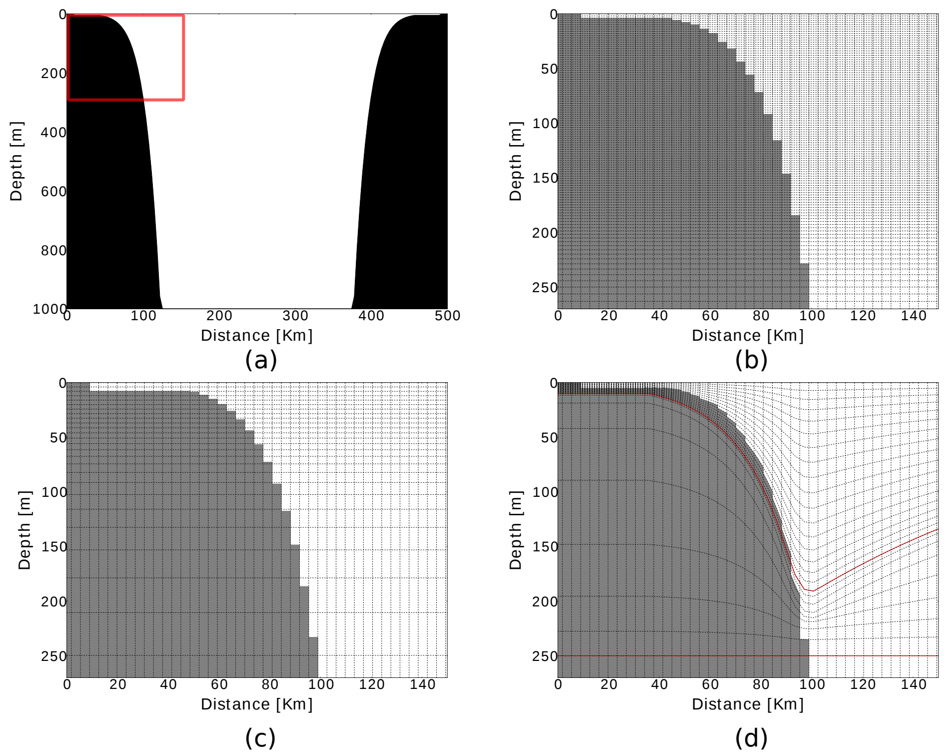

Fig. 3.4: Cross sections of the topography H_B of the idealised domain (a) and zfs-150 (b), zps-34 (c) and MEs-34 vertical (d) grids configured for this study. For the numerical grids, only the portion of the domain highlighted with the red square in panel (a) is shown for clarity.

in the ocean interior, following a typical shape of the thermocline in a sea with a cyclonic circulation, but it follows an 'enveloping'-bathymetry over the continental slope and shelf.

The 'enveloping'-bathymetry is a smoothed version of the actual bathymetry with a maximum depth of 200 m and a minimum depth of 10 m. It is obtained by applying the Martinho and Batteen (2006) smoothing algorithm to the actual topography, which reduces the maximum value of the slope parameter (Mellor et al., 1998) defined as

$$r \equiv \frac{\mid H_b - H_a \mid}{H_b + H_a}, \tag{3.8}$$

where H_a and H_b are the depths of adjacent grid cells. With the H_e^1 envelope, the

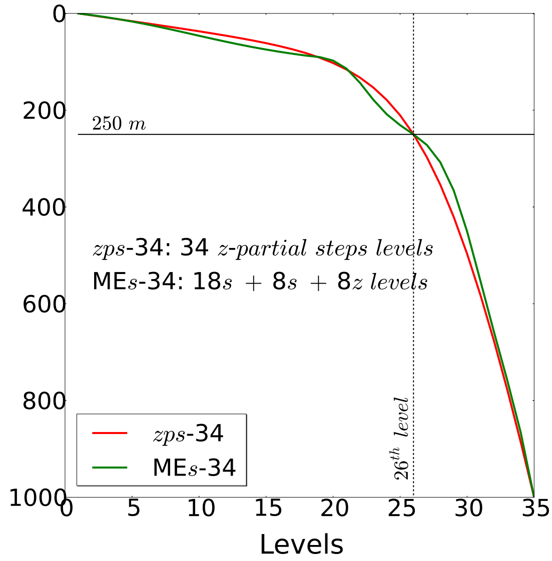

Fig. 3.5: Vertical distribution of *zps*-34 (red) and ME*s*-34 (green) model levels in the middle of the computational domain. The depth of the 26^{th} level (250 m) is also shown.

value of r is reduced from $r = 0.13$ (actual bathymetry) to 0.09 (H_e^1 envelope), allowing the reduction of pressure gradients errors.

The uppermost envelope H_e^1 has a parabolic shape in deep areas ($H_B(x, y) \geq 200$ m) given by equation

$$H_e^1 = A + B(x^2 + y^2), \tag{3.9}$$

where $A = 87.22$ and $B = 273.33$. The ME*s*-34 configuration uses 18 levels in the upper (D_1) zone, 8 levels in the central (D_2) zone and 8 levels in the deeper (D_3) zone. The configurations of the two 34 levels vertical grids are presented in Fig. 3.5, where the vertical distributions of *zps*-34 (red) and ME*s*-34 (green) model levels in the middle of the computational domain are compared.

The zfs-150 model uses a standard NEMO-3.6 z-full step grid (Madec, 2008) with the stretched function tuned in such a way that layers thickness up to 200 m depth

Exp. Name	Oceanic process	Ideal test process	Initial ocean setup	Perturb.	Assess. of models' skills
HPGE (Sec. 3.3.2)	Ocean circulat.	Evolution of a stably stratified ocean at rest	Horiz. uniform vert. stable stratification, no motion	-	Comparison with analytical solution
CASC (Sec. 3.3.2)	Dense water cascading upon the shelf	Gravity current over steep topography	No stratific., no motion	Dense ring upon the shelf and the shelf-break	Comparison with analytical solution
CILF (Sec. 3.3.2)	CIL formation in the ocean interior	Sinking and spreading of a dense cold patch	Cyclonic ocean with 2 density layers	Cylindrical dense water patch in the upper layer	Comparison with high vert. resol. model solut.

Table 3.1: Oceanic processes tested in this study together with the associated experiment setup and the method used to evaluate models skills.

is almost constant with a value of ≈ 2 m (Fig. 3.4(b)).

3.3.2 Experiment set-up

We carry out three idealised process-oriented numerical experiments which mimic three typical oceanic conditions. The first experiment (hereinafter called HPGE) is designed to assess the generation of spurious currents due to horizontal pressure gradient errors (see Section 3.3.2). The second experiment (hereafter called CASC) represents dense water cascading from the continental shelf (Ivanov et al., 2004), see Section 3.3.2. The third experiment (hereinafter CILF) simulates the formation of a cold intermediate layer over a permanent thermocline, a process observed in many subarctic seas (Chubarenko and Demchenko, 2010; Cyr et al., 2011). The latter process is monitored in our simulations by using a passive tracer (see Section 3.3.2). The inventory of the experiments is given in Table 3.1.

The skills of MEs-34 and zps-34 models are assessed by comparison with known analytical solutions for the first and the second experiments. In the third experiment the analytical solution is not available and the comparison is made against a reference numerical simulation which uses zfs-150.

Physical and Comput. NEMO specific setup	**HPGE EXP.**	**CASC EXP.**	**CILF EXP.**
EOS	non-linear (TEOS10)	non-linear (TEOS10)	linear (Roquet et al., 2015) $\lambda_1 = \lambda_2 = 0.0$ $\mu_1 = \mu_2 = \nu = 0.0$
Lateral diffusivity	8 $[m^2 s^{-1}]$	8 $[m^2 s^{-1}]$	10^{-7} $[m^2 s^{-1}]$
Vertical diffusivity	10^{-7} $[m^2 s^{-1}]$	GLS	10^{-7} $[m^2 s^{-1}]$
Vertical viscosity	10^{-5} $[m^2 s^{-1}]$	GLS	10^{-5} $[m^2 s^{-1}]$

Table 3.2: Physical and computational NEMO setup specific of the three experiments. If not specified, NEMO standard values are used (see Madec 2008).

In all the numerical experiments, the time-splitting formulation for the non-linear free surface is applied, with the baroclinic and barotropic time-steps equal to 150 s and 7.5 s, respectively. We use the pressure Jacobian scheme together with a leapfrog time scheme for calculation of the hydrostatic pressure gradient term. The Asselin time filter parameter is 0.1. The Total Variance Dissipation (TVD) and Energy and ENstrophy (EEN) conservative schemes are used for tracer and momentum advection, respectively. All the simulations are performed using the *f-plane* approximation ($f \approx 10^{-4}$). For the lateral diffusion of momentum, we use a second order operator aligned with horizontal levels together with a forth order operator discretised along model levels (O'Dea et al., 2012). The Laplacian and bi-laplacian viscosity coefficients are constant with values equal to 10^2 $m^2 s^{-1}$ and $-2 \cdot 10^9$ $m^4 s^{-1}$, respectively. The lateral diffusion is simulated by using a horizontal harmonic operator with constant diffusivity (see Table 3.2 for the values used in each experiment). The vertical diffusivity and viscosity coefficients are constant in the HPGE and CILF experiments while are computed using the Generic Length Scale (GLS) turbulent closure scheme (Umlauf and Burchard, 2003, 2005) tuned following Wobus et al. (2013) in the CASC experiment (see Table 3.2). In the HPGE and CILF experiments we reduce the explicit vertical diffusivity to the minimum value allowed by model stability (10^{-7} $m^2 s^{-1}$), in order to isolate the effect of spurious numerical diffusion linked to the vertical discretisation scheme. All the models use no-slip lateral boundary conditions and a log-layer enhanced quadratic bottom friction parametrisation with minimum and maximum bottom drag coefficient values equal to $2.5 \cdot 10^{-3}$ and 10^{-1}, respectively (see Madec (2008) for the details). Convection is parameterised by applying enhanced vertical diffusion on tracers in regions where the stratification is unstable. The enhanced vertical mixing coefficient is set equal to 10 $m^2 s^{-1}$.

Generation of spurious currents

In these experiments we assess the accuracy of the *zps* and ME*s* vertical schemes in representing horizontal pressure gradients. In *zps* models, the near bottom grid points within a vertical level are not necessarily at the same depth as the grid points in the interior, resulting in problems with pressure gradient errors and spurious diapycnal diffusion (Pacanowski et al., 1998).

The initial condition for each run is obtained by horizontally spreading the temperature and salinity profiles showed in Fig. 3.6, so that there are no horizontal pressure gradients, there is no initial circulation and the sea surface is flat. There is no meteorological forcing or river discharge. In the absence of any external forcing, the analytical solution for current velocities and horizontal density gradients is zero. However, numerical errors due to the vertical discretisation may lead to errors in the pressure gradient computation, generating spurious current velocities (see for example Berntsen 2002).

The HPGE experiments consist of two prognostic simulations, one for each vertical grid, where the NEMO model is run for 30 days without any external forcing. The computational and physical NEMO settings are listed in Table 3.2 (HPGE experiments).

Dense water cascading on the shelf

In the second experiment we investigate the ability of the two 34 levels models to properly represent the flow of dense water down a steep topographic slope.

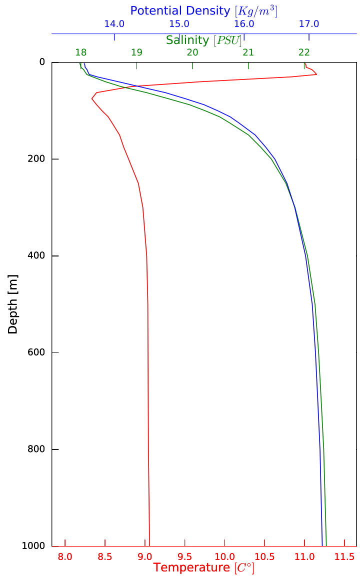

Fig. 3.6: Vertical profiles of temperature, salinity and potential density anomaly used as initial condition for the HPGR experiment. They are basin averaged mean annual climatologies computed from MyOcean Black Sea Reanalysis from 1992 to 2012 (MyOcean2, 2014).

We consider an initial axisymmetric, three-dimensional density ring of dense water with a homogeneous density $\rho + \Delta\rho$, situated upon the shelf and an ambient ocean with constant density ρ. The initial velocity is zero everywhere.

The initial condition used for the numerical simulations is shown in Fig. 3.7. The axisymmetric dense ring is confined in coastal areas, has a maximum depth of 50 m and temperature, salinity and potential density anomaly σ_r of 10°C, 21 PSU and 16.00 $kg\ m^{-3}$, respectively. Ambient water temperature is 12°C and salinity is 20 PSU, yielding a potential density anomaly of $\sigma_o = 14.94\ kg\ m^{-3}$.

If such initial condition is allowed to evolve freely, the dense water will tend to descend downslope driven by the gravitational force while the Coriolis force will deflect such motion toward the right (in the Northern hemisphere). In the absence of friction, an equilibrium eventually will be reached. For a constant bottom slope angle θ, the geostrophic current velocity u_g is given by $u_g = \frac{g'}{f} \tan\theta$ (Nof, 1983),

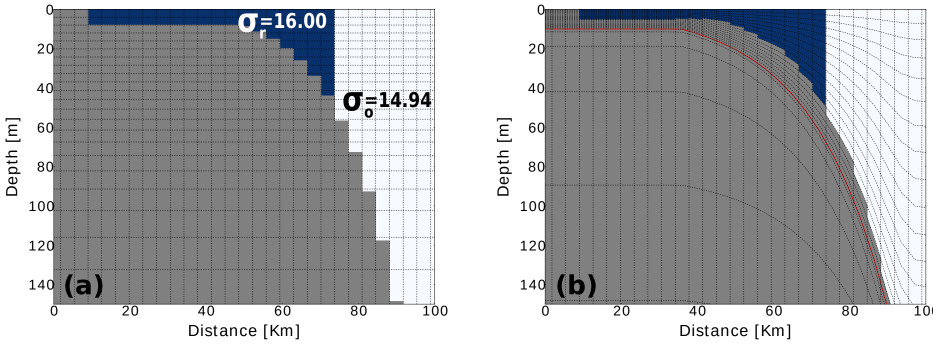

Fig. 3.7: Meridional cross-sections in the middle of the domain of the potential density initial condition for CASC experiments.

where g' is the reduced gravity $g' = \frac{g\Delta\rho}{\rho_0}$ and f is the Coriolis parameter. In the presence of friction, a tongue of dense water of approximately 2 Ekman depths will continue to descend.

In the case of a fully developed cascading without entrainment and ambient current, there is an analytical solution for the downslope velocity (Shapiro and Hill, 1997) given by

$$u_{SH97} = 0.2u_g, \tag{3.10}$$

where u_g is the along slope geostrophic velocity (Nof, 1983). While the formula by Shapiro and Hill (1997) was derived for constant slopes, we compare our model results against this formula as the horizontal curvature of our domain is negligible as compared to the topographic slope, and the change of the slope over the length of the tongue is small. A similar approach was used in Wobus et al. (2011, 2013).

One month-long NEMO runs are performed with the computational and physical settings listed in Table 3.2 (CASC experiments). The GLS turbulence closure scheme is configured according to Wobus et al. (2013). The convective adjustment parameterization is used following Laanaia et al. (2010). The experiment is conducted with 2 vertical grids, the *zps*-34 and the ME*s*-34.

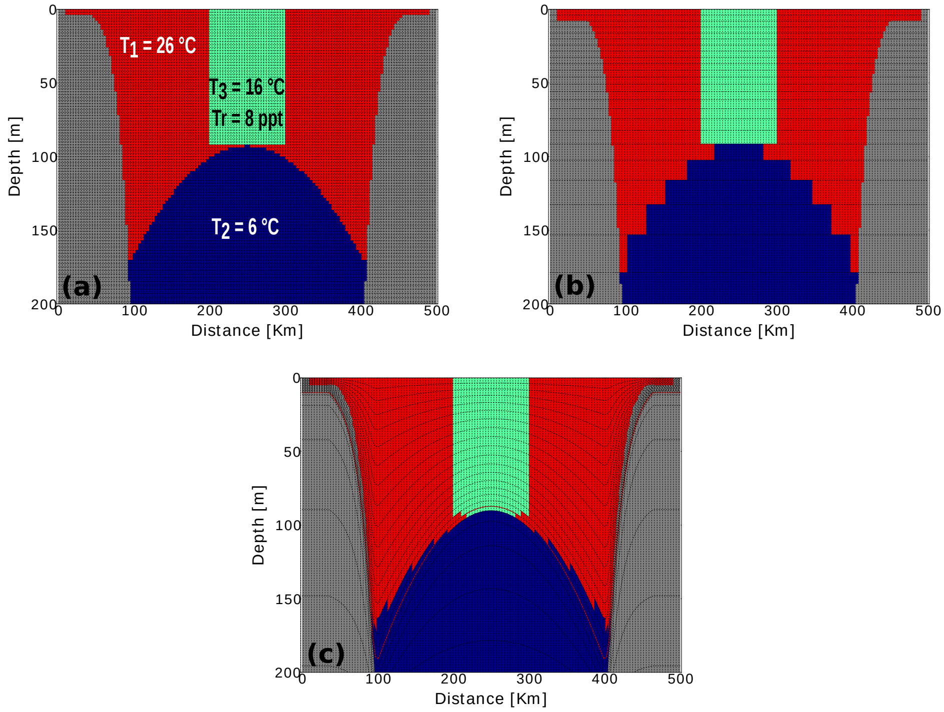

Fig. 3.8: Meridional cross-sections in the middle of the domain of temperature and salinity initial condition fields defined on zfs-150 (a), zps-34 (b) and MEs-34 (c) models' grids for the CILF experiment.

Formation of Cold Intermediate Layer

In the third experiment, we assess the ability of the zps-34 and MEs-34 vertical grids to represent the formation of a Cold Intermediate Layer (CIL) over a permanent pycnocline by monitoring the advection of a passive tracer in the ocean interior. The experiment simulates the sinking and spreading of a dense (cold) patch of water in an idealised cyclonic ocean with a doming pycnocline.

The initial condition is axisymmetric and represents a two-layer fluid with a cold cylindrical patch at the centre of the basin (see Fig. 3.8). The main pycnocline is defined by Equation 3.9 with $A = 92.92$ and $B = 193.33$ (note: the pycnocline does not coincide with the H_e^1 envelope). Salinity is equal to 35 PSU and is constant everywhere. The initial velocity is zero. We use a linear equation of state with coefficients shown in Tab. 3.2 (CILF experiment). Temperature and density anomaly σ (where $\sigma = \rho - 1000$ and ρ is the in-situ density) above (i.e. in layer 1) and below (layer 2) the pycnocline are $T_1 = 26$°C, $\sigma_1 = 23.4$ $kg\ m^{-3}$ and $T_2 = 6$°C, $\sigma_2 = 26.7$ $kg\ m^{-3}$, respectively. The cylindrical dense convective patch has a radius of 50 km, a maximum depth of 92.94 m and temperature, density anomaly and passive tracer concentration equal to $T_3 = 16$°C, $\sigma_3 = 25.0$ $kg\ m^{-3}$ and $C = 8$ ppt, respectively. The ratio between the volume of the cold dense patch (green slug in Fig. 3.8) and the volume of the domed denser layer (blue fluid portion in Fig. 3.8) is 0.011 in all the models.

Explicit tracer diffusion is negligibly small in order to isolate the numerical diffusion linked to advection schemes. However, we use a standard high value (10 m^2s^{-1}) of vertical diffusivity for convective adjustment. The computational and physical settings are listed in Table 3.2 (CILF experiment). We use the numerical solution of the very high vertical resolution zfs-150 model as a reference to evaluate the performance of both zps-34 and MEs-34 vertical schemes.

The numerical simulations are performed for 60 days. When the lateral exchange and spreading of an oceanic cold water patch occurs, baroclinic instabilities break up the mixed patch and homogeneous water sinks and spreads out at its neutrally buoyant level (see fig. 3 in Marshall and Schott 1999).

3.4 Results and Discussion

3.4.1 Horizontal pressure gradients errors

The numerical results of this experiment demonstrate that horizontal pressure gradient errors appear in both MEs and zps models. After 31 days, spurious currents develop in both models, however their absolute values are small in both cases. In the zps-34 model they are localized only in proximity of the sloping sea-floor while

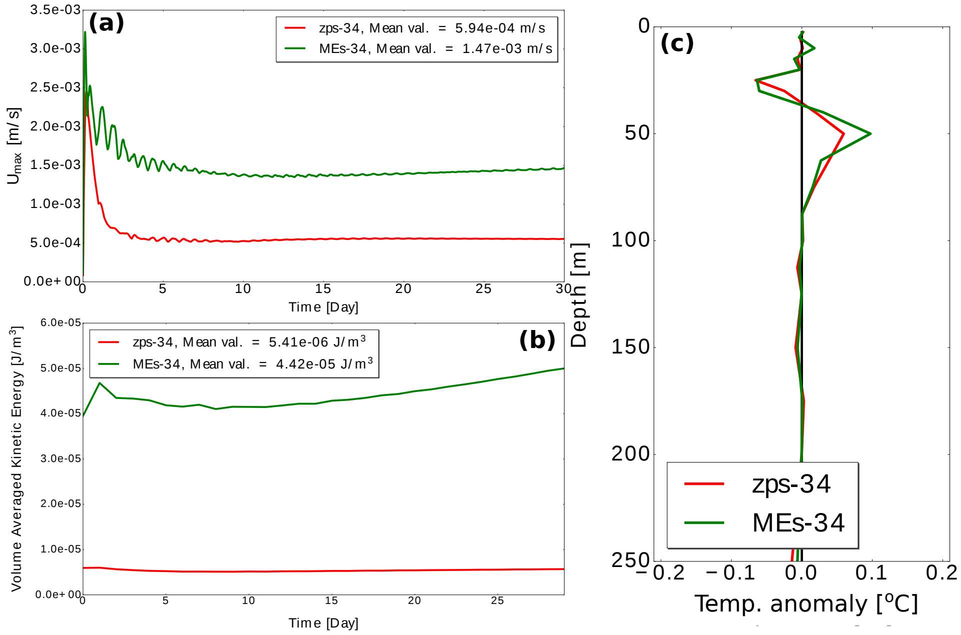

Fig. 3.9: (a) Time series of spurious currents maximum values, (b) time series of basin averaged Kinetic Energy and (c) differences between temperature profiles extracted in the middle of the domain after 30 days of simulation and the initial condition of *zps*-34 (red) and MEs-34 (green) models.

in the MEs-34 model they affect all the domain.

Time series of the maximum value of spurious currents computed over the whole domain (Fig. 3.9(a)) show that u_{max} values are less than $5 \cdot 10^{-3}$ ms^{-1}, i.e. well within the acceptable margin of error and are comparable with the accuracy of high-precision instruments (Valeport, 2017). The averaged over the length of the simulation maximum error for the *zps*-34 model is $0.59 \cdot 10^{-3}$ ms^{-1}, which is slightly better than the one of the MEs model, where the average maximum value is $1.47 \cdot 10^{-3}$ ms^{-1}.

The time series of the basin averaged Kinetic Energy (KE) due to spurious currents are compared in Fig. 3.9(b). The *zps*-34 model has a time averaged KE of $5.41 \cdot 10^{-6}$ Jm^{-3}, which corresponds to an average speed of $1.02 \cdot 10^{-4}$ ms^{-1}. The MEs-34 model shows slightly higher but still very low values: basin averaged KE of $4.42 \cdot 10^{-5}$ Jm^{-3}

and average speed of $2.93 \cdot 10^{-4}$ ms^{-1}. After one month of simulation, the KE in the MEs model does not reach an equilibrium. In the case of σ-coordinates, this behaviour has been classified as *sigma error of the second kind* (SESK) (Mellor et al., 1998) and it has been reported and studied in a number of publication (see for example Shchepetkin 2003 and references therein).

Figure 3.9(c) presents differences between the temperature profiles extracted in the middle of the domain of the two models after 30 days of simulation and the initial condition, showing that the same level of spurious mixing is obtained with both the models.

As discussed in Sec. 3.3.1, the doming of the computational levels in MEs-34 was introduced to deal with ocean domains characterized by a cyclonic circulation. In this experiment we use MEs-34 for an ocean with largely horizontal isopycnals and an absence of any background circulation. In order to evaluate a potential negative effect of curved computational levels in the ocean interior we also performed an additional simulation with the same grid set-up of the MEs-34 grid but using a modified upper envelope H_e^1 which is horizontal in the ocean interior. Hereinafter we call this grid SH13-34, since it follows Shapiro et al. (2013), see Fig. 3.1(d). Comparisons of numerical results obtained with the MEs-34 and the SH13-34 grids demonstrate that inclining the model levels in the ocean interior (used in MEs-34) does not increase the magnitude of spurious currents. The time-averaged maximum value of spurious currents in the SH13-34 is $1.46 \cdot 10^{-3}$ ms^{-1} as compared to $1.47 \cdot 10^{-3}$ ms^{-1} in MEs-34. This result supports the use of MEs-34 type models with the curved upper envelope even in areas without cyclonic circulations or where ocean fronts are weak or moderate.

3.4.2 Dense water cascading on the shelf

We evaluate the zps-34 and MEs-34 models' performance in representing dense water overflows down a steep topography by comparing the numerical results of the

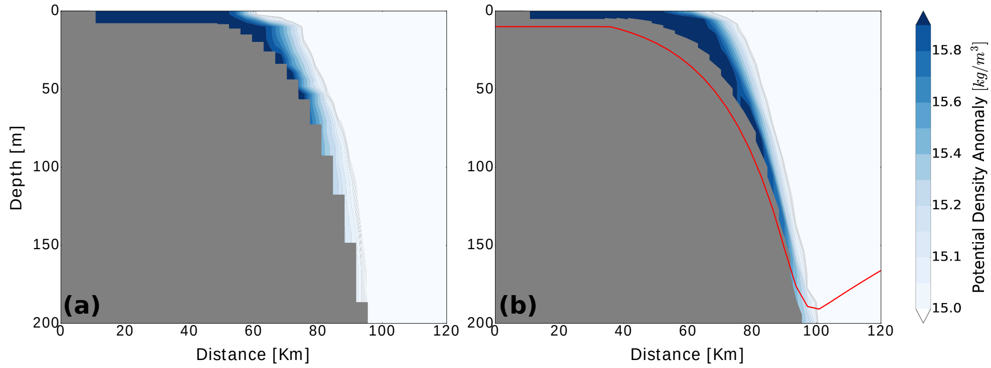

Fig. 3.10: Cross section in the middle of the domain showing the cascade simulated by the *zps*-34 (a) and the ME*s*-34 (b) models at day 6.

downslope velocity with theoretical values given by Shapiro and Hill (1997).

The downslope speed is defined as the speed of the plume head in an azimuthally averaged sense. The plume is defined as a water mass with potential density $\geq$ 1014.99 $kg\ m^{-3}$. The speed is computed using the horizontal distance of each grid cell representing the plume head from the middle of the domain.

Time series of the plume edge depths show that both models reproduce a dense water cascading with nearly constant downward speed (Fig. 3.10). The plume head reaches the deepest zone of the model topography (1000 m) after 11 days in the case of the ME*s*-34 model and after 14 days with the *zps*-34 grid.

In order to compare the numerical and analytical solutions, we compute the downslope velocity u_{model} of the simulated cascades only when the plume edge is located in areas where the topographic slope is between 0.006 and 0.020 and the depth is less then 800 m (see Fig. 3.11(a)). To compute the Nof velocity we use a slope of 0.014, the mean value of the actual bottom slope.

In order to compute the reduced gravity g', we consider a reference potential density ρ_0 given by the daily mean of azimuthally-averaged potential densities in model cells just above the model bathymetry. The ambient water density ρ_a is obtained by computing the daily mean of azimuthally-averaged potential densities in model

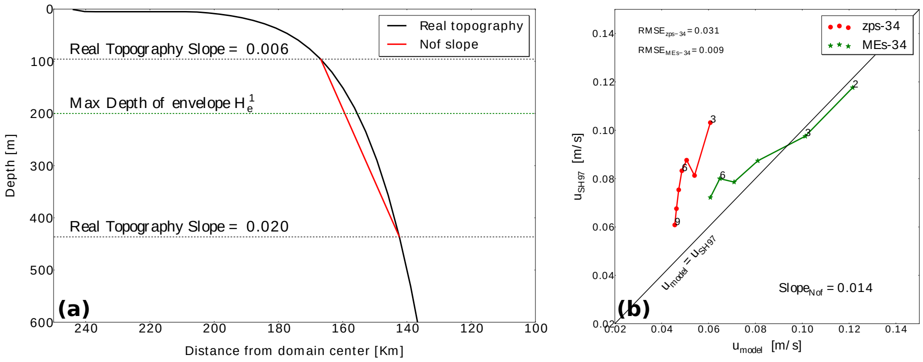

Fig. 3.11: (a) Actual topography of the model domain (black) and the slope used to compute the Nof (1983) velocity (red). The locations where the topographic slope is equal to 0.006 and 0.020 and the maximum depth of envelope H_e^1 of the MEs model are shown as well. (b) Comparison between the daily values of the downslope velocity predicted by the Shapiro and Hill (1997) theoretical model with the numerical ones obtained with the *zps*-34 (red) and the ME*s*-34 (green) models. Numbers indicate the day.

bottom cells with values less than 1014.99 $kg\ m^{-3}$. Finally, the daily potential density ρ_c representative of the dense cascade of each model run is computed by daily averaging potential densities of bottom cells where the azimuthally-averaged potential density is between 1015.35 and 1014.99 $kg\ m^{-3}$.

Figure 3.11(b) shows the comparison between the daily values of the downslope velocity given by the analytical solution (Shapiro and Hill, 1997) and the numerical solutions obtained with the *zps*-34 and the ME*s*-34 models.

Results show that the ME*s*-34 model performs significantly better than the *zps*-34 model. In the *zps*-34 model, the dense water cascade crosses the analysed zone (i.e. the area between the water depths of 90 and 450 m, see Fig. 3.11(a)) from day three to day 9. Throughout the entire period, the *zps*-34 underestimates the downslope speed of cascading, especially in the beginning of the event (day 3). The RMS error of the *zps*-34 model is 0.031 ms^{-1}, which is high (about 50%) compared to the average downslope speed of 0.05 - 0.07 ms^{-1}. On the other hand, in the ME*s*-34 model the plume descends faster, has lower loss of density due to entrainment, and crosses the analysed zone from day 2 to 7. The modelled downslope speeds are in the range of 0.06-0.12 ms^{-1} and are almost equal to the analytical solution, with a RMS error of 0.009 ms^{-1}, or about 10% of the average speed. The fact that the downslope cascading in *zps*-34 is slower than in ME*s*-34 is probably due to the enhanced artificial mixing (reducing g') which characterises z-type models with step-like topography (see Fig. 3.10). This agrees with other gravity current overflow experiments results (see for example fig. 2 in Ezer 2005).

Figure 3.11(b) shows that during the days 6 and 7 of the ME*s*-34 simulation, the plume reaches the lower computational zone D2, which has some horizontal (geopotential) levels. The accuracy of the simulation slightly decreases at this point in time as the cascade head reaches a point in the vertical coordinate system which begins to resemble a z-level grid.

3.4.3 Formation of Cold Intermediate Layer

For this experiment, an analytical solution is not available. Therefore, we compare the results of *zps*-34 and ME*s*-34 models with the reference solution produced by the high resolution zfs-150 model.

A zfs-150 simulation is significantly more expensive computationally than a simulation performed with the other two low resolution models. In this experiment for example, the duration of the zfs-150 simulation on our HPC cluster was 70556 s ($\approx$ 19.6 hr), while *zps*-34 and ME*s*-34 numerical runs took 17579 s ($\approx$ 4.9 hr) and 21646 s ($\approx$ 6.0 hr), respectively. The difference in computer time between the two coarse resolution models is due to the fact that the ME*s*-34 model has more computationally active (i.e., wet) grid cells than the *zps*-34, where levels hit the sloping bottom and part of the mesh is used to discretize land areas.

We begin the analysis with the comparison of the 60 days long time series of the volume averaged Kinetic Energy (KE) of the three models (Fig. 3.12).

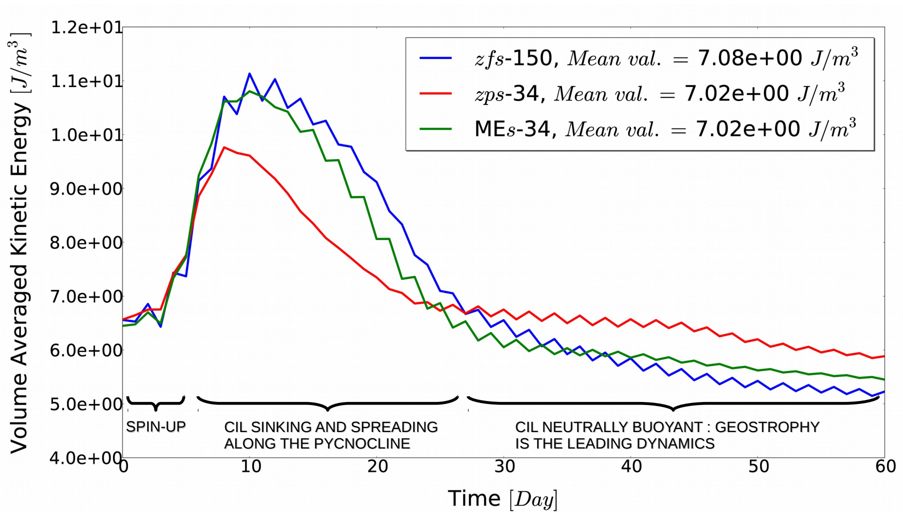

Fig. 3.12: Time series of the volume averaged KE for the zfs-150 (blue), zps-34 (red) and MEs-34 (green) models.

After a few days of spin-up, all the simulations seem to represent the same general dynamics: a first energetic stage where the dense cold patch sinks and spreads along the permanent pycnocline and a second less active regime where the CIL is at its neutrally buoyant level and geostrophy is the leading dynamics.

The time series of basin averaged KE produced with MEs-34 and the reference zfs-150 models are quite similar, with a RMS error equal to 0.15 Jm^{-3} (or approximately 2% of the mean KE). Both models show a maximum of KE at day 10 with values of 10.81 Jm^{-3} in the case of the MEs-34 model and 11.13 Jm^{-3} for the reference zfs-150 model.

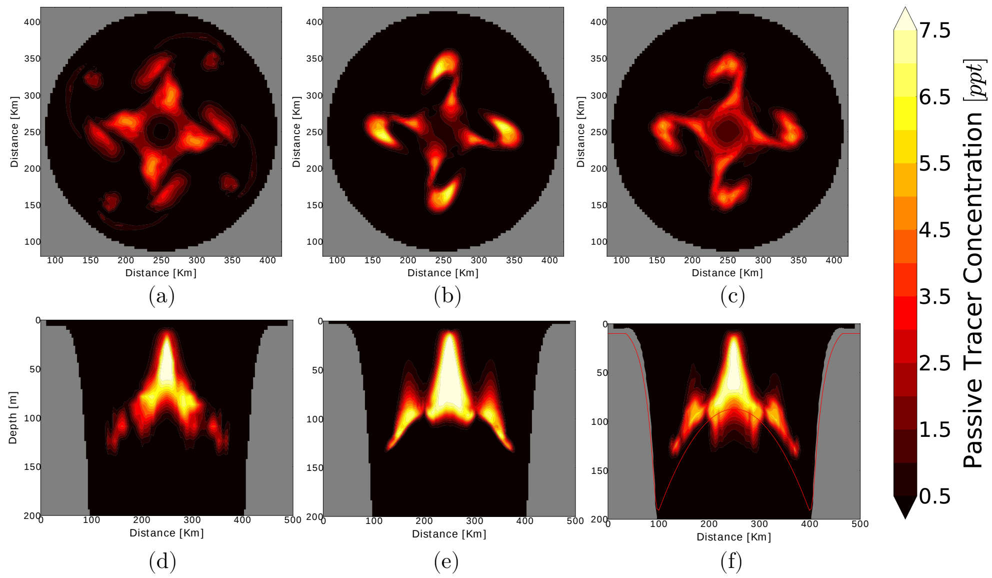

Fig. 3.13: Passive tracer concentration after 18 days. *First row*: horizontal distribution maps obtained at 105 m depth with the *zps*-34 (a), the zfs-150 (b) and the MEs-34 (c) models. *Second row*: meridional cross sections obtained with the *zps*-34 (d), the zfs-150 (e) and the MEs-34 (f) models.

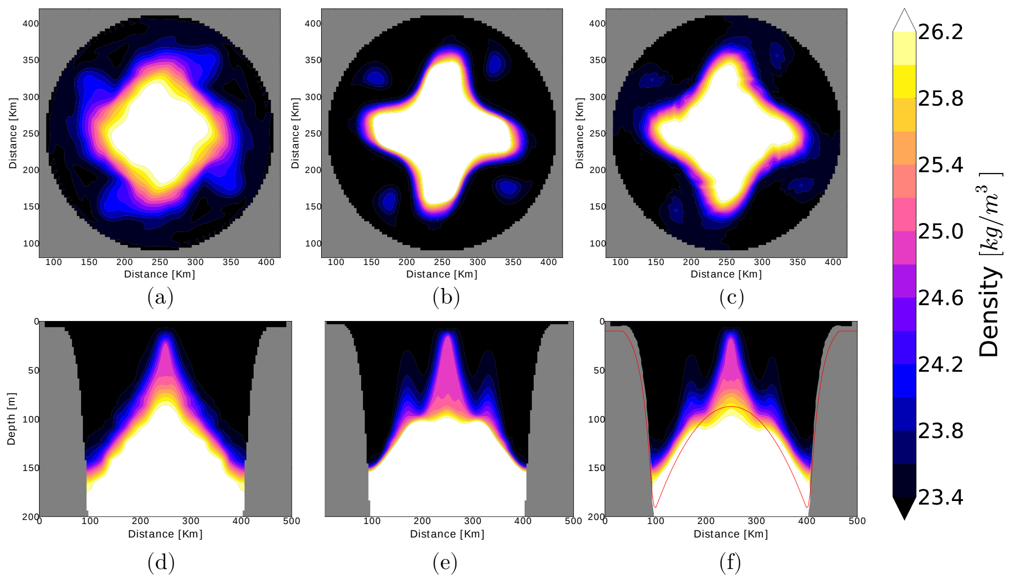

Fig. 3.14: Density anomaly distribution after 18 days. *First row*: horizontal maps at a depth of 120 m obtained with the *zps*-34 (a), the zfs-150 (b) and the MEs-34 (c) models. *Second row*: meridional cross sections obtained with the *zps*-34 (d), the zfs-150 (e) and the MEs-34 (f) models.

On the other hand, the *zps*-34 model simulates a shorter and less energetic first phase and a moderately more vigorous geostrophic stage, with a RMS error of 0.96 Jm^{-3} (or 14% of the mean KE). The maximum of KE in the *zps*-34 simulation is 9.76 Jm^{-3} and is reached at day 8, i.e. 2 days earlier than the reference.

Daily averaged horizontal distribution maps and vertical cross sections of density anomaly and passive tracer concentration after 18 and 50 days illustrate how the more energetic (day 18) and the less dynamical (day 50) stages of the CIL formation are represented by the three models.

After 18 days, the zfs-150 and MEs-34 models represent similar mesoscale baroclinic structures (see Fig. 3.13(b)-(c) and Fig. 3.14(b)-(e)-(d)-(f)). As expected, the high resolution reference model zfs-150 is able to maintain the sharp pycnocline, both in the lateral and in the vertical directions (Fig. 3.14(b)-(e)). The MEs-34 model demonstrates a similar capability, especially for horizontal gradients (Fig. 3.14(c)-(f)). On the other hand, Fig. 3.13(a) and Fig. 3.14(a)-(d) show that the *zps*-34 model generates stronger diapycnal diffusion and entrainment than MEs-34.

The transport of the passive tracer along the pycnocline after 18 days is similarly represented by both the zfs-150 and MEs-34 models (Fig. 3.13(e)-(f)). To the contrary, the *zps*-34 model generates spurious mixed patches of tracer concentration shown in blue in Fig. 3.13(d). This effect is probably due to the fact that the horizontal computational levels create a staggered representation of the pycnocline, and hence are subject to the same spurious mixing as when z-levels hit the sloping bottom.

Figure 3.15(a) shows a vertical profile of temperature simulated by the reference zfs-150 model in the proximity of the head of spreading dense water (blue profile, left sub-panel). It also shows the errors relative to the reference produced by the *zps*-34 (red) and MEs-34 (green) models, demonstrating that the MEs-34 grid has a significantly smaller error than the *zps*-34 model.

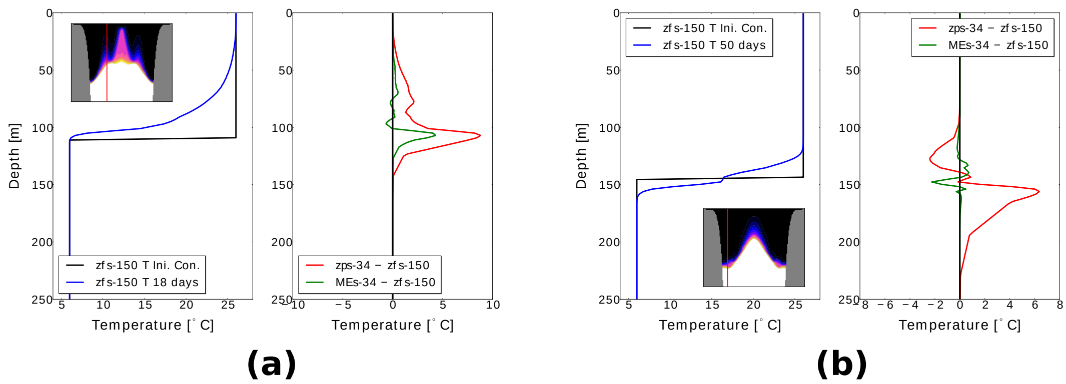

Fig. 3.15: Temperature vertical profiles simulated with the reference zfs-150 model (blue) and errors relative to the reference produced by the *zps*-34 (red) and the MEs-34 (green) models. The location of the profiles is shown in each cross section. (a) After 18 days and (b) after 50 days of simulations. The initial condition is shown in black.

The vertical profiles of errors in horizontally averaged density and passive tracer concentration relative to the reference zfs-150 numerical solution after 18 days are presented in Fig. 3.16(a)-(b). They show that the error generated by MEs-34 model is approximately 50% smaller in comparison to the *zps*-34 model.

At day 50, all three models simulate a less active dynamics, where the lateral exchange and spreading of the dense cold water to its neutrally buoyant level is terminated and geostrophic adjustment is the driving process, see Figures 3.17 and 3.18.

The reference zfs-150 solution shows that after 50 days the initial dense cold patch has formed a nearly uniform well-defined density layer with sharp fronts above the main pycnocline (see Fig. 3.18(b)-(e)). The passive tracer is advected with low numerical diffusion, reaching depths of around 150 m at almost the original concentration (Fig. 3.17(b)-(e)).

Figures 3.17(a)-(d) show the impact of the higher numerical diffusion of the *zps*-34 model in the transport of the passive tracer: the nearly uniform distribution along the pycnocline of the reference solution is lost and the passive tracer is mostly

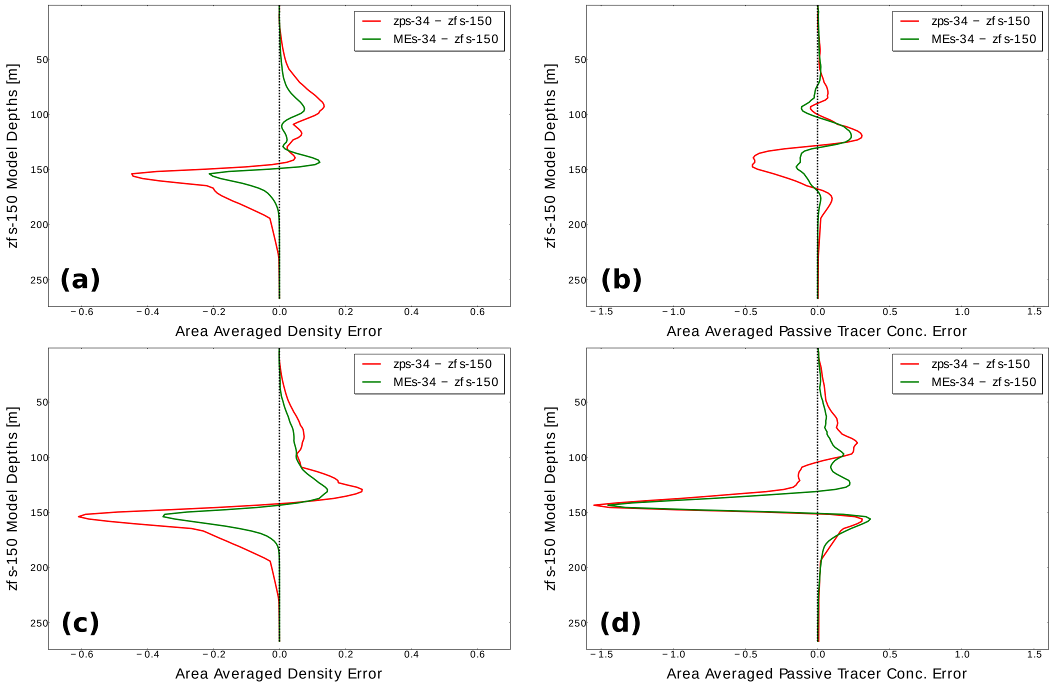

Fig. 3.16: Area averaged density and passive tracer concentration difference between the *zps*-34 (red) and the ME*s*-34 solutions and the reference *zfs*-150 one after 18 days (a-b) and 50 days (c-d) of simulation.

confined at depths shallower than 120 *m*. The maximum of tracer concentration is located at depths around 80-90 *m*. Figure 3.16(d) confirms that this is the case for the whole domain: at day 50, the *zps*-34 model simulates moderately higher tracer concentrations than the *zfs*-150 model at depths between 90-110 *m* and importantly lower values between 110-150 *m*.

After 50 days, the ME*s*-34 model represents a nearly uniform tracer distribution along the main pycnocline up to 120-130 *m* (see Fig. 3.17(f)). The ME*s*-34 model simulates a horizontal passive tracer ring-shaped distribution at a depth of 120 *m* (Fig. 3.17(c)) which is very similar to the reference *zfs*-150 solution (Fig. 3.17(b)). This proves a lower artificial diffusion of the ME*s*-34 model in comparison to the *zps*-34 one. Figure 3.16(d) shows that at day 50 both *zps*-34 and ME*s*-34 models generate slightly higher values than the reference solution.

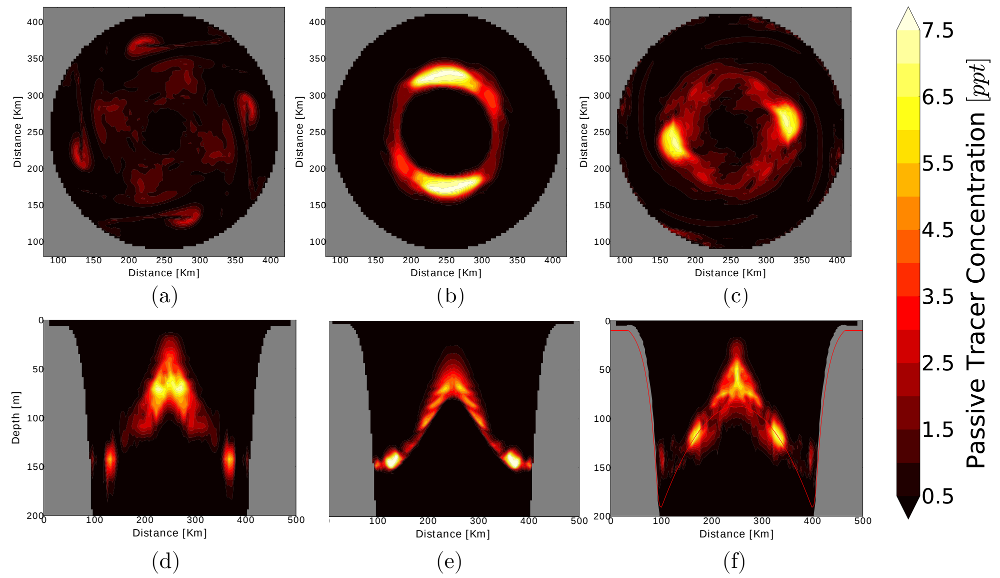

Fig. 3.17: Passive tracer concentration after 50 days. *First row*: horizontal distribution maps obtained at 120 m depth with the *zps*-34 (a), the zfs-150 (b) and the MEs-34 (c) models. *Second row*: zonal cross sections obtained with the *zps*-34 (d), the zfs-150 (e) and the MEs-34 (f) models.

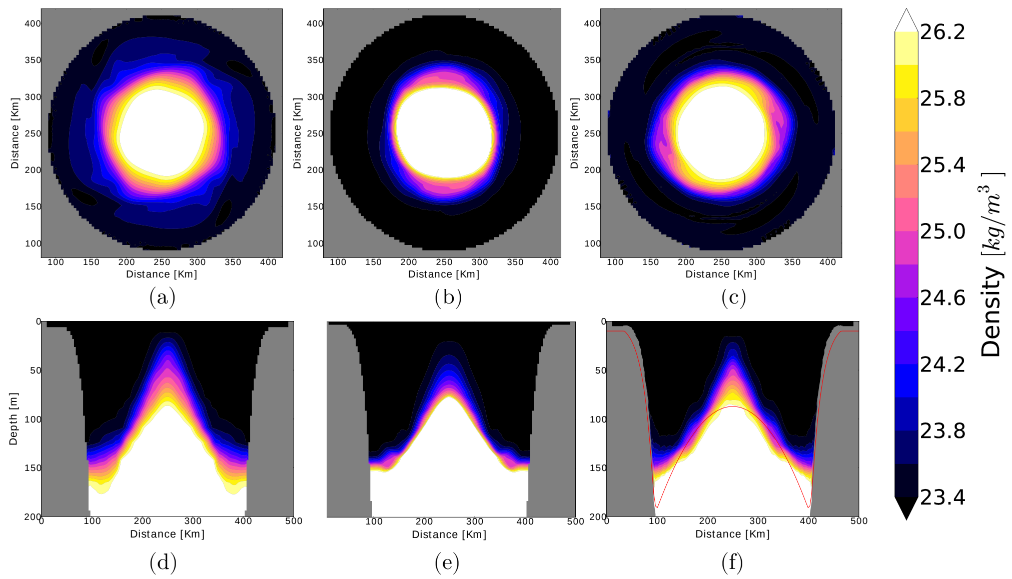

Fig. 3.18: Density anomaly distribution after 50 days. *First row*: horizontal maps at a depth of 120 m obtained with the *zps*-34 (a), the zfs-150 (b) and the MEs-34 (c) models. *Second row*: zonal cross sections obtained with the *zps*-34 (d), the zfs-150 (e) and the MEs-34 (f) models.

At depths around 150 m, both *zps*-34 and ME*s*-34 simulate lower values than the reference.

The *zps*-34 model shows the formation of a more extended and diffusive CIL, with weaker horizontal and vertical gradients (Fig. 3.18(a)-(d)). These artefacts are the result of the low vertical resolution combined with the step-like representations of both pycnocline and advection. A spurious downwelling event is produced with the *zps*-34 model, while it is not present either in the reference zfs-150 or ME*s*-34 solutions (see Fig. 3.18(d)-(e)-(f) and Fig. 3.15(b)).

Figures 3.15(b), 3.16(c) and 3.18(c)-(f) show that the ME*s*-34 model simulates the formation of a CIL closer to the reference zfs-150 model, with lower diapycnal diffusion and sharper density fronts than the *zps*-34 model.

The numerical mixing due to discretisation errors of tracer advection schemes causes decay in time of the passive tracer total variance (Maqueda and Holloway, 2006; Burchard and Rennau, 2008; Klingbeil et al., 2014), which is defined for a Boussinesq fluid as

$$Var(C) = \langle C^2 \rangle_V - \langle C \rangle_V^2, \tag{3.11}$$

where C is the concentration of the passive tracer and $\langle \bullet \rangle_V = V^{-1} \int \bullet \, dV$ represents a global averaging operator in a ocean with volume $V = \int dV$.

Following James (1996), in Fig. 3.19 we compare the cumulative loss with time of the discrete passive tracer total variance in the three models in terms of the ratio $Var(C)^n / Var(C)^0$, where n indicates the discrete time level and $n = 0$ is the initial condition. Numerical results show that, as expected, the reference zfs-150 model has the lowest loss of variance with time, and hence the smallest numerical diffusion. The ME*s*-34 model performs generally better than *zps*-34, especially during the more dynamic phase of the simulation. Both models give similar results after the end of the active phase.

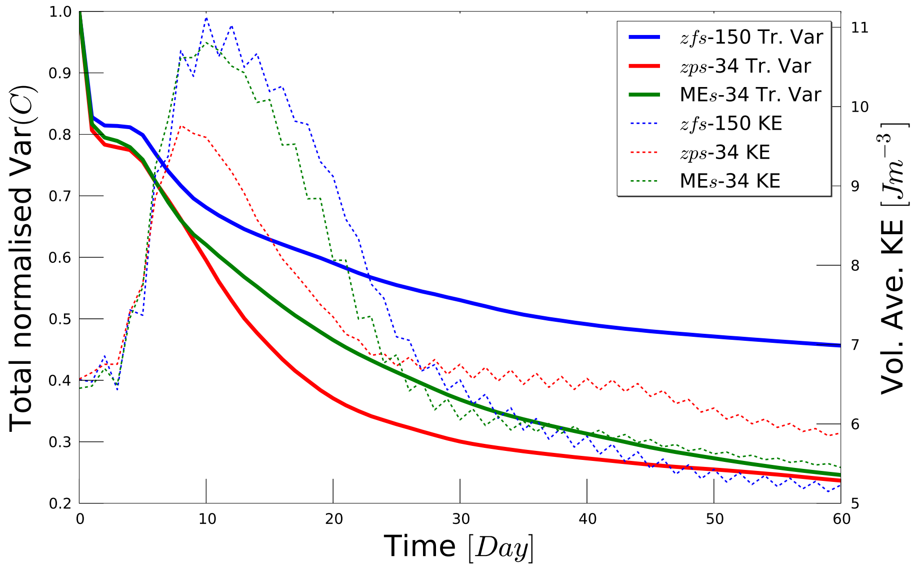

Fig. 3.19: Time series of the normalised passive tracer total variance (bold lines) and volume averaged KE (dashed lines) for the zfs-150 (blue), zps-34 (red) and MEs-34 (green) models. Normalisation is done with respect to the total variance of the initial condition.

3.5 Conclusions

In this study we have presented and assessed the skills of a new vertical discretisation scheme which we call the 'Multi-Envelope s-coordinate system' or 'MEs'. Our new system further develops the earlier concept of 'enveloped bathymetry', where model levels followed a 'virtual bottom' (aka envelope) rather than the actual bathymetry. Such 'single-envelope' system could be classed as an extreme case of the new 'multi-envelope' system. The multi-enveloping method allows the definition of computational surfaces which are optimised to best represent the physical processes in question. This method provides greater flexibility in the designing of a vertical grid than currently available geopotential level or terrain-following systems. All of these systems can be obtained as specific implementations of MEs.

An assessment of the MEs model skill for a number of idealized process studies has shown that MEs generates a small pressure gradient error, gives a better representation of dense water cascades down the continental slope and provides a more accurate simulation of formation of a cold intermediate layer, than a comparable z-partial steps system.

The MEs systems allows achieving a quality of simulation similar to a standard geopotential grid which has a much higher number of levels, and hence the MEs system is more computationally efficient.

The algorithm of creating MEs has been implemented in NEMO for this study, but can easily adapted for any 3D ocean model.

4. A 3D computational mesh to improve the representation of dynamic processes in the Black Sea

This Chapter has been published as Bruciaferri, D., Shapiro, G., Stanichny, S., Zatsepin, A., Ezer, T., Wobus, F., Francis, X., Hilton, D. *The development of a 3D computational mesh to improve the representation of dynamic processes: the Black Sea test case*, Ocean Modelling, 146 (2020), 101534, doi:10.1016/j.ocemod.2019.101534.

4.1 Introduction

The Black Sea is one of the largest land-locked basin in the world, located on the border between Europe and Asia. It communicates with the Atlantic Ocean via the Marmara, Aegean and Mediterranean seas and through a system of narrow straits, namely the Bosphorus, Dardanelles and Gibraltar (Shapiro, 2008).

In 2004, the population of states bordering the Black Sea counted a total of about 294 million inhabitants (Vespremeanu and Golumbeanu, 2018), making the coastal and shelf zones of this sea areas of prime economical and social importance (Shapiro et al., 2011). During the end of the last century, the increased Black Sea anthropogenic pollution caused one of the worst environmental crises of the world oceans, resulting in the collapse of much of its coastal ecosystem (Mee, 1992).

The Black Sea oxygen-rich surface layer is separated from the oxygen-depleted deeper waters contaminated with hydrogen sulphide by the Cold Intermediate Layer (CIL). Recent studies indicate a weakening of the CIL (e.g. Capet et al. (2016)), which could result in greater mixing between deep and surface water with potential catastrophic consequences for the biota. Hence there is a need for accurate long-term modelling of the Black Sea marine environment including the variability of the CIL, trends in its circulation and other parameters underpinning the state of its ecosystem.

Several Black Sea ocean models exist, the majority of which combines a regular geographical horizontal grid with constant resolution, with one of the standard vertical coordinate systems, either z-level (geopotential) or terrain-following. For example, z-level coordinates are used in the studies by Staneva et al. (2001), Korotaev et al. (2011) and many others. Terrain-following coordinates were used, among the others, by Besiktepe et al. (2001) and Cannaby et al. (2015).

None of these two discretization schemes are free from errors (Griffies, 2004). In z-coordinate systems, the step-like representation of the bottom topography leads to overmixing over the continental slope while terrain-following models are known to have errors in computing the pressure gradient force, particularly in areas of steep continetal slope (e.g. Ezer and Mellor (2004)). Moreover, both vertical discretization methods are prone to the contamination of weak diapycnal exchanges with strong isopycnal processes when computational surfaces cross the isopycnals. Vertical grids where computational levels follow isopycnals (known as isopycnal grids, e.g. Bleck (1998)) have their own disadvantages, especially in weakly stratified areas, such as over the continental shelf or in the upper or bottom mixed layers (Griffies, 2004).

In order to minimise computational errors of the various vertical coordinate systems, several methods were developed. For instance, Grayek et al. (2010) and Ciliberti et al. (2016) used the NEMO ocean model with a z-levels with partial steps vertical discretization scheme. Regarding terrain-following models, several different methods were developed to improve their accuracy in the Black Sea. Stanev and Beckers (1999) and Capet et al. (2012) used a model with the double-sigma vertical coordinates system. Enriquez et al. (2005) used an artificial flat bottom at a depth of 1500 m to reduce the curvature of the terrain-following coordinate system while Shapiro et al. (2013) introduced a novel s-on-top-of-z vertical discretization scheme. Recently, Miladinova et al. (2017) used a generalised boundary-following vertical grid to study the long-term variability of Black Sea thermohaline properties.

Regarding the horizontal discretization, two main approaches are used in high-resolution ocean modelling: either nesting the high-resolution model into a lower-resolution one, or using a horizontal grid with variable resolution. For example, Diansky et al. (2013) and Gusev et al. (2017) used a structured horizontal grid (i.e with trapezoidal cells) with increased resolution ($\approx 50\ m$) near Big Sochi coast to study the evolution of oil spills. Divinsky et al. (2015) used unstructured grids with triangular cells to study the currents on the Black Sea northeastern shelf. Recently, Stanev et al. (2017) used an unstructured grid combining triangular and quadrilateral cells to study the circulation and inter-basin exchange in the Azov-Black-Marmara-Mediterranean Seas system.

A widely used method to improve model skills is data assimilation (DA). Whilst there is abundance of data on the sea surface parameters, such as temperature or sea level anomalies obtained from satellites, observations of water column profiles are much scarcer. Therefore there is a need for a model which generates smaller errors in free-run (without DA) and hence would require less observational data.

The aim of this study is to assess and quantify the effect of optimising the 3D computational mesh for the prevailing physical processes on the accuracy of the simulation in the Black Sea. We implement four numerical models of the Black Sea hydrodynamics based on NEMO 3.6-stable ocean code (Madec, 2008). They use the same initial condition and external forcing while they differ in the combination of the horizontal and vertical discretization schemes. Two different type of numerical experiments are carried out. In the first one, we compare the modelling skills of the four models in a series of free-running simulations and we identify the one with the best accuracy. In the second, we compare our 'best' model in free-run with the data from EU Copernicus Marine Environment Monitoring Service (CMEMS) Black Sea reanalysis dataset, which is a data-assimilating system and currently represents the official EU best estimate of the 1995-2015 Black Sea state. Finally, we investigate the seasonal and inter-annual variability of the Mean Kinetic Energy (MKE) and the CIL simulated by our new model and CMEMS reanalysis.

The Chapter is organised as follow. In Section 4.2 we describe in detail the four numerical models implemented for this study (Section 4.2.1), the design of the numerical experiments performed (Section 4.2.2), the external datasets used to validate or to compare with models results (Section 4.2.3) and metrics used to asses models accuracy (Section 4.2.4). In Section 4.3, numerical results of the first and second experiments are presented and discussed in Sections 4.3.1 and 4.3.2, respectively, while in Section 4.3.3 we analyse the variability of the MKE of geostrophic currents and the CIL simulated by the new model and CMEMS reanalysis. Section 4.4 summarises our main conclusions.

4.2 Materials and Methods

In this study, we simulate the Black Sea hydrodynamics by using a modified version of NEMO General Circulation model (Madec, 2008) along with real external forcing. The governing equations solved by NEMO ocean model together with parameters and numerical techniques adopted in this study are detailed in Section 2.5 and Appendix 4A.

4.2.1 Numerical models setup

Four numerical models are implemented which differ only in the type of the 3D mesh. Two of them use a regular geographical horizontal grid (hereafter called GEO), while the other two implement a shelf-break following curvilinear grid (hereafter

MODEL	HORIZONTAL GRID TYPE	HORIZONTAL RESOL. [m]	VERTICAL GRID TYPE	VERTICAL RESOL. [m]
GEO-*zps*	Regular Geograph. (GEO)	min = 2757 max = 3035 mean= 2908	*z*-coord.+ part. steps (*zps*)	min = 1 max = 176 mean= 44
GEO-ME*s*	Regular Geograph. (GEO)	min = 2757 max = 3035 mean= 2908	Multi-Env. *s*-coord. (ME*s*)	min = 1 max = 171 mean= 42
CUR-*zps*	Shelf-break following (CUR)	min = 984 max = 6172 mean= 2646	*z*-coord.+ part. steps (*zps*)	min = 1 max = 176 mean= 44
CUR-MEs	**Shelf-break following (CUR)**	**min = 984** **max = 6172** **mean= 2646**	**Multi-Env s-coord. (MEs)**	**min = 1** **max = 171** **mean= 42**

Table 4.1: Features of the numerical mesh of the four Black Sea models developed in this study. The CUR-ME*s* model, which is the model showing the best accuracy in the first experiment (see Sec. 4.3.1), is highlighted in bold. Statistics of vertical grids are computed in the deep basin.

called CUR), where grid lines are designed to follow the 200 m isobath. Both type of horizontal grids are combined with two different type of vertical grids: one is a standard z-levels with partial steps vertical grid (hereafter called zps) while the other one uses the new Multi-Envelope s-coordinate system of Bruciaferri et al. (2018) (hereafter called MEs). The four numerical models are identified in the Chapter as GEO-zps, GEO-MEs, CUR-zps and CUR-MEs and their features are summarized in Table 5.1.

Models domain

The models' domain covers the total Black Sea, from 27.4°E to 41.9°E in the zonal direction and 40.8°N to 46.7°N in the meridional one (Figure 5.1a). The current implementation considers closed lateral boundaries and Bosphorus exchanges are parameterized as a two-layers river.

The bottom topography dataset used in this study is the very high-resolution EMODnet Digital Topography Model 2018 (Shom, 2018) (Fig. 5.1a). The models' bathymetry is computed by averaging all the EMODnet topography points within a particular wet cell of models' grid. Such an approach allows one to create a remapped lower resolution bathymetry which is highly representative of the finer resolution one, especially in regions where steep bathymetric changes occur (Sikirić et al., 2009). The minimum depth of models' bathymetry is 6 m while maximum is 2208 m.

Horizontal grids

Two different horizontal grids with the same number of grid points 405×225 are implemented. The first one is a regular geographical grid with grid lines aligned with parallels and meridians and a zonal and meridional resolution of ≈ 3 km. We named it GEO.

The second one is a general orthogonal curvilinear grid and it is identified as CUR in this thesis. It is designed to have grid lines following the shelf-break line (the 200 m isobath) and variable grid cells sizes, with higher resolution near the shelf-break. The minimum grid size of the CUR grid is ≈ 1 km, while its maximum value is ≈ 6 km.

The generation of horizontal general curvilinear grids involves the usage of 2D conformal transformations which allow the mapping of physical domains with irregular boundaries and physical coordinates (x, y) to regular computational domains with orthogonal coordinates (i, j) (Ives, 1982). The CUR horizontal grid is generated by using *pygridgen* software (`https://phobson.github.io/pygridgen/`), a Python interface to the *gridgen* C-library of Sakov (2015) based on Schwarz-Christoffel conformal mappings (Driscoll and Trefethen, 2002; Xu et al., 2015). In this study, *pygridgen* has been modified to work accordingly to NEMO requirements.

One of the most defining feature of the Black Sea circulation is its Rim Current, a basin-scale coherent cyclonic current flowing in proximity of the shelf-break (Shapiro et al., 2010). The Rim Current is subject to instabilities which eventually lead to the generation of meso-scale anticyclonic coastal eddies (Staneva et al., 2001; Shapiro, 2008). Meso-scale eddies contribute to shelf-deep sea water exchanges and hence to

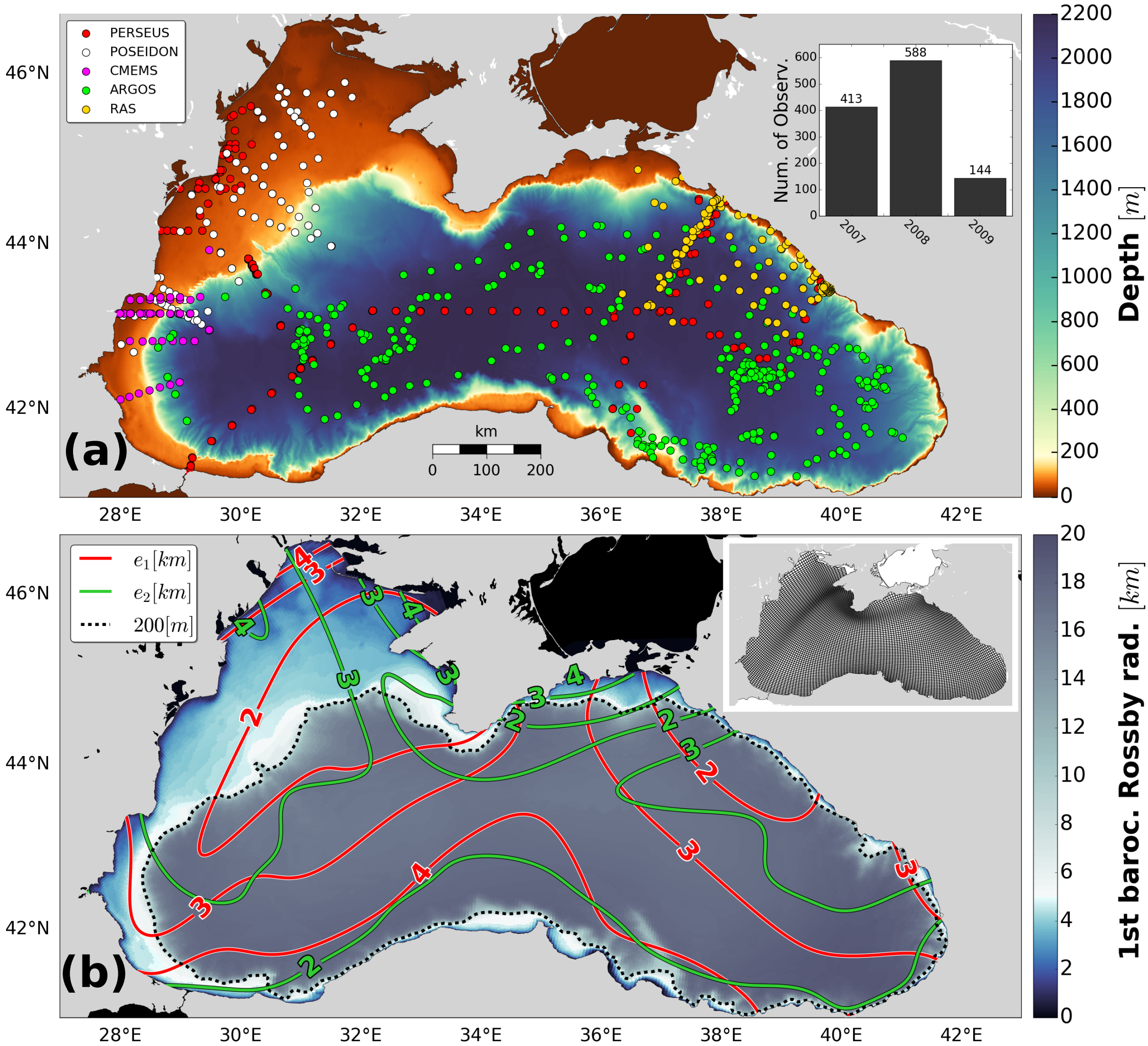

Fig. 4.1: (a) EMODnet DTM 2018 Black Sea topography map and locations of hydrographic stations (see Sec. 4.2.3) used to validate models results. (b) Map of the first baroclinic Rossby radius of deformation L_D in the Black Sea and CUR horizontal grid resolution (e_1 and e_2 are grid cells sizes in km). In the inset, a map of the orthogonal curvilinear grid (CUR) with increased resolution in proximity of the shelf-break developed for this study is shown (grid nodes are plotted every 3 points in each direction for clarity).

the health of the marine ecosystem (e.g., Zatsepin et al. (2003); Shapiro et al. (2010); Zhou et al. (2014) and references therein).

In order to better resolve mesoscale and sub-mesoscale dynamics, the CUR grid has an increased resolution in proximity of the 200 m isobath, especially along the cross shelf-break direction. This approach should allow to:

1. improve the accuracy in simulating the interaction between meso-scale eddies and large-scale circulation since we better resolve the first baroclinic Rossby radius of deformation L_D;

2. reduce horizontal pressure gradient errors arising from discretization of governing equations with curved vertical levels, since we reduce the slope parameter, i.e. the change of depths of adjacent grid points divided by their mean (e.g. Ezer and Mellor (2000));

3. have a more realistic (in terms of resolution) bathymetry in proximity of the shelf-break and hence a more accurate simulation of the influence of topography on the oceanic flow.

Figure 5.1b describes the relationship between the first baroclinic Rossby radius of deformation L_D in the Black Sea and CUR grid resolution (e_1 and e_2 are grid cells sizes). The Black Sea Rossby radius of deformation is computed in Wentzel-Kramers-Brillouin (WKB) approximation as

$$L_D = \frac{1}{f\pi} \int_{-H}^{0} N(z)\, dz, \tag{4.1}$$

where $N = \sqrt{-g\rho_0^{-1}\partial_z \rho}$ is the buoyancy frequency, H is the depth, f is the Coriolis parameter, g is the gravitational acceleration, ρ is the potential density and ρ_0 is a reference density. Monthly climatological temperature and salinity data from the Black Sea Atlas (Suvorov et al., 2003) are used to compute $N(z)$. Figure 5.1b shows that the CUR grid is eddy resolving, except in limited areas near the cost where the

Rossby radius is very small. The grid anisotropy e_2/e_1 is ≤ 3.3 (Xu et al., 2015).

Vertical grids

Two different vertical grids with 51 levels are implemented in this Chapter (see Fig. 5.2): one uses the common z-level with partial steps (zps) scheme while the second uses the novel Multi-Envelope s-coordinate (MEs) system (Bruciaferri et al., 2018). For better comparison, both MEs and zps grids have the computational level $n°$ 36 placed at the same depth of 310 m.

The zps grid (Fig. 5.2a,c) uses a standard NEMO v3.6 z-partial steps scheme (Madec, 2008) with a minimum layer thickness $e_3 = 1.2$ m. Partial steps parameters are given in Appendix A.

The MEs grid is configured by using five envelopes (see Fig. 5.2b, 5.2d and 5.2f) and the same number of levels as the zps scheme (i.e. 51). It has 27 levels allocated to the uppermost sub-zone D_1, 6 to the intermediate sub-zone D_3 and 5 to the deeper sub-zone D_5, while 9 and 4 computational surfaces are assigned to transition sub-zones D_2 and D_4, respectively. Envelopes H_e^2, H_e^3 and H_e^4 are geopotential surfaces located at depths of 310, 1200 and 1500 m respectively. This means that sub-zone D_3 of MEs grid is effectively discretised with z-levels. The deeper envelope H_e^5 is a smoothed version of the actual bathymetry with depths greater than 1800 m. Smoothing is performed by applying the Martinho and Batteen (2006) algorithm with a maximum slope parameter $r_{max} = 0.06$.

A specific thermal feature of the Black Sea is the Cold Intermediate Layer (CIL). It is a distinct well preserved sub-surface water mass with temperature minimums located between the seasonal and permanent pycnoclines (e.g., Ivanov and Belokopytov (2012) and references therein). The origin and replenishment of the CIL is classically attributed to the mutual interaction of two main processes (Stanev et al., 2003; Korotaev et al., 2014): the cascading of cold water formed during winter in the

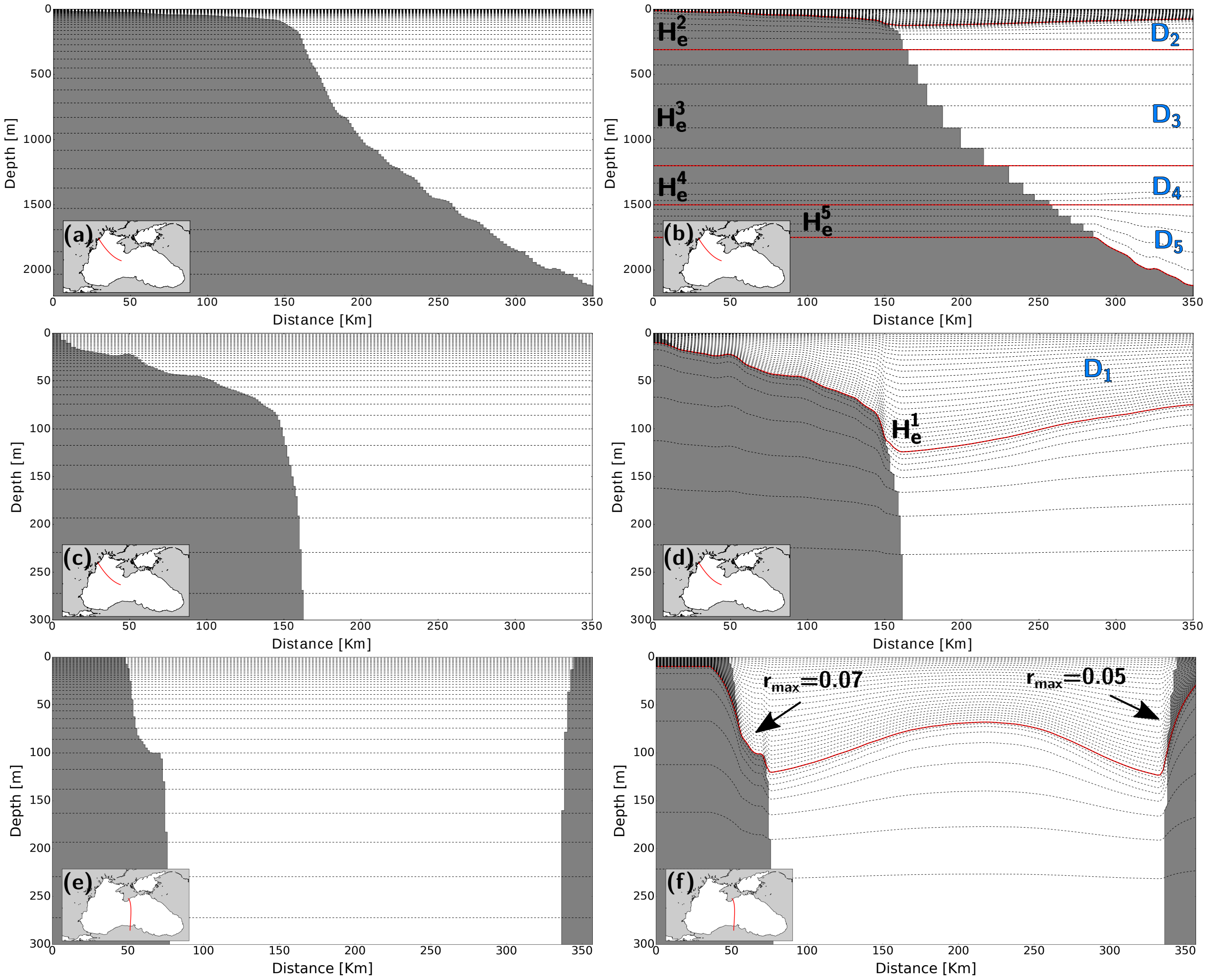

Fig. 4.2: Model bathymetry and computational levels configuration in the *zps* (a, c and e) and ME*s* (b, d and f) vertical grids along sections shown in the inset. Panels a, b, c and d show the same vertical transect, with c and d showing the zoomed part between the surface and 300 m depth.

north-western shelf and winter convective mixing in the middle of cyclonic gyres.

In order to properly represent these two physical processes, the upper envelope H_e^1 is designed to follow an 'enveloping'-bathymetry over the continental slope and shelf while it follows the climatological winter isopycnic surface with density $\sigma_e = 15.4$ $kg\ m^{-3}$ in open ocean areas. Such isopycnic surface is typically used to identify the deeper boundary of the Cold Intermediate Layer (CIL) (Ivanov and Belokopytov, 2012) and we compute it by using January, February and March climatological temperature and salinity data from the Black Sea Atlas (Suvorov et al., 2003).

The terrain-following portion of envelope H_e^1 has minimum and maximum depths equal to 10 and 140 m, respectively. The envelope is obtained by smoothing the actual topography according to local criteria: Hanning filter is applied in proximity of Danube canyon, while different slope parameter threshold values for the Martinho and Batteen (2006) smoothing algorithm are used in different areas of the domain. For example, in the north-western shelf a maximum slope parameter $r_{max} = 0.07$ is used, while in the south-eastern part of the domain we use $r_{max} = 0.05$ to handle wall-like topography. When the slope parameter is higher than the prescribed r_{max}, the envelope is smoothed, resulting in computational levels going below the actual bottom (see Fig. 5.2f). With this approach we are able to reduce numerical errors linked to the computation of horizontal pressure gradients with curved levels without changing the model bathymetry. The thickness of the uppermost model cell in the middle of the domain is ≈ 1.2 m.

Models' external forcings and initial conditions

Numerical simulations span the 2007-2009 period. This time interval was chosen due to data availability, for both external forcing and observations (see Sec. 4.2.3). Momentum and heat fluxes are computed by using the CORE bulk formulae (Large and Yeager, 2009) along with atmospheric fields from SKIRON weather forecasting system (Kallos et al., 1997) (see Appendix A). SKIRON forecast dataset has horizontal and temporal resolutions of $0.1° \times 0.1°$ and 2 hours, respectively, and it includes wind speed at 10 m, air temperature and specific humidity at 2 m, short and long wave radiation and total precipitation.

Accurate atmospheric forcing is crucial for the adequate performance of ocean models. This is especially true for the Black Sea, where small errors in the freshwater and heat forcing could result in large inaccuracies in long-term simulations of water masses formation processes (Stanev et al., 1997). In particular, cloud-related short-wave errors may cause excessive downward surface short-wave radiation, affecting the ability of a Black Sea model to properly represent the CIL inter-annual variability (Staneva et al., 1995).

Recently, Miladinova et al. (2018) showed that the ECMWF ERA-Interim reanalysis atmospheric dataset can be used to realistically simulate the multi-year CIL dynamics. For this reason, we weight the SKIRON short-wave radiation forcing with monthly climatological factors determined by fitting the area averaged SKIRON short-wave signal with the ERA-INTERIM reanalysis one. Panels a,b,c,d,e,f in Fig. 5.3 present time-series of the basin averaged SKIRON atmospheric fields used in this study.

Our models consider 11 main rivers and rivers discharges are estimated by using data from the Global Run-off Data Centre (GRDC, 2014). For the Danube we use daily data for 2007 and 2008 while for 2009 we use monthly climatological values. For all the other rivers, daily or monthly data are not available for the period of our study so we use monthly climatological values computed using the entire GRDC dataset. The salinity of the rivers is set at 1 PSU. Time-series of river discharges for the main rivers of the Black Sea used in this study are shown in Fig. 5.3g.

The Bosphorus strait is characterised by a two-layer exchange system: an upper current transports low salinity water from the Black Sea towards the Marmara Sea while a deeper flow runs in the opposite direction pouring high salinity water of Mediterranean origin into the Black Sea. Upper and lower layers climatological

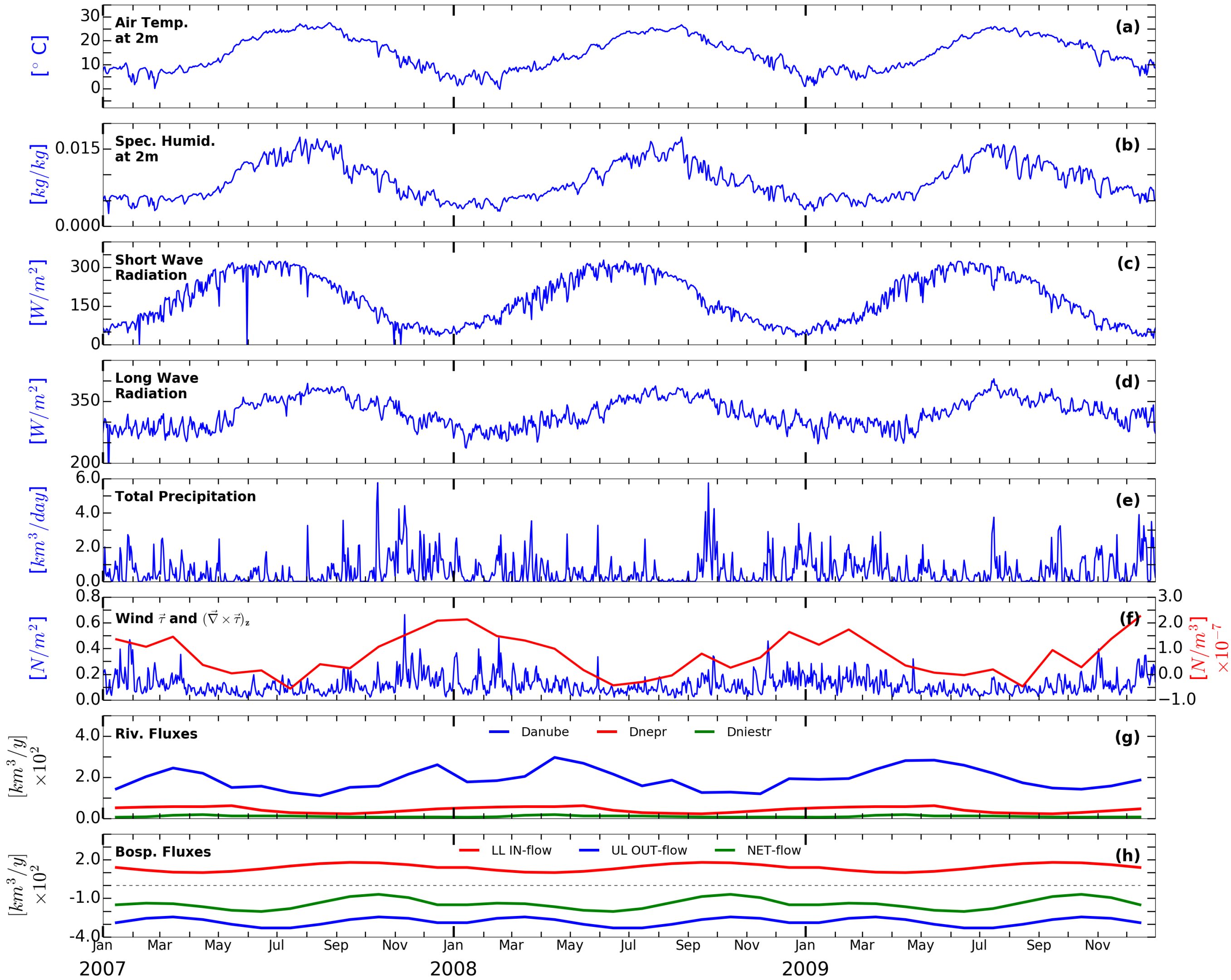

Fig. 4.3: (a-f) Timeseries of basin averaged SKIRON atmospheric fields used to force the four Black Sea models: (a) Air temperature at 2m $[°C]$; (b) Specific humidity at 2m $[kg/kg]$; (c) Short wave radiation $[Wm^{-2}]$; (d) Long wave radiation $[Wm^{-2}]$; (e) Total precipitation $[km^3 \text{ day}^{-1}]$; (f) Wind stress $\vec{\tau}$ (blue line) $[Nm^{-2}]$ and wind stress curl $(\vec{\nabla} \times \vec{\tau})_z$ (red line) $[Nm^{-3}]$. (g) Monthly timeseries of river discharges $[km^3$ year$^{-1}]$ of Danube (black), Dnepr (red) and Dniester (blue) rivers; (i) Bosphorus fluxes in the upper (blue) and lower (red) layers, while the net flux is shown in green. Negative values identify flows from the Black Sea to the Marmara sea.

fluxes are estimated approximating monthly values given by Aydogdu et al. (2018) (see their fig. 14b) with two analytical functions (see blue, red and green lines in Fig. 5.3h for upper layer out-flow, lower layer in-flow and net-flow, respectively). Salinity of incoming Mediterranean water is set to 36 PSU.

Our models have closed lateral boundary conditions and volume conservation is ensured redistributing the excess or deficit of water flux between surface model cells according to their corresponding area. (see Appendix 4A for the details).

All the numerical experiments start from 15 January 2007. The model is initialised as follows. The initial condition for temperature and salinity (T/S hereafter) is obtained by using January climatological data from the Black Sea Atlas (Suvorov et al., 2003). Then, the matching initial velocities are obtained with the 'semi-diagnostic adjustment' method (Ezer and Mellor, 1994; Enriquez et al., 2005), i.e. running the model for one year without any external forcing and not allowing the evolution in time of T/S initial fields. After the model has been initialised, numerical experiments are run in fully prognostic 'free' mode, without any data assimilation or relaxation to climatology. We consider the first 5 months of the simulation as spin up period and numerical results are analysed starting from 01 June 2007. Figure 4.4 presents the time-series of the basin averaged monthly SKIRON wind stress curl and daily KE of the upper 200 m of the water column of GEO-zps and CUR-MEs models (the ones of GEO-zps and CUR-MEs are very similar and are not shown here). It shows that after 5 months of simulation the barotropic wind-generated ocean dynamics is fully adjusted to the atmospheric forcing.

4.2.2 Experiments design

Two different type of numerical experiments are carried out. In the first one, the modelling skills of the four models implemented in this study are compared in (i) an initial test to assess the generation of spurious currents and (ii) a realistic simulation of the Black Sea hydrodynamics. The 90 days long initial test starts from

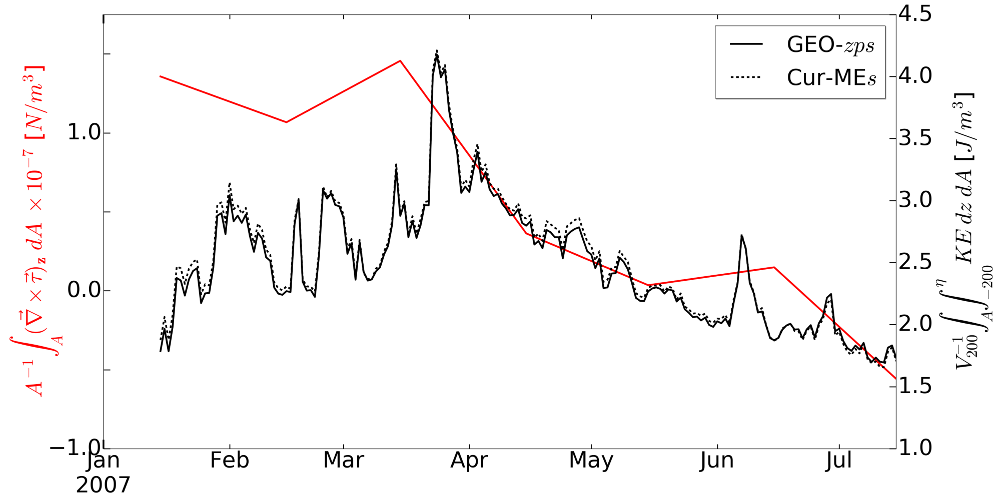

Fig. 4.4: Timeseries of the basin averaged monthly SKIRON wind stress curl $(\vec{\nabla}\times\vec{\tau})_z$ $[Nm^{-3}]$ (red line) and daily KE $[Jm^{-3}]$ of the upper 200 m of the water column of GEO-*zps* (black continuos line) and CUR-ME*s* (black dashed line) models. The timeseries of the basin averaged KE of CUR-*zps* and GEO-ME*s* models are not shown for clarity, being very similar to the ones of GEO-*zps* and CUR-ME*s*, respectively.

a horizontally uniform T/S distribution and zero velocity, with no river discharges, exchanges via Bosphorus and no meteo forcing. In such conditions the current velocities should remain zero, and any emerging currents should be attributed to the model errors. The realistic simulations are carried out from 15 January 2007 to 31 December 2008 and numerical results are validated against a number of observational datasets detailed in the next section. All simulation are carried out in a ‘free-run’ mode, without data assimilation or relaxation to climatology. The aim of this series of simulations with progressively increase of realism is to compare and contrast the effect of a particular combination of horizontal and vertical discretization schemes on the accuracy of the simulation and identify the model with most accurate numerical mesh.

In the second experiment, we simulate the Black Sea circulation from 15 January 2007 to 31 December 2009 with the CUR-ME*s* model, which resulted to be the model with the best accuracy in the first experiment (see Sec. 4.3.1). Then, we validate the numerical results of our CUR-ME*s* model and data from CMEMS reanalysis against a number of observational datasets and we compare the skills of the two models. CMEMS reanalysis can be considered to be the state-of-the art operational system for the Black Sea and, since it uses data assimilation, we concentrate our analysis on comparison with independent data sets not used in data assimilation. The aim of this experiment is to determine whether an optimal discretization scheme and hence a better representation of physical processes in a non-assimilating model can achieve similar or better skill than those shown by a good assimilation model which uses existing standard techniques.

After comparing the accuracy of the two modelling systems against available observations, the new CUR-ME*s* model and CMEMS reanalysis are used to investigate the 2007-2009 Black Sea variability of the Mean Kinetic Energy (MKE) of geostrophic currents and Cold Intermediate Layer (CIL) properties.

4.2.3 External datasets used for validation or comparison

Six independent datasets are used to validate the numerical results. They include five datasets of T/S measured profiles and one dataset of gridded SST. In this Chapter, the five hydrographic datasets are named as Perseus, Poseidon, CMEMS-Black Sea, Argo and RAS while the SST dataset is named OSTIA.

The *Perseus* dataset includes T/S observational profiles collected by sampling the water column with CTD and Niskin bottles during several cruises carried out in the Black Sea in the period 2007-2009 in the course of Perseus project (Crise et al., 2015). In total, the dataset contains 370 T/S profiles (they are represented with red circles in Fig. 5.1a): 40 CTD and 17 Niskin bottles profiles in 2007, 162 CTD and 101 Niskin bottles profiles in 2008 and 50 T/S profiles from Niskin bottles in 2009. The dataset covers the north-western shelf, the deep basin, the Bosphorus area and north-eastern part of the Black sea.

The *Poseidon* dataset includes 124 CTD T/S profiles measured during the POS 363 RV 'Poseidon' oceanographic cruise (Friedrich et al., 2008) carried out from March 7 to 25 2008 on the Black Sea north-western shelf, in Romanian waters (see white circles in Fig. 5.1a).

The *CMEMS-Black Sea* dataset includes T/S profiles collected during the period 1990-2015 from national observing systems operated by Black Sea GOOS members and scientific cruises from SeaDataNet NODCs completed by main global networks (Marinova and Valcheva, 2017). In this study we use a total of 62 CTD profiles measured in the south-western shelf of the Black Sea (see purple circles in Fig. 5.1a). Observations cover the whole 2007-2009 period, and they include 13 measurements in 2007, 45 in 2008 and 4 in 2009.

The *Argo* dataset (Argo, 2018) contains a total of 295 T/S profiles measured by Argo floats deployed in the Black Sea in the period 2007-2009. The dataset covers the deep basin of the Black Sea (see green circles in Fig. 5.1a) and includes 138 profiles in 2007, 100 in 2008 and 57 in 2009.

The *RAS* dataset is obtained from a number of Russian national research projects operating in the Black Sea and collecting T/S profiles from CTD over the period 2007-2014. In this study we use a the total number of 294 observations (see yellow circles in Fig. 5.1a), 205 in 2007, 56 in 2008 and 33 in 2009.

The *Operational Sea Surface Temperature and Sea Ice Analysis* (OSTIA) dataset is used to validate SST of CUR-ME*s* and CMEMS. It is a freely available high resolution analysis of the global ocean SST produced at the UK Met Office by combining satellite and in-situ SST observations. The accuracy (RMSE) of the OSTIA SST product is 0.57 K with zero BIAS (Donlon et al., 2012). In this study we use daily maps.

In the second experiment of this study we compare the accuracy of our CUR-ME*s* 'free-running' model with the one of the Copernicus Marine Environment Monitoring

Model	Horizontal grid type	Vertical grid type	Mesh points	Meteo forcing	Rivers runoff	Bathym.	Data assimil.	Type of simul.	NEMO code version
CUR-MEs	Shelf-break following (CUR)	Multi-Env s-coord. (MEs)	405×225 $\times 51$	Skiron Forec.	GRDC dataset	EMODnet	NO	Free-run hindcast	3.6
CMEMS	Regular Geograph. (GEO)	z-coord.+ part. steps	395×215 $\times 31$	ERA-Int. Reanal. + GPCP	Sesame dataset	GEBCO	SLA, SST, T/S profiles, LSBC scheme	Reanal.	3.4

Table 4.2: Comparison of the main characteristics distinguishing CUR-MEs model and CMEMS reanalysis.

Service (CMEMS) Black Sea Physical Reanalysis dataset.

CMEMS reanalysis covers the period 1995-2015 and are produced by the Centro Euro-Mediterraneo per i Cambiamenti Climatici (CMCC) institute (Lemieux-Dudon et al., 2018). The numerical ocean model used by the CMEMS Reanalysis system is based on NEMO version 3.4 hydrodynamic code (Madec, 2008) and it implements a regular geographical horizontal grid with zonal and meridional resolutions of $\approx 3\ km$ while it uses 31 z-levels with partial steps in the vertical direction (Ciliberti et al., 2016). Bathymetry is based on the GEBCO dataset. Three-hourly atmospheric fields from ECMWF ERA-Interim atmospheric reanalysis and precipitation fields from GPCP rainfall monthly dataset are used to force the model. River discharges are estimated by using the monthly mean dataset provided by SESAME project while the Bosphorus barotropic transport is computed to balance the freshwater fluxes on monthly basis. The CMEMS reanalysis system assimilates in-situ hydrographic profiles (mostly Argo floats), along-track sea level anomalies (SLA) from all available missions and CMEMS gridded sea surface temperature (SST) observations. Large Scale Bias Correction (LSBC) scheme is also applied, restoring T/S fields to their climatological values. Features of CUR-MEs model and CMEMS reanalysis are compared in Table 4.2.

4.2.4 Metrics used to assess models' accuracy

The accuracy of the four models implemented in this Chapter and CMEMS reanalysis is quantified with respect to six independent external observational datasets (see Sec. 4.2.3).

Gridded T/S daily numerical outputs are bilinearly interpolated on the geographical location of each T/S observation. Then, in the case of hydrographic datasets, both observed and modelled profiles are linearly interpolated on 75 reference depths h_r, with vertical step Δh_r varying from 2.5 m in the first 100 m of the water column to 50 m for $250 < h_r \leq 1000$ m.

Modelling skill of the four models and CMEMS reanalysis is assessed by computing time averaged BIAS and root mean square error (RMSE) between simulated (Ψ^m) and observed quantities (Ψ^o), defined as

$$BIAS = N_t^{-1} \sum_i^{N_t} N_d^{-1} \sum_k^{N_d} (\Psi_{i,k}^m - \Psi_{i,k}^o)$$
$$RMSE = N_t^{-1} \sum_i^{N_t} \left[N_d^{-1} \sum_k^{N_d} (\Psi_{i,k}^m - \Psi_{i,k}^o)^2 \right]^{1/2}$$

where Ψ stands for either temperature or salinity, N_t is the number of observational profiles used for the time averages and $N_d \leq 75$ is the total number of depths of each profile.

Recently, Lishaev et al. (2018) and Mizyuk et al. (2018) compared the accuracy of a number of reanalysis and forecasting systems of the Black Sea by computing BIAS and the RMSE for specific layers of the water column. They defined four depth layers in the upper 300 m of the Black Sea: a surface layer from 0 to 5 m, two sub-surface layers from 5 to 30 m and from 30 to 100 m, respectively, and one deeper layer with depths ranging from 100 to 300.

In order to better understand the effect of using a particular combination of horizontal and vertical grid with respect to the others, in the first experiment we follow the same approach and we also calculate the BIAS and the RMSE for the same four depth layers. Metrics for layers are defined as before, but in this case N_d is the number of reference depths included in a particular depth layer.

4.3 Results and discussion

4.3.1 The effect of different discretization schemes on the accuracy of the simulations

The results of the preliminary test (see Sec. 4.2.2) show that spurious currents develop in all the four models, although with small values in all the four cases. After 90 days, the maximum error is 0.001 ms^{-1} for both GEO-zps and CUR-zps models, while it is 0.008 ms^{-1} and 0.004 ms^{-1} for GEO-MEs and CUR-MEs models, respectively.

In agreement with Bruciaferri et al. (2018), these results prove the ability of the MEs vertical discretization scheme to reduce errors in the computation of horizontal pressure gradients to a level comparable with the one of standard z-levels with partial steps grids. We noted that a combination of MEs with the curvilinear horizontal grid (CUR-MEs) gives a further reduction of spurious currents as compared to to GEO-MEs. We attribute this improvement to the fact that the curvilinear grid aligned with the shelf-break reduces the slope parameter in the proximity of the shelf-break.

The numerical results of the 2007-2008 Black Sea circulation simulations carried out with the four models are validated against five datasets of T/S measured profiles collected during 2007-2008 in the Black Sea (see Sec. 4.2.3). No information is provided regarding the uncertainty in the T/S measurements. Typical values of the uncertainty associated with measurements performed by a Conductivity-Temperature-Depth profiler (CTD) are 0.02 °C for temperature and 0.01 PSU for practical salinity

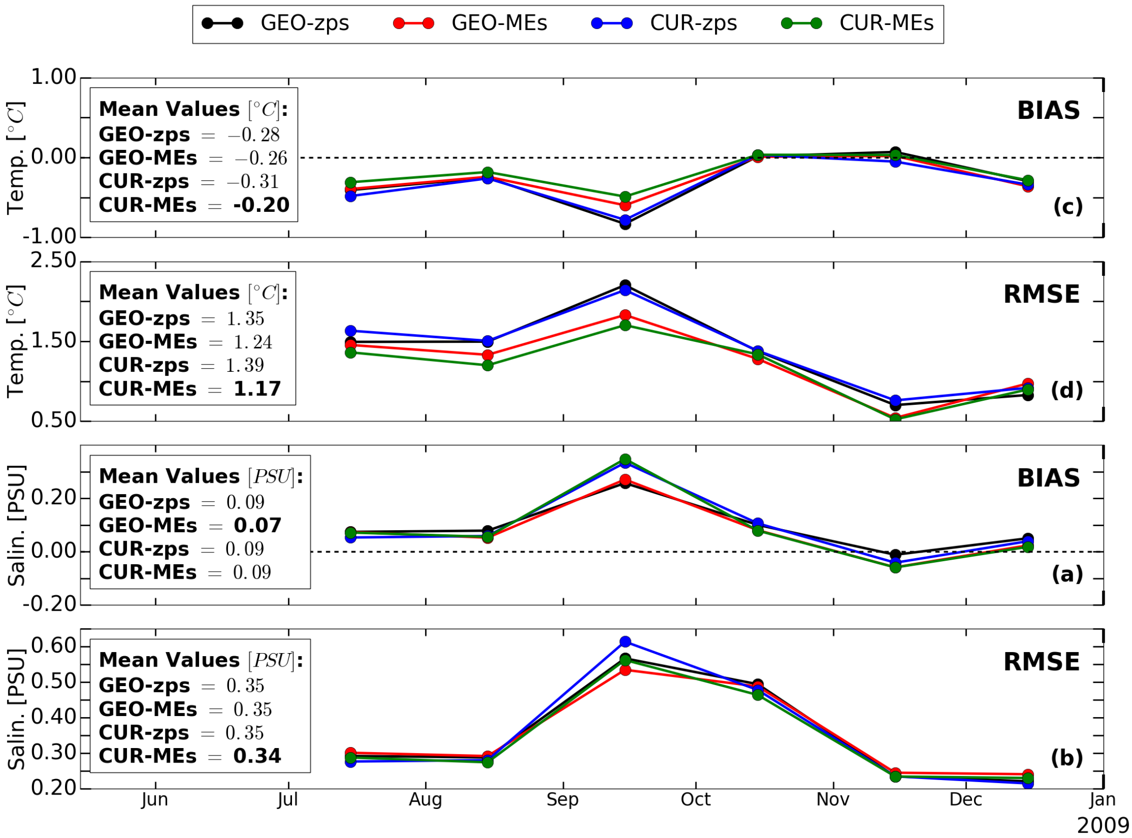

Fig. 4.5: 2008 summer-autumn timeseries of monthly averaged BIAS and RMSE of salinity (a and b) and temperature (c and d) profiles simulated with the GEO-*zps* (black), GEO-ME*s* (red), CUR-*zps* (blue) and CUR-ME*s* (green) models with respect to observed T/S profiles. 2008 summer-autumn averaged metrics are also given.

(e.g. Raiteri et al. (2018) and references therein).

The performance of the four models differs mainly in the summer-autumn seasons, with CUR-MEs showing consistently better results, see Fig. 4.5. This can be attributed to the fact that during that season the nearly-geostrophic Rim Current weakens and meso-scale activity in the Black Sea increases (Zatsepin et al., 2003; Ivanov and Belokopytov, 2012) and the CUR-ME*s* model better resolves meso- and sub-mesoscale dynamics near the shelf break. For example, summer-autumn averaged BIAS and RMSE of GEO-*zps* model are -0.28 and $1.35\ °C$, respectively, while

	Layer 5 − 30 m				Layer 30 − 100 m			
MODEL	SALIN. BIAS	SALIN. RMSE	TEMPER. BIAS	TEMPER. RMSE	SALIN. BIAS	SALIN. RMSE	TEMPER. BIAS	TEMPER. RMSE
GEO-*zps*	0.29	0.42	−0.99	2.38	0.13	0.39	−0.28	0.91
GEO-ME*s*	0.26	0.37	−0.88	2.13	0.12	0.41	−0.28	0.90
CUR-*zps*	0.26	0.39	−1.12	2.45	0.12	0.40	−0.33	0.91
CUR-ME*s*	0.25	0.35	−0.61	1.95	0.12	0.40	−0.22	0.86

Table 4.3: 2008 summer-autumn averaged temperature and salinity BIAS and RMSE of T/S profiles simulated by the four models with respect to measured T/S profiles in water column layers with depth between $5-30$ m and $30-100$ m.

they are reduced to -0.20 and 1.17 $°C$ in the case of the CUR-MEs model. In the case of salinity, the GEO-MEs model presents the smallest BIAS (0.07 PSU), while the CUR-MEs model has the smallest RMSE (0.34 PSU). However, improvements are less notable than the ones for temperature. The differences between the predictions of the different models are large compared with the measurements' uncertainties, indicating that the difference in the skills of the four models might be considered significant in a statistical sense.

In order to better understand the effect of using a particular combination of horizontal and vertical grid with respect to the others, we continue the analysis by computing the BIAS and RMSE of the four models for the four depth layers defined by Lishaev et al. (2018) and Mizyuk et al. (2018). For each depth layer, we consider four metrics, BIAS and RMSE for temperature and salinity.

Numerical results show that the accuracy of the four models is notably different in the two sub-surface layers with depths between $5-30$ m and $30-100$ m, respectively (see Tab. 4.3). These layers represent the active portion of the Black Sea, where the CIL is formed and advected all over the basin (Ivanov and Belokopytov, 2012) and where models' meshes differ the most.

The CUR-MEs model has the highest accuracy in both layers. It has smaller errors for both salinity and temperature in layer $5-30$ m, especially with respect to GEO-zps and CUR-zps models, which present the worst modelling skill. In layer $30-100$

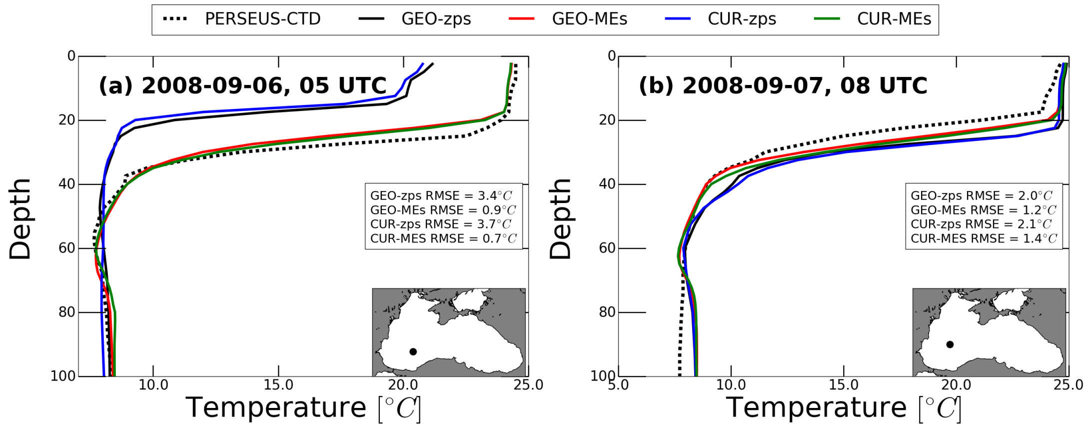

Fig. 4.6: Comparison between T profiles measured by CTD profilers (in dashed black) on 2008-09-06 (a) and 2008-09-07 (b) and T profiles simulated by GEO-*zps* (black), GEO-MEs (red), CUR-*zps* and CUR-MEs (green) models for the same days. The day and hour of the measurement is indicated in the upper-left corner of each sub-panel while the location of the observation is shown in the inset map. RMSE of the four models with respect to measurements are also given.

m, the CUR-MEs model presents improved accuracy for temperature in comparison to all the other models, while for salinity differences are small (≤ 0.02 PSU) and all the models seems to be equivalent.

The GEO-MEs model presents the second best accuracy in both layers, although with important differences with respect to the CUR-MEs model, especially for temperature. Figure 4.5 and Tab. 4.3 clearly show that GEO-*zps* and CUR-*zps* models have similar modelling skills, with differences mostly due to isolated outlayers rather than to a systematic effect of the horizontal grid. These results seem to indicate that the usage of a CUR-type grid significantly improves the quality of the simulation only if combined with the MEs vertical scheme, confirming the fundamental role of the vertical grid in ocean modelling.

In September 2008 the modelling skill of the four models differs the most (see Fig. 4.5), with the CUR-MEs model showing the best accuracy in simulating temperature. The details of the differences which lead to a better overall performance (better

RMSE and BIAS) of the CUR-MEs model are shown in Fig. 4.6, which presents two examples of CTD-measured temperature profiles in September 2008 compared with temperature profiles simulated by the four models for the same days. Within the layer $20 - 70$ m MEs models better represent the CIL, probably due to the nearly isopycnal curvature of the computational levels and hence lower contamination of slow diapycnal mixing by fast isopycnic processes. The differences between the two MEs based models - CUR-MEs and GEO-MEs - can be attributed to their different horizontal resolution - the CUR grid has a coarser resolution in the deep sea.

The difference in representing the horizontal structure of temperature distribution is seen in Fig. 4.7, which shows monthly averaged maps and transects produced by the four models in September 2008. The CIL represented in both GEO-MEs and CUR-MEs models (which have the best accuracy) is generally colder and has larger spatial extension than the one represented by zps models (Fig. 4.7, Left column). The CUR-MEs model simulates an almost homogeneous CIL with $T \leq 7.6°C$ extending from the shelf to off-shore areas (Fig. 4.7, Middle column). The GEO-MEs model gives a similar result, although its coarser horizontal resolution on the shelf seems to increase lateral diffusion, forming CIL with $T \approx 7.9°C$ in this areas. In the GEO-zps model the CIL disappears over the continental slope. The CUR-zps model simulates the CIL on the slope but is warmer than any of the MEs models.

The inspection of the meridional cross-sections (Fig. 4.7, Right column) reveals that all the four models simulate cold dense water cascading in proximity of the shelf-break. Since the MEs vertical grid has terrain-following levels at depths shallower than $\approx$ 120 m, the models using this vertical discretization scheme have higher vertical resolution in the bottom boundary layer where the cascading takes place. To the contrary, the step-like representation of the bottom topography of zps models seems to stop the cascading on the shelf, in agreement with previous studies (e.g. Ezer (2005); Shapiro et al. (2013); Bruciaferri et al. (2018)). The CUR-zps model generates a deeper and less diffused cascade than the one of the GEO-zps model,

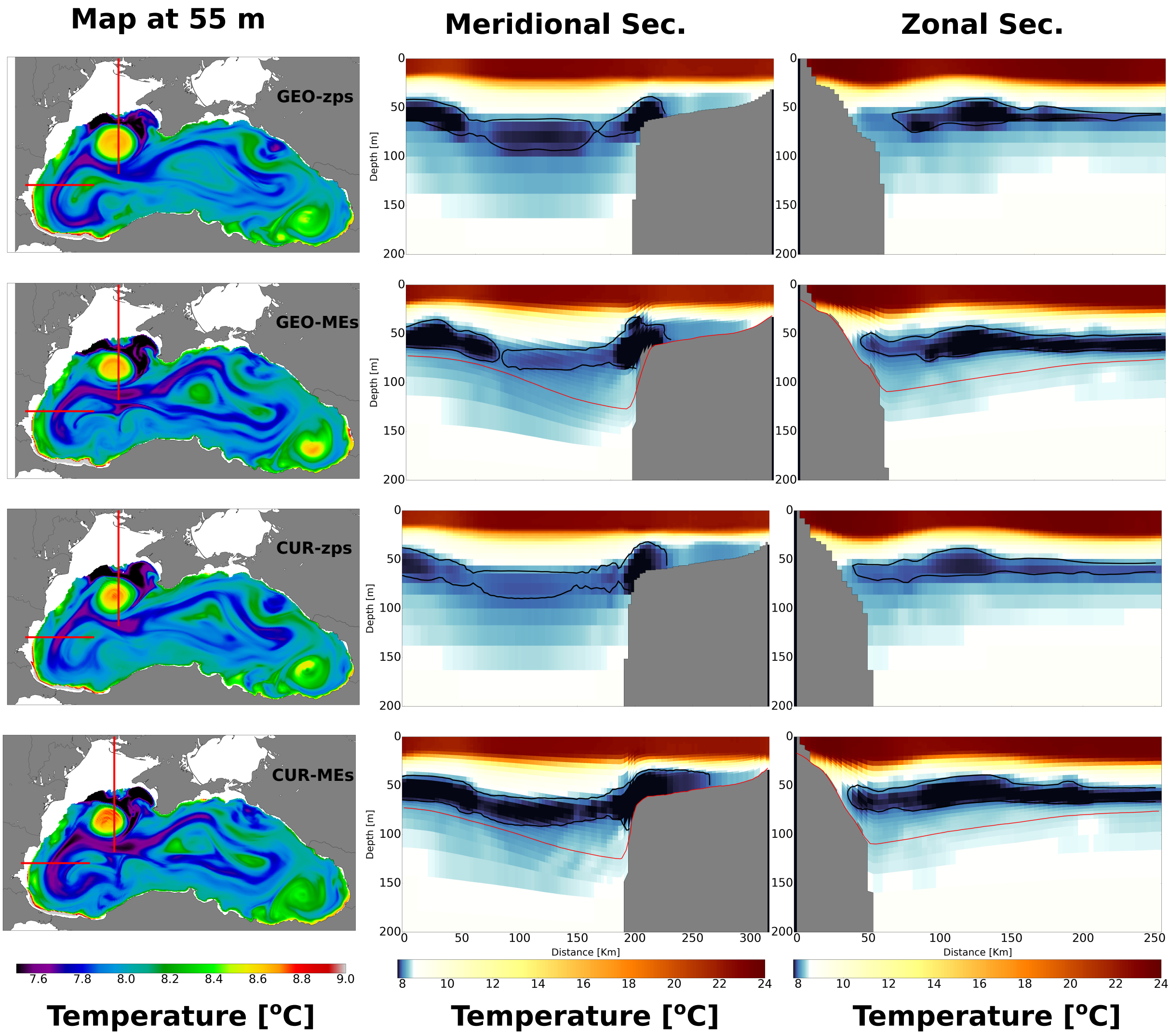

Fig. 4.7: September 2008 monthly averaged (*Left column*) maps at 55 m and (*Middle column*) meridional (31.7°E) and (*Right column*) zonal (42.9°N) cross-sections of the Black Sea temperature. In the maps, the red lines show the locations of the cross-sections. In the cross-sections, the thick black lines identify isotherms with $T = 8°C$ while the red lines show the upper envelope H_e^1 of MEs models.

probably due to the increased horizontal resolution of the CUR-*zps* model at the shelf-break.

4.3.2 Comparing the accuracy of the CUR-MEs model and CMEMS reanalysis

In Section 4.3.1 the CUR-ME*s* model is proven to be the most accurate model between the four developed for this study. In the second experiment, we use our CUR-ME*s* model to simulate the 2007-2009 Black Sea circulation and we validate its numerical results against six datasets of measurements. At the same time, we validate data from CMEMS Black Sea reanalysis against the same set of independent observations and then we compare the accuracy of the two models. The CMEMS model highly assimilates observations and currently represents the official EU best estimate of the 1995-2015 Black Sea state.

We start the analysis by comparing CUR-ME*s* and CMEMS SST daily model outputs with OSTIA SST daily maps (SST from model outputs is retrieved by considering the temperature of the first model level). Figure 5.6a shows time-series of the volume averaged SST of OSTIA dataset and simulated by the two models, while Fig. 5.6b and 5.6c present time-series of BIAS and RMSE, respectively, of CUR-ME*s* and CMEMS model outputs with respect to OSTIA observations. The OSTIA SST product provides also map of the uncertainty associated with each monthly value (magenta error bars in Fig. 5.6b and 5.6c).

The numerical results demonstrate that the seasonal and inter-annual variability of the basin averaged SST simulated by the free-running CUR-ME*s* model and the SST-assimilative CMEMS reanalysis agrees well with the one reproduced with OSTIA observations. Averaged over the length of the simulation metrics show that the mean SST BIAS of the CUR-ME*s* model is $\approx 0.3°C$ warmer than the one of CMEMS reanalysis, while the difference between the mean CUR-ME*s* and CMEMS SST RMSE is $\approx 0.6°C$.

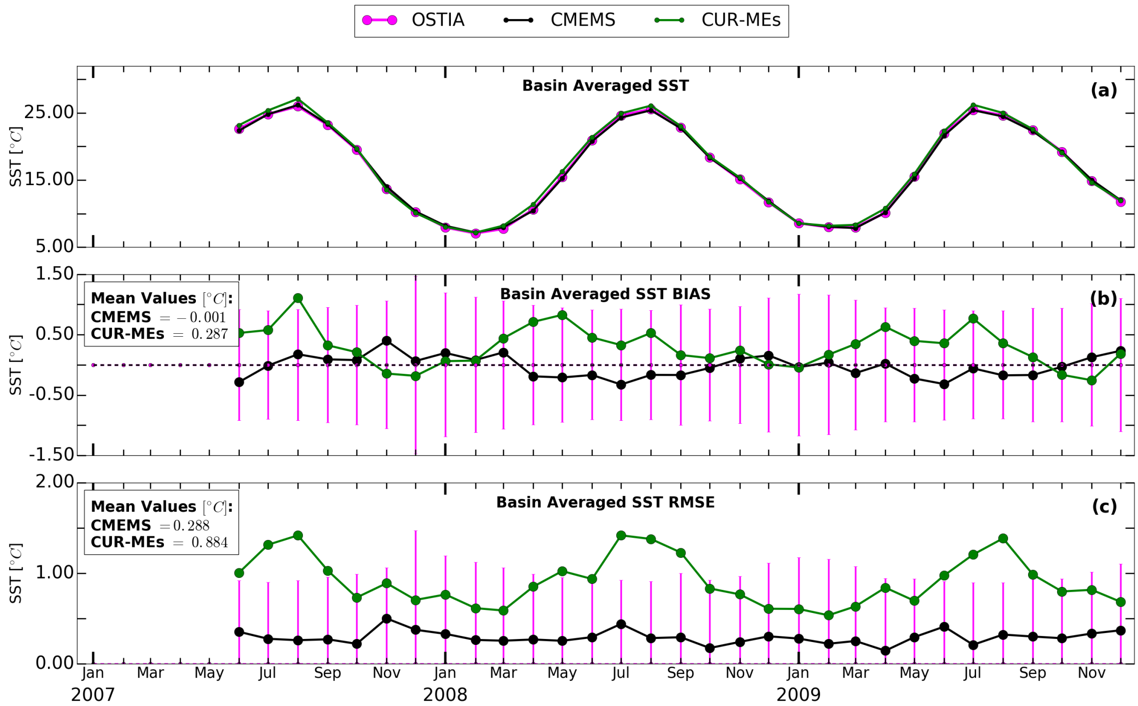

Fig. 4.8: (a) Timeseries of the monthly basin averaged SST retrieved from OSTIA observational dataset (magenta) and simulated by the CUR-MEs model (green) and CMEMS reanalysis (black); (b) Timeseries of monthly averaged SST BIAS of CUR-MEs (green) and CMEMS (black) model outputs with respect to OSTIA observations; (c) Timeseries of monthly averaged SST RMSE of CUR-MEs (green) and CMEMS (black) model outputs with respect to OSTIA observations. Averaged over the length of the simulation metrics are also given. In magenta is represented the basin averaged uncertainty associated with OSTIA SST monthly values.

Timeseries of SST metrics show that the BIAS and RMSE of CUR-MEs and CMEMS SST simulations are quite similar in late autumn-winter, with an average difference of $\approx 0.1°C$ and $\approx 0.25°C$, respectively, well below the associated basin averaged uncertainty. In summer, the accuracy of CUR-MEs model decreases and mean BIAS and RMSE differences between our free-running model and CMEMS reanalysis are of $\approx 0.5°C$ and $\approx 1.0°C$, respectively. Differences between CUR-MEs and CMEMS SST RMSE values can be considered statistically significant being larger than the associated basin averaged measurements' uncertainties. Summer SST overestimation is a known problem of ocean models (see e.g., Ezer (2000); Hordoir et al. (2018)).

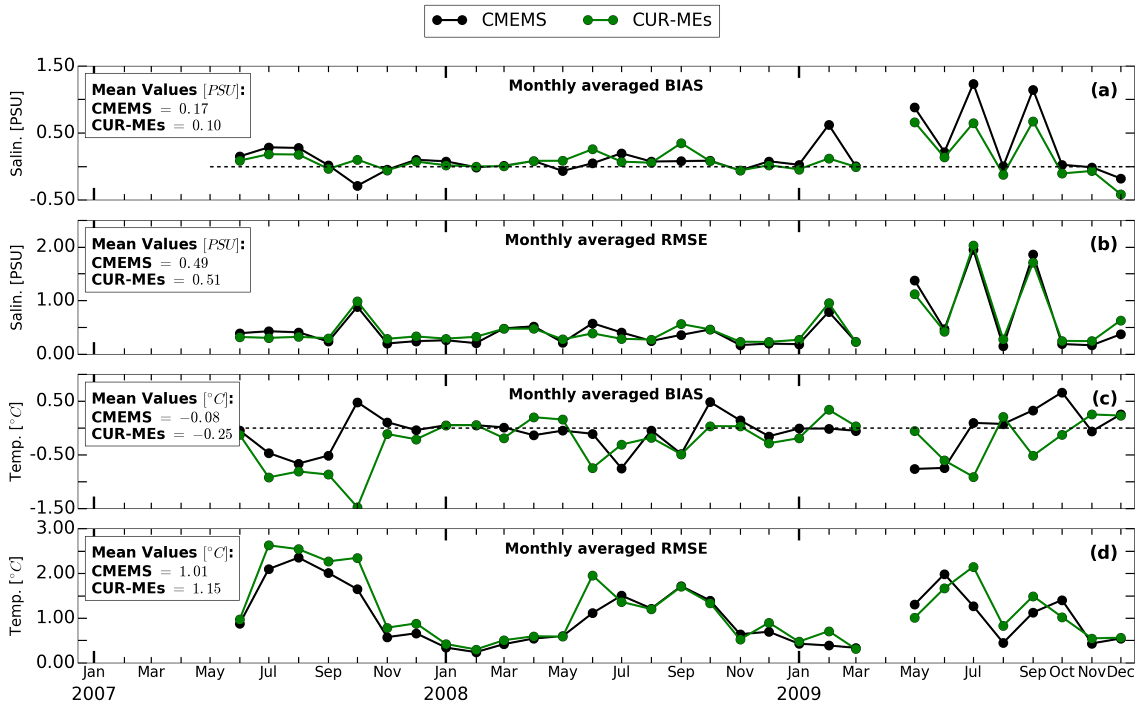

Fig. 4.9: Timeseries of monthly averaged BIAS and RMSE of salinity (a and b) and temperature (c and d) profiles simulated with the CUR-ME*s* model (green) and by CMEMS reanalysis (black) with respect to observed T/S profiles. Averaged over the length of the simulation metrics are also given. In May 2009 there are no observations available.

It can be attribuited to inaccuracies in the atmospheric forcings and/or in the poor representation of the upper ocean mixed layer physics and SST data assimilation is usually used to improve such model deficencies (see e.g, O'Dea et al. (2012)).

We continue the comparison of CUR-ME*s* model and CMEMS reanalysis by validating their numerical results against five independent datasets of observed T/S profiles (see Sec. 4.2.3). Figure 5.11 presents time-series of BIAS and RMSE of salinity (Fig. 5.11a, 5.11b) and temperature (Fig. 5.11c, 5.11d) profiles simulated with the CUR-ME*s* and CMEMS models with respect to in-situ hydrographic profiles.

CMEMS reanalysis assimilates satellite SST and SLA, T/S profiles and restores T/S fields to their climatological values. CUR-ME*s* model is run in a free mode, without any data assimilation or relaxation to climatology. Nevertheless, the accuracy of the free-running CUR-MEs model is very similar to assimilative CMEMS reanalysis.

Averaged over the length of the simulation metrics shows that the difference between mean salinity BIAS of CUR-MEs and CMEMS is 0.07 PSU, while the difference of their mean salinity RMSE is 0.02 PSU. Regarding temperature, the CUR-MEs model has a mean BIAS of $0.17°C$ colder than the one of CMEMS, while the RMSE of our free-running model is $0.14°C$ higher than the one of CMEMS reanalysis. Differences between CUR-MEs and CMEMS statistics can be considered statistically significant being larger than typical uncertainties associated with CTD measurements (0.02 °C for temperature and 0.01 PSU for practical salinity). However, the differences of salinity statistics are very close to the values of typical observations' uncertainties.

A more in depth analysis of monthly time-series of BIAS and RMSE confirms that the performance of CUR-MEs and CMEMS models in simulating salinity field evolution is practically the same. In the case of temperature, they present small differences, mainly concentrated in summer-autumn 2007. The inspection of the actual T profiles simulated with the two models reveals that CUR-MEs inaccuracies in the last part of 2007 mostly originate in shelf areas, where it is likely that the local stratification has still to completely recover from the climatological initial condition and where it is easier that SST errors might affect thermal properties of the underlying water column.

Figure 4.10 presents the basin averaged vertical profiles of the yearly mean salinity and temperature BIAS and RMSE of the CUR-MEs model and CMEMS reanalysis with respect to observed T/S profiles for 2007 (*Upper row*), 2008 (*Middle row*) and 2009 (*Lower row*). The CUR-MEs model has greater accuracy (both BIAS and RMSE) in the active CIL layer of the sea (at depths between $\approx 35 - 100\ m$) in comparison to CMEMS reanalysis for both salinity and temperature. On the other hand, SST assimilating CMEMS reanalysis shows a better accuracy in simulating

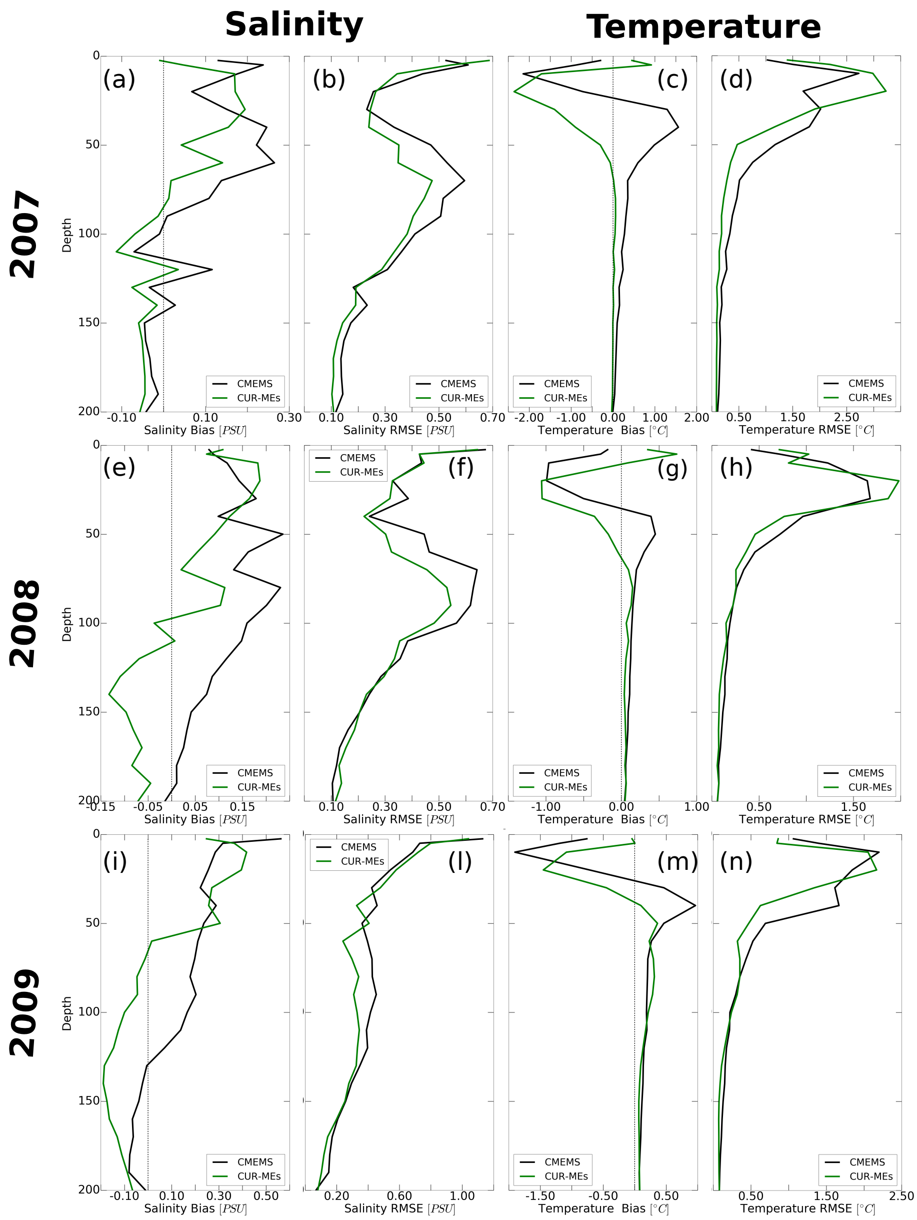

Fig. 4.10: Basin averaged vertical profiles of yearly mean BIAS and RMSE of salinity and temperature profiles simulated with the CUR-MEs model (green) and by CMEMS reanalysis (black) with respect to observed T/S profiles for 2007 (*Upper row*), 2008 (*Middle row*) and 2009 (*Lower row*).

sea surface temperature (at depths between $\approx 0 - 30\ m$) while for the sea surface salinity both models seems to be equivalent.

4.3.3 2007-2009 variability of Black Sea MKE and CIL

In this section, we use the numerical outputs from CUR-MEs model and CMEMS reanalysis to study the 2007-2009 seasonal and inter-annual variability of (i) the Mean Kinetic Energy of currents and (ii) the CIL heat content. Numerical results are compared with observations or data from existing literature.

Mean Kinetic Energy (MKE) of geostrophic currents

The seasonal and interannual variability of the MKE generated by the geostrophic component of the surface currents averaged over the entire Black Sea surface for the period 2007-2009 is obtained from three sources: (i) the CUR-MEs model, (ii) CMEMS reanalysis and (iii) satellite altimetry data presented in Kubryakov and Stanichny (2015).

The MKE is computed as

$$MKE = \frac{1}{2}(\langle u_g^2 \rangle + \langle v_g^2 \rangle) \tag{4.2}$$

where $\langle \bullet \rangle$ is an area averaging operator. The geostrophic current velocity $\vec{u}_g = (u_g, v_g)$ has zonal and meridional components given by the geostrophic balance

$$u_g = -\frac{g}{f}\frac{\partial \eta}{\partial y} \tag{4.3}$$

$$v_g = \frac{g}{f}\frac{\partial \eta}{\partial x} \tag{4.4}$$

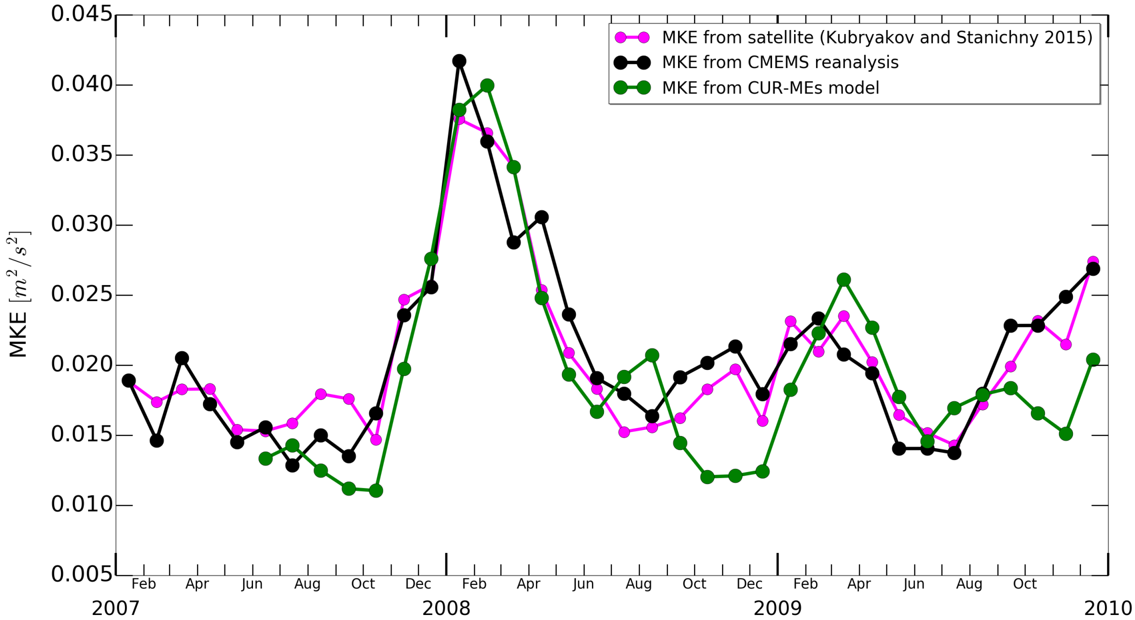

Fig. 4.11: Monthly timeseries of the MKE simulated with the CUR-ME*s* (green) and CMEMS (black) reanalysis models together with the MKE computed from satellite altimetry observations of Kubryakov and Stanichny (2015) (magenta).

where g is the gravitational acceleration, f is the Coriolis parameter, η is the sea-surface height (SSH) and x and y are the zonal and meridional directions, respectively. In the case of geostrophic currents computed from satellite measurements, $\eta = MDT + SLA$, where MDT is the 1999-2007 mean dynamic topography calculated by Kubryakov and Stanichny (2011) and SLA is the sea level anomalies field from satellite altimetry (Kubryakov and Stanichny, 2015).

Figure 5.12 presents monthly timeseries of the MKE simulated with the CUR-ME*s* and CMEMS reanalysis models together with the MKE of Kubryakov and Stanichny (2015). The CUR-ME*s* MKE monthly time-series starts in June 2007 because of the five months spin-up. The variability of the MKE simulated with the CUR-ME*s* model and by the SLA-assimilative CMEMS reanalysis are both in very good agreement with those obtained from satellite observations: the RMSE and correlation coefficient R of our CUR-ME*s* model are 0.004 m^2/s^2 ($\approx$ 20% of the average MKE) and 0.86,

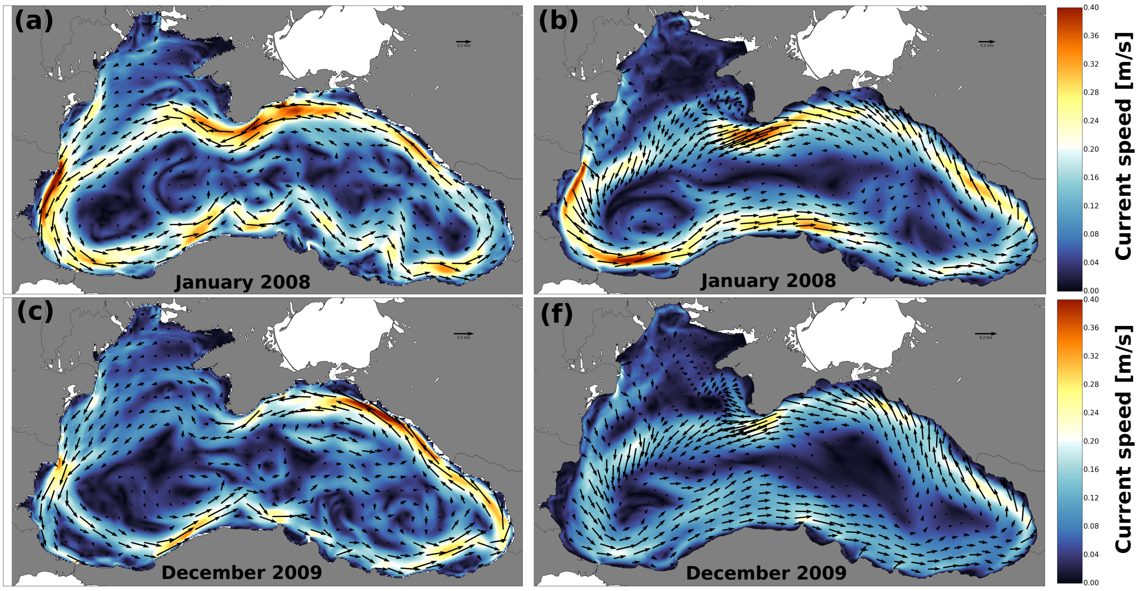

Fig. 4.12: Monthly averaged Black Sea surface circulation simulated with the CUR-MEs model and CMEMS reanalysis. *First column:* results from CMEMS reanalysis. *Second column:* results of the CUR-MEs model. *First row:* January 2008 averaged Black Sea surface circulation. *Second row:* December 2009 averaged Black Sea surface circulation.

respectively, while statistics of CMEMS reanalysis are RMSE= 0.002 m^2/s^2 ($\approx$ 10% of the average MKE) and R= 0.92.

Both models capture the seasonal MKE cycle, with winter peaks and summer weakening of the large-scale dynamics. Moreover, they also describe a very similar interannual variability, with a more active winter in 2008 than 2009. The curl of the wind stress is the main forcing of the Rim Current (e.g. Korotaev et al. (2003)). The 2007-2009 time-series of the basin-averaged wind stress curl over the Black Sea from SKIRON forecast dataset (red line in Fig. 5.3f) clearly shows its correlation with the MKE cycle, proving that the atmospheric forcing adequately represents the 2007-2009 Black Sea wind conditions.

As an example of the winter circulation obtained with the two models, Fig. 5.10a and 5.10b present the January 2008 averaged Black Sea surface circulation simulated with

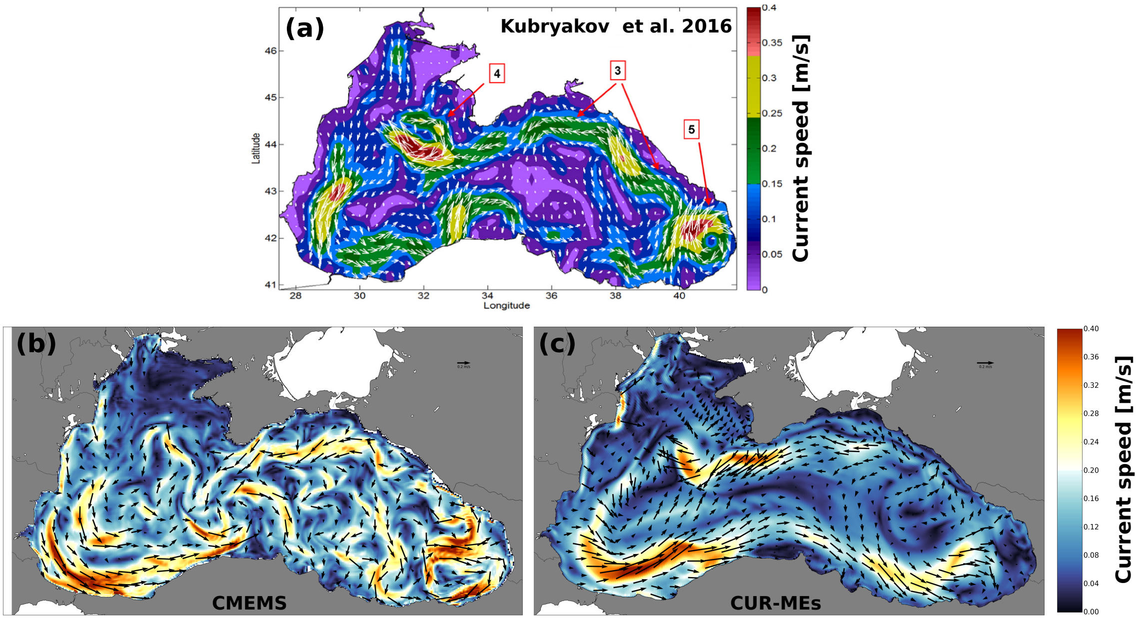

Fig. 4.13: Black Sea surface circulation for 16 April 2008. (a) Surface geostrophic currents reconstructed from altimetry data, redrawn after Kubryakov et al. (2016). (b) Daily averaged Black Sea surface circulation from CMEMS reanalysis. (c) Daily averaged Black Sea surface circulation simulated with the CUR-ME*s* model.

CMEMS reanalysis and the CUR-ME*s* model, respectively. Both models represent a very similar coherent and well defined Rim Current, flowing along the shelf-break with velocities ranging between 0.2 and 0.4 ms^{-1}. They are in good agreement with results presented in other studies, e.g. the January 2008 surface circulation reproduced with the 2000-2012 Black Sea physical reanalysis of the Russian Marine Hydrophysical Institute (MHI) and showed by Sukhikh and Dorofeyev (2016) (their fig. 6a).

Figures 5.10c and 5.10d give an example of the autumn Black Sea hydrodynamic reproduced by the two models. They show the December 2009 averaged surface circulation simulated by CMEMS reanalysis (Fig. 5.10c) and with the CUR-ME*s* model (Fig. 5.10d). Both models represent a Rim Current recovering from the summer weakening. The circulation simulated by the two models on the north-western shelf and in front of the Crimean peninsula is similar, with current velocities ranging between 0.15 and 0.25 ms^{-1}. Those are the areas where the CUR-MEs model has increased horizontal resolution, demonstrating that the usage of the CUR grid allows to achieve an accuracy comparable to the one of the CMEMS reanalysis. In the south-eastern part of the basin the horizontal resolution of the CUR-MEs model is not as high and this seems to affect the accuracy of the model, resulting in slower currents in the Batumi area and along Caucasian coasts. This is probably also the cause of the CUR-MEs tiny underestimation of Black Sea MKE in autumn in comparison to the one from satellite (Fig. 5.12).

In Figure 5.13, the surface geostrophic circulation for 16-04-2008 computed from altimetry data by Kubryakov et al. (2016) (5.13a) is compared with the daily averaged Black Sea surface circulation simulated with CMEMS reanalysis (5.13b) and the CUR-MEs model (5.13c) for the same day. The circulation simulated by the CUR-MEs model is very similar to the one retrieved from satellite observations on the north-western part of the basin, particularly in proximity of the Sevastopol anticyclonic eddy and along Crimean coasts, while currents are slower in the south-eastern part, especially in the Batumi area. On the other hand, the circulation given by CMEMS reanalysis reproduces a Batumi eddy very similar to that in the Kubryakov et al. (2016) calculations, while in the proximity of the Crimean peninsula it describes weaker currents, particularly for the quasi-permanent anticyclonic eddy in front of Sevastopol.

Cold Intermediate Layer (CIL)

The 2007-2009 seasonal and inter-annual variability of the Black Sea CIL is analysed in terms of the time evolution of the basin averaged CIL Cold Content (Stanev et al., 2003).

The CIL Cold Content [Jm^{-2}] (hereafter CCC) is computed as

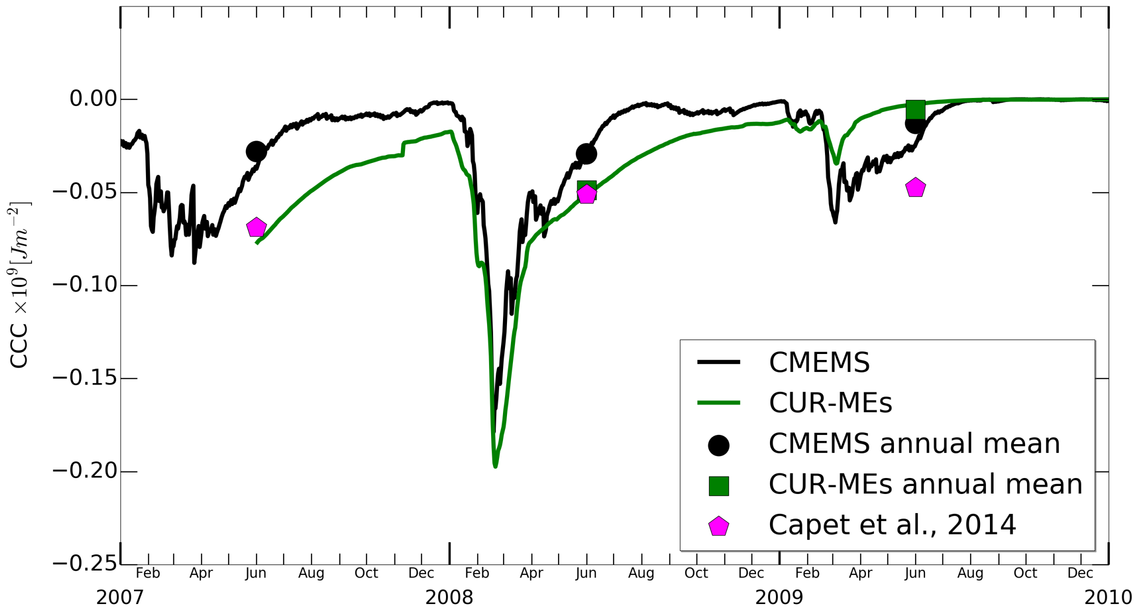

Fig. 4.14: Daily timeseries of the 2007-2009 basin averaged CCC according to CUR-ME*s* model (green line) and CMEMS reanalysis (black line). CCC annual mean values of CMEMS reanalysis (black circle) and CUR-ME*s* model (green square) together with annual data redrawn from Capet et al. (2014) (magenta pentagon) are also shown.

$$CCC = \begin{cases} \displaystyle\int_{CIL} c\rho(T - T_r)dz & ,\text{if } T \leq T_r \text{ and } \rho > 1014 \\ \\ 0 & ,\text{if } T > T_r \text{ or } \rho \leq 1014 \end{cases} \tag{4.5}$$

where $c(z)$ is the specific heat capacity $[Jkg^{-1}K^{-1}]$, $\rho(z)$ is the sea water density $[kgm^{-3}]$, $T(z)$ is the water temperature $[°C]$ and $T_r = 8°C$ is the reference temperature historically used to identify the CIL (Ivanov and Belokopytov, 2012). The vertical integration is limited by the $8°C$ isotherms and it is performed only in areas where density $\rho > 1014$ kgm^{-3} (Stanev et al., 2003).

Figure 4.14 presents daily timeseries and annual mean values of the 2007-2009 basin averaged CCC computed by using daily model outputs from the CUR-ME*s* model and CMEMS reanalysis, respectively. The CUR-MEs timeseries starts from 01-06-2007 because of the five months spin-up. For model-data intercomparison, the annual CCC values calculated by Capet et al. (2014) are shown as well. They were computed by using Black Sea temperature profiles with depths > 50 m for the period 1955-2011 extracted from the World Ocean Database and applying the Data Interpolating Variational Analysis (DIVA) and Eq. 4.5 (Capet et al., 2014).

A typical seasonal variability is reproduced by both models, with CIL formation at the beginning of each year and CIL horizontal mixing in summer-autumn. When compared to Capet et al. (2014) data, CCC annual values of CMEMS reanalysis prove that they systematically underestimates the Black Sea CCC, with an error of ≈ 0.05 Jm^{-2} in 2007, ≈ 0.025 Jm^{-2} in 2008 and ≈ 0.035 Jm^{-2} in 2009. On the other hand, CUR-MEs annual averages show a very good agreement with Capet et al. (2014) estimations in 2008 (error < 0.01), while in 2009 our model also simulates a lower CIL cold content (error ≈ 0.04 Jm^{-2}).

In order to better characterise the CIL seasonal and interannual variability, in Fig. 4.15 the temporal evolution of the monthly mean basin averaged temperature profile of the upper 100 m of the Black Sea according to CMEMS and CUR-MEs numerical simulations is shown. Qualitative model-data intercomparison is performed with results from Akpinar et al. (2017), where the authors characterised the 2002-2015 CIL meso-scale and monthly-to-inter-annual variability by analysing weekly Argo floats T/S profiles.

In 2007, the volume of the CIL simulated by CMEMS reanalysis drastically reduces after July, to such a level that its signal disappears from summer-autumn basin averaged temperature profiles. On the other hand, the CUR-MEs model represents a well defined 2007 CIL with depths ranging between $30-100$ m until November. This seems to be in good agreement with Akpinar et al. (2017) data, where the existence of a distinct CIL located at depths between $40-110$ m in the west-central interior basin and in the southeast basin of the Black Sea from March to November-

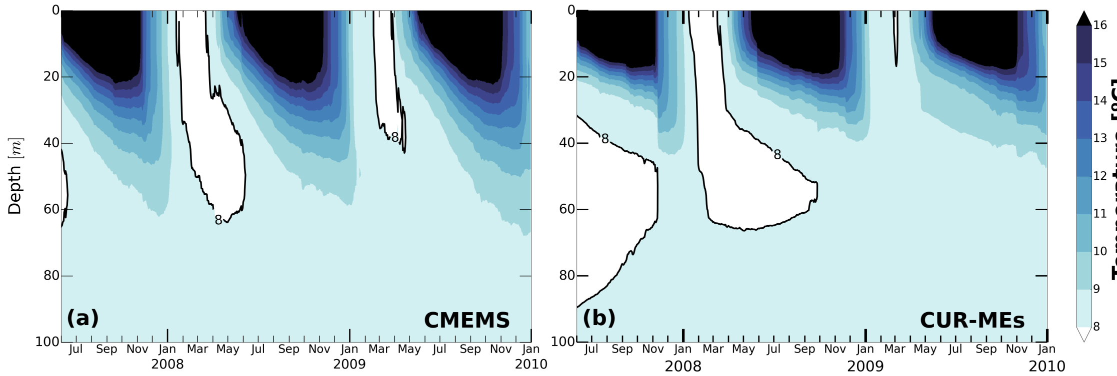

Fig. 4.15: Time versus depth plot of monthly mean basin averaged temperature profiles [$°C$] of the upper 100 m of the Black Sea according to CMEMS reanalysis (a) and CUR-MEs (b) numerical simulations. The thick black lines identifies the CIL (water with temperature lower than $8°C$).

December 2007 is documented.

In 2008, both the CUR-MEs model and CMEMS reanalysis reproduce a quite important CIL replenishment event in January-March, with strong convection reaching depths of about 60 m. The observational study of Akpinar et al. (2017) reports a very similar CIL formation episode in winter 2008, which promoted the deepening of the mixed layer up to a depth of 80 m. In addition, Akpinar et al. (2017) data shows that a CIL with depths between $40 - 60$ m is maintained in the west-central interior basin and in the southeast basin of the Black Sea until October-December 2008. Similarly, the CUR-MEs model shows a well defined CIL with depth between $40-60$ m until October-November 2008. To the contrary, 2008 basin averaged temperature profiles of CMEMS reanalysis do not show any CIL after July.

In 2009, both the CUR-MEs model and CMEMS reanalysis describe a short replenishment event in March, with a weak winter convective cooling which is not able to maintain the CIL structure for the rest of the year. In Akpinar et al. (2017) there are no data for 2009. However, Sukhikh and Dorofeyev (2016) results obtained with the Russian MHI 2000-2012 Black Sea physical reanalysis show a similar CIL dynamic for 2009, with weak CIL formation in March and no CIL for the rest of the

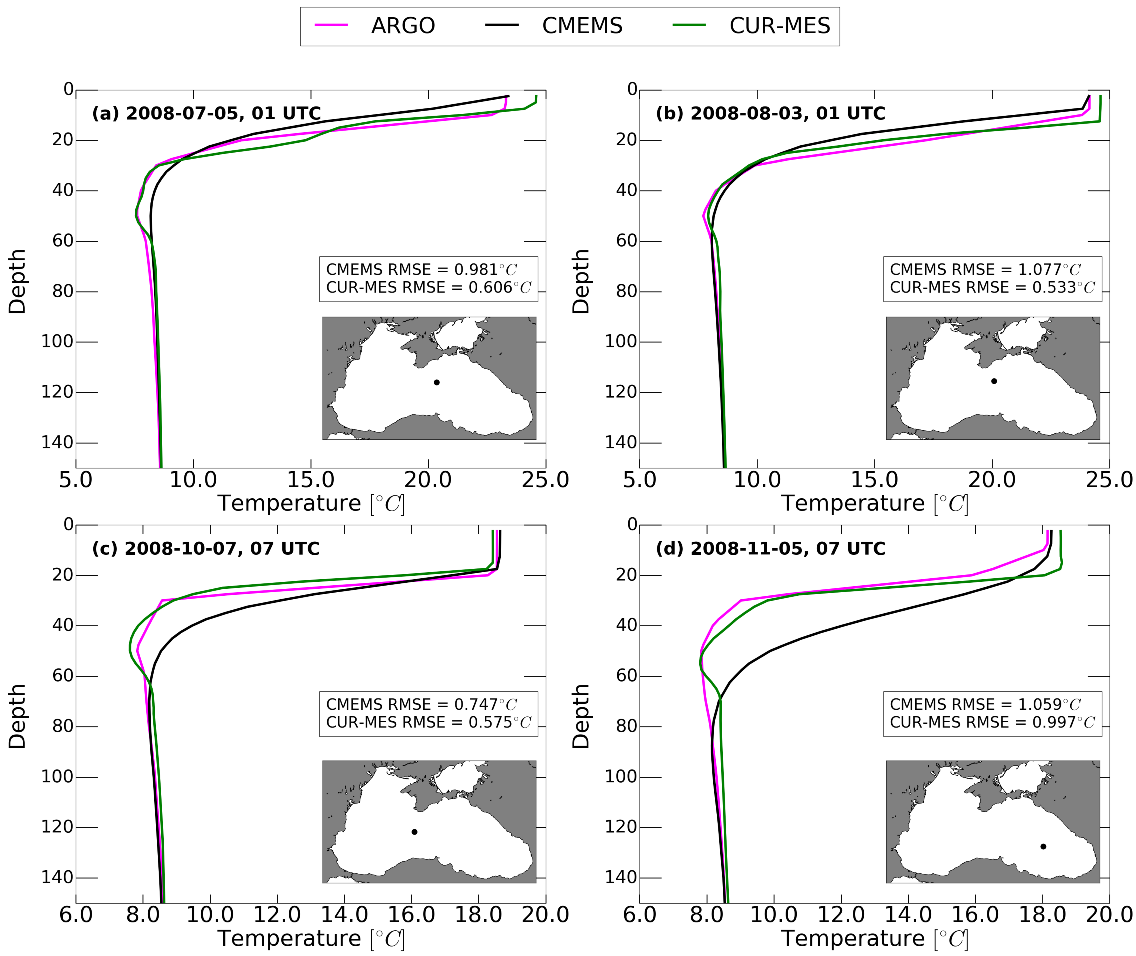

Fig. 4.16: Comparison between T profiles measured by Argo profilers (in magenta) in summer (4.16a and 4.16b) and autumn (4.16c and 4.16d) and T profiles simulated by CMEMS (black) and CUR-MEs (green) models for the same day. The day and hour of the measurement is indicated in the upper-left corner of each sub-panel while the location of the observation is shown in the inset map. RMSE of CMEMS and CUR-MEs models with respect to measurements are also given.

year. Similar results were also obtained by Piotukh et al. (2011), where the authors analysed the 1982-2008 CIL heat content by using CTD observations carried out in the NE part of the Black Sea. The CUR-MEs model reproduce a shorter and weaker CIL formation event in comparison to the other two reanalysis models, probably due to inaccuracies in the heat fluxes of the atmospheric forcing.

Results presented in Fig.4.10, Fig.4.14 and Fig. 4.15 and the comparison with data from existing literature seem to suggest that CMEMS reanalysis might be affected by a too high diapycnal mixing in the active sub-surface layer of the Black Sea. In fact, this could explain the disappearing of the CIL signal from basin averaged temperature profiles after July in 2007 and 2008 and the formation of a sub-surface water mass ($40-60$ m deep) with basin-averaged temperatures between ($9-10°C$) in autumn of all the three years.

In Figure 4.16 we present examples of T profiles measured by Argo profilers in summer (4.16a and 4.16b) and autumn (4.16c and 4.16d) 2008 compared with T profiles simulated by CMEMS and CUR-MEs models for the same day. They clearly confirm the tendency of CMEMS Black Reanalysis to over-mix waters between 30 and 100 m, causing a premature summer disappearing of the CIL and the formation of a too warm ($\approx 1-2°C$) sub-surface active layer.

On the other hand, Figure 4.16 further demonstrates the good agreement of CUR-MEs model results with observational data, indicating that our multi-scale model, without any data assimilation, is able to correctly reproduce the formation and spreading of the CIL, with limited undesired diapycnal mixing between the surface layer and the CIL.

4.4 Conclusion

In this study, we have developed four ocean models for the Black Sea which use the same codebase (NEMO v3.6-stable) and the same initial conditions and external forcing. The only difference is in the discretization schemes, both in the vertical and horizontal directions. One of the models uses the standard z-partial steps in the vertical and lat/long discretization in the horizontal. The other three models use bespoke schemes with curved grid cells and are designed to better capture important physical processes specific to the Black Sea: instability of the Rim Current, meso- and sub-mesoscale eddies, steep continental slope outside the shelf break and CIL variability. Some of such features are also present in other regional seas of the World Ocean.

Inter-comparison of the models shows that the CUR-MEs model, which has grid cells optimised for the main physical processes in all the three directions, produces the best results. Further comparison of the CUR-MEs model with CMEMS reanalysis shows that the CUR-MEs model in free-run and without relaxation to climatology produces similar and sometimes even better simulation of observed data than the highly assimilative CMEMS reanalysis which currently is considered as a reference for the state of the Black Sea.

Data assimilation is a computationally expensive process and requires supply of data which are more sparse in the Black Sea than in some other well monitored areas of the ocean. Highly accurate results obtained with CUR-MEs suggest that a future use of this model in operational forecasting systems would require less intensive data assimilation and be computationally more efficient.

The use of CUR-MEs even without data assimilation reveals the details of the inter- and intra- annual variability of the mean kinetic energy. It captures the effect of the warming and weakening of the Cold Intermediate Layer, which was indicated in some recent observations and allows to study this process with high granularity.

4.5 Appendix 4A: NEMO setup

The Black Sea models implemented in this study use the NEMO version 3.6 code (see Madec (2008) and Sec. 2.5). The EOS-80 (UNESCO, 1983) formulation for the equation of state $\rho(\theta, S, p)$ is used while the lateral Laplacian viscosity coefficient A_h is set equal to $1.2 \cdot 10^2$ $[m^2 s^{-1}]$ and the bi-laplacian viscosity coefficient B_h equal to $-4 \cdot 10^7$ $[m^4 s^{-1}]$. A Smagorinsky (Smagorinsky, 1993) lateral diffusivity coefficient $1 \leq K_h \leq 10$ $[m^2 s^{-1}]$ tuned following Shapiro et al. (2013) is used to simulate tracers diffusion.

The vertical viscosity A_v and diffusivity K_v coefficients are computed using the Generic Length Scale (GLS) turbulent closure scheme (Umlauf and Burchard, 2003). After tuning experiments, the set-up of the GLS scheme is the following: $k - \epsilon$ turbulent closure togheter with the Kantha and Clayson (1994) stability function and the Galperin limit equal to 0.267.

Our Black Sea models have closed lateral boundaries with no-slip condition and parameterize Bosphorus exchanges as a two-layers river. In order to include the Bosphorus parameterization, the NEMO code has been modified accordingly and two new subroutines named `sbc_str`, `sbc_str_div` have been introduced in the `sbcrnf` module.

The surface kinematic boundary condition for the Black sea is:

$$w\Big|_{z=\eta} - \partial_t \eta - \mathbf{u}_h\Big|_{z=\eta} \cdot \nabla\eta = E - P - R/A + Q_B + \epsilon_w, \tag{4.6}$$

where η is is the deviation of the sea surface from its unperturbed position and $E - P - R/A + Q_B$ represents the freshwater budget defined in terms of water fluxes due to evaporation (E), precipitation (P), river discharge per river mouth's area (R/A) and Bosphorus barotropic transport $Q_B = Q_B^u - Q_B^l$, where Q_B^u and Q_B^l are the upper and lower layer Bosphorus fluxes, respectively. In Equation 4.6 ϵ_w

represents a correction factor applied to close the freshwater budget. It is computed every time step as

$$\epsilon_w = \frac{1}{A^*} \int_{A^*} (E - P - R/A + Q_B)\, dA^*, \tag{4.7}$$

with A^* the model domain area, and added to the atmospheric $E - P$ flux equally at each node of the mesh.

The prognostic equation for non-linear free surface of the Black Sea models reads:

$$\partial_t \eta + \nabla \cdot \int_{-H}^{\eta} \mathbf{u}_h \, dz = -\left(E - P - R/A + Q_B + \epsilon_w\right), \tag{4.8}$$

The surface dynamic boundary condition for the freshwater is modified as follows:

$$F^S \equiv A_v^m \partial_z S\Big|_{z=\eta} = S\Big|_{z=\eta} (E - P - R/A + \epsilon_w) + S_B^l Q_B^l, \tag{4.9}$$

where S_B is the salinity of lower layer Bosphorus flux. The penetration in the water column of the short wave radiation Q_{sr} (L^θ term in Equation 2.8) is parameterized as follows:

$$I(z) = Q_{sr} \left[R\, e^{-z/\xi_0} + \frac{(1-R)}{3} \left(e^{-z/rr} + e^{-z/gg} + e^{-z/bb} \right) \right], \tag{4.10}$$

$$L^\theta \equiv (\rho C_p)^{-1} \, \partial_z I, \tag{4.11}$$

where $I(z)$ is the downward irradiance, R is a constant defining the fraction of non-penetrating light with ξ_0 specifying the very near surface depth of extinction and bb, gg and rr are chlorophyll dependent attenuation coefficients for wavebands blue ($400 - 500\ nm$), green ($500 - 600\ nm$) and red ($600 - 700\ nm$). For the dynamic bottom boundary condition we adopt a log-layer enhanced quadratic bottom friction parametrisation with minimum and maximum bottom drag coefficient values equal to $2.5 \cdot 10^{-3}$ and 10^{-1}, respectively.

All the models use baroclinic and barotropic time-steps equal to 200.0 and 6.1 s, respectively. In models using the z with partial steps vertical discretization scheme, the partial steps parameters are tuned as follows: $e_{3,zps}^{min} = 20.0\ m$, $e_{3,zps}^{ratio} = 0.1$, $ppkth = 40.363$ and $ppacr = 9.0$.

5. A numerical investigation of vertical mixing effects in the Dead Sea and potential impact on the evaporation rate

5.1 Introduction

For decades before the 1950s, the Dead Sea water level underwent natural fluctuations from about 380 m to 430 m below mean sea level (bmsl). These fluctuations were associated with inter-annual variability of precipitation and evaporation in the Levant region (Kushnir and Stein, 2010). Until 1978 the Dead Sea consisted of two basins: a large and deep northern basin and a smaller and shallower southern basin (Neev and Emery, 1967) which were interconnected by the Lynch Straits. In 1978 the Dead Sea level dropped to 400 m bmsl, approximately the same level as the sill in the Lynch Straits, while in 2015 it was 430 m bmsl (Lensky and Dente, 2017), a further drop of 30 m over 37 years.

Following the recession of the water level, the entire southern basin would have dried up. However, dikes were erected to transform the southern basin into evaporation ponds for production of minerals (Anati, 1997). The rate of recession has been increasing over this period (Lensky and Dente, 2017). The two basins lost their natural communication and the only exchange of water is now via pumping stations and release of brine leftover waters from the evaporation ponds located in the southern basin.

Since early 1960's, the anthropogenic reduction in the Dead Sea runoff outweighed its natural variability because Israel, Jordan and Syria increased the water consumption intensively. Production of minerals in the evaporation ponds also contributes to water deficit. The water level in the Dead Sea is currently decreasing at an unprecedented rate of approximately 1.1 $m\ year^{-1}$ (Lensky and Dente, 2017). The drop of the water level brought dramatic degradation to the coastal regions including intensive development of sinkholes (Frumkin et al., 2011).

Before 1978, the Dead Sea had stable saline stratification supported by runoff. Winter mixing was limited to about 20 m, and there was no evidence of step-like structures also known as thermohaline staircases. Such structures have been observed in many areas of the world ocean (Fedorov, 1970; Garrett, 1979; Zodiatis and Gasparini, 1996). They are the most dramatic manifestation of double-diffusion convection in the ocean, where vertical profiles of temperature and salinity are characterised by well-mixed layers separated by high-gradient interfaces (Radko, 2003). Observational studies indicated that the vertical mixing within the well-mixed layers of step-like structures is increased by as much as an order of magnitude relative to analogous smooth-gradient regions (Schmitt, 2005).

Due to runoff reduction, the surface salinity of the Dead Sea increased and the gravitational stability diminished. In winter of 1978-1979, the Dead Sea water column overturned, ending the natural long-term stable regime (Steinhorn and Gat, 1983). Following the changeover of the Dead Sea, haline stability is negative usually during summer and salt fingering develops below the pycnocline (Anati and Stiller, 1991). After 2000, when vertical profiles started to be observed by equipment with high vertical resolution, staircases formed by salt fingering have been observed regularly during summer (Gertman et al., 2015; Arnon et al., 2016).

Despite the increasing role of anthropogenic pressures, the evaporation−precipitation balance is still a significant factor which contributes to the recess of the water level. A recent research by Radko et al. (2014) carried out in the Atlantic indicated that the vertical flux of temperature and salinity, their surface values, and hence the rate of evaporation could depend on the structure of the underlying water column. It was found that step-like structures modulate vertical fluxes to sea surface.

Double-diffusion processes arise from the different magnitude of the molecular diffusivities of temperature and salt and are a quite common process in the ocean (Stern, 1960; Radko, 2013). In order to explicitely resolve for oceanic salt fingering, a non-hydrostatic ocean model operating on spatial scales of centimeters would be needed (Kantha and Clayson, 2000a; Radko, 2013). However, in this study we are not interested in simulating the formation of thermohaline staircases (i.e. computing or parameterizing double-diffusion convective transport). The aim of this chapter is to investigate the effect of different vertical mixing regimes on the water column of the Dead Sea and their potential impact on the evaporation rate of this inland sea. The methodology is based on simulating the evolution of a Dead Sea water column presenting thermohaline staircases with two contrasting numerical models. One uses a standard vertical mixing scheme which has been succesfully applied to simulate a wide range of oceanic conditions but does not take into account the presence of thermohaline staircases. The second uses a vertical mixing parameterization developed in this study which aims to mimic the diapycnal mixing regime of a water column presenting step-like structures in temperature and salinity, i.e. convecting layers with high vertical mixing separated by a high-gradient interfaces.

The outcome of the study would assess the importance of including the development and dynamics of thermohaline staircases into predictive models of the Dead Sea, despite the increased computational cost.

5.2 The Dead Sea numerical models

In this study, we use the NEMO ocean model v3.6-stable (Madec (2008)) with the new Multi-Enveloped s-coordinate system (Bruciaferri et al. (2018), see also Chapter

3) to study the impact of different vertical mixing parameterizations on the Dead Sea dynamics and its evaporation rate.

Two numerical models of the Dead Sea hydrodynamics are implemented. They differ only in the type of the diapycnal mixing formulation: one model, named SPP, uses the standard NEMO 3.6 Pacanowsky-Philander vertical mixing parameterization (Pacanowski and Philander (1981), hereafter $PP81$) while the second, named MPP, uses a modified version of $PP81$ specifically adapted to the Dead Sea conditions.

A description of the governing equations solved by NEMO model and the parameters and numerical techniques adopted in this study are detailed in Sec. 2.5 and Appendix 5.6.

5.2.1 Models set-up

The domain of the numerical models covers the northern deeper basin of the Dead Sea, extending from 35.388°E to 35.591°E in the zonal direction and from 31.302°N to 31.776°N in the meridional one (Figure 5.1). Since we are interested in the effect of different vertical mixing regimes in the deeper part of the northern basin, the models have closed lateral boundaries and water exchanges on the coast, including rivers and evaporation ponds in- and out-flows, are not considered.

Model bathymetry is obtained by using the high resolution IOLR Dead Sea digital topography dataset (Hall, 1997), which is defined on a regular grid with zonal and meridional resolution of 50 m (Figure 5.1). The bathymetry of our models is computed by averaging all depth measurements within a particular wet cell of models horizontal grid (Sikirić et al., 2009). The shoreline is identified by using the sea level value of 430 m below Mean Sea Level (MSL) observed on 31-07-2016 (measurements by Israel Hydrological Service). The minimum depth of model bathymetry is 15 m while the maximum is 298 m.

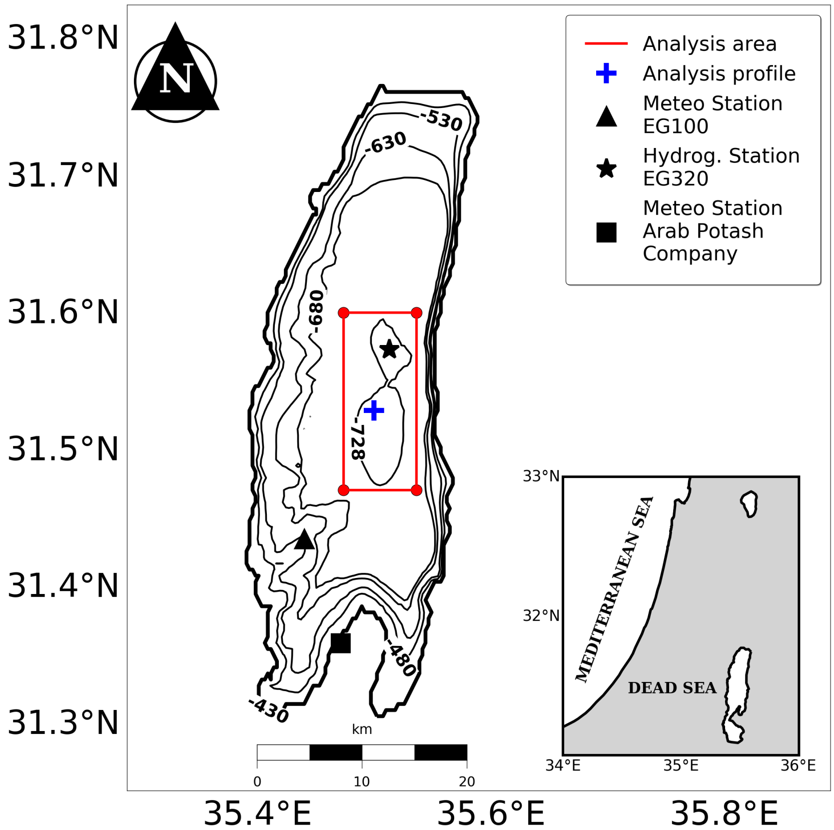

Fig. 5.1: Dead Sea topography according to the very high resoution IOLR digital topography dataset (resolution equal to 50 m). The rectangle in red identifies the area considered for the analysis. In the inset, the location of the Dead Sea with respect to the Mediterranean Sea is shown.

The models use a regular geographical horizontal grid with 79×107 grid points in the zonal and meridional directions, respectively, corresponding to a costant horizontal resolution of 500 m (meridional) and 250 m (zonal). In the vertical direction, the model domain is discretized with 99 computational levels and the Multi-Enveloped s-coordinate system is configured with three envelopes (see Figure 5.2).

The upper envelope H_e^1 follows an 'enveloping'-bathymetry surface over the continental slope and shelf while in deep water areas it follows the geopotential surface located at 180 m depth. The 'enveloping'-bathymetry surface is obtained by smoothing the upper 180 m of the actual bathymetry with the Martinho and Batteen (2006) algorithm, reducing the maximum slope parameter (Mellor et al., 1998) from a value of 0.7 to a value of 0.08.

Following the method of introducing a 'false bottom' to reduce unnecessary undulations of computational levels (Enriquez et al., 2005; Shapiro et al., 2013), the second and third envelopes H_e^2 and H_e^3 are geopotential surfaces with depths equal to 298 m (the maximum depth of the basin) and 408 m, respectively. The third envelope H_e^3 can be regarded as a 'ghost' envelope, since it is not used to 'shape' any computational level but it is only used to define the coefficients of cubic splines of sub-zone D_2.

Radko et al. (2014) suggests to use a vertical resolution of ≈ 1 m to account for step-like structures when performing large-scale simulations. Our models use 78 computational levels in sub-zone D_1 and 21 in sub-zone D_2, with a vertical resolution varying from 1 m in the top 50 m of the water column to 5 m in the deeper part of the model domain, in order to properly resolve the thermohaline staircases observed in the summer-stratified upper part of the Dead Sea water column.

Salinity in the Dead Sea (about 340 $g\ l^{-1}$) is much higher than in the open ocean so that the usual equations of state (e.g. TEOS-2010) can not be used. Therefore, in this study we use the linear equation of state with thermal expansion and haline contraction coefficients adjusted for the Dead Sea (Gertman et al., 2010).

The SPP model computes vertical diffusivities and viscosities according to the standard NEMO 3.6 $PP81$ formulation:

$$\begin{cases} A_v = \dfrac{A_v^0}{(1 + a\,Ri)^n} + A_v^b & \text{(5.1a)} \\ K_v = \dfrac{A_v^0}{(1 + a\,Ri)^{n+1}} + K_v^b & \text{(5.1b)} \end{cases}$$

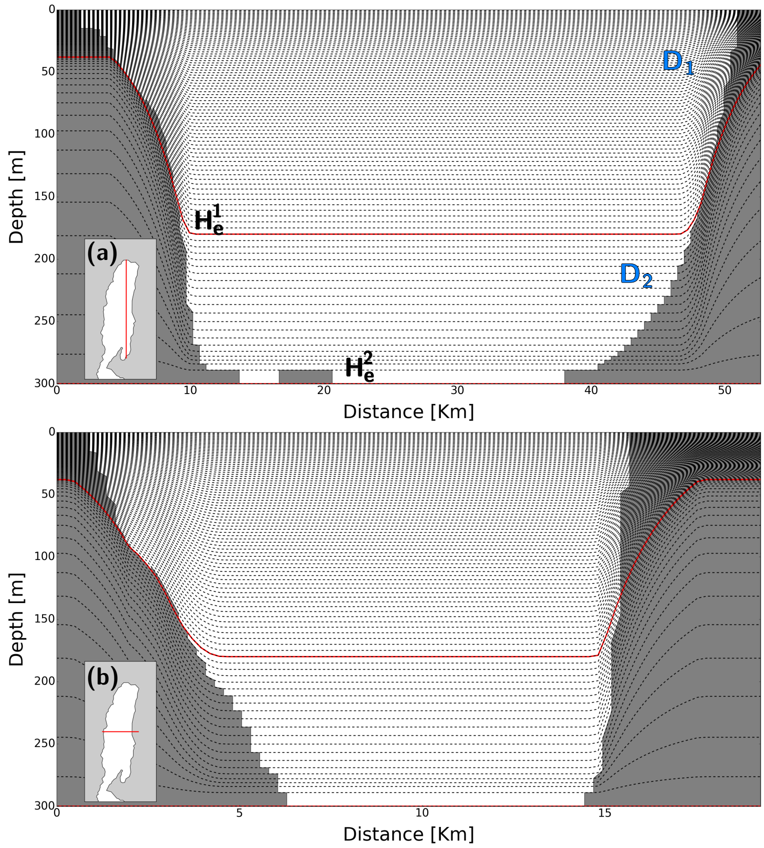

Fig. 5.2: Meridional (a) and zonal (b) vertical cross sections of the model vertical grid. Red lines identify the upper H_e^1 and the second H_e^2 envelopes while dashed black lines represent computational levels.

where A_v is the vertical viscosity, K_v is the vertical diffusivity, $Ri = N^2(\partial_z U_h)^{-2}$ is the local Richardson number function of the local Brunt-Väisälä frequency N and the horizontal velocity U_h, a and n are two tunable parameters, A_v^0 is the shear eddy viscosity at $Ri = 0$ and A_v^b and K_v^b represent the background vertical viscosity and diffusivity, respectively. The $PP81$ formulation has been succesfully applied to simulate a wide range of oceanic conditions (e.g. Smith and Hess (1993); Lermusiaux (2001); Timmermann and Beckmann (2004); Trotta et al. (2016)).

The MPP model uses a modified version of the $PP81$ formulation for the diapycnal diffusivity. It is designed to reflect the property of thermohaline staircases, namely

	A_v^b $[m^2\ s^{-1}]$	K_v^b $[m^2\ s^{-1}]$	A_V^0 $[m^2\ s^{-1}]$	a	n	N_{crit} $[s^{-1}]$	K_{crit} $[m^2\ s^{-1}]$	d_{max} $[m]$
SPP	$7.5 \cdot 10^{-5}$	$5.0 \cdot 10^{-6}$	$1.0 \cdot 10^{-3}$	5	2	–	–	–
MPP	$7.5 \cdot 10^{-6}$	$5.0 \cdot 10^{-7}$	$1.0 \cdot 10^{-3}$	5	2	$7.5 \cdot 10^{-5}$	$1.0 \cdot 10^{-3}$	50

Table 5.1: Values of the parameters used in the SPP and MPP vertical mixing parameteizations.

that the mixing across the sharp interface is much lower than inside the mixed portion of the 'step' (Radko et al., 2014). The scheme introduces a 'critical' Brunt-Väisälä frequency N_{crit} for depths shallower then d_{max}: if the local buoyancy frequency N is less than or equal to N_{crit}, then the model uses a prescribed maximum value of vertical diffusivity K_{crit} while if not it uses the original $PP81$ scheme. The MMP vertical mixing parameterization is introduced in the NEMO code by modifying the `zdf_ric` subroutine of `zdfric` module. Table 5.1 summarises the value of the coefficients used in the SPP and MPP vertical mixing schemes.

Both models use a standard NEMO approach where the water column is hydrostatically unstable, increasing the coefficients A_v and K_v to a value of 7.5×10^{-3} $m^2\ s^{-1}$. The vertical mixing within the surface Ekman layer is computed using the Lermusiaux (2001) parameterization: the Ekman depth $h_E(x, y, t)$ is estimated by the equation

$$h_E = E_k u^* f_0^{-1} \tag{5.2}$$

where u^* is the friction velocity computed as function of the wind stress vector $\vec{\tau}$ and the reference density ρ_0, f_0 is the Coriolis parameter and h_E is capped between 1 m and 20 m. The coefficient E_k is set equal to 0.7, the viscosity (A_v) and diffusivity (K_v) coefficients are set to 5.0×10^{-3} and 1.0×10^{-3}, respectively. Surface boundary conditions are computed using the CORE bulk formulation (Large and Yeager, 2004).

5.2.2 Atmospheric forcing

The models are forced by using meteorological data measured during 2016 and provided by the Marine Science Station of the University of Jordan in Aqaba (MSS) and the Israeli Oceanographic and Limnology Research Centre in Haifa (IOLR).

Meteorological parameters available from IOLR were measured at the anchored meteo-oceanographic buoy EG100, operational since June 1992 (see triangle marker in Fig. 5.1) while data provided by MSS were measured by the Arab Potash Company at the meteorological station shown in Fig. 5.1 (square marker).

The meteorological dataset used to force the models include total incoming radiation (short wave + long wave downward radiation, $W\ m^{-2}$) and total precipitations (mm/day) from IOLR and air temperature (°C) and humidity (%) at 2 m and wind direction (°) and speed ($m\ s^{-1}$) at 10 m from MSS (Fig. 5.3). The time interval between observations is 1 day for the total incoming radiation while it is 30 min for all the other variables. Total precipitations were equal to zero mm/day during the entire simulated period. The models are forced with daily data for the total incoming radiation and six-hourly data for all the other variables. The diurnal cycle of the incoming radiation flux is reconstracted using Bernie et al. (2007) algorithm as implemented in NEMO.

Due to a very low spatial resolution of available atmospheric data, the two-dimensional atmospheric forcing fields needed for the modelling were obtained by assuming uniform atmospheric conditions over the whole Dead Sea. This is achieved by horizontally spreading the time-series measured at the EG100 and Arab Potash Company meteo stations over the whole computational domain.

The values of the meteorological variables used to force the Dead Sea models are consistent with recent observational studies, e.g. Kishcha et al. (2017); Lensky et al. (2018); Metzger et al. (2018). Air temperature data (Fig. 3(a)) show a well defined and quite regular diurnal cycle, with peaks at noon and an average diurnal excursion

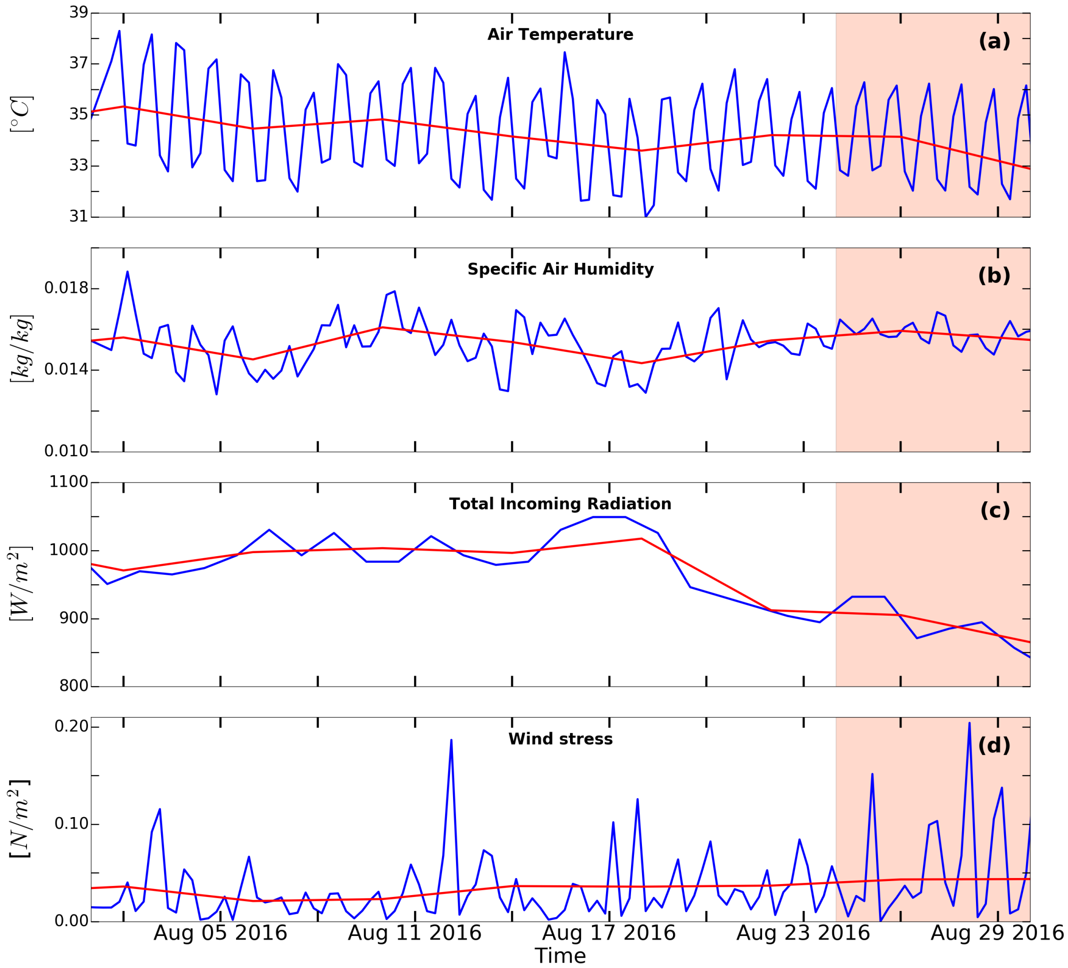

Fig. 5.3: Meteorological parameters: (a) Six-hourly (blue) and 4-days averaged (red) timeseries of air temperature at 2m; (b) Six-hourly (blue) and 4-days averaged (red) timeseries of specific air humidity at 2m; (c) Daily (blue) and 4-days averaged (red) timeseries of total incoming radiation (short + long wave radiation); (d) Six-hourly (blue) and 4-days averaged (red) timeseries of wind stress computed using wind velocity at 10 m. The rectangle in light-red shows the period considered for the analysis. After Shapiro et al. (2019).

of $\approx 4 - 5°C$. The daily total incoming radiative flux is almost constant (≈ 1000 $W\ m^{-2}$) during the first 20 days while in the last 10 days it decreases to values around 850 $W\ m^{-2}$.

Similarly, the wind stress is almost constant during the first two weeks, fluctuating around a mean value of ≈ 0.035 $N\ m^{-2}$ and presenting only two episodes with magnitude > 0.1 $N\ m^{-2}$. To the contrary, in the last two weeks the wind stress shows more variability and higher values, with the 4-days averaged signal increasing up to 0.05 $N\ m^{-2}$ in the end of the month and showing 7 episodes of wind stress with magnitude > 0.1 $N\ m^{-2}$.

5.2.3 Initial Condition

The aim of this study is to investigate the effect of different vertical mixing regimes on the evolution of a Dead Sea water column initially presenting thermohaline staircases and whether they have an impact on the evaporation rate of the Dead Sea. Since the purpose of this research is the proof of concept, we use temperature and salinity initial conditions which clearly show the step-like structure.

Hydrological measurements for the same period as the meteorological forcing were not available. Therefore, the initial conditions for the numerical experiments are obtained by using potential temperature and density profiles measured by IOLR on 27-08-2012 at EG320 hydrographic station (Fig. 5.4) and assuming that the hydrological condition during summer 2012 were similar to the ones of summer 2016.

Due to its extremely high salinity and unique ionic composition, common methods to measure water salinity can not be used in the Dead Sea (e.g., Gertman et al. (2010) and Sec. 2.4). Therefore, in order to characterize the Dead Sea salinity structure and variability a water density anomaly from 1000 $kg\ m^{-3}$ at specific reference temperature is used instead (Anati, 1997)). This quantity is termed 'quasi-salinity' (Gertman and Hecht, 2002) and is widely used in observational studies of the Dead

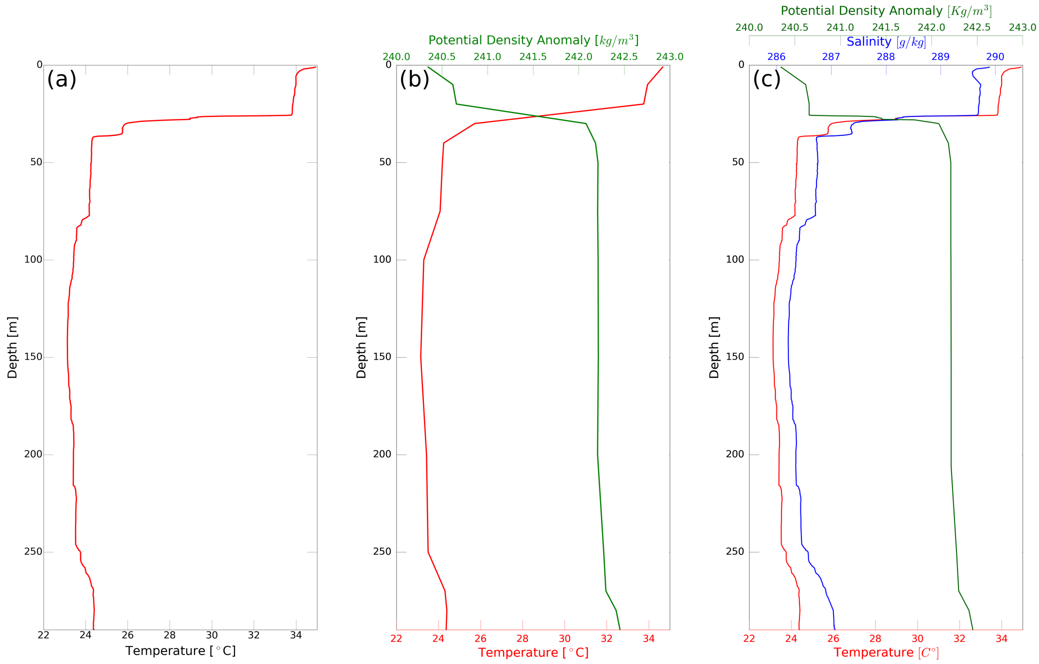

Fig. 5.4: (a) High Resolution potential temperature profile measured by IOLR on 27-08-2012 at EG320 hydrographic station with CTD; (b) Low resolution potential temperature and potential density anomaly profiles measured by IOLR on 27-08-2012 at EG320 hydrographic station with Niskin bottle; (c) High Resolution potential temperature, equivalent salinity and potential density anomaly profiles used as initial condition in the numerical experiments.

Sea (see e.g. Gertman et al. (2010)).

However the NEMO model is not able to work with 'quasi-salinity'. This issue is solved as follows. First, low-resolution measured potential density anomaly σ_θ is interpolated onto high-resolution depths levels. After, by reverse engineering the linear equation of state with thermal expansion and haline contraction coefficients given by Gertman et al. (2010), we calculated a quantity which we name 'equivalent salinity' S from measured potential density anomaly σ_θ and potential temperature θ profiles as

$$S = S_0 + \Big[\rho - \rho_0 - \alpha(\theta - \theta_0)\Big]\beta^{-1}, \tag{5.3}$$

where $\rho = 1000 + \sigma_\theta$ is the potential density, $\alpha = 0.450\ kg(m^3\ °C)^{-1}$, $\beta = 0.936\ kg^2(m^3\ g)^{-1}$, $\rho_0 = 1240.76\ kg\ m^{-3}$, $\theta_0 = 28°C$ and $S_0 = 287\ g\ kg^{-1}$.

This approach allowed us to reconstruct high-resolution 'equivalent' salinity S profiles from measured high-resolution temperature profiles and low-resolution potential density profiles (see Fig.5.4(c)) and to use the standard linear equation of state as implemented in NEMO.

Hydrological observations used for the initial conditions were carried out only at few points. Therefore, information regarding horizontal variations of water column properties are not available. However, we are interested in the the main (deep) area of the Dead Sea, focusing on the relevant vertical processes linked to the different vertical mixing parameterizations used in the two models. Therefore, horizontal variations in temperature and salinity are not considered in this study, ignoring a narrow strip of water alongshore where floods, springs, and end-brines may cause local changes.

For this reason, the temperature and salinity initial condition of the numerical experiments is obtained by horizontally spreading the high resolution temperature profile measured by IOLR on 27-08-2012 and the high-resolution 'equivalent' salinity S profile calculated for the same day.

Initial condition profiles (Fig.5.4(c)) show a number of steps in potential temperature, density and 'equivalent' salinity. There are 5 well pronounced steps in within the depth range 5 to 70 m and 5 weak steps in the near bottom layer. Some of the weaker steps are compensated in density, so there are only 3 steps in density.

5.3 Numerical experiments setup

Two different type of numerical experiments are carried out. First we assess the ability of the two vertical mixing parameterizations in (i) preserving the sharp pycnocline and the thermohaline staircases of the initial condition and (ii) reducing numerical errors arising from using curved computational levels. The 15 days long sensitivity experiment starts with zero velocity and no atmosphering forcing. In such conditions, current velocities should remain zero, and any emerging currents should be attributed to model errors.

In the second experiment, we exploit the fact that the MPP model is able to preserve the thermohaline staircases of the initial condition while the SPP is not to investigate the effect of the two different vertical mixing parameterizations on the Dead Sea water column and its evaporation rate. The Dead Sea hydrodynamics is simulated from 1 to 31 August 2016 with both models and using realistic atmospheric forcing (see Sec. 5.2.2). The initial 3D velocity field is obtained by spinning up the models for two months in diagnostic mode and cycling the atmospheric forcing of 1-08-2016. After two months, the basin averaged kinetic energy (hereafter KE) is perfectly stationary (see Fig. 5.5), indicating a full adjustment of the lake dynamics to the atmospheric forcing.

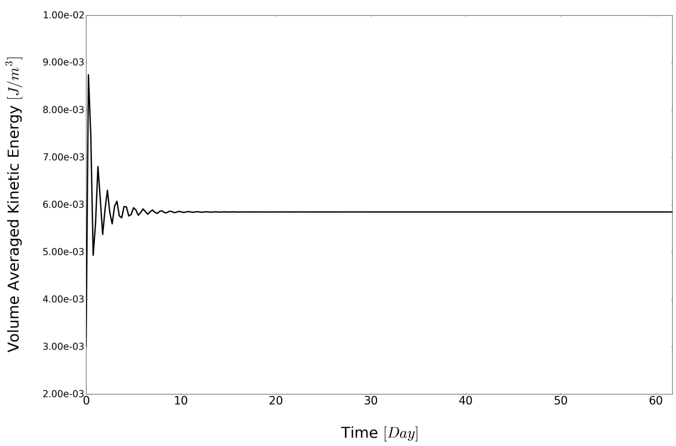

Fig. 5.5: Evolution of the basin averaged kinetic energy during the spin-up period of the second experiment.

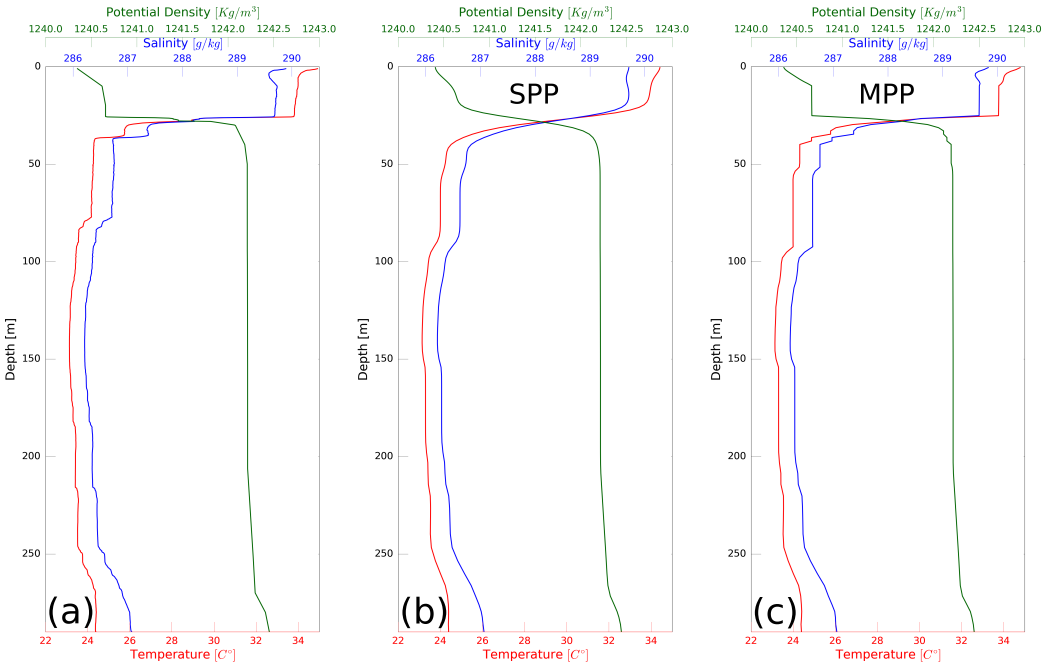

Fig. 5.6: Potential temperature (red), salinity (blue) and potential density (green) profiles extracted in the middle of the computational domain (blue cross marker in Fig.5.1) in the beginning of the simulation (a) and after 15 days for the SPP (b) and MPP models (c)

5.4 Results and Discussion

5.4.1 Sensitivity to vertical mixing formulations

In the first experiment, we investigate the properties of the two different vertical mixing parameterizations used in this study. Figure 5.6 presents a comparison between potential temperature, salinity and potential density profiles extracted in the middle of the computational domain (blue cross marker in Fig. 5.1) in the beginning of the simulation (Fig. 5.6(a)) and after 15 days for the SPP (Fig. 5.6(b)) and MPP models (Fig. 5.6(c)).

Numerical results show that the vertical mixing reproduced by the SPP parameter-

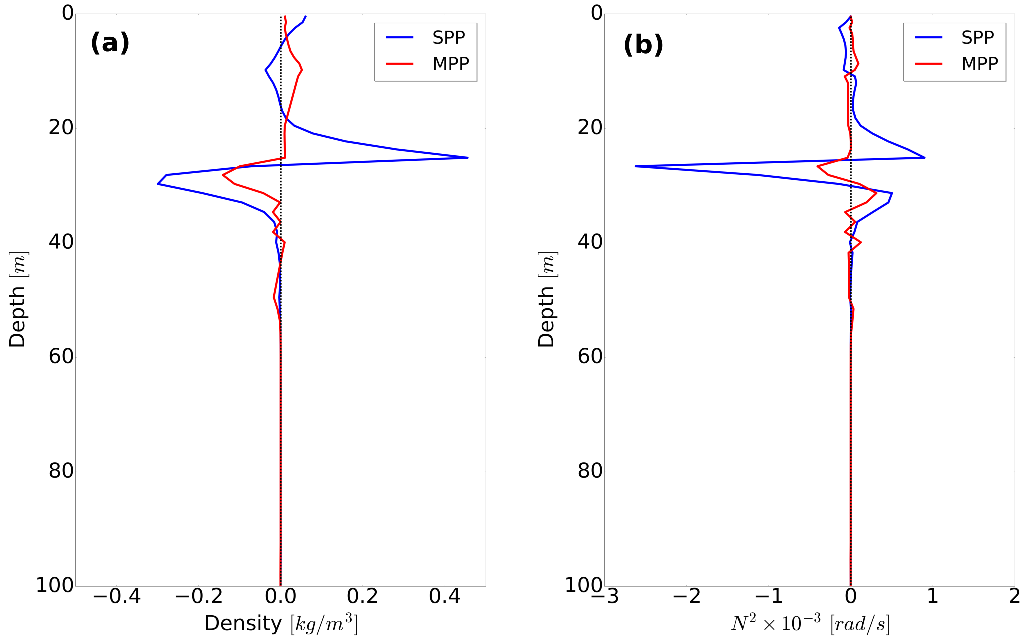

Fig. 5.7: Vertical profiles of anomalies with respect to the initial condition of (a) density and (b) buoyancy frequency square (N^2) simulated by the SPP (blue) and MPP (red) Dead Sea models.

ization tends to smooth quite importantly tracers vertical profiles, resulting in the complete disappearing of the step-like structure of the water column of the initial condition after 15 days of simulation. This is also confirmed by Fig. 5.7, where the vertical profiles of density and buoyancy freqency anomalies with respect to the initial condition simulated by the two models are shown. To the contrary, the MPP scheme seems to be able to preserve the thermohaline staircases of the initial stratification in the upper 50 m of the water column, although in a modified version. While in the upper 50 m the initial stratification shows 3 well-pronounced staircases in potential temperature and salinity and 2 in potential density, after 15 days the MPP model presents 5 thermohaline staircases which exist also in density.

Figure 5.8 presents the 15 days time series of zonal currents maximum values (Fig.5.8(a)) and basin averaged KE (Fig.5.8(b)) simulated by the SPP and MPP Dead Sea mod-

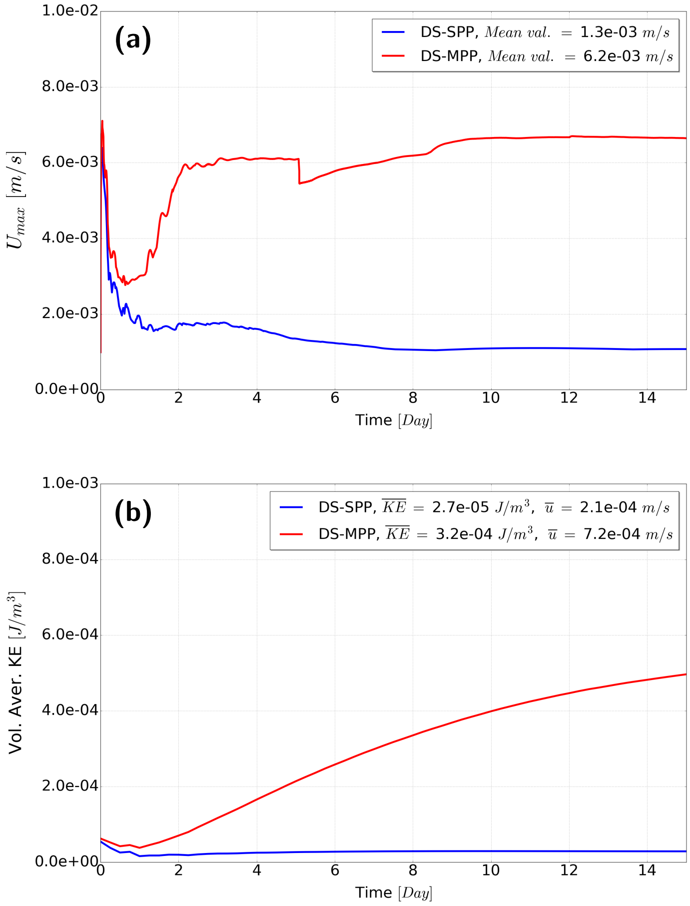

Fig. 5.8: Time series of (a) spurious currents maximum values and (b) basin averaged Kinetic Energy simulated by the SPP (blue) and MPP (red) models.

els. Numerical results show that after 15 days spurious currents develop in both models. The averaged over the length of the simulation zonal velocity maximum error is $1.3 \cdot 10^{-3}$ $m\ s^{-1}$ in the case of the SPP model, while it is $6.2 \cdot 10^{-3}$ $m\ s^{-1}$ for the MPP model. In addition, the time averaged KE of the SPP model is $2.7 \cdot 10^{-5}$ $J\ m^{-3}$, which corresponds to an average speed of $2.1 \cdot 10^{-4}$ $m\ s^{-1}$, while the MPP model presents a time averaged KE of $3.2 \cdot 10^{-4}$ $J\ m^{-3}$ with an average speed of $7.2 \cdot 10^{-4}$ $m\ s^{-1}$. Real currents in the Dead Sea present typical values of $\approx 5 - 10 \cdot 10^{-2}$ $m\ s^{-1}$ (Allan et al., 2011), demonstrating a good quality of both models.

The MPP (step-preserving) model presents larger values of spurious currents than the SPP model. Mellor et al. (1994) showed that in the case of a horizontally homogeneous density field, the local truncation error in the calculation of horizontal density gradients in $\sigma-$coordinates and with a second-order central differences scheme is given by

$$E\Big(\frac{\partial b^*}{\partial x^*}\Big) = \frac{H}{4}\frac{\Delta H}{\Delta x}\Big[(\Delta\sigma)^2 - \sigma^2\Big(\frac{\Delta H}{H}\Big)\Big] \cdot \Big[\Big(\frac{\partial^2 b}{\partial z^2}\Big) + \frac{\sigma H}{3}\Big(\frac{\partial^3 b}{\partial z^3}\Big) + ...\Big], \tag{5.4}$$

where (x^*, y^*, z) are Cartesian coordinates, (x, y, σ) are terrain-following coordinates with $\sigma = z/H$, $H(x, y)$ is the bottom depth, $b(z) = g\rho/\rho_0$ is the buoyancy, Δx and $\Delta\sigma$ are the horizontal and vertical grid spacing, respectively and ΔH is the grid-cell variation of H.

Equation 5.4 shows that the error depends on the resolution of vertical and horizontal grid and on the curvature and the higher-order vertical derivatives of the density profile. After 15 days, the SPP model presents a smooth density vertical profile which reduces the numerical errors in the computation of horizontal pressure gradients with respect to the MPP step-preserving model.

After two days of simulation, the basin averaged KE of the MPP model grows with time, while in the case of the SPP model it is almost constant (Fig. 5.8(b)). This difference can be explained comparing zonal cross sections of density and meridional velocity component simulated by the two models (Fig. 5.9). In the case of the SPP model, after 15 days spurious currents are small ($\approx \pm 0.001$ m s^{-1}, Fig. 5.9(c)) and a tiny compensating density change is created by the model (Fig. 5.9(a)), in accordance with Mellor et al. (1998). To the contrary, in the step-preserving model the MPP vertical mixing parameterization seems to induce greater density changes in costal shallow areas (Fig. 5.9(b)), causing the formation of larger physical currents (($\approx \pm 0.006$ m s^{-1}, Fig. 5.9(d)). This seems to indicate that in the case of the MPP model the increase with time of the basin averaged KE might be physically driven,

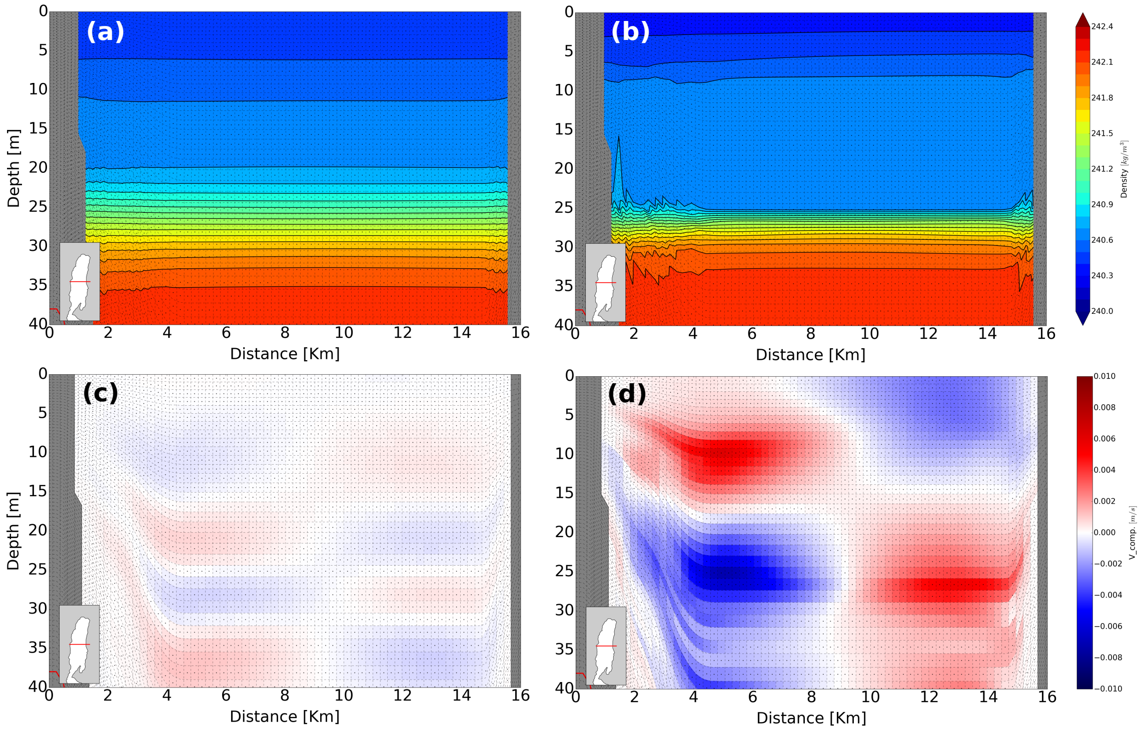

Fig. 5.9: Zonal cross sections of density (upper row) and meridional velocity component (lower row) simulated by the SPP (left column) and MPP (right column) models.

rather than linked to numerical horizontal pressure gradient errors.

Figures 5.9(b) and (d) shows that in the MPP model changes in density affect more the western part of the basin, resulting in stronger meridional currents along the west coasts. This might be due to the interaction betwen the relatively wider shelf of the western part of the basin (see Fig. 5.1 and Fig. 5.2) and the d_{max} parameter used in the MPP vertical mixing parameterizations.

5.4.2 The effect of vertical mixing on the Dead Sea water column dynamics

The first three weeks of August were characterised by a relatively weak wind and hence limited mixing in the upper layer (see Fig. 5.3). Therefore, the analysis of numerical results of the second experiment considers the last week of August (light-red rectangle in Fig. 5.3), when a typical wind stress was $\approx 0.1\ N\ m^{-2}$ (Fig. 3(d)) and the total incoming radiative flux was $\approx 875\ W\ m^{-2}$ (Fig. 3(b)), sufficient conditions for good mixing above the pycnocline. In addition, since we are interested in the vertical processes occurring in the bulk part of the Dead Sea, the analysis of numerical results is carried out in the area identified by the green rectangle in Fig. 5.1.

Upper panels of Fig. 5.10 present the evolution of the temperature vertical profile extracted in the middle of the analysis area of the SPP (Fig. 5.10(a)) and the MPP (Fig. 5.10(b)) models. In addition, the time series of the temperature at 10 m and 40 m depths averaged over the analysis area for both models are showed in Fig. 5.10(c) and 5.10(d), respectively.

Both models simulate a stable thermocline located around 25 m depth, in agreement with previous observational study (e.g. Gertman and Hecht (2002)). However, the MPP model is able to represent a stronger thermocline, with mean values around $-2\ °C\ m^{-1}$ and peaks up to $-2.6\ °C\ m^{-1}$, in good agreement with the values observed in July 2012 by Arnon et al. (2014) (i.e., mean value $\approx -1.8\ °C\ m^{-1}$ and peaks up to $-2.5\ °C\ m^{-1}$). In the case of the SPP model, the simulated thermocline is weaker and more diffused, with a mean value of $\approx -1.5\ °C\ m^{-1}$ and peaks up to $-2\ °C\ m^{-1}$.

Both models simulate an average water temperature around 35 °C at 10 m depth and around 24.5 °C at 40 m, in agreement with measurments by Arnon et al. (2014, 2016); Lensky et al. (2018). The MPP (step-preserving) model seems to simulate a warmer upper part of the water column with respect to the SPP model, with a mean difference of ≈ 0.3 °C at 10 m depth.

Figure 5.11 presents maps of currents velocity at the surface and 30 m depth simulated by both models on the 29-08-2016 at 15:00. In both cases currents are within the range 2-5 $\cdot 10^{-2}\ m\ s^{-1}$, in agreement with measurments carried out by Allan

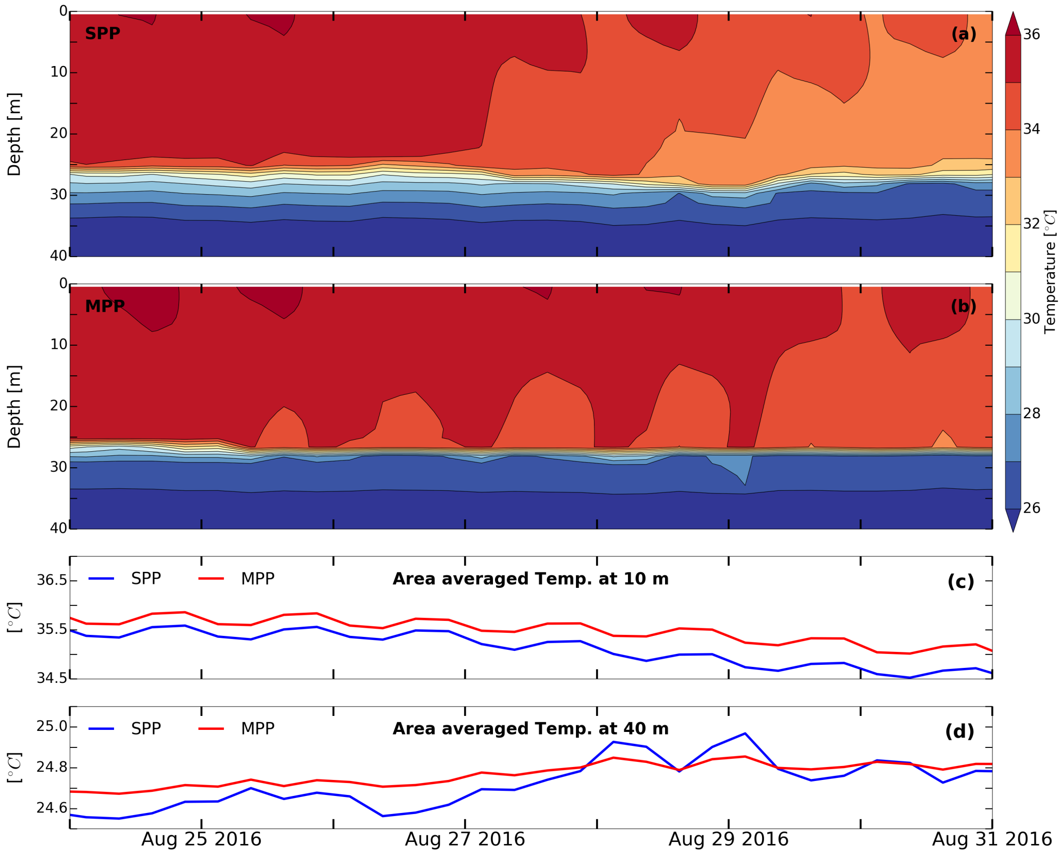

Fig. 5.10: Evolution of the temperature vertical profile extracted in the middle of the analysis area (see blue cross marker in Fig. 5.1) for (a) the SPP model and (b) the MPP model. Time series of the area-averaged temperature over the analysis area (see green rectangle in Fig. 5.1) (c) at 10 m and (d) at 40 m

et al. (2011) in August 2010. Both models simulate a similar two-layer circulation structure, with surface currents directed mainly southward and currents directed in the opposite direction at 30 m (below the pycnocline). This is confirmed by Fig. 5.12, where zonal cross sections of meridional currents velocity simulated by both models on the 29-08-2016 at 15:00 are presented. These results are in good agreement with Allan et al. (2011) measurements, which found a typical summer two-layer circulation with stronger currents in the upper mixed layer and weaker currents below the pycnocline. We conclude that both models reasonably simulate the main characteristics of the Dead Sea hydrodynamics.

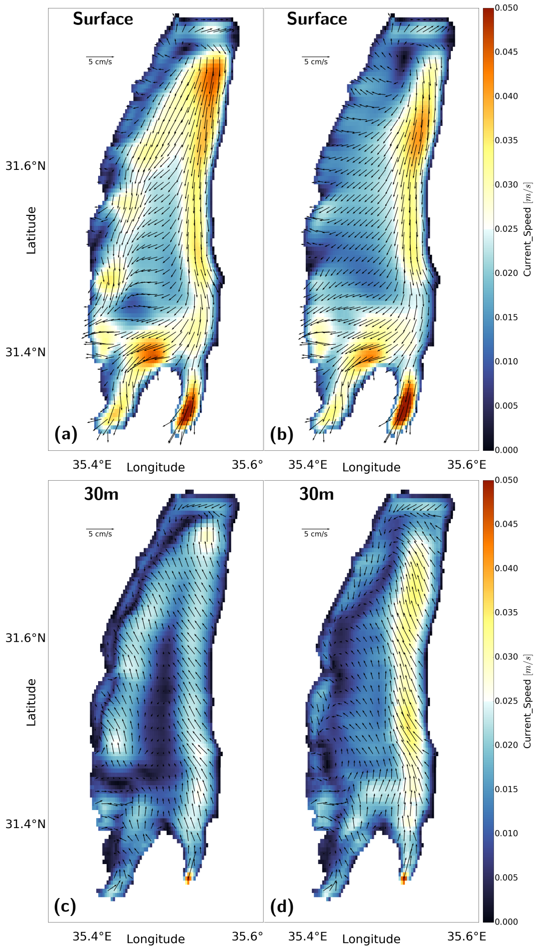

Fig. 5.11: Maps of 6-hourly current velocity simulated by (a) the SPP and (b) the MPP models at the surface and by (c) the SPP and (d) the MPP models at 30 m depth on the 29-08-2016 at 15:00.

In comparison with the SPP model, the MPP simulation shows weaker southward currents along the west coast of the Dead Sea at the surface and northward currents at 30 m which are weaker along the west coast but stronger on the esatern side of the basin. This seems to confirm that the different vertical mixing parameterizations affected the western and eastern sides of the lake differently, as in the first numerical experiment (see 5.9(b)). This may be related to differences in mixing between the models in the shallower shelf regions in proximity of the west coasts.

Figure 5.13(a) shows the evolution of the sea surface temperature averaged over the

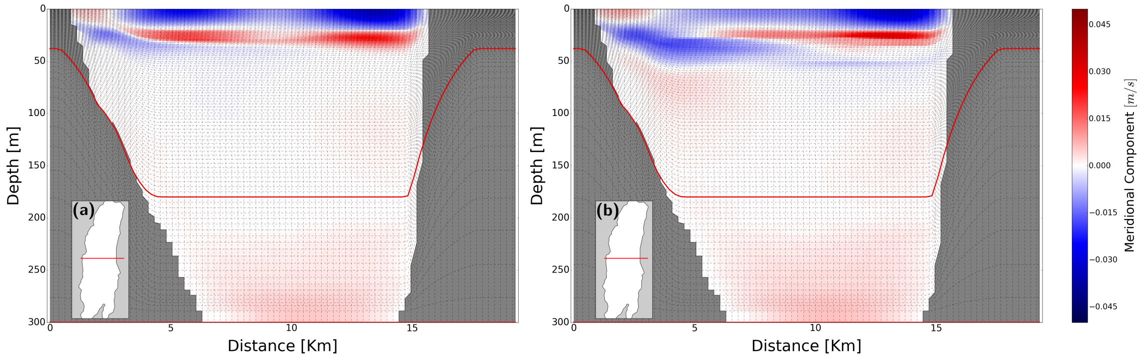

Fig. 5.12: Zonal cross section in the middle of the domain (see the inset map) of meridional current velocity simulated by (a) the SPP and (b) the MPP models on the 29-08-2016 at 15:00.

analysis area in the central deep part of the Dead Sea. The surface temperature in the MPP (step-preserving) model is higher than in the SPP model, showing that the amount of solar energy confined in the upper layer is greater in the MPP than in the SPP model. This is probably due to the reduced downward heat fluxes through a sharp pycnocline at the bottom of the upper step as compared to a smooth pycnocline when the steps are not present. One can expect that higher sea surface temperature will lead to higher evaporation rates subject to all other parameters (e.g. wind speed) being the same. This fact is confirmed by the calculation of the evaporation rate, see Fig.5.13(b).

The difference in the evaporation rate between the step-like and smooth cases is presented in Fig.5.11(c), showing an average augmented sea level drop of about 0.1-0.2 $m\ year^{-1}$ due to increased evaporation. The difference in the vertical structure of temperature, salinity and potential density is shown in Fig.5.11(d,e) for a grid point located in the middle of the analysed area (blue cross marker in Fig. 5.1).

Figure 5.13(b) presents the timeseries of the analysis-area averaged sea surface salinity (SSS) simulated by the two models. It shows that the augmented evaporation of the MPP model induces an increasing in the SSS of about 0.3 PSU during the last four days of the simulation in comparison with the SPP model.

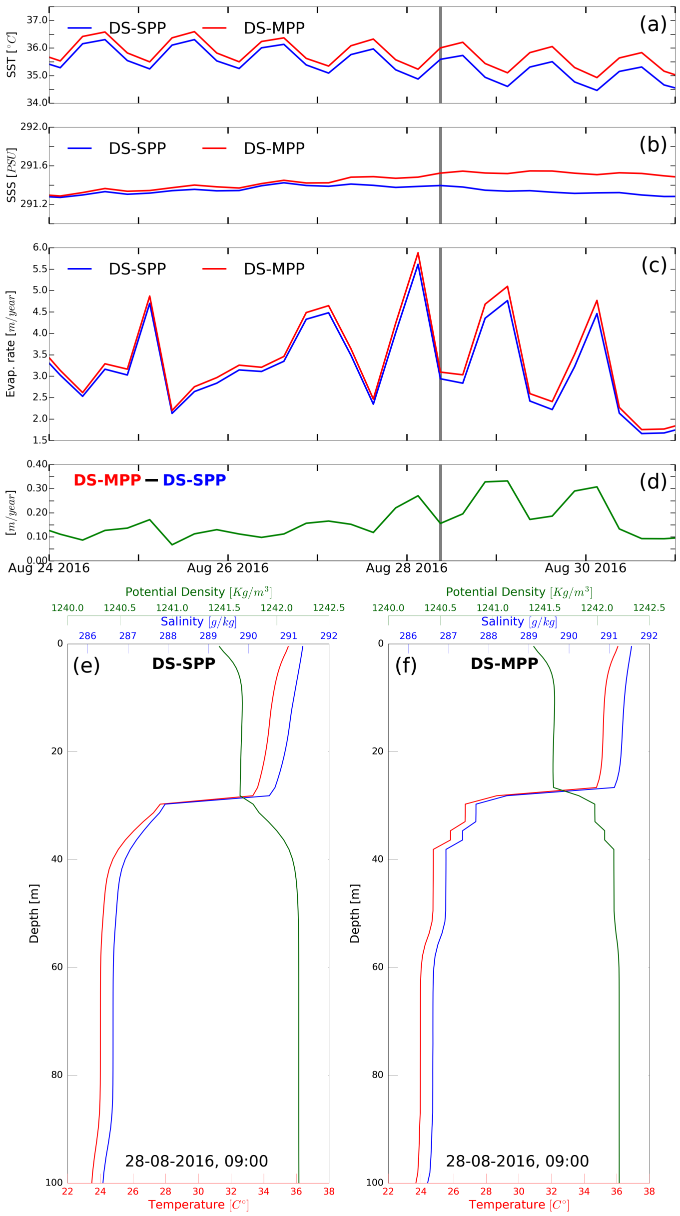

Fig. 5.13: (a) Six-hourly timeseries of the analysis-area averaged SST simulated with the DS model using the SPP (blue) and MPP (red) vertical mixing parameterizations in the period 24-30 August 2016. (b) Six-hourly timeseries of the analysis-area averaged SSS simulated with the DS model using the SPP (blue) and MPP (red) vertical mixing parameterizations in the period 24-30 August 2016. (c) Six-hourly timeseries of the analysis-area averaged evaporation rate simulated with the DS model using the SPP (blue) and MPP (red) vertical mixing parameterizations in the period 24-30 August 2016. (d) Six-hourly timeseries of the difference between the analysis-area averaged evaporation rate simulated with the DS-MPP model and the one simulated with the DS-SPP model in the period 8-14 August 2016. (e) Temperature, salinity and potential density vertical profiles simulated by the DS-SPP model at the grid point located in the middle of the analysis area on the 28^{th} of August 2016 at 09:00. (f) The same as in panel (g) but for the DS-MPP model.

While our models use a number of simplified assumptions, for example horizontal homogeneity of parameters, and do not include effects of other factors, such as climate change, increase of anthropogenic pressures or salinity effects on the evaporation rate, they are a helpful tool for assessing the effect of different vertical mixing schemes on the water column of the Dead Sea.

Our results seem to indicate that a vertical mixing regime compatible with the existence of thermohaline staircase might reduce the heat transport to a greater depth, in particular in the upper part of the water column, leading to higher sea surface temperatures, higher evaporation rates and higher sea surface salinity.

These results might suggest a potential role of thermohaline staircases on the increased rates of the sea level drop of about 0.1 $m\ year^{-1}$ observed in the Dead Sea since 2000 (Lensky and Dente, 2017).

5.5 Conclusion

In this Chapter we have developed two contrasting NEMO-based numerical models of the Dead Sea hydrodynamics to investigate the effect of different vertical mixing parameterizations on the Dead Sea water column dynamics and its evaporation rate. The models differ only in the type of the vertical mixing parameterization. One model, named SPP, applied a widely used diapycnal mixing formulation which does not take into account the presence of thermohaline staircases. On the other hand, the second model, named MPP, used a vertical mixing scheme compatible with the existence of thermohaline step-like structures.

Sensitivity experiments show that the MPP model is able to preserve the observed step-like structures of the initial condition while the SPP model smooths them out. Numerical horizontal pressure gradients errors, small in both models ($U_{max} < 0.007$ $m\ s^{-1}$), are higher in the MPP simulation, due to its ability to simulate sharper density interfaces than the SPP model.

Realistic numerical experiments indicate that, under the same atmospheric conditions, a vertical mixing regime typical of a water column presenting step-like structures might be able to reduce the heat transport to greater depths in comparison to a more diffusive diapycnal mixing, inducing higher sea surface temperatures, evaporation rate and sea surface salinity. Our results show that the increased evaporation rate may contribute to the Dead Sea water level recession with a rate up to 0.1 $m/year$ on certain days.

The long-term effect of the above mechanism would require a specialised study based on longer-term observations and modelling.

5.6 Appendix 5A: NEMO setup

The Dead Sea models implemented in this study use the NEMO version 3.6 code (see Madec (2008) and Sec. 2.5) with the lateral Laplacian viscosity coefficient A_h equal to 72 $[m^2 s^{-1}]$ and the constant lateral Laplacian diffusivity coefficient K_h equal to 0.1 $[m^2 s^{-1}]$.

The models have closed lateral boundaries with no-slip condition. The penetration in the water column of the short wave radiation Q_{sr} (L^θ term in Equation 2.8) is parameterized as follows:

$$I(z) = Q_{sr}\left[R\, e^{-z/\xi_0} + (1-R)e^{-z/\xi_1}\right], \tag{5.5}$$

$$L^\theta \equiv (\rho C_p)^{-1}\,\partial_z I, \tag{5.6}$$

where $I(z)$ is the downward irradiance, $R = 0.8$ is a constant defining the fraction of non-penetrating light, $\xi_0 = 0.5\ m$ specifies the very near surface depth of extinction and $\xi_1 = 2.2\ m$ is the second extinction length scale associated with the shorter wavelengths. For the dynamic bottom boundary condition we adopt a log-layer enhanced quadratic bottom friction parametrisation with minimum and maximum bottom drag coefficient values equal to $2.5 \cdot 10^{-3}$ and 10^{-1}, respectively.

The models use baroclinic and barotropic time-steps equal to 60.0 and 22 s, respectively.

6. Conclusions and future work

6.1 Summary of the main findings

In this thesis, advanced methods for numerical ocean modelling of regional seas have been investigated. The study has been carried out developing a novel vertical discretisation scheme for numerical ocean modelling and conducting numerical experiments with NEMO-3.6-MEs code which is based on NEMO 3.6 (Madec, 2008) ocean model. The modifications/additions in the NEMO-3.6-MEs code as compared with the publicly available NEMO 3.6 model were coded by the author and included the addition of an extra module, modifications in 22 other modules and the structure of the namelist. The numerical experiments were conducted in an idealized domain as well as in two real study cases with complex and contrasting marine environments, the Black Sea and the Dead Sea.

In Chapter 3, a new vertical discretisation scheme named 'Multi-Envelope s-coordinate system' or 'MEs' has been introduced. This new system allows the definition of computational surfaces which are optimised to best represent the physical processes in question. The multi-enveloping method further develops the earlier concept of 'enveloped bathymetry', where model levels followed a 'virtual bottom' (aka envelope) rather than the actual bathymetry. An assessment of the MEs model skill for a number of idealized process studies shows that MEs generates a small pressure gradient error, gives a better representation of dense water cascades down the continental slope and provides a more accurate simulation of formation of a cold intermediate layer, than a comparable z-partial steps model. The MEs systems allows achieving a quality of simulation similar to a standard geopotential grid with a much higher number of levels, and hence the MEs system is more computationally efficient.

In Chapter 4, we have assessed and quantified the effect of optimising the 3D computational mesh for the prevailing physical processes on the accuracy of a Black Sea simulation in free-run mode. Four Black Sea ocean models have been implemented, differing only in type of the horizontal and/or vertical discretization schemes. One of the models uses a standard z-partial steps in the vertical direction and a regular geographical discretization in the horizontal while the other three models use bespoke schemes with curved grid cells designed to better capture important physical processes of the Black Sea dynamics. Models' inter-comparison showed that the best results are obtained with the CUR-MEs model, which combines the Multi-Envelope s-coordinate scheme with a curvilinear horizontal grid with increased resolution over the shelf-break. In particular, numerical results show that the vertical grid of the CUR-MEs model, which has computational levels nearly following isopycnal surfaces and increased resolution in the active layer of the sea (i.e., at depths between 5 and 100 m), is able to reduce spurious numerical diapycnal mixing improving the representation of the CIL dynamics. Further comparison of the free-running CUR-MEs model with the CMEMS assimilative reanalysis shows that two models have similar accuracy, with CUR-MEs being slightly better in representing independently obtained profiles. The difference between the mean BIAS and RMSE of the two models with respect to independent observations is $\approx 0.15°C$ for temperature and ≈ 0.07 for salinity. Basin averaged annual mean profiles of the same metrics show that the CMEMS reanalysis, which assimilates SST, has better accuracy in simulating the temperature of the upper layer, while the CUR-MEs model presents higher accuracy (both BIAS and RMSE) in the active CIL layer of the sea. Despite the lack of data assimilation, the CUR-MEs model is able to reveal the details of the inter-and intra- annual variability of the Mean Kinetic Energy and the Cold Intermediate Water, capturing the warming and weakening of the CIL which was indicated in some recent observations and allowing to study this process with high granularity.

In Chapter 5 we have investigated the effect of different vertical mixing regimes on the structure of the water column in the Dead Sea (an highly saline inland sea) and the potential impact on its evaporation rate. We have simulated the evolution of a Dead Sea water column initially presenting thermohaline staircases with two contrasting numerical models: one, named SPP, uses a widely used diapycnal mixing formulation which does not take into account the presence of thermohaline staircases while the second, named MPP, uses a vertical mixing scheme compatible with the existence of thermohaline step-like structures. Sensitivity experiments show that numerical horizontal pressure gradients errors, though small in both models, are higher in the MPP model, due to its ability to preserve the step-like structures of the initial condition which conversely are smoothed out in the SPP model. Realistic numerical experiments indicate that when the vertical mixing parameterization is able to mimic the diapycnal mixing regime typical of a water column presenting step-like structures, the transport of heat to greater depths might be reduced in comparison to a more diffusive diapycnal mixing. This results in higher values of sea surface temperature, evaporation rate and sea surface salinity in the MPP scenario than in the SPP model. Results show that the increased evaporation rate may contribute to the sea level recession with a rate up to 0.1 m/year on certain days, identifying a potential role of thermohaline staircases in the increased evaporation rate of the Dead Sea. The long-term effect of the above mechanism would require a specialised study based on longer-term observations and modelling.

6.2 Future work

In this thesis, we have introduced and tested in idealised and realistic model setup a novel generalised Multi-Envelope s-coordinate system (Chapter 3) where computational surfaces can be optimised to best represent the leading physical processes at stake. The skills of the MEs system have been investigated and assessed for simulations spanning periods of months (Chapter 3 and Chapter 5) or years (Chapter

4). However, the behavior of this new scheme when applied for longer climate-type runs has not been investigated in this thesis. Therefore, one important unanswered question is whether a ME*s* vertical grid optimized for the current oceanic state of a particular domain may be also appropriate for future scenarios. One possibility could be that, under long-term changes of the thermohaline state of the sea, ME*s* computational levels might not mimic anymore the stratification of the basin. This could result in undesired numerical diapycnal mixing, as it is the case for all the other non-isopycnic vertical coordinate system. Therefore, a further improvement of the MEs scheme could be the development of an arbitrary Lagrangian-Eulerian ME*s*-coordinate system, where envelopes and model levels will be able to move in time adapting to the main baroclinic features of the flow (e.g. combining the ideas of Hofmeister et al. (2010) and Leclair and Madec (2011).

The free-running CUR-ME*s* model developed in this thesis (Chapter 4) has been proven to be a useful and skilful tool to study the Black Sea hydrodynamics, with an accuracy similar to CMEMS assimilative reanalysis. The next step could be using this model to investigate the intra- and inter-annual variability of the CIL dynamics in the last 20 years, contributing to elucidate the mechanisms behind the recently observed warming and weakening of the Cold Intermediate Water (e.g., Piotukh et al. (2011); Akpinar et al. (2017); Stanev et al. (2019)).

In Chapter 5 we have shown that the ME*s* scheme can be used to succesfully investigate the effect of different vertical mixing regimes on the structure of the water column in the Dead Sea. Our study might suggest a potential role of thermohaline staircases in the recent increased evaporation rate of the Dead Sea. A challenging further step to deeper investigate this mechanism could be implementing a longer-term model of the Dead Sea circulation using a parameterization for the double-diffusive transport (e.g, Radko et al. (2014)).

One of the main finding of our research is that optimising the numerical mesh for the main physical processes might allow to improve the accuracy of a free-running

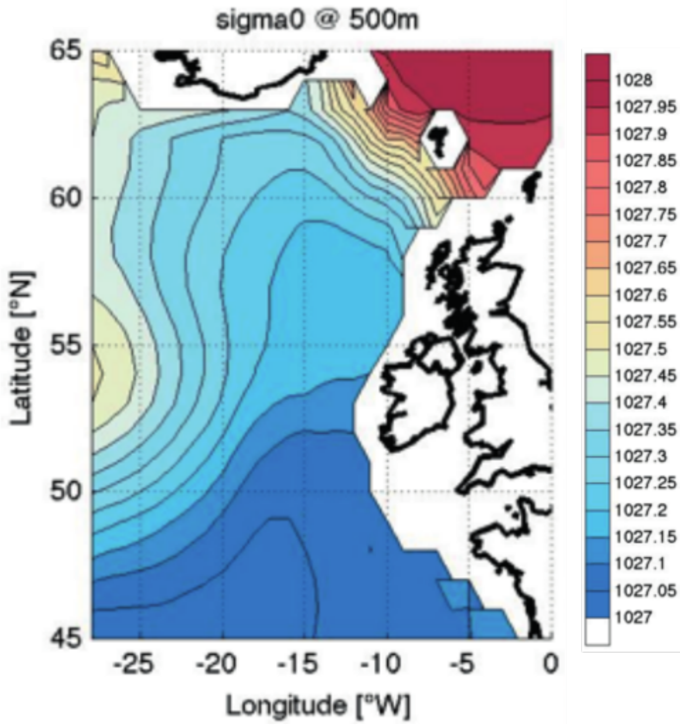

Fig. 6.1: Map of annual climatological potential density referenced to the surface at 500 m (from Marsh et al. (2017)) The annual climatology is obtained using monthly estimates of ocean temperature and salinity spanning the period 1993-2013 available as objectively analysed gridded fields from the EN4 dataset provided by the UK Met Office Hadley Centre (Good et al., 2013).

Black Sea ocean model. An interesting further step would be to test this approach in other regions of the World Ocean, where different physical processes may drive the main dynamics. Recently, Graham et al. (2018a,b) and Tonani et al. (2019) have shown that increasing the horizontal resolution of the Atlantic Margin Model (AMM) from eddy permitting (7 km, named AMM7) to eddy resolving (1.5 km, named AMM15) might allow to obtain a better representation of dynamical features such as coastal currents, fronts, mesoscale eddies and shelf-break exchanges in the Northwest European shelf. However, they also showed that increasing the lateral resolution is not sufficient to reduce the biases in the thermohaline structure of the water column which affect both model configurations in open ocean an shelf areas. Such biases seem to be ultimately linked to the resolution of the hybrid z^*-s vertical grid (Siddorn and Furner, 2013) used by both models (see Graham et al. (2018b) and O'Dea et al. (2017) for the details). This seems to be in agreement with our research, where we find that the CUR horizontal grid is an additive improvement only when combined with the MEs vertical grid, indicating that the the best improvements are achieved when the model is able to correctly reproduce the underpinning 3D generating mechanisms. The multi-envelope method could be used to optimise the vertical grid of AMM7 and AMM15 models for the main dynamical features of the Northwest European shelf and trying to reduce those biases. In particular, it would be interesting to assess whether using an envelope mimicking the meridional sloping of North Atlantic isopycnals (see Fig. 6.1) might help to obtain more accurate simulations of the European slope current.

Global ocean models typically use geopotential vertical levels and coarse horizontal resolution. As a result, they usually experience difficulties in representing dense water cascading and overflows (e.g. Griffies (2004)), two fundamental processes for water masses formation at planetary scale (e.g. Shapiro (2003); Ezer (2006); Wobus et al. (2013)). It would be interesting to test whether the multi-envelope approach could be used in global configurations to improve the representation of oceanic gravity currents. For example, a global ME*s* grid could use envelopes which are bended to follow the bottom topography only in local areas where cascading and overflows are known to occur (e.g. Denmark strait), reducing to the minimum horizontal pressure gradient errors and spurious diapycnal contaminations.

Bibliography

Adcroft, A. and Campin, J.-M. (2004). Rescaled height coordinates for accurate representation of free-surface flows in ocean circulation models. *Ocean Modelling*, 7(3-4):269–284.

Adcroft, A., Hill, C., and Marshall, J. (1997). Representation of Topography by Shaved Cells in a Height Coordinate Ocean Model. *Monthly Weather Review*, 125(9):2293–2315.

Adcroft, A. and Marshall, D. (1998). How slippery are piecewise-constant coastlines in numerical ocean models? *Tellus A: Dynamic Meteorology and Oceanography*, 50(1):95–108.

Akpinar, A., Fach, B. A., and Oguz, T. (2017). Observing the subsurface thermal signature of the Black Sea cold intermediate layer with Argo profiling floats. *Deep Sea Research Part I: Oceanographic Research Papers*, 124:140–152.

Allan, J., Malkawi, A. I. H., and Tsur, Y. (2011). Red Sea Dead Sea conveyance study program - Dead Sea study. Final Report. Technical report, TAHAL group in association with the Geological Survey of Israel (GSI Report Number: GSI/10/2011, TAHAL Report Number: IL201280-R11-218).

Anati, D. (1997). The hydrography of a hypersaline lake. In Niemi, T. M., Ben-Avraham, Z., and Gat, J. R., editors, *The Dead Sea: the lake and its setting*, pages 89–103. Oxford University Press, Oxford.

Anati, D. (1999). The salinity of hypersaline brines: concepts and misconceptions. *International Journal of Salt Research*, 8:1–16.

Anati, D. and Shasha, S. (1989). Dead Sea surface-level changes. *Israel Journal of Earth Sciences*, 38:29–32.

Anati, D., Stiller, M., Shasha, S., and Gat, J. (1987). Changes in the thermo-haline structure of the Dead Sea: 1979âĂŞ1984. *Earth and Planetary Science Letters*, 84(1):109–121.

Anati, D. A. and Stiller, M. (1991). The post- 1979 thermohaline structure of the Dead Sea and the role of double-diffusive mixing. *Limnology and Oceanography*, 36(2):342–353.

Argo (2018). Argo float data and metadata from Global Data Assembly Centre (Argo GDAC).

Arnon, A., Lensky, N. G., and Selker, J. S. (2014). High-resolution temperature sensing in the Dead Sea using fiber optics. *Water Resources Research*, 50(2):1756–1772.

Arnon, A., Selker, J. S., and Lensky, N. G. (2016). Thermohaline stratification and double diffusion diapycnal fluxes in the hypersaline Dead Sea. *Limnology and Oceanography*, 61(4):1214–1231.

Asmar, B. and Ergenzinger, P. (2002). Dynamic simulation of the Dead Sea. *Advances in Water Resources*, 25(3):263–277.

Asmar, B. N. and Ergenzinger, P. (2003). Effect of the Dead Sea-Red Sea canal modelling on the prediction of the Dead Sea conditions. *Hydrological Processes*, 17(8):1607–1621.

Aydogdu, A., Pinardi, N., Özsoy, E., Danabasoglu, G., Gürses, Ö., and Karspeck, A. (2018). Circulation of the Turkish Straits System under interannual atmospheric forcing. *Ocean Science*, 14(5):999–1019.

Badin, G., Williams, R. G., Holt, J. T., and Fernand, L. J. (2009). Are mesoscale eddies in shelf seas formed by baroclinic instability of tidal fronts? *Journal of Geophysical Research*, 114(C10):C10021.

Barnier, B., Madec, G., Penduff, T., Molines, J.-M., Treguier, A.-M., Le Sommer, J., Beckmann, A., Biastoch, A., Böning, C., Dengg, J., Derval, C., Durand, E., Gulev, S., Remy, E., Talandier, C., Theetten, S., Maltrud, M., McClean, J., and De Cuevas, B. (2006). Impact of partial steps and momentum advection schemes in a global ocean circulation model at eddy-permitting resolution. *Ocean Dynamics*, 56(5-6):543–567.

Barnier, B., Marchesiello, P., De Miranda, A. P., Molines, J.-M., and Coulibaly, M. (1998). A sigma-coordinate primitive equation model for studying the circulation in the South Atlantic. Part I: Model configuration with error estimates. *Deep Sea Research I*, 45:543–572.

Beckers, J. M., Burchard, H., Deleersnijder, E., and Mathieu, P. P. (2000). Numerical discretization of rotated diffusion operators in ocean models. *Monthly Weather Review*, 128(8):2711–2733.

Bernie, D. J., Guilyardi, E., Madec, G., Slingo, J. M., and Woolnough, S. J. (2007). Impact of resolving the diurnal cycle in an oceanâĂŞatmosphere GCM. Part 1: a diurnally forced OGCM. *Climate Dynamics*, 29(6):575–590.

Berntsen, J. (2002). Internal pressure errors in sigma coordinate ocean models. *Journal of Atmospheric and Oceanic Technology*, 21(1994):1403–1413.

Besiktepe, S. T., Lozano, C. J., Robinson, A. R., BeÅ§iktepe, Å., Lozano, C. J., and Robinson, A. R. (2001). On the summer mesoscale variability of the Black Sea. *Journal of Marine Research*, 59(4):475–515.

Blatov, A. S., Bulgakov, N. P., Ivanov, V. A., Kosarev, A. N., and Tuzhilkin, V. S. (1984). *Variability of Hydrophysical Fileds in the Black Sea*. Gidrometeoizdat.

Bleck, R. (1998). Ocean modeling in isopycnic coordinates. In Chassignet, E. P. and Verron, J., editors, *Ocean Modeling and Parameterization, NATO ASI Mathematical and Physical Sciences Series, Vol. 516*, pages 423–448. Kluwer Academic Publishers, Dordrecht.

Bleck, R. (2002). An oceanic general circulation model framed in hybrid isopycnic-Cartesian coordinates. *Ocean Modelling*, 4(1):55–88.

Bleck, R. and Boudra, D. (1981). Initial Testing of a Numerical Ocean Circulation Model Using a Hybrid (Quasi-Isopycnic) Vertical Coordinate. *Journal of Physical Oceanography*, 11(6):755–770.

Blokhina, M. D. and Afanasyev, Y. D. (2003). Baroclinic instability and transient features of mesoscale surface circulation in the Black Sea: Laboratory experiment. *Journal of Geophysical Research*, 108(C10):3322.

Blumberg, A. F. and Mellor, G. L. (1987). A description of a three-dimensional coastal ocean circulation model. In *Three-Dimensional Coastal Ocean Models*, pages 1–16.

Boguslavsky, S., Bukatov, A., and Kazakov, S. (2001). Features of the velocity field and the vertical exchange in the Black Sea. In *Ecological Safety of Coastal and Shelf Zones and Complex Use of the Shelf Resources*, pages 62–71. Marine Hydrophysical Institute, Sevastopol, Ukraine.

Brenner, S., Lensky, N., and Gertman, I. (2015). Modeling the circulation of the Dead Sea. In *EGU General Assembly Conference Abstracts*, page 7219, Vienna, Austria.

Brink, K. (2016). Cross-Shelf Exchange. *Annual Review of Marine Science*, 8(1):59–78.

Brink, K. and Robinson, A., editors (2005a). *The Global Coastal Ocean: Multiscale*

Interdisciplinary Processes, The Sea, Vol. 13. Harvard University Press, reprinted edition.

Brink, K. and Robinson, A., editors (2005b). *The Global Coastal Ocean: Regional Studies and Syntheses, The Sea, Vol. 11.* Harvard University Press, reprinted edition.

Brink, K. H. (1991). Coastal-Trapped Waves and Wind-Driven Currents Over the Continental Shelf. *Annual Review of Fluid Mechanics*, 23(1):389–412.

Brink, K. H. and Cherian, D. A. (2013). Instability of an idealized tidal mixing front: Symmetric instabilities and frictional effects. *Journal of Marine Research*, 71(6):425–450.

Bruciaferri, D., Shapiro, G. I., and Wobus, F. (2018). A multi-envelope vertical coordinate system for numerical ocean modelling. *Ocean Dynamics*, 68(10):1239–1258.

Bryan, K. (1969). A numerical method for the study of the circulation of the world ocean. *Journal of Computational Physics*, 4(3):347–376.

Bulgakov, S. N. and Korotaev, G. K. (1984). A possible mechanism of permanent water circulation of the Black Sea. In Institute, M. H., editor, *Comprehensive studies of the Black Sea*, pages 32–40. Sevastopol, USSR.

Bulgakov, S. N. and Korotayev, G. K. (1989). The role of haline factors in the formation of the water circulation in the Black Sea. In *Modeling of hydrophysical processes and fields in enclosed reservoirs and seas*, pages 71–78. Nauka, Moscow.

Burchard, H., Craig, P. D., Gemmrich, J. R., van Haren, H., Mathieu, P.-P., Meier, H. M., Smith, W. A. M. N., Prandke, H., Rippeth, T. P., Skyllingstad, E. D., Smyth, W. D., Welsh, D. J., and Wijesekera, H. W. (2008). Observational and numerical modeling methods for quantifying coastal ocean turbulence and mixing. *Progress in Oceanography*, 76(4):399–442.

Burchard, H. and Rennau, H. (2008). Comparative quantification of physically and numerically induced mixing in ocean models. *Ocean Modelling*, 20(3):293–311.

Cane, M. A., Kamenkovich, V. M., and Krupitsky, A. (1998). On the Utility and Disutility of JEBAR*. *Journal of Physical Oceanography*, 28(3):519–526.

Cannaby, H., Fach, B. A., Arkin, S. S., and Salihoglu, B. (2015). Climatic controls on biophysical interactions in the Black Sea under present day conditions and a potential future (A1B) climate scenario. *Journal of Marine Systems*, 141:149–166.

Canuto, C., Quarteroni, A., Hussaini, M. Y., and Zang, T. A. (2007). *Spectral Methods*. Scientific Computation. Springer Berlin Heidelberg, Berlin, Heidelberg.

Capet, A., Barth, A., Beckers, J.-M., and Marilaure, G. (2012). Interannual variability of Black Sea's hydrodynamics and connection to atmospheric patterns. *Deep Sea Research Part II: Topical Studies in Oceanography*, 77-80:128–142.

Capet, A., Stanev, E. V., Beckers, J.-M., Murray, J. W., and Grégoire, M. (2016). Decline of the Black Sea oxygen inventory. *Biogeosciences*, 13(4):1287–1297.

Capet, A., Troupin, C., Carstensen, J., Grégoire, M., and Beckers, J.-M. (2014). Untangling spatial and temporal trends in the variability of the Black Sea Cold Intermediate Layer and mixed Layer Depth using the DIVA detrending procedure. *Ocean Dynamics*, 64(3):315–324.

Carpenter, A. (2018). Oil pollution in the North Sea: the impact of governance measures on oil pollution over several decades. *Hydrobiologia*.

Cenedese, C., Todd, R. E., Gawarkiewicz, G. G., Owens, W. B., and Shcherbina, A. Y. (2013). Offshore Transport of Shelf Waters through Interaction of Vortices with a Shelfbreak Current. *Journal of Physical Oceanography*, 43(5):905–919.

Chapman, D. C. (2000). Boundary Layer Control of Buoyant Coastal Currents and the Establishment of a Shelfbreak Front*. *Journal of Physical Oceanography*, 30(11):2941–2955.

Chassignet, E. P., Hurlburt, H. E., Smedstad, O. M., Halliwell, G. R., Hogan, P. J., Wallcraft, A. J., and Bleck, R. (2006). Ocean Prediction with the Hybrid Coordinate Ocean Model (HYCOM). In Chassignet, E. P. and Verron, J., editors, *Ocean Weather Forecasting*, pages 413–426. Springer-Verlag, Berlin/Heidelberg.

Chassignet, E. P. and Marshall, D. P. (2008). Gulf Stream separation in numerical ocean models. pages 39–61.

Chern, C.-S., Wang, J., and Wang, D.-P. (1990). The exchange of Kuroshio and East China Sea shelf water. *Journal of Geophysical Research*, 95(C9):16017.

Chubarenko, I. and Demchenko, N. (2010). On contribution of horizontal and intra-layer convection to the formation of the Baltic Sea cold intermediate layer. *Ocean Science*, 6(1):285–299.

Ciliberti, S., Pinardi, N., Coppini, G., Oddo, P., Vukicevic, T., Lecci, R. Verri, G., Kumkar, Y., and Creti', S. (2015). A high resolution Adriatic-Ionian Sea circulation model for operational forecasting. In *EGU General Assembly Conference Abstracts*, page 10899.

Ciliberti, S. A., Peneva, E., Storto, A., Kandilarov, R., Lecci, R., Yang, C., Coppini, G., Masina, S., and Pinardi, N. (2016). Implementation of Black Sea numerical model based on NEMO and 3DVAR data assimilation scheme for operational forecasting. In *EGU General Assembly Conference Abstracts*, volume 18, page 16222.

Condie, K. C. (2016). *Earth as an Evolving Planetary System*. Elsevier.

Conley, D. J., Paerl, H. W., Howarth, R. W., Boesch, D. F., Seitzinger, S. P., Havens, K. E., Lancelot, C., and Likens, G. E. (2009). ECOLOGY: Controlling Eutrophication: Nitrogen and Phosphorus. *Science*, 323(5917):1014–1015.

Cooper, L. N. H. and Vaux, D. (1949). Cascading over the continental slope of water from the Celtic Sea. *Journal of the Marine Biological Association of the United Kingdom*, 28:719–750.

Crise, A., Kaberi, H., Ruiz, J., Zatsepin, A., Arashkevich, E., Giani, M., Karageorgis, A., Prieto, L., Pantazi, M., Gonzalez-Fernandez, D., Ribera d'Alcalà, M., Tornero, V., Vassilopoulou, V., Durrieu de Madron, X., Guieu, C., Puig, P., Zenetos, A., Andral, B., Angel, D., Altukhov, D., Ayata, S., Aktan, Y., BalcÄśoÄ§lu, E., Benedetti, F., Bouchoucha, M., Buia, M.-C., Cadiou, J.-F., Canals, M., Chakroun, M., Christou, E., Christidis, M., Civitarese, G., Coatu, V., Corsini-Foka, M., Cozzi, S., Deidun, A., Dell'Aquila, A., Dogrammatzi, A., Dumitrache, C., Edelist, D., Ettahiri, O., Fonda-Umani, S., Gana, S., Galgani, F., Gasparini, S., Giannakourou, A., Gomoiu, M.-T., Gubanova, A., Gücü, A.-C., Gürses, Ö., Hanke, G., Hatzianestis, I., Herut, B., Hone, R., Huertas, E., Irisson, J.-O., ÄřÅ§inibilir, M., Jimenez, J., Kalogirou, S., Kapiris, K., Karamfilov, V., Kavadas, S., Keskin, Ç., KideyÅ§, A., Kocak, M., Kondylatos, G., Kontogiannis, C., Kosyan, R., Koubbi, P., Kušpilić, G., La Ferla, R., Langone, L., Laroche, S., Lazar, L., Lefkaditou, E., Lemeshko, I., Machias, A., Malej, A., Mazzocchi, M.-G., Medinets, V., Mihalopoulos, N., Miserocchi, S., Moncheva, S., Mukhanov, V., Oaie, G., Oros, A., Öztürk, A., Öztürk, B., Panayotova, M., Prospathopoulos, A., Radu, G., Raykov, V., Reglero, P., Reygondeau, G., Rougeron, N., Salihoglu, B., Sanchez-Vidal, A., Sannino, G., Santinelli, C., Secrieru, D., Shapiro, G., Simboura, N., Shiganova, T., Sprovieri, M., Stefanova, K., Streftaris, N., Tirelli, V., Tom, M., TopaloÄ§lu, B., Topçu, N., Tsagarakis, K., Tsangaris, C., Tserpes, G., TuÄ§rul, S., Uysal, Z., Vasile, D., Violaki, K., Xu, J., Yüksek, A., and Papathanassiou, E. (2015). A MSFD complementary approach for the assessment of pressures, knowledge and data gaps in Southern European Seas: The PERSEUS experience. *Marine Pollution Bulletin*, 95(1):28–39.

Csanady, G. T. (1982). *Circulation in the Coastal Ocean*. Springer Netherlands, Dordrecht.

Cushman-Roisin, B. and Beckers, J.-M. (2011). Introduction to Geophysical Fluid Dynamics - Physical and Numerical Aspects. page 875. 2nd edition.

Cyr, F., Bourgault, D., and Galbraith, P. S. (2011). Interior versus boundary mixing of a cold intermediate layer. *Journal of Geophysical Research*, 116(C12):C12029.

Danilov, S. (2013). Ocean modeling on unstructured meshes. *Ocean Modelling*, 69:195–210.

Danilov, S. and Wang, Q. (2015). Resolving eddies by local mesh refinement. *Ocean Modelling*, 93:75–83.

de Boor, C. (1978). *A Practical Guide to Splines*. Springer-Verlag New York, New York.

De Dominicis, M., Wolf, J., and O'Hara Murray, R. (2018). Comparative Effects of Climate Change and Tidal Stream Energy Extraction in a Shelf Sea. *Journal of Geophysical Research: Oceans*, 123(7):5041–5067.

Demyshev, S. G. (2011). Prognostic numerical analysis of currents in the black sea with high horizontal resolution. *Physical Oceanography*, 21(1):33–44.

Dennis, S., Ingham, D., and Cook, R. (1979). Finite-difference methods for calculating steady incompressible flows in three dimensions. *Journal of Computational Physics*, 33(3):325–339.

Diansky, N. A., Fomin, V. V., Zhokhova, N. V., and Korshenko, A. N. (2013). Simulations of currents and pollution transport in the coastal waters of Big Sochi. *Izvestiya, Atmospheric and Oceanic Physics*, 49(6):611–621.

Divinsky, B. V., Kuklev, S. B., Zatsepin, A. G., and Chubarenko, B. V. (2015). Simulation of submesoscale variability of currents in the Black Sea coastal zone. *Oceanology*, 55(6):814–819.

Donlon, C. J., Martin, M., Stark, J., Roberts-Jones, J., Fiedler, E., and Wimmer, W. (2012). The Operational Sea Surface Temperature and Sea Ice Analysis (OSTIA) system. *Remote Sensing of Environment*, 116:140–158.

Doukakis, E. (2008). Impacts of Climate Change on the Coastal Zone. *8th International Scientific Conference - SGEM2008*, 1(May):599–608.

Driscoll, T. and Trefethen, L. (2002). *Schwarz-Christoffel mapping*. Cambridge University Press.

Dukhovskoy, D. S., Morey, S. L., Martin, P. J., O'Brien, J. J., and Cooper, C. (2009). Application of a vanishing, quasi-sigma, vertical coordinate for simulation of high-speed, deep currents over the Sigsbee Escarpment in the Gulf of Mexico. *Ocean Modelling*, 28(4):250–265.

Durski, S. M. (2004). Vertical mixing schemes in the coastal ocean: Comparison of the level 2.5 Mellor-Yamada scheme with an enhanced version of the K profile parameterization. *Journal of Geophysical Research*, 109(C1):C01015.

Dyke, P. (2001). *Coastal and Shelf Sea Modelling*. SPRINGER SCIENCE+BUSINESS MEDIA, LLC.

Dzioev, T. Z. and Sarkisyan, A. S. (1976). Numerical computations of the Black Sea currents. *Atmos. Ocean Phys.*, 6(1):217–223.

Edwards, C. A., Moore, A. M., Hoteit, I., and Cornuelle, B. D. (2015). Regional Ocean Data Assimilation. *Annual Review of Marine Science*, 7(1):21–42.

Efimov, V., Shokurov, M. V., and Barabanov, V. S. (2002). Physical mechanisms of generation of wind circulation in the enclosed seas. *Izvestiya, Atmospheric and Oceanic Physics*, 38(4):476–485.

Efimov, V. V. and Timofeev, N. A. (1990). *Heat balance studies in the Black sea and the Sea of Azov*. VNIIGMI-MCD, Obninsk, USSR.

Enriquez, C. E., Shapiro, G. I., Souza, A. J., and Zatsepin, A. G. (2005). Hydrodynamic modelling of mesoscale eddies in the Black Sea. *Ocean Dynamics*, 55(5-6):476–489.

Eremeev, V., Ivanov, L., Kochergin, S., and Melnichenko, O. (1991). Seasonal variability and types of currents in the upper layer of the Black Sea. *Morskoy Gidrofizicheskiy Zhurnal*, 3:26–38.

Ezer, T. (1984). *Simulation of Drift Currents in the Dead-Sea.* Master's thesis, Hebrew University, Jerusalem, Israel.

Ezer, T. (2000). On the seasonal mixed layer simulated by a basin-scale ocean model and the Mellor-Yamada turbulence scheme. *Journal of Geophysical Research: Oceans*, 105(C7):16843–16855.

Ezer, T. (2005). Entrainment, diapycnal mixing and transport in three-dimensional bottom gravity current simulations using the MellorâĂŞYamada turbulence scheme. *Ocean Modelling*, 9(2):151–168.

Ezer, T. (2006). Topographic influence on overflow dynamics: Idealized numerical simulations and the Faroe Bank Channel overflow. *Journal of Geophysical Research*, 111(C2):C02002.

Ezer, T. (2016). Revisiting the problem of the Gulf Stream separation: on the representation of topography in ocean models with different types of vertical grids. *Ocean Modelling*, 104:15–27.

Ezer, T., Arango, H., and Shchepetkin, A. F. (2002). Developments in terrain-following ocean models: Intercomparisons of numerical aspects. *Ocean Modelling*, 4(3-4):249–267.

Ezer, T. and Mellor, G. L. (1992). A Numerical Study of the Variability and the Separation of the Gulf Stream, Induced by Surface Atmospheric Forcing and Lateral Boundary Flows. *Journal of Physical Oceanography*, 22(6):660–682.

Ezer, T. and Mellor, G. L. (1994). Diagnostic and prognostic calculations of the North Atlantic circulation and sea level using a sigma coordinate ocean model. *Journal of Geophysical Research*, 99(C7):14159.

Ezer, T. and Mellor, G. L. (2000). Sensitivity studies with the North Atlantic sigma coordinate Princeton Ocean Model. *Dynamics of Atmospheres and Oceans*, 32:185–208.

Ezer, T. and Mellor, G. L. (2004). A generalized coordinate ocean model and a comparison of the bottom boundary layer dynamics in terrain-following and in z-level grids. *Ocean Modelling*, 6(3-4):379–403.

Ezer, T., Thattai, D. V., Kjerfve, B., and Heyman, W. D. (2005). On the variability of the flow along the Meso-American Barrier Reef system: a numerical model study of the influence of the Caribbean current and eddies. *Ocean Dynamics*, 55(5-6):458–475.

Fedorov, K. (1970). On the step-like structure of temperature inversions in the ocean. *Izv., Atmospheric and Oceanic Physics*, 6:1178–1188.

Fennel, W., Seifert, T., and Kayser, B. (1991). Rossby radii and phase speeds in the Baltic Sea. *Continental Shelf Research*, 11(1):23–36.

Filippov, D. M. (1968). *Water Circulation and Structure of the Black Sea*. Nauka, Moscow.

Flemming, N. C. (2002). Strategic Planning for Operational Oceanography. In Pinardi, N. and Woods, J., editors, *Ocean Forecasting: Conceptual Basis and Applications*, chapter 1, page 472. Springer-Verlag, Berlin Heidelberg.

Friedrich, J., Aleynik, D., Kusch, S., Mee, L., Minicheva, G., Shapiro, G., Soloview, D., Stevens, T., and Teaca, A. (2008). Cruise report POS 363 RV "Poseidon" [POS363], March 7 to 25 2008, Varna/Varna. *Alfred Wegener Institute for Polar and Marine Research.*

Frumkin, A., Ezersky, M., Al-Zoubi, A., Akkawi, E., and Abueladas, A.-R. (2011). The Dead Sea sinkhole hazard: Geophysical assessment of salt dissolution and collapse. *Geomorphology*, 134(1-2):102–117.

Furner, R. (2012). A review of lateral diffusion for Met Office ocean shelf modelling. Technical report, Met Office.

Galperin, B., Kantha, L., Hassid, S., and Rosati, A. (1988). A quasi-equilibrium turbulent energy model for geophysical flows. *Journal of Atmospheric Sciences*, 45:55–62.

Gangopadhyay, A. and Robinson, A. R. (2002). Feature-oriented regional modeling of oceanic fronts. *Dynamics of Atmospheres and Oceans*, 36(1-3):201–232.

Garfunkel, Z. and Ben-Avraham, Z. (1996). The structure of the Dead Sea basin. *Tectonophysics*, 266(1-4):155–176.

Garrett, C. (1979). Mixing in the ocean interior. *Dynamics of Atmospheres and Oceans*, 3(2-4):239–265.

Gavrieli, I., Dvorkin, Y., Lyakhovsky, V., Lensky, N., and Gazit-Yaari, N. (2003). Formulating a dynamic limnological model for the Dead Sea: Selection of the computer code and preliminary simulations. Technical report, Isr. Geol. Surv. Rep. GSI/3/2003.

Gerdes, R. (1993a). A primitive equation ocean circulation model using a general vertical coordinate transformation: 1. Description and testing of the model. *Journal of Geophysical Research*, 98(C8):14683.

Gerdes, R. (1993b). A primitive equation ocean circulation model using a general vertical coordinate transformation: 2. Application to an overflow problem. *Journal of Geophysical Research*, 98(C8):14703.

Gertman, I. and Hecht, A. (2002). The Dead Sea hydrography from 1992 to 2000. *Journal of Marine Systems*, 35(3-4):169–181.

Gertman, I., Kress, N., Katsenelson, B., and Zavialov, P. (2010). Equation of state for the Dead Sea and Aral Sea. Technical report, IOLR.

Gertman, I., Ozer, T., Katsenelson, B., and Lensky, N. (2015). Vertical Mixing in the Dead Sea. *EGU General Assembly Conference Abstracts*, 17:14173.

Gill, A. E. and Schumann, E. H. (1974). The Generation of Long Shelf Waves by the Wind. *Journal of Physical Oceanography*, 4(1):83–90.

Gill, A. E. A. E. (1982). Atmosphere-Ocean Dynamics. *Astrophysics and Space Science*, 30(30):662.

Good, S. A., Martin, M. J., and Rayner, N. A. (2013). EN4: Quality controlled ocean temperature and salinity profiles and monthly objective analyses with uncertainty estimates. *Journal of Geophysical Research: Oceans*, 118(12):6704–6716.

Graham, J. A., O'Dea, E., Holt, J., Polton, J., Hewitt, H. T., Furner, R., Guihou, K., Brereton, A., Arnold, A., Wakelin, S., Castillo Sanchez, J. M., and Mayorga Adame, C. G. (2018a). AMM15: a new high-resolution NEMO configuration for operational simulation of the European north-west shelf. *Geoscientific Model Development*, 11(2):681–696.

Graham, J. A., Rosser, J. P., O'Dea, E., and Hewitt, H. T. (2018b). Resolving Shelf Break Exchange Around the European Northwest Shelf. *Geophysical Research Letters*, 45(22):12,386–12,395.

Grayek, S., Stanev, E. V., and Kandilarov, R. (2010). On the response of Black Sea level to external forcing: altimeter data and numerical modelling. *Ocean Dynamics*, 60(1):123–140.

GRDC (2014). Global Freshwater Fluxes into the World Oceans - Online provided by Global Runoff Data Centre.

Greenberg, D. A., Dupont, F., Lyard, F. H., Lynch, D. R., and Werner, F. E. (2007). Resolution issues in numerical models of oceanic and coastal circulation. *Continental Shelf Research*, 27(9):1317–1343.

Gregg, M. C. and Özsoy, E. (2002). Flow, water mass changes, and hydraulics in the Bosphorus. *Journal of Geophysical Research*, 107(C3):3016.

Griffies, S. M. (2004). *Fundamentals of Ocean Climate Models*. Princeton University Press, Princeton, NJ.

Griffies, S. M., Böning, C., Bryan, F. O., Chassignet, E. P., Gerdes, R., Hasumi, H., Hirst, A., Treguier, A.-M., and Webb, D. (2000a). Developments in ocean climate modelling. *Journal of Computational Physics*, 2(3-4):123–192.

Griffies, S. M., Pacanowski, R. C., and Hallberg, R. W. (2000b). Spurious Diapycnal Mixing Associated with Advection in a z -Coordinate Ocean Model. *Monthly Weather Review*, 128(3):538–564.

Griffiths, S. D. (2013). Kelvin wave propagation along straight boundaries in C-grid finite-difference models. *Journal of Computational Physics*, 255:639–659.

Gusev, A. V., Zalesny, V. B., and Fomin, V. V. (2017). Technique for Simulation of Black Sea Circulation with Increased Resolution in the Area of the IO RAS Polygon. *Oceanology*, 57(6):880–891.

Haidvogel, D. and Beckmann, A. (1999). *Numerical Ocean Circulation Modeling*. Imperial College Press.

Haidvogel, D., Blanton, J., Kindle, J., and Lynch, D. (2000). Coastal Ocean Modeling : Processes and Real-Time Systems. *Oceanography*, 13(1):35–46.

Haidvogel, D. B., Beckmann, A., and Hedström, K. S. (1991). Dynamical simulations of filament formation and evolution in the Coastal Transition Zone. *Journal of Geophysical Research*, 96(C8):15017.

Haidvogel, D. B., Curchitser, E. N., Danilov, S., and Fox-Kemper, B. (2017). Numerical modelling in a multiscale ocean. *Journal of Marine Research*, 75(6):683–725.

Hall, J. K. (1997). Topography and bathymetry of the Dead Sea depression. In Niemi, T., Ben- Avraham, Z., and Gat, J. R., editors, *The Dead SeaâĂŞthe Lake and Its Setting*, pages 11–21. Oxford University Press, Oxford.

Haney, R. L. (1991). On the pressure gradient force over steep topography in sigma coordinate ocean models. *Journal of Physical Oceanography*, 21:610–619.

Hecht, A. and Gertman, I. (2003). Dead Sea meteorological climate. In Nevo, E., Oren, A., and Wasser, S. P., editors, *Fungal Life in the Dead Sea*, pages 68–114. A.R.G. Gantner, Ruggell (Liechtenstein).

Hecht, M. W. and Hasumi, H., editors (2008). *Ocean Modeling in an Eddying Regime*, volume 177 of *Geophysical Monograph Series*. American Geophysical Union, Washington, D. C.

Hill, A. E., Brown, J., Fernand, L., Holt, J., Horsburgh, K. J., Proctor, R., Raine, R., and Turrell, W. R. (2008). Thermohaline circulation of shallow tidal seas. *Geophysical Research Letters*, 35(11):L11605.

Hirt, C., Amsden, A., and Cook, J. (1974). An arbitrary LagrangianâĂŞEulerian computing method for all flow speeds. *Journal of Computational Physics*, 14(3):227–253.

Hofmeister, R., Burchard, H., and Beckers, J. M. (2010). Non-uniform adaptive vertical grids for 3D numerical ocean models. *Ocean Modelling*, 33(1-2):70–86.

Holligan, P. M., Pingree, R. D., and Mardell, G. (1985). Oceanic solitions, nutrient pulses and phytoplankton growth. *Nature*, 314(6009):348–50.

Holt, J., Hyder, P., Ashworth, M., Harle, J., Hewitt, H. T., Liu, H., New, A. L., Pickles, S., Porter, A., Popova, E., Allen, J. I., Siddorn, J., and Wood, R. (2017).

Prospects for improving the representation of coastal and shelf seas in global ocean models. *Geoscientific Model Development*, 10(1):499–523.

Holt, J., Polton, J., Huthnance, J., Wakelin, S., O'Dea, E., Harle, J., Yool, A., Artioli, Y., Blackford, J., Siddorn, J., and Inall, M. (2018). Climate-Driven Change in the North Atlantic and Arctic Oceans Can Greatly Reduce the Circulation of the North Sea. *Geophysical Research Letters*, 45(21):11,827–11,836.

Holt, J., Schrum, C., Cannaby, H., Daewel, U., Allen, I., Artioli, Y., Bopp, L., Butenschon, M., Fach, B. A., Harle, J., Pushpadas, D., Salihoglu, B., and Wakelin, S. (2014). Physical processes mediating climate change impacts on regional sea ecosystems. *Biogeosciences Discussions*, 11(2):1909–1975.

Holt, J. and Umlauf, L. (2008). Modelling the tidal mixing fronts and seasonal stratification of the Northwest European Continental shelf. *Continental Shelf Research*, 28(7):887–903.

Holt, J., Wakelin, S., and Huthnance, J. (2009). Down-welling circulation of the northwest European continental shelf: A driving mechanism for the continental shelf carbon pump. *Geophysical Research Letters*, 36(14):L14602.

Holt, J., Wakelin, S., Lowe, J., and Tinker, J. (2010). The potential impacts of climate change on the hydrography of the northwest European continental shelf. *Progress in Oceanography*, 86(3-4):361–379.

Holt, J. T. and James, I. D. (2006). An assessment of the fine-scale eddies in a high-resolution model of the shelf seas west of Great Britain. *Ocean Modelling*, 13(3-4):271–291.

Hordoir, R., Axell, L., Höglund, A., Dieterich, C., Fransner, F., Gröger, M., Liu, Y., Pemberton, P., Schimanke, S., Andersson, H., Ljungemyr, P., Nygren, P., Falahat, S., Nord, A., Jönsson, A., Lake, I., Döös, K., Hieronymus, M., Dietze, H., Löptien, U., Kuznetsov, I., Westerlund, A., Tuomi, L., and Haapala, J. (2018). Nemo-Nordic 1.0: A NEMO based ocean model for Baltic & North Seas, research and operational applications. *Geoscientific Model Development Discussions*, 2018:1–29.

Huss, A., Ezer, T., and Hecht, A. (1986). How sluggish are the waters of the Dead Sea. *Israel Journal of Earth Sciences*, 35:207–209.

Huss, A. and Feliks, Y. (1981). A mesometeorological numerical model of the sea and land breezes involving sea-atmospheric interactions. *Beitr. Phys. Atmos.*, 34:238–257.

Hutchinson, G. (1957). *A Treatise on Limnology.* Wiley, New York.

Huthnance, J. (1973). Tidal current asymmetries over the Norfolk Sandbanks. *Estuarine and Coastal Marine Science*, 1(1):89–99.

Huthnance, J. (1981). Waves and currents near the continental shelf edge. *Progress in Oceanography*, 10(4):193–226.

Huthnance, J. M. (1975). On trapped waves over a continental shelf. *Journal of Fluid Mechanics*, 69(4):689–704.

Huthnance, J. M. (1995). Circulation, exchange and water masses at the ocean margin: the role of physical processes at the shelf edge. *Progress in Oceanography*, 35(4):353–431.

Huthnance, J. M., Holt, J. T., and Wakelin, S. L. (2009). Deep ocean exchange with west-European shelf seas. *Ocean Science*, 5(4):621–634.

IOC, SCOR, and IAPSO (2010). The international thermodynamic equation of seawater-2010: Calculation and use of thermodynamic properties. *Tech. rep., Intergovernmental Oceanographic Commission.*

Ivanov, V. A. and Belokopytov, V. N. (2012). *Oceanography of the Black Sea.* Sevastopol.

Ivanov, V. A., Lyubartseva, S. P., Mikhailova, E. N., Shapiro, N. B., and Gertman, I. (2002). Model of the dead sea. Simulation of the variability of the thermohaline water structure in 1992-2000. *Physical Oceanography*, 12(5):237–257.

Ivanov, V. V., Shapiro, G. I., Huthnance, J. M., Aleynik, D. L., and Golovin, P. N. (2004). Cascades of dense water around the world ocean. *Progress in Oceanography*, 60(1):47–98.

Ives, D. C. (1982). Conformal grid generation. *Applied Mathematics and Computation*, 10-11:107–135.

Jackson, J. B. C. (2001). Historical Overfishing and the Recent Collapse of Coastal Ecosystems. *Science*, 293(5530):629–637.

James, I. (1996). Advection schemes for shelf sea models. *Journal of Marine Systems*, 8(3-4):237–254.

Janeković, I. and Kuzmić, M. (2005). Numerical simulation of the Adriatic Sea principal tidal constituents. *Annales Geophysicae*, 23(10):3207–3218.

Joint, I. and Pomroy, A. (1993). Phytoplankton biomass and production in the southern North Sea. *Marine Ecology Progress Series*, 99(August 1988):169–182.

Kallos, G., Nickovic, S., Papadopoulos, A., Jovic, D., Kakaliagou, O., Misirlis, N., Boukas, L., Mimikou, N., and Sakellaridis, G., Papageorgiou, J., Anadranistakis, E. Manousakis, M. (1997). The regional weather forecasting system SKIRON: an overview. In *Proceedings of the International Symposium on Regional Weather Prediction on Parallel Computer Environments*, pages 109–122, Athens, Greece.

Kantha, L. H. and Clayson, C. A. (1994). An improved mixed layer model for geophysical applications. *Journal of Geophysical Research*, 99(C12):25235.

Kantha, L. H. and Clayson, C. A. (2000a). Chapter 7 - Double-Diffusive Processes. In Kantha, L. H. and Clayson, C. A., editors, *Small Scale Processes in Geophysical*

Fluid Flows, volume 67 of *International Geophysics*, pages 685–733. Academic Press.

Kantha, L. H. and Clayson, C. A. (2000b). *Numerical Models of Oceans and Oceanic Processes*. Academic Press.

Kara, A. B., Wallcraft, A. J., and Hurlburt, H. E. (2005). A New Solar Radiation Penetration Scheme for Use in Ocean Mixed Layer Studies: An Application to the Black Sea Using a Fine-Resolution Hybrid Coordinate Ocean Model (HYCOM)*. *Journal of Physical Oceanography*, 35(1):13–32.

Kasahara, A. (1974). Various Vertical Coordinate Systems Used for Numerical Weather Prediction. *Monthly Weather Review*, 102(7):509–522.

Katz, A. and Starinsky, A. (2009). Geochemical History of the Dead Sea. *Aquatic Geochemistry*, 15(1-2):159–194.

Kishcha, P., Starobinets, B., Gertman, I., Ozer, T., and Alpert, P. (2017). Observations of Unexpected Short-Term Heating in the Uppermost Layer of the Dead Sea after a Sharp Decrease in Solar Radiation. *International Journal of Oceanography*, 2017:1–12.

Klein, C. (1982). Morphological evidence of lake level changes, western shore of the Dead Sea. *Isr J Earth Sci*, 31:67–94.

Klingbeil, K., Lemarié, F., Debreu, L., and Burchard, H. (2018). The numerics of hydrostatic structured-grid coastal ocean models: State of the art and future perspectives. *Ocean Modelling*, 125:80–105.

Klingbeil, K., Mohammadi-Aragh, M., Gräwe, U., and Burchard, H. (2014). Quantification of spurious dissipation and mixing âĂŞ Discrete variance decay in a Finite-Volume framework. *Ocean Modelling*, 81:49–64.

Knipovich, N. M. (1932). The hydrological investigations in the Black Sea. *Trudy Azovo-Chernomorskoi Nauchno-promyslovoi Ekspeditsii*, 52(2):187–199.

Kolesnikov, A. (1953). Seasonal course of temperature, stability and vertical turbulent heat exchange in the open part of the Black Sea. *Trudi Mor. Gudrol. Inst. USSR AS*, 3:3–13.

Korotaev, G. K. (1997). Circulation in semi-enclosed seas induced by buoyancy flux through strait. In Özsoy, E. and Mikaelyan, A., editors, *Sensitivity to change: Black Sea, Baltic Sea and Northern Sea, NATO ASI Ser. 2, Vol.27*, pages 197–210. Dordrecht, Kluwer Academic.

Korotaev, G. K. (2001). The reason for the seasonal variations of circulation of the Black Sea. *Morskoy Gidrofizicheskiy Zhurnal*, 6:14–20.

Korotaev, G. K., Knysh, V. V., and Kubryakov, A. I. (2014). Study of formation process of cold intermediate layer based on reanalysis of Black Sea hydrophysical fields for 1971âĂŞ1993. *Izvestiya, Atmospheric and Oceanic Physics*, 50(1):35–48.

Korotaev, G. K., Oguz, T., Dorofeyev, V. L., Demyshev, S. G., Kubryakov, A. I., and Ratner, Y. B. (2011). Development of Black Sea nowcasting and forecasting system. *Ocean Science*, 7(5):629–649.

Korotaev, G. K., Oguz, T., Nikiforov, A., and Koblinsky, C. J. (2003). Seasonal, interannual, and mesoscale variability of the Black Sea upper layer circulation derived from altimeter data. *Journal of Geophysical Research*, 108(C4):3122.

Korotaev, G. K., Saenko, O. A., and Koblinsky, C. J. (2001). Satellite altimetry observations of the Black Sea level. *Journal of Geophysical Research*, 106(C1):917.

Kottek, M., Grieser, J., Beck, C., Rudolf, B., and Rubel, F. (2006). World Map of the Kppen-Geiger climate classification updated. *Meteorologische Zeitschrift*, 15(3):259–263.

Kourafalou, V., De Mey, P., Staneva, J., Ayoub, N., Barth, A., Chao, Y., Cirano, M., Fiechter, J., Herzfeld, M., Kurapov, A., Moore, A., Oddo, P., Pullen, J., van der Westhuysen, A., and Weisberg, R. (2015). Coastal Ocean Forecasting: science foundation and user benefits. *Journal of Operational Oceanography*, 8(sup1):s147–s167.

Kubryakov, A. and Stanichny, S. (2015). Seasonal and interannual variability of the Black Sea eddies and its dependence on characteristics of the large-scale circulation. *Deep Sea Research Part I: Oceanographic Research Papers*, 97:80–91.

Kubryakov, A. A. and Stanichny, S. V. (2011). Mean Dynamic Topography of the Black Sea, computed from altimetry, drifter measurements and hydrology data. *Ocean Science*, 7(6):745–753.

Kubryakov, A. A. and Stanichny, S. V. (2013). Estimating the quality of the retrieval of the surface geostrophic circulation of the Black Sea by satellite altimetry data based on validation with drifting buoy measurements. *Izvestiya, Atmospheric and Oceanic Physics*, 49(9):930–938.

Kubryakov, A. A., Stanichny, S. V., Zatsepin, A. G., and Kremenetskiy, V. V. (2016). Long-term variations of the Black Sea dynamics and their impact on the marine ecosystem. *Journal of Marine Systems*, 163:80–94.

Kushnir, Y. and Stein, M. (2010). North Atlantic influence on 19thâĂŞ20th century rainfall in the Dead Sea watershed, teleconnections with the Sahel, and implication for Holocene climate fluctuations. *Quaternary Science Reviews*, 29(27-28):3843–3860.

Laanaia, N., Wirth, A., Molines, J. M., Barnier, B., and Verron, J. (2010). On the numerical resolution of the bottom layer in simulations of oceanic gravity currents. *Ocean Science*, 6(2):563–572.

Large, W. and Yeager, S. (2004). Diurnal to decadal global forcing for ocean and sea ice models: the data sets and climatologies. Technical report, TN-460+STR, NCAR.

Large, W. G., McWilliams, J. C., and Doney, S. C. (1994). Oceanic vertical mixing: A review and a model with a nonlocal boundary layer parameterization. *Reviews of Geophysics*, 32(4):363.

Large, W. G. and Yeager, S. G. (2009). The global climatology of an interannually varying airâĂŞsea flux data set. *Climate Dynamics*, 33(2-3):341–364.

Leclair, M. and Madec, G. (2011). z-Coordinate, an Arbitrary Lagrangian-Eulerian coordinate separating high and low frequency motions. *Ocean Modelling*, 37(3-4):139–152.

Legg, S., Briegleb, B., Chang, Y., Chassignet, E. P., Danabasoglu, G., Ezer, T., Gordon, A. L., Griffies, S., Hallberg, R., Jackson, L., Large, W., Özgökmen, T. M., Peters, H., Price, J., Riemenschneider, U., Wu, W., Xu, X., and Yang, J. (2009). Improving Oceanic Overflow Representation in Climate Models: The Gravity Current Entrainment Climate Process Team. *Bulletin of the American Meteorological Society*, 90(5):657–670.

Legg, S., Hallberg, R. W., and Girton, J. B. (2006). Comparison of entrainment in overflows simulated by z-coordinate, isopycnal and non-hydrostatic models. *Ocean Modelling*, 11(1-2):69–97.

Lemarié, F., Kurian, J., Shchepetkin, A. F., Jeroen Molemaker, M., Colas, F., and McWilliams, J. C. (2012). Are there inescapable issues prohibiting the use of terrain-following coordinates in climate models? *Ocean Modelling*, 42:57–79.

Lemieux-Dudon, B., Storto, A., Ciliberti, S., Peneva, E., and Macchia, F. (2018). Black Sea CMEMS Reanalysis - Quality Information Document. Technical report, http://marine.copernicus.eu/documents/QUID/CMEMS-BS-QUID-007-004.pdf.

Lengaigne, M., Menkes, C., Aumont, O., Gorgues, T., Bopp, L., André, J.-M., and Madec, G. (2007). Influence of the oceanic biology on the tropical Pacific climate in a coupled general circulation model. *Climate Dynamics*, 28(5):503–516.

Lensky, N. and Dente, E. (2017). The causes for the accelerated rate of Dead Sea level decline in the past decades. *Ecol. Environ.*, 8:328–336 (Hebrew).

Lensky, N. G., Lensky, I. M., Peretz, A., Gertman, I., Tanny, J., and Assouline, S. (2018). Diurnal Course of Evaporation From the Dead Sea in Summer: A Distinct Double Peak Induced by Solar Radiation and Night Sea Breeze. *Water Resources Research*, 54(1):150–160.

Leonov, A. K. (1960). *Regional oceanography, Part 1. The Bering Sea, the Okhotsk Sea, the Japan Sea, the Caspian Sea and the Black Sea.* Gidrometeoizdat, Leningrad.

Lermusiaux, P. (2001). Evolving the subspace of the three-dimensional multiscale ocean variability: Massachusetts Bay. *Journal of Marine Systems*, 29(1-4):385–422.

Lishaev, P. N., Knysh, V. V., and Korotaev, G. K. (2018). Reproduction of Variability of the Black Sea Level and Pycnocline Characteristics Based on the Adaptive Statistics Method. *Physical Oceanography*, 25(4).

Liu, X., Ma, J., Xu, S., and Wang, B. (2017). On the generation of coastline-following grids for ocean models - trade-off between orthogonality and alignment to coastlines. *Ocean Dynamics*, 67(8):1095–1104.

Madec, G. (2008). NEMO ocean engine. *Note du Pôle de modélisation, Institut Pierre-Simon Laplace (IPSL)*, (27):357pp.

Madec, G., Delecluse, P., Crépon, M., and Lott, F. (1996). Large-Scale Preconditioning of Deep-Water Formation in the Northwestern Mediterranean Sea. *Journal of Physical Oceanography*, 26(8):1393–1408.

Mamayev, O. I. (1975). *Temperature-salinity analysis of World Ocean waters.* Elsevier, Amsterdam.

Mamayev, O. I. (1997). The Black Sea: diffusion process on the basis of the analytic theory of TS-curves. *Okeanologia*, 2:168–177.

Maqueda, M. M. and Holloway, G. (2006). Second-order moment advection scheme applied to Arctic Ocean simulation. *Ocean Modelling*, 14(3-4):197–221.

Maraldi, C., Chanut, J., Levier, B., Ayoub, N., De Mey, P., Reffray, G., Lyard, F., Cailleau, S., Drévillon, M., Fanjul, E. A., Sotillo, M. G., and Marsaleix, P. (2013). NEMO on the shelf: assessment of the Iberia-Biscay-Ireland configuration. *Ocean Science*, 9(4):745–771.

Marchesiello, P., Debreu, L., and Couvelard, X. (2009). Spurious diapycnal mixing in terrain-following coordinate models: The problem and a solution. *Ocean Modelling*, 26(3-4):156–169.

Marchuk, G. I., Kordzadze, A. A., and Skiba, J. N. (1975). Calculations of the basic hydrological fields in the Black Sea. *J. Atmos. Ocean. Phys.*, 11(4):379–393.

Marinova, V. and Valcheva, N. (2017). Black Sea CMEMS reprocessed in-situ temperature and salinity - Quality Information Document. Technical report, http://cmems-resources.cls.fr/documents/QUID/CMEMS-INS-QUID-013-042.pdf.

Marsh, R., Haigh, I. D., Cunningham, S. A., Inall, M. E., Porter, M., and Moat, B. I. (2017). Large-scale forcing of the European Slope Current and associated inflows to the North Sea. *Ocean Science*, 13(2):315–335.

Marshall, J. and Schott, F. (1999). Open-ocean convection: Observations, theory, and models. *Reviews of Geophysics*, 37(1):1–64.

Marti, O., Madec, G., and Delecluse, P. (1992). Comment on 'Net diffusivity in ocean general circulation models with nonuniform grids' by F. L. Yin and I. Y. Fung. *Journal of Geophysical Research*, 97(C8):12763.

Martinho, A. S. and Batteen, M. L. (2006). On reducing the slope parameter in terrain-following numerical ocean models. *Ocean Modelling*, 13(2):166–175.

Masselink, G., Scott, T., Poate, T., Russell, P., Davidson, M., and Conley, D. (2016). The extreme 2013/2014 winter storms: hydrodynamic forcing and coastal response along the southwest coast of England. *Earth Surface Processes and Landforms*, 41(3):378–391.

Medvedev, I. P., Rabinovich, A. B., and Kulikov, E. A. (2016). Tides in Three Enclosed Basins: The Baltic, Black, and Caspian Seas. *Frontiers in Marine Science*, 3.

Mee, L. D. (1992). The Black Sea in Crisis: A Need for Concerted International Action. *Ambio*, 21(4):278–286.

Mellor, G. L. and Blumberg, A. F. (1985). Modeling Vertical and Horizontal Diffusivities with the Sigma Coordinate System. *Monthly Weather Review*, 113(8):1379–1383.

Mellor, G. L., Ezer, T., and Oey, L.-Y. (1994). The Pressure Gradient Conundrum of Sigma Coordinate Ocean Models. *Journal of Atmospheric and Oceanic Technology*, 11(4):1126–1134.

Mellor, G. L., Häkkinen, S. M., Ezer, T., and Patchen, R. C. (2002). A Generalization of a Sigma Coordinate Ocean Model and an Intercomparison of Model Vertical Grids. In Pinardi, N. and Woods, J., editors, *Ocean Forecasting: Conceptual Basis and Applications*, pages 55–72. Springer Berlin Heidelberg, Berlin, Heidelberg.

Mellor, G. L., Oey, L. Y., and Ezer, T. (1998). Sigma coordinate pressure gradient errors and the seamount Problem. *Journal of Atmospheric and Oceanic Technology*, 15(5):1122–1131.

Mellor, G. L. and Yamada, T. (1982). Development of a turbulence closure model for geophysical fluid problems. *Reviews of Geophysics*, 20(4):851.

Metzger, J., Nied, M., Corsmeier, U., Kleffmann, J., and Kottmeier, C. (2018). Dead Sea evaporation by eddy covariance measurements vs. aerodynamic, energy budget, PriestleyâĂŞTaylor, and Penman estimates. *Hydrology and Earth System Sciences*, 22(2):1135–1155.

Miladinova, S., Stips, A., Garcia-Gorriz, E., and Macias Moy, D. (2017). Black Sea thermohaline properties: Long-term trends and variations. *Journal of Geophysical Research: Oceans*, 122(7):5624–5644.

Miladinova, S., Stips, A., Garcia-Gorriz, E., and Macias Moy, D. (2018). Formation and changes of the Black Sea cold intermediate layer. *Progress in Oceanography*, 167:11–23.

Mizyuk, A. I., Puzina, O. S., and Senderov, M. V. (2018). Accuracy of the reconstructed temperature in the Black Sea upper layer from nowcasting/forecasting systems. *Journal of Physics: Conference Series*, 1128(1):12146.

Mooers, C. N. K., editor (1999). *Coastal Ocean Prediction*, volume 56 of *Coastal and Estuarine Studies*. American Geophysical Union, Washington, D. C.

Moskalenko, L. (1975). The numerical calculation of stationary circulation in the Black Sea by the typical wind fields. *Meteorol Gidrol*, 1:58–64 (in Russian).

Murray, J. W., Top, Z., and Özsoy, E. (1991). Hydrographic properties and ventilation of the Black Sea. *Deep Sea Research Part A. Oceanographic Research Papers*, 38(2):683–689.

MyOcean2 (2014). MyOcean catalogue of PRODUCTS, V4.0.

Nansen, F. (1913). The waters of the north-eastern North Atlantic. *International Review of Hydrobiology*, 4:139.

Neev, D. and Emery, K. (1967). The Dead Sea. Depositional processes and environments of evaporites. Technical report, Geological Survey of Israel, Bulletin 41.

Neev, D. and Hall, J. (1979). Geophysical investigations in the Dead Sea. *Sedimentary Geology*, 23:209–238.

Nencioli, F., Petrenko, A. A., and Doglioli, A. M. (2016). Diagnosing cross-shelf transport along an ocean front: An observational case study in the Gulf of Lion. *Journal of Geophysical Research: Oceans*, 121(10):7218–7243.

Neumann, G. (1942). Die absolute Topografie des physikalischen Meeresniveaus und die Oberfl{ä}chenstr{ö}mungen des Schwarzen Meeres. *Annalen der Hydrographie und Maritimen Meteorologie*, 70:265–282.

Nof, D. (1983). The translation of isolated cold eddies on a sloping bottom. *Deep Sea Research Part A, Oceanographic Research Papers*, 30(2):171–182.

Oddo, P., Adani, M., Pinardi, N., Fratianni, C., Tonani, M., and Pettenuzzo, D. (2009). A nested Atlantic-Mediterranean Sea general circulation model for operational forecasting. *Ocean Science*, 5:461–473.

O'Dea, E., Furner, R., Wakelin, S., Siddorn, J., While, J., Sykes, P., King, R., Holt, J., and Hewitt, H. (2017). The CO5 configuration of the 7 km Atlantic Margin Model: large-scale biases and sensitivity to forcing, physics options and vertical resolution. *Geoscientific Model Development*, 10(8):2947–2969.

O'Dea, E. J., Arnold, A. K., Edwards, K. P., Furner, R., Hyder, P., Martin, M. J., Siddorn, J. R., Storkey, D., While, J., Holt, J. T., and Liu, H. (2012). An operational ocean forecast system incorporating NEMO and SST data assimilation for the tidally driven European North-West shelf. *Journal of Operational Oceanography*, 5(1):3–17.

Oguz, T., La Violette, P. E., and Unluata, U. (1992). The upper layer circulation of the Black Sea: Its variability as inferred from hydrographic and satellite observations. *Journal of Geophysical Research*, 97(C8):12569.

Oguz, T., Latun, V., Latif, M., Vladimirov, V., Sur, H., Markov, A., Özsoy, E., Kotovshchikov, B., Eremeev, V., and Ünlüata, Ü. (1993). Circulation in the surface and intermediate layers of the Black Sea. *Deep Sea Research Part I: Oceanographic Research Papers*, 40(8):1597–1612.

Oguz, T., Malanotte-Rizzoli, P., and Aubrey, D. (1995). Wind and thermohaline circulation of the Black Sea driven by yearly mean climatological forcing. *Geophysical Research*, 100(C4):6845–6863.

Oguz, T., Malanotte-Rizzoli, P., and Malanotte, R. (1996). Seasonal variability of wind and thermohaline-driven circulation in the Black Sea: modeling studies. *Journal of Geophysical Research*, 101(C7):16551–16569.

Oguz, T., Tugrul, S., Kideys, A. E., Ediger, V., and Kubilay, N. (2006). Pyhsical and Biogeochemical Characteristics of the Black Sea. In Robinson, A. R. and Brink, K. H., editors, *The Sea. The Global Coastal Ocean: Interdisciplinary Regional Studies and Syntheses*, volume 14A, pages 1333–1372. Harvard University Press.

Ovchinnikov, I. M. and Popov, Y. I. (1987). Evolution of the cold intermediate layer in the Black Sea. *Oceanology*, 27:555–560.

Özsoy, E., Top, Z., White, G., and Murray, J. W. (1991). Double diffusive intrusions, mixing and deep sea convection processes in the Black Sea. In Izdar, E. and Murray, J. M., editors, *The Black Sea Oceanography NATO/ASI Series*, pages 17–42. Kluwer Academic Publishers, Dordrecht.

Pacanowski, R. C., Gnanadesikan, A., and Olume, V. (1998). Transient Response in a Z -Level Ocean Model That Resolves Topography with Partial Cells. *Monthly Weather Review*, 126(12):3248–3270.

Pacanowski, R. C. and Philander, S. G. H. (1981). Parameterization of Vertical Mixing in Numerical Models of Tropical Oceans. *Journal of Physical Oceanography*, 11(11):1443–1451.

Padon, O. and Ashkenazy, Y. (2018). Non-hydrostatic effects in the Dead Sea. *Journal of Marine Systems*, 187:36–51.

Paulson, C. A. and Simpson, J. J. (1977). Irradiance Measurements in the Upper Ocean. *Journal of Physical Oceanography*, 7(6):952–956.

Pedlosky, J. (1982). *Geophysical Fluid Dynamics*, volume 53. Springer Berlin Heidelberg, Berlin, Heidelberg.

Peel, B. L., Finlayson, B. L., and McMahon, T. a. (2007). Updated world map of the K{ö}ppen-Geiger climate classiïňĄcation.pdf. *Hydrology and Earth System Sciences*, 11:1633–1644.

Peneva, E. L. and Stips, A. K. (2005). Numerical simulations of Black Sea and adjoined Azov Sea, forced with climatological and meteorological reanalysis data. Technical report, EUR 21505 EN. CEC JRC, Ispra, Italy.

Pickard, G. L. and Emery, W. J. (1982). *Descriptive Physical Oceanography: An Introduction*. PERGAMON PRESS, 4th edition.

Piggott, M. D., Pain, C. C., Gorman, G. J., Marshall, D. P., and Killworth, P. D. (2008). Unstructured adaptive meshes for ocean modeling. In *Ocean Modeling in an Eddying Regime, Geophysical Monograph Series 177*, pages 383–408. American Geophysical Union.

Pinardi, N. and Woods, J. (2002). *Ocean Forecasting: Conceptual Basis and Applications*. Springer-Verlag, Berlin Heidelberg.

Pingree, R., Mardell, G., Holligan, P., Griffiths, D., and Smithers, J. (1982). Celtic Sea and Armorican current structure and the vertical distributions of temperature and chlorophyll. *Continental Shelf Research*, 1(1):99–116.

Piotukh, V. B., Zatsepin, A. G., Kazmin, A. S., and Yakubenko, V. G. (2011). Impact of the winter cooling on the variability of the thermohaline characteristics of the active layer in the Black Sea. *Oceanology*, 51(2):221–230.

Polton, J. A. (2015). Tidally induced mean flow over bathymetric features: a contemporary challenge for high-resolution wide-area models. *Geophysical & Astrophysical Fluid Dynamics*, 109(3):207–215.

Poulain, P.-M., Barbanti, R., Motyzhev, S., and Zatsepin, A. (2005). Statistical description of the Black Sea near-surface circulation using drifters in 1999âĂŞ2003. *Deep Sea Research Part I: Oceanographic Research Papers*, 52(12):2250–2274.

Qiao, F., Yuan, Y., Yang, Y., Zheng, Q., Xia, C., and Ma, J. (2004). Wave-induced mixing in the upper ocean: Distribution and application to a global ocean circulation model. *Geophysical Research Letters*, 31(11):n/a–n/a.

Rachev, N. H. and Stanev, E. V. (1997). Eddy Processes in Semienclosed Seas: A Case Study for the Black Sea. *Journal of Physical Oceanography*, 27(8):1581–1601.

Radko, T. (2003). A mechanism for layer formation in a double-diffusive fluid. *Journal of Fluid Mechanics*, 497:S0022112003006785.

Radko, T. (2013). *Double-Diffusive Convection*. Cambridge University Press, Cambridge.

Radko, T., Bulters, A., Flanagan, J. D., and Campin, J.-M. (2014). Double-Diffusive Recipes. Part I: Large-Scale Dynamics of Thermohaline Staircases. *Journal of Physical Oceanography*, 44(5):1269–1284.

Raiteri, G., Bordone, A., Ciuffardi, T., and Pennecchi, F. (2018). Uncertainty evaluation of CTD measurements: a metrological approach to water-column coastal parameters in the Gulf of La Spezia area. *Measurement*, 126:156–163.

Redi, M. H. (1982). Oceanic Isopycnal Mixing by Coordinate Rotation. *Journal of Physical Oceanography*, 12(10):1154–1158.

Rippeth, T. P. (2005). Mixing in seasonally stratified shelf seas: a shifting paradigm. *Philosophical Transactions of the Royal Society A: Mathematical, Physical and Engineering Sciences*, 363(1837):2837–2854.

Rippeth, T. P., Fisher, N. R., and Simpson, J. H. (2001). The Cycle of Turbulent Dissipation in the Presence of Tidal Straining. *Journal of Physical Oceanography*, 31(8):2458–2471.

Roberts, M. and Marshall, D. (1998). Do We Require Adiabatic Dissipation Schemes in Eddy-Resolving Ocean Models? *Journal of Physical Oceanography*, 28(10):2050–2063.

Robinson, A. and Brink, K., editors (2006). *The Global Coastal Ocean: Interdisciplinary Regional Studies and Syntheses, The Sea, Vol. 14A-B*. Harvard University Press, reprinted edition.

Robinson, A. R. and Sellschopp, J. (2002). Rapid Assessment of the Coastal Ocean Environment. In Pinardi, N. and Woods, J., editors, *Ocean Forecasting: Conceptual Basis and Applications*, chapter 11, page 472. Springer-Verlag, Berlin Heidelberg.

Robinson, I. (1983). Tidally Induced Residual Flows. In Johns, B., editor, *Physical Oceanography of Coastal and Shelf Seas*, chapter 7, pages 321–356. Elsevier Oceanography Series, vol. 35 edition.

Roquet, F., Madec, G., Brodeau, L., and Nycander, J. (2015). Defining a Simplified Yet Realistic Equation of State for Seawater. *Journal of Physical Oceanography*, 45(10):2564–2579.

Sakov, P. (2015). Orthogonal multi-corner grid generator. *https://github.com/sakov/gridgen-c*.

Salameh, E. and Khawaj, M. (1984). The Mediterranean - Dead Sea canal and its environmental impacts. Technical report, University of Jordan - Water Research and Study Center, Aman.

Samodurov, A. S. (2009). Near-bottom boundary layer in the Black Sea: formation of a steady state. *Morskoy Gidrofizicheskiy Zhurnal*, 1:16–25.

Samodurov, A. S. and Ivanov, L. I. (2002). Balance model to calculate the average vertical flow, heat, salt and dissolved chemicals in the Black Sea termo-halokline. *Morskoy Gidrofizicheskiy Zhurnal*, 1:7–24.

Sarkisyan, A. (1969). Deficiencies of Barotropic Models of Ocean Currents. *Izv. Akad. Nauk SSSR, Fiz. Atmos. Okeana*, 5:818–836.

Sarkisyan, A. and Ivanov, V. (1971). The combined effect of baroclinicity and bottom relief as an important factor in the dynamics of ocean currents (AGU translation). *Izv. Acad. Sci. USSR, Atmos. Oceanic Phys*, pages 173–188.

Sarkisyan, A. S. and Dzioev, T. Z. (1974). A numerical model and calculation of currents in the Black Sea. *Meteorol. Gidrol.*, 3:71–76.

Schmitt, R. W. (2005). Enhanced Diapycnal Mixing by Salt Fingers in the Thermocline of the Tropical Atlantic. *Science*, 308(5722):685–688.

Schrum, C., Staneva, J., Stanev, E., and Özsoy, E. (2001). AirâĂŞsea exchange in the Black Sea estimated from atmospheric analysis for the period 1979âĂŞ1993. *Journal of Marine Systems*, 31(1-3):3–19.

Shapiro, G., Akivis, T., Pykhov, N., and Antsyferov, S. (2000). Transport of fine sediment with mesoscale currents in the shelf- slope zone of the sea. *Oceanology*, 40:305–311.

Shapiro, G., Gertman, I., Manasrah, R., and Bruciaferri, D. (2019). The effect of thermohaline staircases on the sea level in the Dead Sea. *Journal of Marine Systems*, under revi.

Shapiro, G. I. (2003). Dense water cascading off the continental shelf. *Journal of Geophysical Research*, 108(C12):1–19.

Shapiro, G. I. (2008). Black Sea Circulation. *Encyclopedia of Ocean Sciences*, pages 401–414.

Shapiro, G. I. (2011). Effect of tidal stream power generation on the region-wide circulation in a shallow sea. *Ocean Science*, 7(1):165–174.

Shapiro, G. I. and Hill, A. E. (1997). Dynamics of Dense Water Cascades at the Shelf Edge. *Journal of Physical Oceanography*, 27(11):2381–2394.

Shapiro, G. I., Luneva, M., Pickering, J., and Storkey, D. (2013). The effect of various vertical discretization schemes and horizontal diffusion parameterization on the performance of a 3-D ocean model: the Black Sea case study. *Ocean Science*, 9(2):377–390.

Shapiro, G. I., Stanichny, S. V., and Stanychna, R. R. (2010). Anatomy of shelf-deep sea exchanges by a mesoscale eddy in the North West Black Sea as derived from remotely sensed data. *Remote Sensing of Environment*, 114(4):867–875.

Shapiro, G. I., Wobus, F., and Aleynik, D. L. (2011). Seasonal and inter-annual temperature variability in the bottom waters over the western Black Sea shelf. *Ocean Science*, 7(5):585–596.

Sharples, J., Moore, C. M., and Abraham, E. R. (2001). Internal tide dissipation, mixing, and vertical nitrate flux at the shelf edge of NE New Zealand. *Journal of Geophysical Research: Oceans*, 106(C7):14069–14081.

Sharples, J. and Simpson, J. (2009). Shelf Sea and Shelf Slope Fronts. In *Encyclopedia of Ocean Sciences*, pages 391–400. Elsevier.

Shchepetkin, A. F. (2003). A method for computing horizontal pressure-gradient force in an oceanic model with a nonaligned vertical coordinate. *Journal of Geophysical Research*, 108(C3):3090.

Shchepetkin, A. F. and McWilliams, J. C. (2005). The regional oceanic modeling system (ROMS): a split-explicit, free-surface, topography-following-coordinate oceanic model. *Ocean Modelling*, 9(4):347–404.

Shom (2018). EMODnet Digital Bathymetry (DTM 2018).

Siddorn, J. R. and Furner, R. (2013). An analytical stretching function that combines the best attributes of geopotential and terrain-following vertical coordinates. *Ocean Modelling*, 66:1–13.

Sikirić, M. D., Janeković, I., and Kuzmić, M. (2009). A new approach to bathymetry smoothing in sigma-coordinate ocean models. *Ocean Modelling*, 29(2):128–136.

Simonov, A. I. and Altman, E. N. (1991). *Hydrometeorology and hydrochemistry of seas in the USSR, vol IV. Black Sea. Issue 1. Hydrometeorological conditions.* Gidrometeoizdat, Leningrad.

Simpson, J. (1997). Physical processes in the ROFI regime. *Journal of Marine Systems*, 12(1-4):3–15.

Simpson, J. and Bowers, D. (1981). Models of stratification and frontal movement in shelf seas. *Deep Sea Research Part A. Oceanographic Research Papers*, 28(7):727–738.

Simpson, J. H. (1998). Tidal processes in shelf seas. In Brink, K. H. and Robinson, A. R., editors, *The Sea Vol. 10*, pages 113–150. John Wiley & Sons, New York.

Simpson, J. H., Allen, C. M., and Morris, N. C. G. (1978). Fronts on the continental shelf. *Journal of Geophysical Research*, 83(C9):4607.

Simpson, J. H., Crisp, D. J., and Hearn, C. (1981). The Shelf-Sea Fronts: Implications of their Existence and Behaviour [and Discussion]. *Philosophical Transactions of the Royal Society A: Mathematical, Physical and Engineering Sciences*, 302(1472):531–546.

Simpson, J. H. and Hunter, J. R. (1974). Fronts in the Irish Sea. *Nature*, 250(5465):404–406.

Simpson, J. H. and Sharples, J. (2012). *Introduction to the Physical and Biological oceanography of Shelf Seas.* Cambridge and New York: Cambridge University Press.

Sirkes, Z. (1986). *Seiches and Currents in the Dead Sea.* Ph.d. thesis, Weizmann Institute of Science, Israel.

Smagorinsky, J. (1963). General circulation experiments with the primitive equations. *Monthly Weather Review*, 91(3):99–164.

Smagorinsky, J. (1993). Large Eddy Simulation of Complex Engineering and Geophysical Flows. In Galperin, B. and Orszag, S., editors, *Evolution of Physical Oceanography*, pages 3–36. Cambridge University Press.

Smith, N. R. and Hess, G. D. (1993). A Comparison of Vertical Eddy Mixing Parameterizations for Equatorial Ocean Models. *Journal of Physical Oceanography*, 23(8):1823–1830.

Song, Y. and Haidvogel, D. (1994). A Semi-implicit Ocean Circulation Model Using a Generalized Topography-Following Coordinate System. *Journal of Computational Physics*, 115(1):228–244.

Song, Y. T. and Hou, T. Y. (2006). Parametric vertical coordinate formulation for multiscale, Boussinesq, and non-Boussinesq ocean modeling. *Ocean Modelling*, 11(3-4):298–332.

Speziale, C. G. (1987). On the advantages of the vorticity-velocity formulation of the equations of fluid dynamics. *Journal of Computational Physics*, 73(2):476–480.

Stanev, E., Beckers, J., Lancelot, C., Staneva, J., Le Traon, P., Peneva, E., and Gregoire, M. (2002). CoastalâĂŞopen Ocean Exchange in the Black Sea: Observations and Modelling. *Estuarine, Coastal and Shelf Science*, 54(3):601–620.

Stanev, E., Staneva, J., Bullister, J., and Murray, J. (2004). Ventilation of the Black Sea pycnocline. Parameterization of convection, numerical simulations and validations against observed chlorofluorocarbon data. *Deep Sea Research Part I: Oceanographic Research Papers*, 51(12):2137–2169.

Stanev, E. V. (1990). On the mechanisms of the Black Sea circulation. *Earth-Science Reviews*, 28(4):285–319.

Stanev, E. V. (2005). Understanding Black Sea Dynamics: Overview of Recent Numerical Modeling. *Oceanography*, 18(2):56–75.

Stanev, E. V. and Beckers, J.-M. M. (1999). Numerical simulations of seasonal and interannual variability of the Black Sea thermohaline circulation. *Journal of Marine Systems*, 22(4):241–267.

Stanev, E. V., Bowman, M. J., Peneva, E. L., and Staneva, J. V. (2003). Control of Black Sea intermediate water mass formation by dynamics and topography: Comparison of numerical simulations, surveys and satellite data. *Journal of Marine Research*, 61(1):59–99.

Stanev, E. V., Grashorn, S., and Zhang, Y. J. (2017). Cascading ocean basins: numerical simulations of the circulation and interbasin exchange in the Azov-Black-Marmara-Mediterranean Seas system. *Ocean Dynamics*, 67(8):1003–1025.

Stanev, E. V., Peneva, E., and Chtirkova, B. (2019). Climate Change and Regional Ocean Water Mass Disappearance: Case of the Black Sea. *Journal of Geophysical Research: Oceans*, page 2019JC015076.

Stanev, E. V. and Rachev, N. H. (1999). Numerical study on the planetary Rossby modes in the Black Sea. *Journal of Marine Systems*, 21(November 1997):283–306.

Stanev, E. V. and Staneva, J. V. (2000). The impact of the baroclinic eddies and basin oscillations on the transitions between different quasi-stable states of the Black Sea circulation. *Journal of Marine Systems*, 24(1-2):3–26.

Stanev, E. V., Staneva, J. V., and Roussenov, V. M. (1997). On the Black Sea water mass formation. Model sensitivity study to atmospheric forcing and parameterizations of physical processes. *Journal of Marine Systems*, 13(1-4):245–272.

Staneva, J., Wahle, K., Koch, W., Behrens, A., Fenoglio-Marc, L., and Stanev, E. V. (2016). Coastal flooding: impact of waves on storm surge during extremes – a case study for the German Bight. *Natural Hazards and Earth System Sciences*, 16(11):2373–2389.

Staneva, J. V., Dietrich, D. E., Stanev, E. V., and Bowman, M. J. (2001). Rim current and coastal eddy mechanisms in an eddy-resolving Black Sea general circulation model. *Journal of Marine Systems*, 31(1-3):137–157.

Staneva, J. V., Stanev, E. V., and Rachev, N. H. (1995). Heat balance estimates using atmospheric analysis data: A case study for the Black Sea. *J. Geophys. Res*, 100(C9):518–581.

Steinhorn, I. (1981). *A hydrographical and physical study of the Dead Sea during the destruction of its long-term meromictic stratification.* Phd thesis, Weizman Institute of Science, Rehovot, Israel.

Steinhorn, I. and Assaf, G. (1980). The physical structure of the Dead Sea water column, 1975 - 1977. In Nissenbaum, A., editor, *Hypersaline Brines and Evaporitic Environments*, pages 155–166. Elsevier, Amsterdam.

Steinhorn, I. and Gat, J. (1983). The Dead Sea. *Scientific American*, 249((4)):102–109.

Stern, M. E. (1960). The âĂIJSalt-FountainâĂİ and Thermohaline Convection. *Tellus*, 12(2):172–175.

Stern, M. E. (2003). Initiation of a doubly diffusive convection in a stable halocline. *Journal of Marine Research*, 61(2):211–233.

Stommel, H. (1948). The westward intensification of wind-driven ocean currents. *Transactions, American Geophysical Union*, 29(2):202.

Sukhikh, L. and Dorofeyev, V. (2016). The Study of Sensitivity of the Black Sea Hydrophysical Fields Reanalysis Results to the Applied Atmospheric Forcing. *Physical Oceanography*, (5).

Sündermann, J., Lenz, W., Beddig, S., Huthnance, J., and Mooers, C. N. K. (2001). Impact of climate change on the coastal zone: discussion and conclusions. *Climate Research*, 18(1-2):1–3.

Suvorov, A., Palmer, D., Khaliulin, A., Godin, E., and Belokopytov, V. (2003). Digital atlas and evaluation of the influence of inter-annual variability on climate analyses. In *Oceans 2003. Celebrating the Past ... Teaming Toward the Future (IEEE Cat. No.03CH37492)*, pages 990–995 Vol.2. IEEE.

Sverdrup, H. U., Johnson, M. W., and Fleming, R. H. (1942). *The Oceans: Their Physics, Chemistry, and General Biology.* Prentice-Hall, New Yprk.

Talley, L. D., Pickard, G. L., and Emery, W. J. (2011a). *Descriptive Physical Oceanography: An Introduction.* PERGAMON PRESS, 6th edition.

Talley, L. D., Pickard, G. L., Emery, W. J., and Swift, J. H. (2011b). Dynamical Processes for Descriptive Ocean Circulation. In *Descriptive Physical Oceanography*, pages 1–72. Elsevier.

Thomas, H., Bozec, Y., Elkalay, K., and de Baar, H. J. W. (2004). Enhanced open ocean storage of CO2 from shelf sea pumping. *Science (New York, N.Y.)*, 304(5673):1005–1008.

Timmermann, R. and Beckmann, A. (2004). Parameterization of vertical mixing in the Weddell Sea. *Ocean Modelling*, 6(1):83–100.

Tonani, M., Sykes, P., King, R. R., McConnell, N., Péquignet, A.-C., O'Dea, E., Graham, J. A., Polton, J., and Siddorn, J. (2019). The impact of a new high-resolution ocean model on the Met Office North-West European Shelf forecasting system. *Ocean Science*, 15(4):1133–1158.

Treguier, A. M., Dukowicz, J. K., and Bryan, K. (1996). Properties of nonuniform grids used in ocean general circulation models. *Journal of Geophysical Research: Oceans*, 101(C9):20877–20881.

Trotta, F., Fenu, E., Pinardi, N., Bruciaferri, D., Giacomelli, L., Federico, I., and Coppini, G. (2016). A Structured and Unstructured grid Relocatable ocean platform for Forecasting (SURF). *Deep-Sea Research Part II: Topical Studies in Oceanography*, 133:54–75.

Trotta, F., Pinardi, N., Fenu, E., Grandi, A., and Lyubartsev, V. (2017). Multi-nest high-resolution model of submesoscale circulation features in the Gulf of Taranto. *Ocean Dynamics*, 67(12):1609–1625.

Tuzhilkin, V. S. (2008). Thermohaline structure of the Sea. In Kostianoy, A. and Kosarev, A., editors, *The Black Sea Environment. The Handbook of Environmental Chemistry*, volume 5, chapter Vol. 5, Pa, pages 217–254. Springer-Verlag, Berlin Heidelberg, vol. 5, pa edition.

Umlauf, L. and Burchard, H. (2003). A generic length-scale equation for geophysical turbulence models. *Journal of Marine Research*, 61(2):235–265.

Umlauf, L. and Burchard, H. (2005). Second-order turbulence closure models for geophysical boundary layers. A review of recent work. *Continental Shelf Research*, 25(7-8):795–827.

UNESCO (1983). Algorithms for computation of fundamental property of sea water. *Techn. Paper in Mar. Sci*, 44.

Vadasz, P., Weiner, D., and Zvirin, Y. (1983). A Halo-Thermal Simulation of the Dead Sea for Application to Solar Energy Projects. *Journal of Solar Energy Engineering*, 105(4):348.

Valeport (2017). Model 106 Current Meter.

http://www.valeport.co.uk/Portals/0/Docs/Datasheets/Valeport-Model-106.pdf. Accessed 12 November 2017.

Valiente, N. G., Masselink, G., Scott, T., Conley, D., and McCarroll, R. J. (2019). Role of waves and tides on depth of closure and potential for headland bypassing. *Marine Geology*, 407:60–75.

Vallis, G. (2006). *Atmospheric and Oceanic Fluid Dynamics*. Cambridge University Press, Cambridge, U.K.

Vespremeanu, E. and Golumbeanu, M. (2018). Black Sea Coastal Population. In *The Black Sea*, pages 115 – 124. Springer International Publishing.

Waiser, M. and Robarts, R. (2009). Saline Inland Waters. In *Encyclopedia of Inland Waters*, pages 634–644. Elsevier.

Wakelin, S. L., Holt, J. T., and Proctor, R. (2009). The influence of initial conditions and open boundary conditions on shelf circulation in a 3D ocean-shelf model of the North East Atlantic. *Ocean Dynamics*, 59(1):67–81.

Whitehead, J. A. (1987). Dense water off continents. *Nature*, 327:656.

Wilkin, J. L. (2005). A regional ocean modeling system for the Long-term Ecosystem Observatory. *Journal of Geophysical Research*, 110(C6):C06S91.

Wobus, F., Shapiro, G. I., Huthnance, J. M., and Maqueda, M. A. M. (2013). The piercing of the Atlantic Layer by an Arctic shelf water cascade in an idealised study inspired by the Storfjorden overflow in Svalbard. *Ocean Modelling*, 71:54–65.

Wobus, F., Shapiro, G. I., Maqueda, M., and Huthnance, J. (2011). Numerical simulations of dense water cascading on a steep slope. *Journal of Marine Research*, 69(2):391–415.

Wright, W. R. and Parker, C. E. (1976). A volumetric temperature/salinity census for the Middle Atlantic Bight1. *Limnology and Oceanography*, 21(4):563–571.

Xu, S., Wang, B., and Liu, J. (2015). On the use of SchwarzâĂŞChristoffel conformal mappings to the grid generation for global ocean models. *Geoscientific Model Development*, 8(10):3471–3485.

Yechieli, Y. (2006). Response of the groundwater system to changes in the Dead Sea level. In Enzel, Y., Agnon, A., and Stein, M., editors, *Special Paper 401: New Frontiers in Dead Sea Paleoenvironmental Research*, pages 113–126. Geological Society of America, Boulder.

Zatsepin, A. G., Ginzburg, A. I., Kostianoy, A. G., Kremenetskiy, V. V., Krivosheya, V. G., Stanichny, S. V., and Poulain, P. (2003). Observations of Black Sea mesoscale eddies and associated horizontal mixing. *Journal of Geophysical Research*, 108(C8):3246.

Zavatarelli, M., Pinardi, N., Kourafalou, V., and Maggiore, A. (2002). Diagnostic and prognostic model studies of the Adriatic Sea general circulation: Seasonal variability. *Journal of Geophysical Research*, 107(C1):3004.

Zhang, W. G. and Gawarkiewicz, G. G. (2015). Dynamics of the direct intrusion of Gulf Stream ring water onto the Mid-Atlantic Bight shelf. *Geophysical Research Letters*, 42(18):7687–7695.

Zhou, F., Shapiro, G. I., and Wobus, F. (2014). Cross-shelf exchange in the northwestern Black Sea. *Journal of Geophysical Research: Oceans*, 119(4):2143–2164.

Zodiatis, G. and Gasparini, G. P. (1996). Thermohaline staircase formations in the Tyrrhenian Sea. *Deep Sea Research Part I: Oceanographic Research Papers*, 43(5):655–678.